Stellingen

behorende bij het proefschrift

Modelling of NO_x formation in a high temperature gas-fired furnace

van C.L. Koster

1. De lengte van een turbulente diffusievlam van een gasvormige brandstof is evenredig met de diameter van de injectiepoort en is onafhankelijk van de injectiesnelheid van de brandstof.
2. Menging van brandstof en verbrandingslucht speelt bij de NO_x-vorming in hoge temperatuur ovens een cruciale rol; door de menging te optimaliseren kan de NO_x-vorming geminimaliseerd worden.
   Dit proefschrift
3. De afhankelijkheid van de NO_x-emissie van de menghoek tussen brandstof en verbrandingslucht is niet te verklaren met behulp van alleen de penetratiediepte. Bij een beschouwing dient ook de invloed van de menghoek op de uitbrandsnelheid en de vlamtemperatuur te worden betrokken.
   Kamp, W.L. van de, Smart, J.P., Nakamura, T. and Morgan, M.E. (1989) NO_x reduction and heat transfer characteristics in gas fired glass furnaces. Technical Report IFRF Doc.No. f 90/a/4, IFRF, IJmuiden, The Netherlands.
4. Normen voor de uitstoot van vervuilende stoffen zouden gebaseerd moeten zijn op een emissie per eenheid product en niet op een emissie per eenheid rookgas.
5. Voorkennis van een met een numeriek stromingsmodel te berekenen stroming is gewenst bij de interpretatie van de berekende resultaten.
6. Geen meetrapport is compleet zonder een goede foutenanalyse.
7. De Nederlandse industrie is gebaat bij een streng emissiebeleid van de Nederlandse overheid.
8. Een roman is niet een beschrijving van de werkelijkheid, maar een vervanging hiervan.
9. Een (bedrijfs)reorganisatie dient te worden doorgevoerd met het oog op de toekomst van het bedrijf. Hierbij is een goede timing essentieel, dat wil zeggen dat de reorganisatie moet plaatsvinden vóórdat het bedrijf in de problemen komt.
10. Als de mens zijn vingers zou gebruiken om op binaire wijze te tellen, zou hij in staat zijn op zijn vingers tot 1023 te tellen. Alleen al het feit dat de meeste mensen moeite hebben met het strekken van bepaalde vingers, terwijl de andere vingers gebogen moeten blijven, maakt dat dit voor de meesten geen voordeel zou opleveren.

MODELLING OF NO_x FORMATION IN A HIGH TEMPERATURE GAS-FIRED FURNACE

MODELLING OF NO_x FORMATION IN A HIGH TEMPERATURE GAS-FIRED FURNACE

Proefschrift

ter verkrijging van de graad van doctor
aan de Technische Universiteit Delft,
op gezag van de Rector Magnificus,
Prof. drs. P.A. Schenck,
in het openbaar te verdedigen
ten overstaan van
een commissie aangewezen door
het College van Dekanen
op dinsdag 29 juni 1993 te 10.00 uur

door

Cornelis Lodewijk Koster

geboren te Rotterdam
natuurkundig ingenieur

Dit proefschrift is goedgekeurd door de promotor:
Prof. ir. C.J. Hoogendoorn.

Published and distributed by:

Delft University Press
Stevinweg 1
2628 CN Delft
The Netherlands

Telephone +31 15 783254
Fax +31 15 781661

CIP-DATA KONINKLIJKE BIBLIOTHEEK, THE HAGUE

Koster, C.L.

Modelling of NO_x Formation in a High Temperature Gas-Fired Furnace / C.L. Koster.
- Delft University Press. - Ill.
PhD Thesis Delft University of Technology. - With lit. - With summary in Dutch.
ISBN 90-6275-883-5
NUGI 848
Keywords: combustion, NO_x formation, modelling

Printed in The Netherlands

These investigations were supported by the Netherlands' Foundation for Chemical Research (SON) with financial aid from the Netherlands' Technology Foundation (STW).

Financial support of the N.V. Nederlandse Gasunie is gratefully acknowledged.

'De mens is sterfelijk,' zo denk ik erover. Maar als we nu eenmaal toch geboren zijn — dan is er niets aan te doen, dan moet je echt een beetje leven... 'Het leven is prachtig' — zo denk ik erover.
Uit *Moskou op sterk water*, Venedikt Jerofejev (1979)

Contents

Chapter 1

Introduction

1.1 Background

Fossil fuels are the most important source of energy for the generation of heat needed in industry. However, the combustion of fossil fuels is a source of growing concern for the environment. The greenhouse effect is expected to give rise to climate changes and acid rain has proven to be disastrous to forests. Environmental effects of the use of fossil fuels and growing concern of the public for these matters have been an incentive for governments to enact new legislation on the emission of polluting gases. In The Netherlands the government has recently signed agreements with several industries in which a reduction of the emission of pollutants is arranged. E.g. the Dutch glass industry has recently signed an agreement with the Dutch Ministry of Economic Affairs in which the aim of an efficiency improvement of 20 % is stated. Also, the Dutch government in collaboration with the glass industry, is preparing new directives for the emission of polluting gases. It is likely that the emissions of e.g. NO_x will have to be decreased by 50 to 75 % in 1998, relative to the emissions of a reference year, viz. 1985 or 1990.

Because of the new legislation there is a growing demand for research on combustion and formation of pollutants. In The Netherlands the Dutch gas company, N.V. Nederlandse Gasunie, has initiated several research projects in which the combustion of natural gas is studied. One of these projects is concerned with the glass industry and the combustion of natural gas in high temperature furnaces. The production of glass requires high temperatures, typically 1500 to 1900 K for the molten glass. This requires even hotter furnaces and consequently the emissions of NO_x are high, typically in the range of 900 - 2800 ppm (at 3 % O_2, Kircher (1986)). An international consortium of gas companies, including Gasunie, has commissioned two experimental studies on a semi-industrial scale at the International Flame Research Foundation (IFRF) at IJmuiden, The Netherlands. The aim of these studies was to investigate the combustion of natural gas and the formation of NO_x in a high temperature furnace. Several methods to reduce the NO_x formation were studied experimentally.

At the same time as the experimental study this simulation study at the Delft University of Technology was started. It was funded by the Netherlands' Foundation for Chemical Research (SON), the Netherlands' Technology Foundation (STW) and Gasunie. This thesis describes numerical simulations of the combustion of natural

gas and the formation of thermal NO_x in the geometry of the IFRF furnace that has been used for the experimental studies. Results of experiments performed by the IFRF were made available to us so that the numerical model could be validated and predicted NO_x emission trends could be compared with measured trends. Also, since the experimental study and the numerical study were performed simultaneously the results of the simulations could be helpful in specifying a new experimental program.

The numerical model that was developed previously by Post (1988) has been adapted and extended with an NO_x formation model for this thesis. The model has been used to study NO_x formation and possible ways of reducing NO_x emissions in the framework of two trials by the IFRF (NG6 and NG7). The result of this work, however, is applicable to other furnace configurations than only the IFRF furnace. With the numerical model trend studies can be performed and the range of the NO_x emission for a particular furnace or burner type can be determined.

1.2 High temperature combustion systems

To achieve high temperatures in furnaces, as required for the industrial processes, it is necessary to use preheated combustion air. Usually, combustion air is preheated by some way of heat retrieval from the flue gases of the furnace. Two systems for this heat retrieval can be distinguished , viz. recuperative and regenerative. In a recuperative system hot flue gases are led through a heat exchanger in co- or counter-flow with the combustion air. This is a continuous process, so that the combustion process can be continuous as well. In a regenerative system the hot flue gases are led through a heat resistant brick checker work, which heats up. Another regenerator that has been heated up before supplies the combustion air to the burner system. After a certain period, for glass melting furnaces typically 20 minutes, the flow direction is switched, so that the heated regenerator now supplies the combustion air and the other regenerator is heated. For glass melting furnaces both methods for heat retrieval are used. Regenerators are more efficient in retrieving heat, but are also more expensive. Examples of recuperative and regenerative glass melting furnaces are shown in figure 1.1.

The IFRF furnace uses a regenerative means of combustion air preheating, although not with the flue gases. Three regenerators are separately fired and used to supply the preheated combustion air in a switching scheme with a period of 1 minute. Because of the separate regenerator system the flow direction is not reversed in the IFRF furnace.

In glass furnaces several types of burners can be distinguished by viewing the position of the natural gas injection port with respect to the combustion air port. Underport and sideport firing are commonly used injection modes, but other possible configurations are overport, throughport and parallel sideport firing. In figure 1.2 these firing modes are illustrated for the geometry that was used in the IFRF furnace.

We will only concern ourselves with natural gas firing in the IFRF furnace. In 1981 45 % of the glass furnaces in Western Europe were fired with natural gas

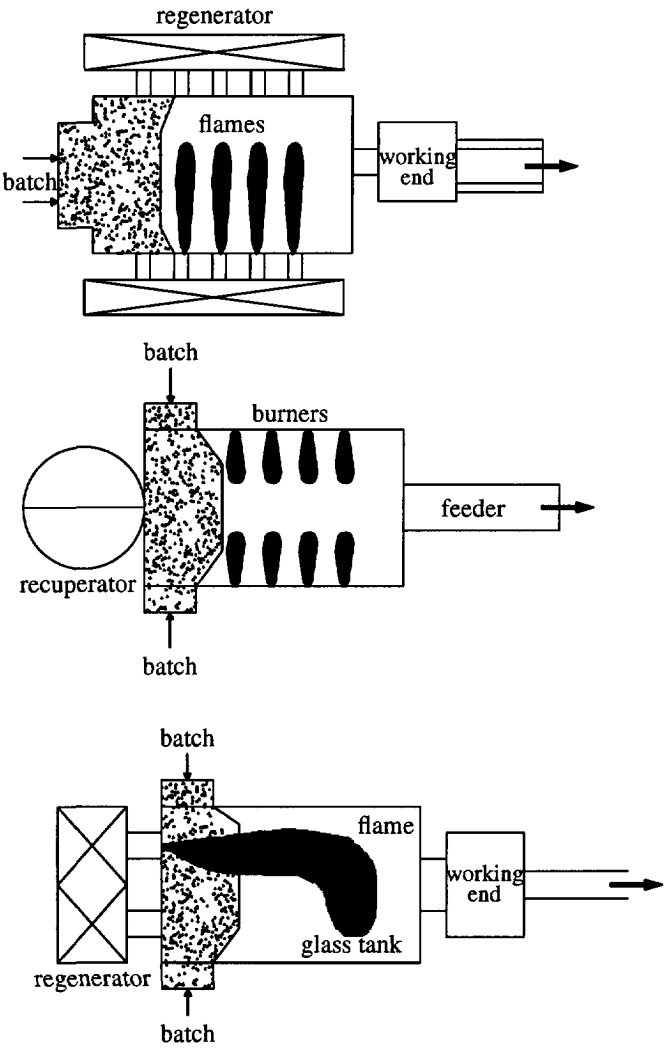

Figure 1.1: Different firing systems: a. cross-fired regenerative furnace, b. cross-fired recuperative system, c. end-fired regenerative system (U-flame).

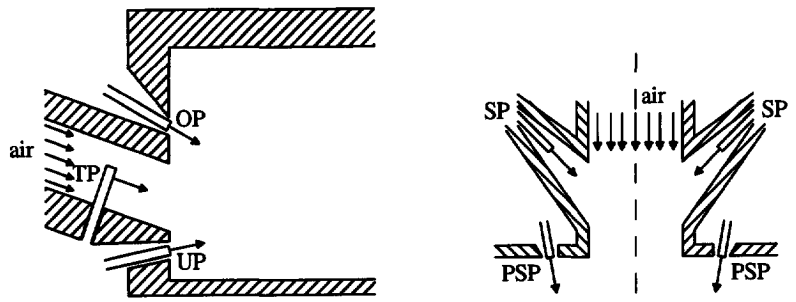

Figure 1.2: Different burner systems: a. cross-section in a vertical plane with fuel inlets for underport (UP), overport (OP) and throughport (TP) firing, b. cross-section in a horizontal plane with fuel inlets for sideport (SP) and parallel sideport (PSP) firing.

(Beerkens (1986)). This has the advantage over oil firing, at least in The Netherlands with its high quality natural gas, that there is no SO_2 emission. Compared with oil firing the NO_x emissions are slightly higher. NO_x is a combination of 95 % NO and 5 % NO_2, but in this thesis the NO_2 formation will be neglected in the modeling. The resulting NO emission will often be called the NO_x emission, because most of the NO_2 will be formed from the NO that was previously formed in the flame. Because of the high temperature in the furnace and the absence of fuel-bound nitrogen in natural gas, thermal NO formation is the predominant way in which the NO is formed.

Normally, to ensure complete burnout of the flame and to prevent high CO emissions, a furnace is fired with some excess air. In the baseline flames as defined by the IFRF the excess air level was 10 %. In this thesis we will often refer to the excess air level in terms of the airfactor. The airfactor λ is defined as (1 + excess air level expressed as a fraction).

1.3 Aims of this study

The model described in this thesis is concerned with flow, combustion, radiative heat transfer and NO_x formation in a glass melting furnace. Previously, the numerical model for the flow, the combustion and the radiative heat transfer had already been developed by Post (1988). This work is the continuation of the study of Post, but the aim is now directed towards the application of the model for practical problems and towards the formation of NO_x in high temperature furnaces.

In the type of furnace that we study in this thesis the turbulent mixing of fuel and air and the radiative heat transfer are the two main processes that determine the

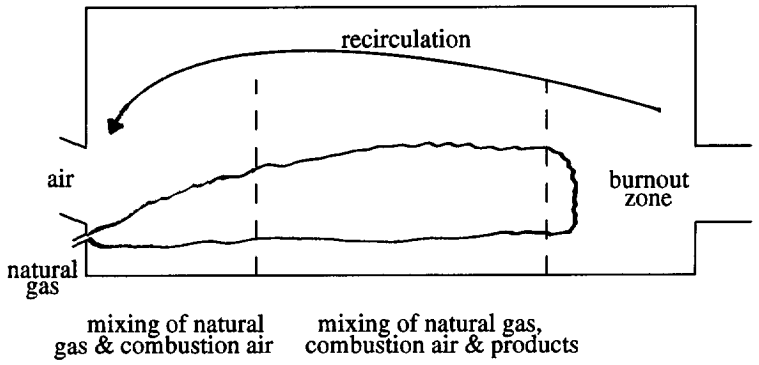

Figure 1.3: Schematic representation of the mixing regions in the IFRF furnace.

flow and the combustion. An illustration of the different mixing regions is given in figure 1.3. Near the inlet of the furnace natural gas mixes with combustion air and some recirculated combustion products. In this region the flame develops and the combustion takes place rapidly in the envelope of the flame. Locally very high temperatures are achieved in the flame envelope. Further downstream the fully developed flame mixes with combustion products and excess combustion air from the envelope of the flame. Because of this mixing and the heat losses upstream the local temperature is not as high as in the beginning of the flame. The large volume of the flame here loses most of its heat by radiation. At the end of the furnace complete burnout is achieved and a part of the combustion products enters the recirculation in the upper half of the furnace. Most of the fluid leaves the furnace through the chimney.

Fuel and air enter the furnace separately. Because the combustion reactions take place very quickly, the rate of combustion is determined by the mixing of the fuel and the air. The heat release and the local temperature are thus also determined by the mixing of the fluids in the furnace. The NO formation is slow compared with the combustion and is determined by the local temperature and the oxygen concentrations throughout the furnace. Thus, the NO formation is influenced by the mixing of fuel and air, by the local heat release and the heat losses. Since the thermal NO formation is highly sensitive to temperature, a local peak temperature influences the flue gas NO_x emission.

Because of the influence of the mixing on the combustion and the consequences for the local temperature, it is an interesting option to try to prevent local peak temperatures. When the total volumetric heat release, that is determined by the flow rate of the fuel, is spread over a large volume, the occurrence of peak temperatures in the flame is avoided. Because the average temperature is still high the heat transfer to the load, e.g. in a glass melting furnace the molten glass in the glass bath, can be maintained at

acceptable values. The thermal NO formation however is only important at temperatures above 1800 K, which is in the peak temperature regions of the flame. If the peak temperature were to be lowered, this could reduce the NO_x emission substantially.

One of the aims of this study can thus be posed now: What is the influence of the mixing of furnace gases on the formation of NO? And consequently: How should one optimize the mixing in the sense that both the process conditions are maintained at the required values and the NO_x emission is minimized?

The first question is the more fundamental one. Many studies have been published on the kinetics of the combustion reactions and the formation of thermal NO_x. Also, detailed flame measurements have been performed to study the formation of NO in laboratory scale flames. These are mostly premixed flames, where the combustion chemistry plays an important role and the flow and the thermal radiation are of minor importance. In this thesis many of the details of the chemical kinetics of the combustion itself have been neglected, but the flow model and the radiative heat transfer model are accurate. For the type of combustion at high temperatures that we are modelling, these are of more importance than the detailed flame chemistry. The influence of the mixing of fuel and air and the resulting temperature and species concentration distributions on the NO_x formation demand a good flow model and accurate temperature predictions. By applying the numerical model to a number of flow configurations one is able to assess the influence of mixing parameters on the NO_x formation.

The second question is a more practical problem. Once the influence of the mixing is understood or the effect has been studied for a number of cases, one would like to be able to use the numerical model for predictions of the NO_x emissions for new types of furnaces or for different burner configurations in the furnace. This requires careful application of the numerical model for a case, where one expects promising results. It is important in such a case, that the limitations of the numerical model are taken into account. Flow situations, where the combustion model is no longer valid, e.g. in cases where the combustion chemistry may become important locally, may give erroneous results for both the combustion and the NO formation predictions. The application of the numerical model requires careful and detailed assessment of the results.

It is very important to be able to verify the results of the simulations with measured results. A well validated model can be applied for predictions in other furnaces more easily, since the limits and the validity of the sub-models are known. Validation of the numerical model FURNACE that we have been using is an important part of this thesis. This study includes the development of an isothermal scale model of the IFRF furnace, from which experimental data have been obtained. These data will be compared with data obtained by performing isothermal simulations with FURNACE to validate our turbulent flow model. Verification of the numerical model for a flow with combustion reveals more of the strengths and weaknesses of the model. Because of our cooperation with Gasunie and the International Flame Research Foundation many experimental data from a test furnace have come at our disposal. We will discuss the important characteristics of relevant flames and will discuss the similarities and

differences between the measurements and the simulations. Based on the verification we will try to determine limits of applicability of the numerical model. For future simulations it is important to know whether the model will (probably) be applicable or not.

Application of numerical models to large scale practical problems is by no means common practise yet. Three-dimensional flow calculations, coupled with combustion and a three dimensional radiative heat transfer model present a complex problem. The formation of thermal NO_x is an important addition to the numerical model and opens up the possibility of applying the numerical model to practical problems, where not only the efficiency of the combustion is important.

This study was performed in phases, for which the time limit was dictated by our cooperation with the International Flame Research Foundation. In the third quarter of 1988 the first series of measurements (NG6) has been performed by the IFRF. Before this time preliminary calculations of the flow in the IFRF furnace were carried out. The grid dependence of the solution was tested and the boundary conditions for several variables, most importantly the temperature, were estimated. Also, the NO_x formation model was formulated, for which models known from literature were used. The NO_x formation model was implemented in the numerical model and used for predictions of the NO_x formation in the IFRF furnace. Comparison of the measured results with the results of the numerical predictions revealed the importance of the temperature boundary condition for the simulations. With the measured boundary conditions, for the cases where they were available, simulations for the parameter variations of the NG6 experiments were also performed.

After the comparison of the measured and the simulated data of the NG6 experiments, model improvements were implemented. Preliminary studies for a new series of measurements, where several burner configurations were going to be tested, were carried out after the implementation of the improved models. These simulations were first carried out for the IFRF furnace with the boundary conditions as dictated by the NG6 experiments. Because the IFRF furnace was less hot during the NG7 experiments, which has a large effect on the results, these simulations were later repeated with the measured boundary conditions. The results of the simulations that will be presented in this thesis have all been obtained with the measured boundary conditions. Due to the differences in the thermal environment, the simulations with the estimated boundary conditions are of minor importance.

In this thesis we will validate the simulated results with the measured results of the IFRF. We will discuss trends of the NO_x emission in several burner geometries and will discuss the influence of mixing parameters on the combustion of natural gas and the formation of thermal NO for the different flames. Apart from the influence of the mixing on the NO_x formation also the influence of other furnace parameters will be quantified.

1.4 Some relevant studies on high temperature furnace modelling

The present study uses concepts and models that have been discussed in literature before. The combination of these models, resulting in the complex model for a high temperature furnace with the formation of thermal NO_x included has not often been reported on. Post (1988) has studied the flow, combustion and radiative heat transfer in a glass melting furnace before. He has developed the numerical model FURNACE, that has been used and extended for this work. Carvalho (1983) used similar techniques as in the present thesis in an end-fired furnace, although with a different radiative heat transfer model. Carvalho *et al.* (1988) also use a comparison with measurements for the validation of a numerical model. Rhine and Tucker (1991) give a comprehensive overview of both numerical and physical modelling of furnaces. In the book of Trier (1984) simpler models than the above mentioned are discussed.

The present study uses the Hottel zone method for the radiative heat transfer. Wieringa (1992) has studied the radiative heat transfer in the IFRF furnace with several models, including spectral effects. The Hottel zone model uses algorithms that were developed by Siddal (1986) for the computation of the direct exchange areas.

Many authors perform detailed computations of the chemistry in simpler flames. Warnatz (1983a) gives detailed chemistry models and rate constants to be used. Also, reduction schemes for the computation of the combustion are presented by Bilger (1980). The use of more elaborate pdf schemes is reported on by Bockhorn (1989); Libby (1975). Peeters and Van der Meer (1992) describe the use of assumed shape pdf models in the FURNACE model.

On the topic of NO_x formation many works have been published. Zel'dovich (1946) published the thermal NO formation scheme, that has been used in this thesis. Surveys of rate constants are given by Warnatz (1983a); Hanson and Salimian (1984). The kinetics of several NO formation routes have been published by Fenimore (1971); Bowman (1975).

Experiments in furnaces have been published by many authors. Reduction of NO_x formation in furnaces with combustion air temperatures up to 1000 °C is reported on by Flamme *et al.* (1989); Flamme and Kremer (1991). Small scale experiments have been done by Abbasi *et al.* (1984). Tests of mixing in different burners and for several air-factors have been reported by Beckervordersandforth *et al.* (1987). Barklage-Hilgefort (1991) reports on NO_x emission reduction by air staging and burner adaptations in a glass melting furnace. Finally, experiments in a scale model of a glass melting furnace were performed by the IFRF. Two trials were performed in 1988 (NG6, Van de Kamp *et al.* (1989)) and in 1990 (NG7, Nakamura *et al.* (1991)).

1.5 Outline of this thesis

In chapter 2 the formulation of the mathematical model is discussed. This model consists of several sub-models that describe the following: three-dimensional flow, turbulence, turbulent combustion, radiative heat exchange and thermal NO_x formation.

Some attention will be given to semi-analytical solutions of jets with and without combustion as an introduction to the jet flame that is encountered in the IFRF furnace. The resulting model consists of a set of non-linear coupled equations. The procedure for solving this set of equations is discussed in chapter 3.

Validation of the mathematical model was done in an isothermal scale model of the IFRF furnace. This scale model was used to obtain information on the flow in the furnace, using relatively simple measurement techniques. Flow computations in the scale model geometry provide material for the validation of the flow model. In chapter 4 the experiments in the scale model and the simulations of the scale model will be discussed.

The experiments that were performed by the IFRF are introduced in chapter 5. The experimental set-up is discussed insofar as needed for a comparison with the numerical results. The results of the relevant measurements are also introduced, so that the necessary overview of the experimental work by the IFRF is available in the rest of the thesis. The work of the IFRF was performed in two series of measurements, the NG6 and NG7 trials. The results of the simulations of these trials will be discussed in chapters 6 and 7, respectively.

First, in chapter 6 we will discuss the sensitivity of the model to several parameters. This will serve as a validation of the numerical model and its parameters. The result is a set of parameters that constitute a standard model for the simulations of the NG6 trials. The experimental program of NG6 provided several parameter studies to assess the influence of these parameters on the NO_x formation.

In chapter 7 we will first describe the model improvements that proved to be necessary after the NG6 trials. The results of these model improvements will be discussed. With the improved model simulations have been performed for the burner geometry variations tested during NG7.

Finally a general discussion of the numerical work, with an assessment of the applicability of the numerical model, will be given in chapter 8.

Chapter 2

The mathematical model

2.1 Introduction

In this chapter the complete set of equations that describe all the relevant physical and chemical phenomena will be presented. First the equations describing the turbulent flow will be presented. Then the modelling of turbulent combustion, radiative heat transfer and NO_x formation will be discussed. Also some analytical solutions and approximations for jet development will be discussed.

The description of the mathematical model will be very brief. The model was described in Post (1988) and has been used with the addition of an NO_x formation model and some minor improvements. Although we have only solved the stationary solution of our problem, for the sake of completeness all equations will be presented in their time-dependent form.

2.2 Modelling of the flow

The flow in our furnace is described by the conservation laws for mass, momentum, energy and species concentrations. These equations can be found in many textbooks, e.g. Bird *et al.* (1960).

Conservation of mass The equation expressing the conservation of mass (continuity equation) is,

$$\frac{\partial \rho}{\partial t} + \frac{\partial}{\partial x_j}(\rho u_j) = 0 \tag{2.1}$$

in which ρ is the density of the fluid and u_j the component of the velocity vector in the j-direction.

Conservation of momentum Conservation of the i-component of the momentum can be expressed as,

$$\frac{\partial}{\partial t}(\rho u_i) + \frac{\partial}{\partial x_j}(\rho u_j u_i) = -\frac{\partial p}{\partial x_i} - \frac{\partial}{\partial x_j}(\tau_{ij}) + \rho g_i \tag{2.2}$$

in which p is the pressure, g_i the i-component of the gravitation and τ_{ij} a component of the stress tensor. All other external forces are neglected. For a Newtonian fluid the stress tensor can be written as,

$$\tau_{ij} = -\mu(\frac{\partial u_i}{\partial x_j} + \frac{\partial u_j}{\partial x_i}) + (\frac{2}{3}\mu - \kappa)\frac{\partial u_k}{\partial x_j}\delta_{kj} \tag{2.3}$$

in which μ is the molecular dynamic viscosity, κ the bulk viscosity and δ_{kj} the Kronecker delta. The bulk viscosity will be neglected.
Equations (2.2) for i= 1, 2, 3 together with (2.3) are called the Navier-Stokes equations.

Conservation of energy The energy equation has been written in the form of the enthalpy equation,

$$\frac{\partial}{\partial t}(\rho H - p) + \frac{\partial}{\partial x_j}(\rho u_j H) = \frac{\partial}{\partial x_j}(\frac{\lambda}{C_p}\frac{\partial H}{\partial x_j}) + S_{\text{rad}} \tag{2.4}$$

in which λ is the thermal conductivity, C_p is the specific heat at constant temperature, S_{rad} is the radiative source term and H is the enthalpy, defined as,

$$H = U + p/\rho \tag{2.5}$$

in which U is the internal energy per unit mass.
To arrive at this equation we have done the following: (1) we have neglected the Dufour effect, (2) we have used Fourier's law to model the conductive part of the energy flux, (3) we have replaced multicomponent diffusion by Fick's law with a single diffusion coefficient, assuming the Lewis number to be 1 (Peters (1984)), (4) we have neglected the viscous dissipation term and the gravitational term in the energy equation, (5) we have neglected the contribution of the kinetic energy term to the enthalpy.

The enthalpy is the sum of the sensible enthalpy and the chemical enthalpy. The sensible enthalpy is related to the temperature T by,

$$dH_{\text{sens}} = C_p dT \tag{2.6}$$

Conservation of species Mass conservation of a species i in the fluid is described by,

$$\frac{\partial}{\partial t}(\rho Y_i) + \frac{\partial}{\partial x_j}(\rho u_j Y_i) = \frac{\partial}{\partial x_j}(\Gamma_i \frac{\partial Y_i}{\partial x_j}) + S_i \tag{2.7}$$

in which Y_i is the mass fraction of species i, Γ_i the exchange coefficient of species i, which is the product of the fluid density and the diffusion coefficient of species i, and S_i the net production of species i by chemical reactions.
By definition of the mass fraction it is sufficient to solve one equation of the type (2.7) less than the number of species in the fluid. Summing eqns. (2.7) for all species and using the continuity equation (2.1), we find,

$$\sum_i S_i = 0 \tag{2.8}$$

Equation of state The set of conservation equations must be completed with an appropriate equation of state. For this we use the ideal gas law,

$$M_{\text{mix}} p = \rho R T \tag{2.9}$$

in which M_{mix} is the molecular mass of the fluid mixture and R the universal gas constant.

2.3 Modelling of turbulence

The flow that we are modelling is turbulent. This means that it exhibits rapid fluctuations and that rates of mass, momentum and heat transfer are increased significantly (Tennekes and Lumley (1972)). The equations that were presented in the previous section also apply for turbulent flows. Solving these equations with adequate space and time resolution is beyond the capability of the current computers. Thus, the introduction of statistical methods is an attractive way to obtain applicable results. For most engineering applications the information of interest is limited; usually it is sufficient to determine the mean values of the fluid-mechanical quantities, some measure of the extent of the variations around those mean values and some measure of the correlation between the various quantities. It is customary to decompose the various quantities into mean and fluctuating components. We use the so-called Reynolds decomposition to compute the time-averaged form of the flow equations of section 2.2. The Reynolds decomposition of a variable ϕ in a mean and fluctuation term is,

$$\phi(\underline{x}, t) = \overline{\phi}(\underline{x}) + \phi'(\underline{x}, t) \tag{2.10}$$

in which $\underline{x}$ is the position, t the time and,

$$\begin{aligned} \overline{\phi}(\underline{x}) &= \lim_{T\to\infty} \tfrac{1}{T} \textstyle\int_0^T \phi(\underline{x}, s) ds \\ \overline{\phi'(\underline{x}, t)} &= \lim_{T\to\infty} \tfrac{1}{T} \textstyle\int_0^T \phi'(\underline{x}, s) ds = 0 \end{aligned} \tag{2.11}$$

in which the time integration is denoted by ds and the integration time T is sufficiently large.
Applying the Reynolds decomposition to the flow equations, we neglect fluctuations of the density and triple order correlations of fluctuations. We also assume that μ, λ, C_p and Γ_i are constant. Then the following equations, with some new and unknown terms, are found.

Conservation of mass

$$\frac{\partial \overline{\rho}}{\partial t} + \frac{\partial}{\partial x_j}(\overline{\rho}\,\overline{u_j}) = 0 \tag{2.12}$$

Conservation of momentum

$$\frac{\partial}{\partial t}(\overline{\rho}\,\overline{u_i}) + \frac{\partial}{\partial x_j}(\overline{\rho}\,\overline{u_j}\,\overline{u_i} + \overline{\rho}\,\overline{u_i'u_j'}) = -\frac{\partial \overline{p}}{\partial x_i} - \frac{\partial}{\partial x_j}(\overline{\tau_{ij}}) + \overline{\rho} g_i \tag{2.13}$$

in which the time-averaged value of the stress tensor is,

$$\overline{\tau_{ij}} = -\mu(\frac{\partial \overline{u_i}}{\partial x_j} + \frac{\partial \overline{u_j}}{\partial x_i}) + \frac{2}{3}\mu\frac{\partial \overline{u_k}}{\partial x_j}\delta_{kj} \tag{2.14}$$

Conservation of energy

$$\frac{\partial}{\partial t}(\overline{\rho}\,\overline{H} - \overline{p}) + \frac{\partial}{\partial x_j}(\overline{\rho}\,\overline{u_j}\,\overline{H} + \overline{\rho}\,\overline{u_j'H'}) = \frac{\partial}{\partial x_j}(\frac{\lambda}{C_p}\frac{\partial \overline{H}}{\partial x_j}) + \overline{S_{\text{rad}}} \tag{2.15}$$

Conservation of species

$$\frac{\partial}{\partial t}(\overline{\rho}\,\overline{Y_i}) + \frac{\partial}{\partial x_j}(\overline{\rho}\,\overline{u_j}\,\overline{Y_i} + \overline{\rho}\,\overline{u_j'Y_i'}) = \frac{\partial}{\partial x_j}(\Gamma_i\frac{\partial \overline{Y_i}}{\partial x_j}) + \overline{S_i} \tag{2.16}$$

The new and unknown terms $\overline{\rho u_i'u_j'}$ (Reynolds stress), $\overline{\rho u_j'H'}$ and $\overline{\rho u_j'Y_i'}$ have to be evaluated. For this we have used the well-known $k-\epsilon$ model (Launder and Spalding (1972)), that uses the turbulent viscosity hypothesis. The Reynolds stress is expressed in terms of a turbulent viscosity μ_t and gradients of the mean velocities as,

$$\overline{\rho}\,\overline{u_i'u_j'} = -\mu_t\left(\frac{\partial \overline{u_i}}{\partial x_j} + \frac{\partial \overline{u_j}}{\partial x_i}\right) + \frac{2}{3}\overline{\rho}k\delta_{ij} \tag{2.17}$$

in which k is the kinetic energy of the turbulence,

$$k = \frac{1}{2}\overline{u_i'u_i'} \tag{2.18}$$

In the $k-\epsilon$ model the turbulent viscosity is defined by,

$$\mu_t = C_\mu \overline{\rho} k^2/\epsilon \tag{2.19}$$

in which C_μ is an empirical constant and ϵ is the dissipation rate of the turbulent kinetic energy, defined as,

$$\epsilon = \mu/\overline{\rho}\left(\overline{\frac{\partial u_i'}{\partial x_j}\frac{\partial u_i'}{\partial x_j}}\right) \tag{2.20}$$

To be able to evaluate the Reynolds stresses the values of k and ϵ must be known. Transport equations for both k and ϵ can be derived from the Navier-Stokes equations, see e.g. Khalil (1982), Rodi (1984), Launder and Spalding (1972). The transport equations for k and ϵ are,

$$\frac{\partial}{\partial t}(\overline{\rho}k) + \frac{\partial}{\partial x_j}(\overline{\rho}\,\overline{u_j}k) = \frac{\partial}{\partial x_j}\left((\mu + \frac{\mu_t}{\sigma_k})\frac{\partial k}{\partial x_j}\right) - \overline{\rho}(G + \epsilon) \tag{2.21}$$

$$\frac{\partial}{\partial t}(\overline{\rho}\epsilon) + \frac{\partial}{\partial x_j}(\overline{\rho}\,\overline{u_j}\epsilon) = \frac{\partial}{\partial x_j}\left((\mu + \frac{\mu_t}{\sigma_\epsilon})\frac{\partial \epsilon}{\partial x_j}\right) - \overline{\rho}(C_{1\epsilon}G + C_{2\epsilon}\epsilon)\frac{\epsilon}{k} \tag{2.22}$$

in which σ_k and σ_ϵ are turbulent Prandtl numbers, $C_{1\epsilon}$ and $C_{2\epsilon}$ are empirical constants and $-\overline{\rho}G$ is the production rate of turbulent kinetic energy, defined as,

$$\begin{aligned} -\overline{\rho}G &= -\overline{\rho u_i' u_i'}\frac{\partial \overline{u_i}}{\partial x_j} \\ &= \left\{\mu_t\left(\frac{\partial \overline{u_i}}{\partial x_j} + \frac{\partial \overline{u_j}}{\partial x_i}\right) - \frac{2}{3}\overline{\rho}k\delta_{ij}\right\}\frac{\partial \overline{u_i}}{\partial x_j} \end{aligned} \tag{2.23}$$

Following the turbulent viscosity approach we can model the turbulent transport of heat and of a chemical species i by defining,

$$\overline{\rho}\,\overline{u_j' H'} = -\frac{\mu_t}{\sigma_H}\frac{\partial \overline{H}}{\partial x_j} \tag{2.24}$$

$$\overline{\rho}\,\overline{u_j' Y_i'} = -\frac{\mu_t}{\sigma_i}\frac{\partial \overline{Y_i}}{\partial x_j} \tag{2.25}$$

in which σ_H is the turbulent Prandtl for the enthalpy and σ_i the turbulent Schmidt number for species i.

Finally the following expressions for the transport equations are found.

Conservation of mass

$$\frac{\partial \overline{\rho}}{\partial t} + \frac{\partial}{\partial x_j}(\overline{\rho}\,\overline{u_j}) = 0 \tag{2.26}$$

Conservation of momentum

$$\frac{\partial}{\partial t}(\overline{\rho}\,\overline{u_i}) + \frac{\partial}{\partial x_j}(\overline{\rho}\,\overline{u_j}\,\overline{u_i}) = -\frac{\partial \overline{p}}{\partial x_i} - \frac{\partial}{\partial x_j}(\overline{\tau_{ij}}) + \overline{\rho}g_i \tag{2.27}$$

in which the stress tensor is,

$$\overline{\tau_{ij}} = -(\mu + \mu_t)(\frac{\partial \overline{u_i}}{\partial x_j} + \frac{\partial \overline{u_j}}{\partial x_i}) + \frac{2}{3}(\mu + \mu_t)\frac{\partial \overline{u_k}}{\partial x_j}\delta_{kj} + \frac{2}{3}\overline{\rho}k\delta_{ij} \tag{2.28}$$

Conservation of energy

$$\frac{\partial}{\partial t}(\overline{\rho}\,\overline{H} - \overline{p}) + \frac{\partial}{\partial x_j}(\overline{\rho}\,\overline{u_j}\,\overline{H}) = \frac{\partial}{\partial x_j}\left((\frac{\lambda}{C_p} + \frac{\mu_t}{\sigma_H})\frac{\partial \overline{H}}{\partial x_j}\right) + \overline{S_{\text{rad}}} \tag{2.29}$$

Conservation of species

$$\frac{\partial}{\partial t}(\overline{\rho}\,\overline{Y_i}) + \frac{\partial}{\partial x_j}(\overline{\rho}\,\overline{u_j}\,\overline{Y_i}) = \frac{\partial}{\partial x_j}\left((\Gamma_i + \frac{\mu_t}{\sigma_i})\frac{\partial \overline{Y_i}}{\partial x_j}\right) + \overline{S_i} \tag{2.30}$$

The constants that appear in the $k-\epsilon$ model and related expressions are (Carvalho (1983)),

$$\begin{aligned} C_\mu &= 0.09 \\ C_{1\epsilon} &= 1.44 \\ C_{2\epsilon} &= 1.92 \\ \sigma_k &= 1.0 \\ \sigma_\epsilon &= 1.3 \\ \sigma_H &= 0.9 \\ \sigma_i &= 0.9 \end{aligned} \tag{2.31}$$

2.3.1 Near wall region

The $k-\epsilon$ model, discussed in this section, was developed for flows with a high Reynolds number (Re $>$ 5000). Near solid walls, the velocities tend to zero due to the no-slip conditions at the wall. In this region, the Reynolds number is small and consequently viscous effects must be accounted for.
We have used the standard wallfunction method (Launder and Spalding (1972); Carvalho (1983); Post (1988)). For the velocity we use the logarithmic velocity profile for the inertial sublayer,

$$\begin{aligned} U^+ &= y^+ && \text{for } y^+ < 11.63 \\ U^+ &= \tfrac{1}{\kappa}\ln(Ey^+) && \text{for } 11.63 < y^+ < 1000 \end{aligned} \tag{2.32}$$

in which the following variables are used,

$$\mu_{\text{eff}} = \mu + \mu_t \tag{2.33}$$

$$\tau_w = \mu_{\text{eff}} \left.\frac{\partial U}{\partial y}\right|_{y=0} \tag{2.34}$$

$$(U^*)^2 = \tau_w/\rho \tag{2.35}$$

$$U^+ = U/U^* \tag{2.36}$$

$$y^+ = (\rho y U^*)/\mu \tag{2.37}$$

In these equations κ is the Von Karman constant, with a value of 0.42, E is an integration constant, experimentally found to be 9.8 (Carvalho (1983)). U is the velocity parallel to the wall, y is the coordinate direction perpendicular to the wall. The wallfunctions for resp. the turbulent kinetic energy, the rate of dissipation of turbulent kinetic energy and the enthalpy are,

$$k = \frac{(U^*)^2}{\sqrt{C_\mu}} \qquad \text{for } y^+ > 11.63 \tag{2.38}$$

$$\epsilon = \frac{(U^*)^3}{\kappa y} \qquad \text{for } y^+ > 11.63 \tag{2.39}$$

$$q_w = \rho U^* \frac{(H - H_w)}{(\sigma_H U^+ + P_j)} \tag{2.40}$$

in which q_w is the heat flux to the wall, as given by Khalil (1982), H_w is the enthalpy at the wall and P_j is given by Carvalho (1983) as,

$$P_j = \frac{\pi/4}{\sin(\pi/4)} \left(\frac{A}{\kappa}\right)^{1/2} \left(\frac{\sigma_{H,l}}{\sigma_H} - 1\right) \left(\frac{\sigma_H}{\sigma_{H,l}}\right)^{1/4} \sigma_H \tag{2.41}$$

in which A is the Van Driest constant, with value 26.0 and $\sigma_{H,l}$ is the laminar Prandtl number.

2.4 Modelling of the combustion

In the modelling of combustion several problems arise which as yet have not been completely solved.

One of the main problems is the description of the chemical kinetics in the flame. A full-blown chemical kinetics model requires that a large number of chemical species, radicals and intermediates is taken into account. Many reactions between these components occur, which requires knowledge of the reaction rates. Warnatz has reviewed 200 elementary reactions that may occur in hydrocarbon combustion (see e.g. Warnatz (1983b), Warnatz (1984)). Based on these reviews Warnatz (1983a) presents a chemical kinetics model for the combustion of methane, with soot precursors and NO formation. This model consists of 130 reactions and 40 species. This is an already reduced chemical kinetics model, where many reactions have been neglected based on simple argumentation (such as large activation energy etc.). For many of the incorporated reactions the reaction rates are known within limited accuracy, especially in the high temperature domain. Besides the modelling difficulties, numerically solving this model poses the problem of computer time. Therefore, for our engineering problem, where we need a three dimensional flow model including radiative heat transfer, we used a very simple model for the combustion reaction.

A second important problem is the influence of turbulence on the combustion process. Following the approach of the decomposition of a quantity into its mean value and a fluctuation term, we can show the importance of the turbulent fluctuations by considering the single step combustion reaction

$$\text{fuel} + \text{oxygen} \rightarrow \text{products} \tag{2.42}$$

The reaction rate of the fuel w_F can be expressed as

$$w_F = -\rho^2 k_f Y_F Y_O \tag{2.43}$$

in which Y_F is the mass fraction of fuel, Y_O is the mass fraction of oxygen and k_f is the forward reaction rate, expressed in its Arrhenius form as,

$$k_f = A \exp(-E/RT) \tag{2.44}$$

The instantaneous value of the reaction rate is, using the Reynolds decomposition,

$$w_F = -(\overline{\rho} + \rho')^2(\overline{k_f} + k_f')(\overline{Y_F} + Y_F')(\overline{Y_O} + Y_O') \tag{2.45}$$

The computation of the instantaneous reaction rate is complicated by the temperature dependence of the reaction rate, where the exponential term in the Arrhenius factor is strongly non-linear in the temperature. For the computation of the reaction rate some averaging procedure needs to be applied to obtain the correct instantaneous reaction rate. However, the theoretical derivation of an averaging procedure is not straightforward and several assumptions have to be made. The validity of the averaging procedure is limited by the assumptions that have to be made. Besides, cross-correlations between k_f', Y_F' and Y_O' complicate matters further. Khalil (1982) gives many expressions for $(\overline{k_f} + k_f')$ and other correlations.

2.4.1 The combustion reaction

Keeping these two major complications in mind, our goal is to find a turbulent combustion model, suitable for the flames in glass melting furnaces. An essential feature of these flames is that the two reactants, viz. natural gas and combustion air, enter the furnace in two streams. Since the combustion reactions are relatively fast, this means that the rate of combustion is, at least for the greatest part, limited by the mixing of the reactants. In other words, we are modelling high Damköhler number flames. This enables us to use the "classical" conserved scalar approach to describe the mixing and the combustion process.

Since the combustion rate is limited by the mixing, we will next assume that the complete chemical kinetics can be reduced to the one-step combustion reaction,

$$\text{fuel} + s \text{ oxygen} \rightarrow (1 + s) \text{ products} \tag{2.46}$$

which we have written in mass units, rather than the more conventional molar form. This reaction may be read as "1 kg of fuel plus s kg of oxygen yields (1+s) kg of products". In the case of natural gas combustion these products are CO_2 and H_2O.
The reaction rates for the three composing species in the combustion reaction satisfy the following,

$$w_F = \frac{1}{s} w_O = -\frac{1}{1+s} w_P \tag{2.47}$$

Thus we can construct the well-known Shvab-Zel'dovich coupling functions, where we have used the following,

$$\xi = Y_F - \frac{1}{s} Y_O \tag{2.48}$$

which is a conserved scalar.

Now, normalizing on the composition of the fuel and oxidant streams, we define the mixture fraction f as,

$$f = \frac{\xi - \xi_{\text{air}}}{\xi_{\text{fuel}} - \xi_{\text{air}}} \tag{2.49}$$

Thus it is easily seen that $f = 1$ in the fuel stream and $f = 0$ in the oxidant stream. At stoichiometric conditions $\xi = 0$, which we will use to define the stoichiometric mixture fraction $f_{\text{st},1}$,

$$\begin{aligned} f_{\text{st},1} &= -\frac{\xi_{\text{air}}}{\xi_{\text{fuel}} - \xi_{\text{air}}} \\ &= \frac{Y_{O,\text{air}} - sY_{F,\text{air}}}{sY_{F,\text{fuel}} - Y_{O,\text{fuel}} - sY_{F,\text{air}} + Y_{O,\text{air}}} \end{aligned} \tag{2.50}$$

Since the fuel stream contains no oxygen and the oxidant stream contains no fuel this can be simplified to give,

$$f_{\text{st},1} = \frac{Y_{O,\text{air}}}{sY_{F,\text{fuel}} + Y_{O,\text{air}}} \tag{2.51}$$

Based on this definition we are able to compute the species mass fractions as a function of the mixture fraction (Carvalho (1983)).

Mass fraction fuel

$$\begin{aligned} Y_F(f) &= 0 && \text{for } 0 \le f < f_{\text{st},1} \\ Y_F(f) &= Y_{F,\text{fuel}} \frac{f - f_{\text{st},1}}{1 - f_{\text{st},1}} && \text{for } f_{\text{st},1} \le f \le 1 \end{aligned} \tag{2.52}$$

Mass fraction oxygen

$$\begin{aligned} Y_O(f) &= Y_{O,\text{air}}\left(1 - \frac{f}{f_{\text{st},1}}\right) && \text{for } 0 \le f < f_{\text{st},1} \\ Y_O(f) &= 0 && \text{for } f_{\text{st},1} \le f \le 1 \end{aligned} \tag{2.53}$$

Mass fraction inert species

$$Y_{\text{inert}}(f) = fY_{\text{inert,fuel}} + (1 - f)Y_{\text{inert,air}} \tag{2.54}$$

Mass fraction products

$$Y_{\text{prod}}(f) = 1 - Y_F(f) - Y_O(f) - Y_{\text{inert}}(f) \tag{2.55}$$

In our study fuel is composed of methane, ethane, propane, butane, carbon dioxide and nitrogen (see Appendix B for the appropriate mass fractions). The combustion air is composed of nitrogen and oxygen. From the composition of the fuel the precise composition of the product can be determined. In figure 2.1 the functional relationships for some of the mass fractions are shown.

There is a number of quantities that can be expressed in terms of the mixture fraction as well. These variables are the mixture enthalpy, the density, the specific heat of the mixture and the temperature of the mixture. The expressions for these variables will be given next.

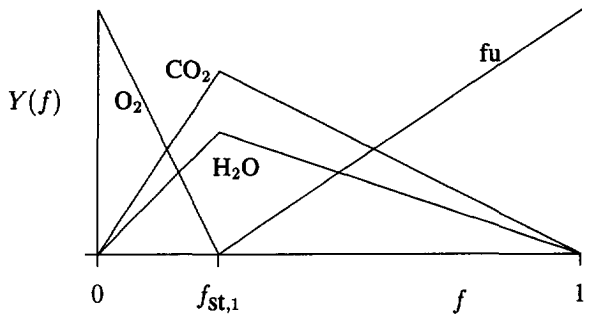

Figure 2.1: Species mass fractions as a function of the mixture fraction *(NB. figure not on scale).*

Mixture enthalpy

$$\begin{aligned} H(f) &= H_{\text{air}} + (\overline{H} - H_{\text{air}})\frac{f}{\overline{f}} && \text{for } 0 \leq f < \overline{f} \\ H(f) &= \overline{H} + (H_{\text{fuel}} - \overline{H})\frac{\overline{f}-f}{\overline{f}-1} && \text{for } \overline{f} \leq f \leq 1 \end{aligned} \tag{2.56}$$

in which $\overline{H}$ is the time-mean enthalpy given by the enthalpy equation (2.29).

Density

$$\rho(f) = \frac{p}{RT(f)\sum_i \frac{Y_i(f)}{M_i}} \tag{2.57}$$

in which p is the pressure, $T(f)$ the instantaneous temperature and M_i is the molecular mass of species i. This is the equation of state (2.9) expressed in its mixture fraction dependent form.

Temperature of the mixture

$$T(f) = T_{\text{ref}} + \frac{H(f) - Y_F(f)H_0}{C_{pm,\text{mix}}(T,f)} \tag{2.58}$$

in which T_{ref} is a reference temperature, $H(f)$ is the instantaneous enthalpy, H_0 is the lower calorific value of the fuel and $C_{pm,\text{mix}}$ the mean specific heat at constant pressure of the mixture, in the temperature interval $[T_{\text{ref}}, T]$. In this equation we identify the sensible enthalpy as,

$$H_{\text{sens}}(f) = H(f) - Y_F(f)H_0 \tag{2.59}$$

Mean specific heat of the mixture

$$C_{pm,\mathrm{mix}}(T,f) = \frac{1}{T(f) - T_{\mathrm{ref}}} \int_{T_{\mathrm{ref}}}^{T(f)} \{\sum_i Y_i(f) C_{p,i}(s)\} ds \tag{2.60}$$

in which $C_{p,i}(T)$ is the specific heat at constant pressure of species i as a function of the temperature T. The polynomial expressions for the specific heat for all species that we have used are given in Appendix B.

It is clear from the expressions for $C_{pm,\mathrm{mix}}$ and T(f) ((2.60) and (2.58) resp.) that a recursion in these equations exists. To compute an accurate temperature we need to iterate the temperature and the specific heat expressions. It is possible, however, to express the temperature as a function of the sensible heat and the mixture fraction only. Through an iterative procedure a temperature table $T(H_{\mathrm{sens}}, f)$ can be computed, enabling efficient table lookup procedures to be used in the flow computations.

2.4.2 The influence of turbulence on combustion

Some of the difficulties that arise when we want to model the influence of turbulence on combustion have previously been discussed. Since we have incorporated a one-step combustion model, which enables us to construct a passive scalar, viz. the mixture fraction, we can model the influence of the turbulence relatively easily. We will use the probability density function (pdf) approach to achieve our goal in a relatively simple way.

Let $\Phi(f)$ denote a scalar, dependent on the mixture fraction f, that has to be time-averaged, then the time-mean value of Φ will be,

$$\overline{\Phi} = \int_0^1 \Phi(f) P(f) df \tag{2.61}$$

in which $P(f)$ is the probability density function. This pdf satisfies the following condition,

$$\int_0^1 P(f) df = 1 \tag{2.62}$$

The problem is now to determine the shape of the pdf, that will give us the correct mean value of Φ and the correct value of the fluctuation of Φ. There are several methods to tackle this problem. O'Brien (1980), after Lundgren (1967) and Pope (1976) develops a transport equation for the pdf directly from the transport equations. This requires the formulation of closures for higher order fluctuation terms. This method has not been employed by us, since one of the drawbacks is the increase in computer time needed for the solution of the transport equations of all relevant pdf's. A less time-consuming method to determine the pdf is via Monte Carlo simulations of the pdf. Since this still requires large amounts of computation time, we have not followed this approach either.

The approach which we did use has long been established in the literature (Spalding (1971), Khalil (1982)). We assume a certain shape for the pdf, which we then use for our computations. The pdf that we employed is constructed in such a way

as to accurately predict the time-mean and fluctuation of a scalar. In the present study we have employed a double delta pdf, after the suggestion of Spalding (1971). For the double delta pdf, two discrete values of the mixture fraction are used in the averaging procedure. At these values of f the relevant scalar is evaluated. The time-mean value is the weighted average of the two scalar values that we find. The weight factors are determined by the values of the mixture fraction f and the fluctuation term of the mixture fraction, denoted as g. In Appendix A the weight factors for the averaging are computed, resulting in the pdf scheme that we have used.

In section 2.3 the time-averaged transport equation for a species i was derived. From this equation we derive the transport equation for the mixture fraction, by summation of two partial differential equations, for Y_F en $\frac{-1}{s}Y_O$ resp., and appropriate normalization, which gives us the mixture fraction as the variable to be solved. This procedure yields,

$$\frac{\partial}{\partial t}(\overline{\rho}\,\overline{f}) + \frac{\partial}{\partial x_j}(\overline{\rho}\,\overline{u_j}\,\overline{f}) = \frac{\partial}{\partial x_j}\left(\Gamma_{f,t}\frac{\partial \overline{f}}{\partial x_j}\right) \tag{2.63}$$

in which $\Gamma_{f,t} = \mu_t/\sigma_f$, with σ_f the turbulent Schmidt number, taken to be 0.9 in the present study.

The mixture fraction fluctuation g is defined as,

$$g = (\overline{f} - f')^2 \tag{2.64}$$

From eqn. (2.63) we can derive a transport equation for the mixture fraction fluctuation, using similar modelling assumptions as for the derivation of the $k-\epsilon$ model. This derivation yields (Spalding (1971)),

$$\frac{\partial}{\partial t}(\overline{\rho}\,g) + \frac{\partial}{\partial x_j}(\overline{\rho}\,\overline{u_j}\,g) = \frac{\partial}{\partial x_j}\left(\Gamma_{g,t}\frac{\partial g}{\partial x_j}\right) + C_{1g}\,\mu_t\frac{\partial \overline{f}}{\partial x_j}\frac{\partial \overline{f}}{\partial x_j} - C_{2g}\,\overline{\rho}g\epsilon k \tag{2.65}$$

in which $\Gamma_{g,t} = \Gamma_{f,t}$, C_{1g} and C_{2g} are model constants with values 2.8 and 2.0 respectively.

Now the time-mean value of a scalar $\Phi(f)$ can be computed for given $\overline{f}$ and g, with $0 \leq \overline{f} \leq 1$ and $g \geq 0$, using the double delta pdf described previously. The precise formulation of the pdf depends on the value of $\overline{f}$ and g. In Appendix A the resulting scheme for all possible combinations of $\overline{f}$ and g is computed.

Although we have chosen a particular shape of the pdf, viz. the double delta pdf, many more shapes are possible. Khalil (1982) presents a number of different pdf shapes, including (clipped) Gaussian and beta-function pdf's. Continuous pdf's, possibly clipped to ensure that the instantaneous mixture fraction satisfies $0 \leq f \leq 1$, are believed to be more realistic, physically spoken, than discrete pdf's. In the case of intermittency, however, the pdf reduces (partially) to delta functions, where a peak in the pdf denotes either fuel or oxidant. Intermittency then describes that in certain intervals of time at a point in space a fuel eddy will pass and in other intervals of time

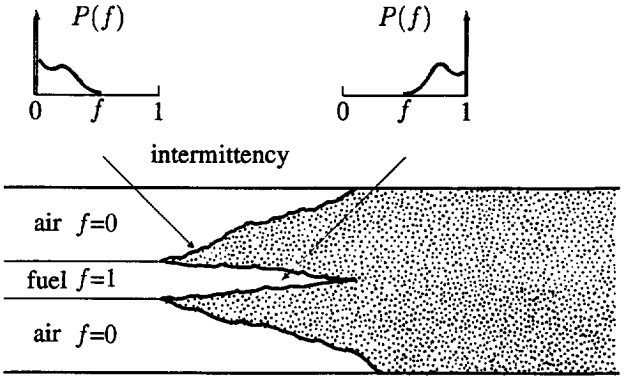

Figure 2.2: Intermittency in a mixing flow.

an oxidant eddy will pass. Figure 2.2 illustrates this notion of intermittency for the case of a jet issuing into a flow.

In the flow configuration of our present study, viz. a furnace with two separate inflow points for the fuel and the combustion air, we assume that intermittency influences the mixing of fuel and air strongest. Thus, the influence of turbulence on combustion is assumed to be adequately described by the intermittency, resulting in the double delta pdf. However, as we will show in chapter 7, other chemical reactions may be influenced less by intermittency, thus requiring a more elaborate pdf description. These reactions often take place further downstream than the initial mixing of the natural gas and the combustion air. For this we have used a continuous pdf, viz. the top hat pdf. In chapter 7 and appendix A more details are given on this extension and on the top hat pdf implementation.

2.5 The radiative heat transfer model

As a consequence of the high furnace temperature radiative heat transfer is the most important means of heat transfer in glass melting furnaces. About 90 to 95 % of the total heat transfer to the load is due to thermal radiation. It is not only important for us to obtain the heat transfer to the load as a result, but it is also important that the temperature distribution is predicted correctly. The NO_x formation is extremely sensitive to the temperature, which is determined mainly by the radiative heat transfer.

Mathematically, we can formulate the radiative heat transfer in an absorbing,

emitting and scattering medium as,

$$\frac{\partial i'_\lambda(s)}{\partial s} = -(k^a_\lambda + k^s_\lambda) i'_\lambda(s) + k^a_\lambda i'_{\lambda b}(s) + \frac{k^s_\lambda}{4\pi} \int_{4\pi} i'_\lambda(\Omega_i) \Phi_\lambda(\Omega_i, \Omega) d\Omega_i \qquad (2.66)$$

in which $i'_\lambda(s)$ is the radiant intensity of wavelength λ, $i'_{\lambda b}(s)$ is the radiant intensity of wavelength λ of a black body at the temperature of the medium at position s and k^a_λ and k^s_λ are the spectral absorption and scattering coefficient of the medium at wavelength λ.

This integro-differential equation is of a different form than the second order partial differential equations with which we described the flow. We will therefore need a submodel of a different kind than the flow model to solve the radiation equation. In the literature several modelling methods have been developed, amongst others zone models, Monte Carlo models, flux models or mixtures of these models. Wieringa (1992) has applied several methods to glass furnace computations, but in this thesis we have only used one method, viz. the Hottel Zone Method. The Hottel Zone Method employs a discretization of the enclosure space in a number of volumes and of the boundary surface in a number of elements, all of uniform properties. The radiative heat transfer is then described in the form of a linear matrix equation.

2.5.1 Radiative heat transfer equations

Since we are discussing natural gas combustion we may assume that scattering does not play a role in the radiative heat transfer, implying that k^s_λ from eqn. (2.66) is zero. Then, the integral form of eqn. (2.66) is (Hyde and Truelove (1977); Wieringa (1992)),

$$i'(\underline{r}, \underline{\Omega}) = i'(\underline{r}', \underline{\Omega}) \tau(\underline{r}, \underline{r}') + \int_{\underline{r}'}^{\underline{r}} k(\underline{r}'') i'_b(\underline{r}'') \tau(\underline{r}, \underline{r}'') d\underline{r}'' \qquad (2.67)$$

This equation is now written in a 3-dimensional vector notation and we have assumed that the medium is grey, which enables us to drop the subscript λ. $\underline{\Omega}$ denotes a direction (θ, ϕ) and $\underline{r}$, $\underline{r}'$ and $\underline{r}''$ are position vectors. The transmittivity τ can be written for a grey gas as,

$$\tau(\underline{r}, \underline{r}') = \exp(-\int_{\underline{r}'}^{\underline{r}} k(\underline{r}'') d\underline{r}'' \qquad (2.68)$$

If k is uniform in space, as we have assumed in our model, this simply becomes,

$$\tau(\underline{r}, \underline{r}') = e^{-k|\underline{r}' - \underline{r}|} \qquad (2.69)$$

The first term of the r.h.s. of eqn. (2.67) represents radiation from the background, transmitted by the gas. The second term represents the radiation emitted by the gas between $\underline{r}$ and $\underline{r}'$.

From eqn. (2.67) we can find the hemispherically incident flux q^+ in a boundary point $\underline{r}$. A schematic diagram of the geometry is presented in figure 2.3. The incident flux is given by (see Hyde and Truelove (1977); Post (1988)),

$$q^+(\underline{r}) = \int_{2\pi, \underline{n} \cdot \underline{\Omega} > 0} (\underline{n} \cdot \underline{\Omega}) i'(\underline{r}, \underline{\Omega}) d\underline{\Omega} \qquad (2.70)$$

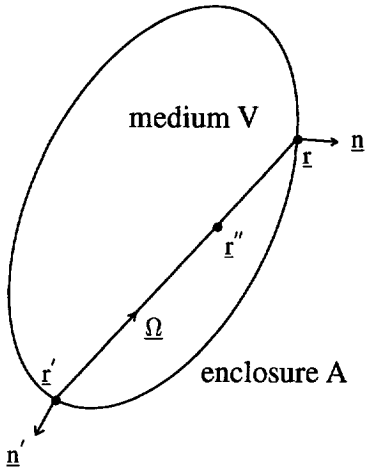

Figure 2.3: General geometry for radiative heat exchange in an enclosure.

in which $\underline{n}$ is the outward normal of the surface in $\underline{r}$. The hemispherically leaving flux q^- is given by,

$$q^-(\underline{r}) = \int_{2\pi, \underline{n}\cdot\underline{\Omega}<0} |\underline{n}\cdot\underline{\Omega}| i'(\underline{r}, \underline{\Omega}) d\underline{\Omega} \tag{2.71}$$

Now, if we substitute eqn. (2.67) into eqn. (2.70) and change the integration variables, we can express the incident flux as,

$$\begin{aligned} q^+(\underline{r}) \;=\; & \int_A \frac{q^-(\underline{r}')\cos\theta\ \cos\theta'\,\tau(\underline{r},\underline{r}')}{\pi|\underline{r}-\underline{r}'|^2} dA' + \\ & \int_V \frac{k(\underline{r}'')e_b(\underline{r}'')\tau(\underline{r},\underline{r}'')\cos\theta}{\pi|\underline{r}-\underline{r}''|^2} dV'' \end{aligned} \tag{2.72}$$

where dA' is an incremental surface element around $\underline{r}'$ and dV'' is an incremental volume around $\underline{r}''$. The definitions of $\cos\theta$ and $\cos\theta'$ are $|\underline{n}\cdot\underline{\Omega}|$ and $|\underline{n}'\cdot\underline{\Omega}|$ respectively. The first part of eqn. (2.72) is the flux emerging from all other boundary points; the second is the contribution of the volume elements.

With the relation,

$$q^- = \epsilon e_b + \rho q^+ \tag{2.73}$$

the system of equations is closed, provided the temperature distribution of the medium is specified. For our problem the temperature distribution is a variable, for which the energy conservation equation is solved. Radiation is included in this equation through a source term S_{rad} (eqn. (2.29)). This source term is the net radiative flux to a gas volume and it can be expressed as,

$$S(\underline{r}) = k(\underline{r}) \int_{4\pi} i'(\underline{r}, \underline{\Omega}) d\underline{\Omega} - 4\pi k(\underline{r}) i_b'(\underline{r}) \tag{2.74}$$

Here, the first term expresses the radiation absorbed by the gas volume and the second term expresses the radiation emitted by the gas volume.

2.5.2 The Hottel Zone Model

The Hottel Zone Method solves the integral form of the equation of radiative transfer by converting it into a matrix of algebraic equations (Hottel and Sarofim (1967)). This is done by dividing the volume into a number of volume zones (in the following we will call these Hottel volumes) and the surface into a number of boundary elements. We assume that these so-called Hottel zones are of uniform properties (temperature, emissivity or absorption coefficient). A set of geometrical factors is defined, which express the heat exchange from one element to another. These factors are usually called direct exhange areas and are written as $\overline{s_i s_j}$ (surface–surface exchange), $\overline{s_i g_k}$ (surface–volume exchange) and $\overline{g_l g_k}$ (volume–volume exchange). Now the incident flux of a surface element A_i is obtained by discretizing eqn. (2.72) for the incident flux, resulting in

$$A_i q_i^+ = \sum_j \overline{s_i s_j} q_j^- + \sum_k \overline{s_i g_k} e_k \tag{2.75}$$

Summation for the first term is over all boundary elements j; the second summation is over all Hottel volumes k. Similarly we can find for the incident flux of a Hottel volume (Hyde and Truelove (1977)),

$$V_k Q_k^+ = \sum_j \overline{s_j g_k} q_j^- + \sum_l \overline{g_l g_k} e_l \tag{2.76}$$

In these equations the direct exchange areas are defined as,

$$\overline{s_i s_j} = \int_{A_i} \int_{A_j} \frac{\cos\theta \, \cos\theta' \, \tau(\underline{r}, \underline{r}')}{\pi |\underline{r} - \underline{r}'|^2} dA' \, dA \tag{2.77}$$

for the exchange between surfaces A_i and A_j, and

$$\overline{s_i g_k} = \int_{A_i} \int_{V_k} \frac{k(\underline{r}'') \cos\theta \, \tau(\underline{r}, \underline{r}'')}{\pi |\underline{r} - \underline{r}''|^2} dV'' \, dA \tag{2.78}$$

for the exchange between surface A_i and volume V_k, and

$$\overline{g_l g_k} = \int_{V_l} \int_{V_k} \frac{k(\underline{r}'') k(\underline{r}''') \, \tau(\underline{r}'', \underline{r}''')}{\pi |\underline{r}'' - \underline{r}'''|^2} dV'' \, dV''' \tag{2.79}$$

for the exchange between volumes V_l and V_k.

To be able to solve the matrix of equations for the surface elements, we need to specify a boundary condition at these elements. We can either specify the temperature of the boundary element or the net flux q_{net} through the surface element.

When the temperature of the boundary is specified the boundary condition becomes eqn. (2.73) for an element A_i,

$$q_i^- = \epsilon_i e_i + \rho_i q_i^+ \tag{2.80}$$

Elimination of q_i^+ from eqns. (2.75) and (2.80) results in the following matrix equation for q_j^-,

$$\sum_j \left(\overline{s_i s_j} - \frac{A_i}{\rho_i} \delta_{ij} \right) q_j^- = -\frac{A_i \epsilon_i e_i}{\rho_i} - \sum_k \overline{s_i g_k} e_k \tag{2.81}$$

In this equation δ_{ij} denotes the Kronecker delta function. When the temperature field is known from the solution of the energy equation or from an initial guess, this matrix equation can be solved. The net flux into a surface A_i is then computed according to,

$$A_i(q_i^+ - q_i^-) = \sum_j \overline{s_i s_j} q_j^- + \sum_k \overline{s_i g_k} e_k - A_i q_i^- \tag{2.82}$$

On the other hand, if the net flux through surface element A_i is specified, the boundary condition is given by,

$$q_i^- = q_i^+ - q_{\text{net},i} \tag{2.83}$$

If we now substitute this equation into eqn. (2.75), we find the following expression for a surface element flux q_j^-, instead of eqn. (2.81),

$$\sum_j (\overline{s_i s_j} - A_i \delta_{ij}) q_j^- = A_i q_{\text{net},i} - \sum_k \overline{s_i g_k} e_k \tag{2.84}$$

The temperature of a boundary element with the net flux boundary condition can be found using eqn. (2.80).

The equation for the Hottel volumes (eqn. (2.76)) can be solved, given an initial guess for the temperature field and after the solution of the surface element equations. The result, viz. the incident flux in a Hottel volume V_k can be used to compute the net radiative source term for the enthalpy equation (2.29).

$$S_k V_k = Q_k^+ V_k - 4 k_k V_k e_k \tag{2.85}$$

in which S_k is the net flux for a Hottel volume V_k.

Computation of the direct exchange factors The computation of the direct exchange factors is a complex and time-consuming task. Because of the furnace geometry and some simplyfying assumptions the work could be drastically reduced. First we can use the following, obvious, reciprocity relations for the direct exchange factors,

$$\begin{aligned} \overline{s_i s_j} &= \overline{s_j s_i} \\ \overline{s_i g_k} &= \overline{g_k s_i} \\ \overline{g_l g_k} &= \overline{g_k g_l} \end{aligned} \tag{2.86}$$

Next, since the furnace geometry was rectangular and symmetrical, it was possible to express many direct exchange factors in terms of another. This gave the most drastic reduction of the computation time. It is necessary, however, to assure the symmetry

of the furnace. In this respect we have made several assumptions. Firstly, we assumed diffusive surface properties in the derivation of the model. Secondly, we used uniform properties of the medium in the furnace. For instance the absorption coefficient was position independent, since otherwise most of the symmetry would be lost.

The direct exchange factors were computed, using an algorithm developed by Siddal (1986), that is applicable for rectangular geometries. The accuracy of this computation could be checked by using the following properties of the direct exchange factors.

The total radiative energy leaving a surface A_i is $A_i q_i^-$. This energy is distributed over all surface elements and all Hottel volumes. Surface element A_j receives an amount of energy equal to $\overline{s_i s_j} q_i^-$ and a volume V_k receives $\overline{s_i g_k} q_i^-$. Conservation of energy requires that,

$$A_i q_i^- = \sum_j \overline{s_i s_j} q_i^- + \sum_k \overline{s_i g_k} q_i^- \tag{2.87}$$

or,

$$A_i = \sum_j \overline{s_i s_j} + \sum_k \overline{s_i g_k} \tag{2.88}$$

A similar argument for the radiation emitted by a Hottel volume V_l yields,

$$4 k_l V_l = \sum_j \overline{g_l s_j} + \sum_k \overline{g_l g_k} \tag{2.89}$$

The algorithm by Siddal yields an accuracy in the order of 10^{-5}.

2.5.3 Coupling the zone model to the flow model

Generally, the number of volumes for the flow computation is much larger than the number of Hottel volumes. The Hottel volumes therefore contain a number of flow volumes. These may be located partly or fully in the Hottel volume. Consequently, the emissive powers of all the flow volumes have to be averaged to obtain the emissive power of a Hottel volume. Likewise, the resulting radiative source term for the enthalpy equation has to be distributed over the flow volumes.

The emissive power of a Hottel volume k is computed according to,

$$e_k = \frac{\sum_i e_{i,\text{flow}} w_i v_i}{\sum_i w_i v_i} \tag{2.90}$$

in which i indicates a flow volume, the summation is over all flow volumes and v_i is the volume of a flow volume i, that is weighted with a factor w_i. w_i is equal to the fraction of a flow volume within a Hottel volume, so w_i is 1 for a flow volume entirely within the Hottel volume and 0 for a volume entirely out of the Hottel volume. The weighting of the emissive power of the flow volumes that constitute a Hottel volume is thus done by the (corrected) volume of the flow volumes.

The radiative power of a Hottel volume k is distributed over the flow volumes i according to,

$$S_{\text{rad},i} = \frac{w_i v_i e_i Q_k^-}{v_i \sum_j e_j w_j v_j} \tag{2.91}$$

in which $S_{\text{rad},i}$ is the radiative source term for a flow volume i. Thus the weighting of the radiative source term is done by a weightfactor that is dependent on the emissive power of the flow volumes in the previous iteration step of the radiation computation.

2.6 The NO_x formation model

2.6.1 The route to NO_x formation

Ultimately, the aim of our study is to predict the NO_x formation in the furnaces and flames that we have discussed so far. This requires the development of a NO_x formation model and including this NO_x model in the combustion code. Since the major part of the NO_x formed in the furnaces that we study is NO and only a small part is NO_2 or N_2O, we have only modelled NO formation and will only discuss the NO formation models here.

The NO_x formation route is the first part of the modelling procedure that we will have to consider. In literature (Glassman (1987); Lefebvre (1983); Miller and Bowman (1989)) three production routes for NO are distinguished. Firstly, there is a NO_x production route via the fuel-bound nitrogen in the fuel. Coal e.g. contains HCN-like components. Via a chain of reactions these amines and cyano compounds react to form nitric oxide, although a part of the mechanism includes the formation of molecular nitrogen from the fuel-bound nitrogen. Since natural gas does not contain any fuel-bound nitrogen, this is not a NO_x production route that we will have to consider.

The second NO_x production route is known as "prompt" NO formation, a term introduced by Fenimore to describe the rapidly formed NO in regions near the flame zone (Fenimore (1971)). Prompt NO is formed primarily by a reaction sequence that is initiated by the rapid reaction of hydrocarbon radicals with molecular nitrogen, leading to formation of amines and cyano compounds, that subsequently react to form NO. In the reaction mechanism many reactions play a role that are also important in the fuel NO formation. A comprehensive summary of the prompt NO mechanism is provided in figure 2.4, where the most important paths are indicated by bold lines. The mechanism of prompt NO formation can be expected to play some role in the turbulent diffusion flames that we are studying. Especially at flow configurations with a low excess air factor, prompt NO formation can be expected to play an important role.

For the present study, however, the most important NO_x production route is the Zel'dovich or thermal mechanism. This is a NO_x production route via a simple chain, that is strongly dependent on temperature. Because of the very high temperature in the furnaces that we are considering in this study, the thermal NO_x formation determines the NO_x emission from the furnaces. This chain was first postulated by Zel'dovich (Zel'dovich (1946)). The three reactions that comprise the thermal NO formation mechanism are,

$$\begin{aligned} O + N_2 &\rightleftharpoons NO + N \\ N + O_2 &\rightleftharpoons NO + O \\ N + OH &\rightleftharpoons NO + H \end{aligned} \qquad (2.92)$$

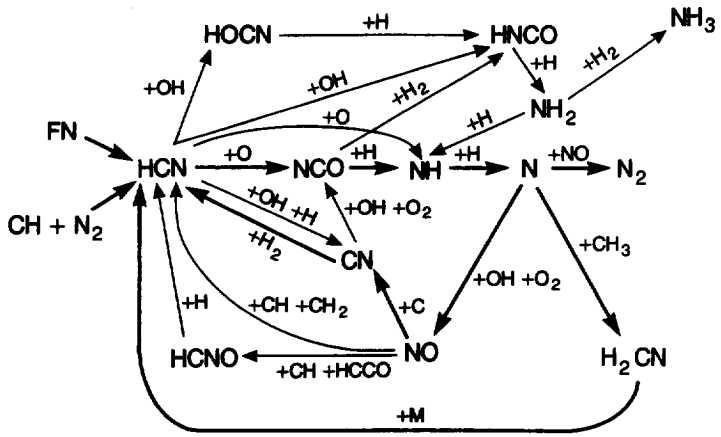

Figure 2.4: Reaction path diagram illustrating the major steps in prompt NO formation. The same reactions play an important part in the fuel-bound NO formation, indicated by FN. The bold lines represent the most important reaction paths. Figure from Miller and Bowman (1989).

The third reaction involves two radicals that are only present in low concentrations in the flame region. Because of the competition with the combustion reactions, since OH is an important intermediate in the combustion of hydrocarbons, the third reaction can often be neglected (Fenimore (1971); Bowman (1975)), except for fuel-rich mixtures. Neglecting reaction (iii) and assuming a stationary-state N-atom concentration (Bowman (1975); Miller and Bowman (1989); Caretto (1976)), we are able to compute the rate of formation of NO,

$$\frac{d[\mathrm{NO}]}{dt} = \frac{2[\mathrm{O}]}{k_{2f}[\mathrm{O_2}] + k_{1b}[\mathrm{NO}]} \left\{ k_{1f} k_{2f} [\mathrm{O_2}][\mathrm{N_2}] - k_{1b} k_{2b} [\mathrm{NO}]^2 \right\} \tag{2.93}$$

where k_{1f} is the forward rate of reaction 1. Due to its high activation energy (see table 2.1) reaction 1 (forward) is the rate determining reaction. In the rate of formation of NO we find the O-atom concentration. In the present study this concentration has been computed from the equilibrium reaction,

$$\mathrm{O_2(+M)} \rightleftharpoons \mathrm{O + O(+M)} \tag{2.94}$$

which yields,

$$[\mathrm{O}] = K_4^{1/2} [\mathrm{O_2}]^{1/2} \tag{2.95}$$

The reaction rates and the equilibrium constant have been reviewed and compiled in literature many times (Baulch *et al.* (1973); Hanson and Salimian (1984); Warnatz (1983a); Westley (1980)). The rate constants that we have used and the literature source are listed in table 2.1. It is generally recognised (Glassman (1987); Miller and Bowman (1989); Drake and Blint (1991)) that the characteristic reaction time for the NO

Table 2.1: Used rate constants for the thermal NO_x formation model,

	A	n	E	source
k_{1f}	$1.8 \cdot 10^{11}$	-	$3.19 \cdot 10^5$	Warnatz (1983a)
k_{1b}	$6.4 \cdot 10^6$	1	$2.61 \cdot 10^4$	Warnatz (1983a)
k_{2f}	$4.01 \cdot 10^{10}$	-	$4.23 \cdot 10^3$	Warnatz (1983a)
k_{2b}	$1.37 \cdot 10^6$	1	$1.5996 \cdot 10^5$	Warnatz (1983a)
K_4	$1.499 \cdot 10^2$	-	$2.48 \cdot 10^5$	Warnatz (1983a)

formation is much larger than the reaction time of the combustion reactions. Moreover, only small amounts of NO are formed — the NO concentrations are generally less than 1 % — and the reaction enthalpy does not influence the gas temperature, nor are the other species concentrations significantly influenced by the reaction. For these reasons it is possible to decouple the thermal NO_x formation process from the combustion process. This decoupling means that in the present study the NO_x formation was computed in a post-processor after the combustion calculations. The NO_x concentration was computed for a given combustion field, i.e. the set of data for a specific flow and parameter configuration. To compute the NO_x concentration distribution in the furnace for a given combustion field the equation for the conservation of species (2.30) was solved. The source term S_i in this equation is given by the NO_x formation rate (2.93).

2.6.2 Interaction of the turbulence with the thermal NO_x formation

In section 2.4 the influence of turbulence on the combustion process was discussed. For the combustion process in our furnace we have assumed that the influence of the turbulence can be accurately modelled by intermittency and we have therefore used the double delta pdf. The NO_x formation however has a larger time scale than the combustion and the assumption that intermittency alone is an adequate description of the influence of turbulence on the NO_x formation is not valid. Also, the NO_x is formed not only in the initial mixing region, but also downstream. In section 2.4 we discussed some pdf forms in the initial mixing region and the region downstream. From this it may be clear, that we need a more elaborate pdf model for the NO_x formation.

In this study we will refer to a number of models for the combustion and the NO_x formation. In the standard model we have used the combustion model that was described in section 2.4 and we have not used any pdf weighting of the NO_x source term for the post-processor computations of the NO_x concentration. In that model we have used the already pdf-weighted temperatures and species concentrations to compute the NO source term.

In chapter 7 we will describe an extension of the NO_x formation model. In this "complete" model we have pdf-weighted the NO source term, however not with a discrete pdf. The pdf model that we have used for the pdf-weighting of the NO source term is a continuous pdf clipped at the boundaries, which gives an adequate description of the influence of the turbulence on the NO formation.

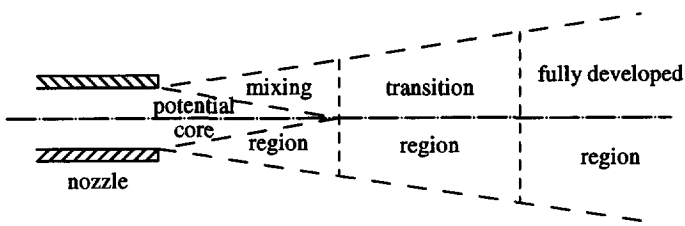

Figure 2.5: Development regions of a jet.

Thus, we have either chosen not to account for the influence of the turbulence on the NO_x formation rate, i.e. the standard model, or to use a pdf model for the NO_x formation that we expected to be satisfactory for our engineering purposes and applicable in our furnace.

2.7 The natural gas jet development

It was already mentioned before that the natural gas and the combustion air enter the furnace separately. The combustion air enters the furnace through an inflow duct of $0.27 * 0.27$ m with an average velocity of about 10 m/s. The natural gas enters the furnace through the burner pipe with a diameter of 8 – 16 mm, depending on the chosen injection velocity. The standard injection velocity was 125 m/s at a pipe diameter of 12 mm.

In the furnace these streams mix, together with the gas from the recirculation zone in the furnace. For a theoretical description of the initial mixing process, we may view the flow situation as a jet of natural gas at ambient temperature issuing into the furnace gas/combustion air at high temperature — the average furnace temperature is 1700 K, the combustion air is approximately 1400 K in the standard case. This opens the way to an approximate analytical solution that we can compare to the numerical results or even may incorporate in the numerical solution procedure to ascertain a valid initial development of the natural gas jet.

2.7.1 Turbulent free jets

The free circular jet has been studied extensively in the past. We will only present a brief description of some results, for thorough investigations we refer to Abramovich (1963).

The free jet development can be divided into three parts. We distinguish, referring to figure 2.5:

1. Potential core zone
2. Transition zone
3. Developed zone

The potential core zone is the region directly downstream of the nozzle, in which the velocity at the axis of the jet remains constant and equal to the injection velocity. The length of the potential core zone is approximately 8 inlet diameters.

In the transition zone the centerline velocity starts decaying. The velocity profile develops into a profile that is independent of the injection nozzle.

In the developed region the velocity profile has reached its final form. The velocity of the jet decays until the effect of a jet has disappeared. In the case of an isodense jet, the centerline velocity decays reciprocally with the distance from the nozzle, giving (Hinze and Van der Hegge Zijnen (1949)),

$$\frac{u_c}{u_0} = \frac{6.39}{x/d_0 + 0.6} \qquad x/d_0 > 8 \tag{2.96}$$

The velocity profile assumes a Gaussian form given by,

$$\frac{u}{u_c} = \exp\left(-K_u(\frac{r}{x})^2\right) \tag{2.97}$$

Since we find streams with different densities in the initial mixing zone, we need to apply a correction. Based on the conservation of momentum Thring and Newby (1953) find an equivalent diameter d_e for non-isodense jets. This can be shown easily, since the momentum flux is,

$$G = A_0\rho_0 u_0^2 = A_e\rho_s u_0^2 \tag{2.98}$$

in which ρ_0 is the density of the jet, ρ_s is the density of the surrounding fluid, u_0 is the injection velocity and A_0 and A_e are the initial and equivalent area respectively. This gives,

$$A_0\rho_0 = A_e\rho_s \tag{2.99}$$

or,

$$A_e = A_o\frac{\rho_0}{\rho_s} \tag{2.100}$$

Thus, since $A = \frac{\pi d^2}{4}$ we find,

$$d_e = d_o\sqrt{\frac{\rho_0}{\rho_s}} \tag{2.101}$$

Now, the relations for the constant density jets may be used with the equivalent diameter for non-isodense jets.

As a consequence of momentum exchange between the jet and the surrounding fluid, the jet entrains fluid from its surroundings. The entrainment, using the equivalent diameter principle, is given by,

$$\frac{m_e}{m_0} = 0.32\sqrt{\frac{\rho_s}{\rho_0}}\frac{x}{d_0} - 1 \tag{2.102}$$

2.7.2 Jet flames

Jet flame development Beér and Chigier (1972) give a literature review on jet flames. Some measurements have been performed in jet flames to determine the influence of the combustion process on entrainment and jet expansion. The results indicate — the measurements were done for hydrogen flames — that jet flames show slower expansion than non-burning jets. This may, at least partly, be explained by the position of the reaction zone. The reaction zone forms an envelope around the fuel jet that emerges from the nozzle. Thus, we can regard the flame jet as a cold high-density jet emerging into hot low-density combustion gases. This then results in little entrainment and a slow rate of decay. Also, based on this analysis, we expect to find the maximum temperature in the envelope of the flame, with the cold fuel jet on the axis. The temperature on the axis rises further downstream, through the mixing of hot combustion products from the flame envelope, until the flame envelope reaches the axis. Through further mixing of combustion products and surrounding air and heat losses to the environment the temperature will then gradually decrease.

Length of the turbulent diffusion flame Based on a rather simple analysis we can show that the flame length of a turbulent diffusion flame is independent of the injection velocity.

The length of a flame can be estimated by assuming that the characteristic diffusion time for a fuel particle to reach the flame envelope is equal to the convection time of the particle downstream (see figure 2.6). The characteristic diffusion time t_D is,

$$t_D \sim \frac{r^2}{I\!D} \tag{2.103}$$

and the convection time t_C is,

$$t_C \sim \frac{L}{V} \tag{2.104}$$

in which r is the nozzle radius, $I\!D$ is the molecular diffusion coefficient, L is the flame length and V is the jet inflow velocity. Thus, the flame length is proportional to,

$$L \sim \frac{r^2 V}{I\!D} \tag{2.105}$$

For a turbulent flame the molecular diffusion should be replaced by the turbulent diffusion. In a simple mixing length model we have,

$$I\!D_t \sim lU \tag{2.106}$$

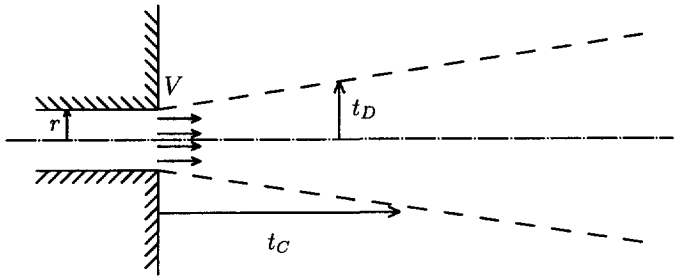

Figure 2.6: Schematic diagram of a flame jet.

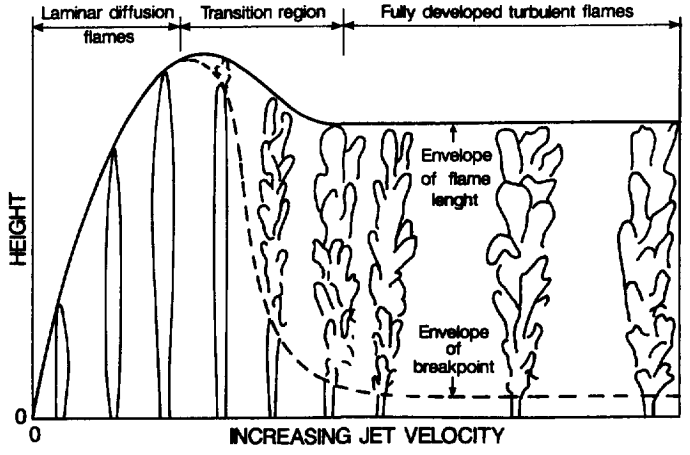

Figure 2.7: Flame length as a function of the jet inflow velocity. Figure from Beér and Chigier (1972).

in which l is a characteristic length scale and U a characteristic velocity. For the turbulent diffusion flame the nozzle radius is an appropriate length scale and the inflow velocity an appropriate velocity. Thus,

$$L \sim \frac{r^2 V}{rV} \sim d_0 \tag{2.107}$$

This analysis is confirmed by experimental results, in which the flame length was measured for different jet velocities (see figure 2.7).

Also, Beér and Chigier (1972) give a semi-empirical relation from Guenther

(1966),

$$\frac{L}{d_0} = 6(s+1)\sqrt{\frac{\rho_f}{\rho_s}} \tag{2.108}$$

in which s is the stoichiometric mass ratio, ρ_f the density of the fuel and ρ_s the density of the combustion products. This equation has been found to be accurate within 10 %. For our flame we find,

$$\begin{aligned} s &= 15.6 \\ \rho_f &= .72 \\ \rho_s &= .22 \\ \frac{L}{d_0} &\approx 200 \end{aligned} \tag{2.109}$$

Chapter 3

The numerical methods

3.1 Introduction

In order to be able to solve the flow equations presented in chapter 2 numerically, the partial differential equations need to be replaced by a system of discrete equations. This discretization has to be consistent: when the number of grid points is increased the difference between the exact solution and the numerical solution has to disappear. In the end this means that when the discretization is done for an infinite number of grid points, we actually are solving the partial differential equations from chapter 2.

The solution method that we have used is the widely known finite volume method that was introduced by Patankar and Spalding (1972). In this chapter we will give a brief description of the followed finite volume approach. To solve the hydrodynamical problem that arises in the solution procedure for the continuity equation we have used the SIMPLE family of algorithms. A brief outline of this algorithm will also be given here. Finally, we will give some attention to the problem of relaxation and convergence.

3.2 The finite volume approach

3.2.1 The general solution procedure

In the finite volume method the computation domain is divided into a number of the so-called control volumes. These control volumes surround a grid node in which all scalar variables are defined. The faces of the control volumes lie halfway inbetween two scalar grid-nodes. In figure 3.1 a two-dimensional example of the grid is given. The grid-nodes of the velocity components are located on the faces of the control volumes. This is the so-called staggered grid approach, which is used to prevent the checkerboard behaviour of the pressure field (Patankar (1980)).

To explain the finite volume technique we will consider the general form of the convection-diffusion equation, in which all flow equations from chapter 2 can be written,

$$\frac{\partial}{\partial t}(\rho\varphi) + \nabla \cdot \underline{J} = S_\varphi \tag{3.1}$$

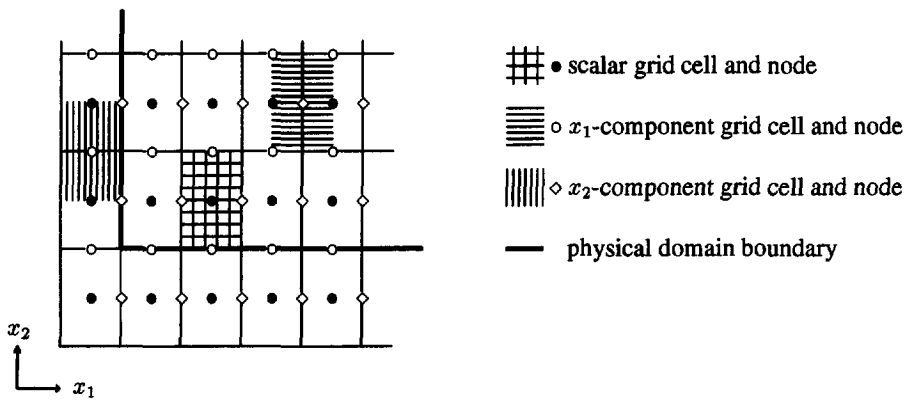

Figure 3.1: A two-dimensional example of the staggered grid.

in which $\underline{J}$ is the flux vector, which is the sum of the convective flux $\rho \underline{u} \varphi$ and the diffusive flux $\Gamma_\varphi \nabla \varphi$. Eqn. (3.1) is integrated over the control volume surrounding grid node P and after applying the Gauß divergence theorem, this leads to a balance equation of the fluxes through the faces of the control volume. In figure 3.2 a control volume is shown, with the grid node denoted as P and the six neighbouring points E(ast), W(est), N(orth), S(outh), T(op) and B(ottom). The corresponding faces of the control volumes are denoted as e, w, n, s, t, b as shown.

The integrated equation can be written as,

$$\left[(\rho\varphi)_\mathrm{P} - (\rho\varphi)_{\mathrm{P},0}\right] \frac{\Delta V}{\Delta t} + (J_\mathrm{e} - J_\mathrm{w}) + (J_\mathrm{n} - J_\mathrm{s}) + (J_\mathrm{t} - J_\mathrm{b}) = \int_{\Delta V} S_\varphi dV \quad (3.2)$$

in which Δt is a time step, ΔV is the volume of the control volume, $(\rho\varphi)_{\mathrm{P},0}$ is the value of $(\rho\varphi)_\mathrm{P}$ at the previous time step and J_i is the flux through face i.

The source term S_φ is linearized, stating that

$$S_\varphi = S_C + S_P \varphi_\mathrm{P} \quad (3.3)$$

in which S_C and S_P are independent of φ_P, which is the value of φ in point P. Thus, the integration of the source term yields,

$$\int_{\Delta V} S_\varphi dV = (S_C + S_P \varphi_\mathrm{P}) \Delta V \quad (3.4)$$

The flux through the control volume faces can be written as, e.g. the east face,

$$J_\mathrm{e} = (\rho u_1 \varphi - \Gamma_\varphi \frac{\partial \varphi}{\partial x_1})_\mathrm{e} A_\mathrm{e} \quad (3.5)$$

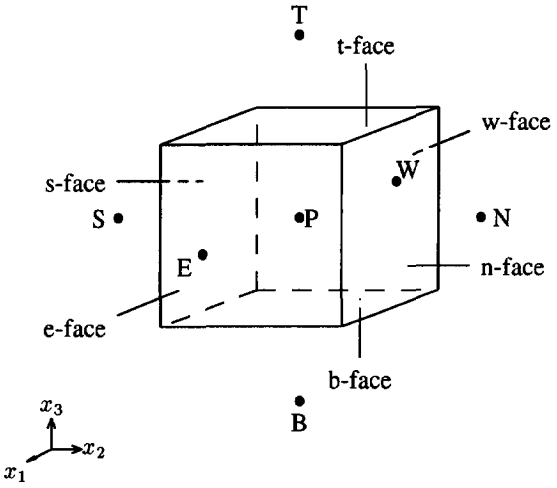

Figure 3.2: A control volume of the scalars, containing one grid node P, with the neighbouring points E – B indicated. The nodes for the velocities lie halfway between the scalar nodes, on the faces of the control volume.

The other fluxes have a similar form. To evaluate the fluxes J_i we have used the hybrid difference scheme, which is a combination of the upwind and central difference scheme. We define the cell-Péclet number as the local ratio of the convective flux to the diffusive flux,

$$\begin{aligned} F_e &= \rho_e u_{1,e} A_e \\ D_e &= \Gamma_{\varphi,e} \frac{A_e}{\delta x_{1,e}} \\ \text{Pé}_e &= \frac{F_e}{D_e} = \frac{\rho_e u_{1,e} \delta x_{1,e}}{\Gamma_{\varphi,e}} \end{aligned} \tag{3.6}$$

in which $\delta x_{1,e}$ is the internode distance between points P and E. F_e is the convective flux through the east face of the control volume and D_e is the diffusive flux. In the discretization upwinding is used for $|\text{Pé}| \geq 2$ and central differencing for $|\text{Pé}| < 2$,

$$\begin{aligned} J_e &= (\rho u_1 A)_e \varphi_E && && \text{Pé}_e &\leq -2 \\ J_e &= \left[(\rho u_1)_e \frac{(\varphi_P + \varphi_E)}{2} - \Gamma_{\varphi,e} \frac{(\varphi_E - \varphi_P)}{\delta x_{1,e}} \right] A_e && -2 < & \text{Pé}_e & < 2 \\ J_e &= (\rho u_1 A)_e \varphi_P && && \text{Pé}_e &\geq 2 \end{aligned} \tag{3.7}$$

This means that for $|\text{Pé}| \geq 2$ the diffusive flux is neglected and only convection is taken into account.

Substituting eqn. (3.7) and analogues for all other fluxes into eqn. (3.2) we find

the following linear equation for φ_P,

$$a_P\varphi_P = \sum_{nb} a_{nb}\varphi_{nb} + b \tag{3.8}$$

in which nb is E, W, N, S, T or B and the coefficients a_P and b are given by,

$$\begin{array}{rcl} a_P & = & \sum_{nb} a_{nb} + \rho_P \frac{\Delta V}{\Delta t} - S_P \Delta V \\ b & = & S_C \Delta V + (\rho\varphi)_{P,0} \frac{\Delta V}{\Delta t} \end{array} \tag{3.9}$$

The coefficients a_E and others can be expressed in the following form,

$$a_E = D_e \max(0, 1 - P\acute{e}/2, -P\acute{e}) \qquad \forall\, P\acute{e} \tag{3.10}$$

From the definition of a_P we derive one constraint for the value of S_P. It is clear, that the numerical solution of (3.8) may become unstable or even diverge if S_P becomes positive. Therefore we have ensured that S_P is negative in the numerical solution procedure.

3.2.2 Boundary conditions

To complete the mathematical description of a variable φ we need a set of boundary conditions for the relevant transport equation of form (3.1). For each separate variable these boundary conditions take the form of an imposed value of the variable (Dirichlet-type condition) or an imposed flux (Neumann-type). In table 3.1 the used boundary conditions are given for all variables. In the inflow most variables have a profile to

Table 3.1: Boundary conditions for all variables.

	solid wall	symmetry	inflow	outflow
U-velocity	$U = 0$	$U = 0$	$U = U_0$	$U = 0$
V-velocity	$V = 0$	$\frac{\partial V}{\partial n} = 0$	$V = V_0$	$\frac{\partial(\rho V)}{\partial n}$
W-velocity	$W = 0$	$\frac{\partial W}{\partial n} = 0$	$W = W_0$	$W = 0$
pressure	-	-	-	-
k	$\frac{\partial k}{\partial n} = 0$	$\frac{\partial k}{\partial n} = 0$	$k = k_0$	$\frac{\partial k}{\partial n} = 0$
ϵ	$\frac{\partial \epsilon}{\partial n} = 0$	$\frac{\partial \epsilon}{\partial n} = 0$	$\epsilon = \epsilon_0$	$\frac{\partial \epsilon}{\partial n} = 0$
enthalpy H	$\frac{\partial H}{\partial n} = q_w$	$\frac{\partial H}{\partial n} = 0$	$H = H_0$	$\frac{\partial H}{\partial n} = 0$
mixture fraction f	$\frac{\partial f}{\partial n} = 0$	$\frac{\partial f}{\partial n} = 0$	$f = f_0$	$\frac{\partial f}{\partial n} = 0$
fluctuation g	$\frac{\partial g}{\partial n} = 0$	$\frac{\partial g}{\partial n} = 0$	$g = 0$	$g = 0$

account for the different flows, viz. the combustion air and the natural gas. The profiles of the velocities and the mixture fraction are chosen in such a way that the prescribed total massflow and natural gas flow are satisfied. The profile of the turbulent kinetic energy is given by (Carvalho (1983)),

$$k = \frac{3}{2} I_t^2 (U^2 + V^2 + W^2) \tag{3.11}$$

in which I_t is the turbulent intensity, defined as,

$$I_t^2 = \frac{1}{3}\frac{(U')^2 + (V')^2 + (W')^2}{(U^2 + V^2 + W^2)} \tag{3.12}$$

Post (1988) recommends a value of 0.30 for I_t^2. The profile of ϵ at the inflow is given by (Carvalho (1983)),

$$\epsilon = \frac{(C_\mu)^{3/4} k^{3/2}}{0.03 L_t} \tag{3.13}$$

in which L is a length scale, taken to be the hydrodynamical diameter of the combustion air inflow channel or natural gas pipe, and $0.03L$ signifies the turbulent macroscale. These inlet profiles are often used in the literature although the coefficient of 0.03 is valid only for fully developed turbulent pipe flow.

The boundary conditions are imposed by the use of virtual points. This was done by extending the computational grid one grid node outside the domain and by assigning the proper boundary values to these points. Thus, for the virtual points we do not solve a linear equation of type (3.8) with modified coefficients — the so-called source term manipulation (Van Doormaal and Raithby (1984)).

3.2.3 Wallfunctions

In section 2.3 the wallfunctions for a number of variables were given. The implementation of these wallfunctions gives rise to some adaptations of the standard linear equation (3.8). In the case of a grid cell adjacent to a wall a special procedure is followed. Given the value of k in the control volume near the wall, we can compute the dimensionless distance to the wall, using eqns. (2.37) and (2.38). This distance needs to be larger than 11.63. Then the transport equations for the velocity components are solved, resulting in non-zero values of the velocities parallel to the wall. The shear stresses for both velocities can then be computed. E.g. for velocity component U the corresponding wall shear stress is given by,

$$\begin{aligned} \tau_{w,U} &= \rho(U^*)^2 = \rho\frac{U}{U^+}U^* \\ &= \rho\frac{\kappa}{\ln(Ey^+)}U(kC_\mu^{1/2})^{1/2} \\ &= \frac{\rho\kappa C_\mu^{1/4}}{\ln(Ey^+)}k^{1/2}U \qquad (y^+ > 11.63) \end{aligned} \tag{3.14}$$

For the other velocities similar equations can be derived. In the solution of the velocity component U the diffusion of momentum is given by $\tau_{w,U}A$, in which $\tau_{w,U}$ is given by (3.14) and A is the area of the wall of the control volume.

The value of ϵ in the near-wall grid point is given by,

$$\epsilon = \frac{C_\mu^{3/4} k^{3/2}}{\kappa y} \qquad (y^+ > 11.63) \tag{3.15}$$

The dissipation term $-\overline{\rho}\epsilon$ in the equation of the turbulent kinetic energy k (2.21) is replaced by,

$$-\overline{\rho}\epsilon = -\frac{\overline{\rho}C_\mu^{3/4}k^{3/2}}{\kappa y}\ln(Ey^+) \qquad (y^+ > 11.63) \tag{3.16}$$

The production term $-\overline{\rho}G$ gives rise to terms $\mu_t(\frac{\partial U}{\partial y})^2$ and $\mu_t(\frac{\partial W}{\partial y})^2$ These terms are replaced by,

$$\mu_t(\frac{\partial U}{\partial y})^2 = \tau_{w,U}\frac{U}{y} \tag{3.17}$$

and

$$\mu_t(\frac{\partial W}{\partial y})^2 = \tau_{w,W}\frac{W}{y} \tag{3.18}$$

in which the τ's are given by eqn. (3.14) for U and a similar equation for W.

Diffusion of turbulent kinetic energy k towards the wall is set to zero. The heat flux to the wall is computed using eqn. (2.40). For the energy equation this flux is implemented through source term manipulation.

3.2.4 Adaptation for non-rectangular geometries

In the general solution procedure we use rectangular control volumes to discretize the domain. The actual furnace that we will model is not necessarily rectangular nor can physical boundaries always be made to coincide with the walls of the control volumes. This problem is solved by using a porosity method (Post (1988)) in which we adapt the coefficients used to evaluate φ in a grid node. We define a porosity of a control volume, which is the fraction of the control volume open for the flow, and a corresponding porosity for all walls.

The volumes, areas and distances that arise in the coefficients (3.10) are now replaced by porosity corrected values. Thus, the volume ΔV is replaced by $P_V\Delta V$, in which P_V is the volume porosity of the control volume, the east face A_e is replaced by P_eA_e and internode distance δx_e is replaced by $P_V\delta x_e$. In a similar way all faces and distances are adapted. In the following, we will not mention the porosities in the equations. For all volumes, areas and distances one should use the porosity corrected values to obtain the implemented model.

3.3 The solution of the discretized system

3.3.1 The hydrodynamic solver

In section 3.2 we have derived finite difference equations for the scalar variables (k, ϵ, H, f and g) and for the three velocity components. There is, however, no equation in which we explicitly solve for the pressure, the fourth variable that we need to describe the flow. The pressure does appear in the momentum equations directly — in the pressure gradient that is a driving force for the flow — but it appears in the continuity equation only indirectly. The problem of finding a velocity field $\underline{u}$

that matches the pressure field p to give conservation of mass is often called the hydrodynamical problem. This problem can be solved by using a pressure correction method that links the pressure gradients in the momentum equations to the continuity equation. A frequently used method to achieve this is the SIMPLE method (acronym of Semi Implicit Method for Pressure Linked Equations, Patankar (1980)). In SIMPLE, the pressure field is initially guessed (p^*). The corresponding velocity field (u^*) is then computed by solving the momentum equations. This velocity field generally does not satisfy the continuity of mass. Then, a pressure and velocity correction are computed so that when the p^* and u^* are corrected the resulting fields do satisfy continuity of mass. The procedure is repeated with the finally obtained corrected pressure and velocities as initial guesses.

Consider the discretized momentum equation for velocity component u_1, in which we explicitly separate the pressure gradient from the other source terms,

$$a_P u_{1,P} = \sum_{nb} a_{nb} u_{1,nb} + b + (p_P - p_E) A_e \tag{3.19}$$

We define the correct pressure and u_1-velocity as,

$$p = p^* + p' \tag{3.20}$$

$$u_1 = u_1^* + u_1' \tag{3.21}$$

Now we first solve the discretized equation for u_1^*, in which the initial guess p^* is used,

$$a_P u_{1,P}^* = \sum_{nb} a_{nb} u_{1,nb}^* + b + (p_P^* - p_E^*) A_e \tag{3.22}$$

In this equation we have assumed that the coefficients a_P, a_{nb} and b are equal to the coefficients in the original equation (3.19). Now subtracting eqn. (3.22) from (3.19) and substituting (3.20) and (3.21) we find for the velocity correction,

$$a_P u_{1,P}' = \sum_{nb} a_{nb} u_{1,nb}' + (p_P' - p_E') A_e \tag{3.23}$$

Now, in this equation we assume that $\sum_{nb} a_{nb} u_{1,nb}' = 0$, which is true in the case of a converged solution, though not necessarily when the solution is not converged. Thus, we find for the velocity correction,

$$u_{1,P}' = \frac{(p_P' - p_E') A_e}{a_P} \tag{3.24}$$

Now, to be able to solve this equation, we first need to solve the pressure correction. We discretize the continuity equation, finding,

$$(\rho_P - \rho_{P,0}) \frac{\Delta V}{\Delta t} + (\rho u_1 A)_e - (\rho u_1 A)_w + (\rho u_2 A)_n - (\rho u_2 A)_s + (\rho u_3 A)_t - (\rho u_3 A)_b = 0 \tag{3.25}$$

Now the equations for the velocities (3.21) and velocity corrections (3.24) can be substituted, which results in a linear equation of type (3.8) for the pressure correction p', in which the coefficients are given by,

$$\begin{aligned} a_{\mathrm{P}} &= \sum_{\mathrm{nb}} a_{\mathrm{nb}} \\ a_{\mathrm{E}} &= \frac{\rho_{\mathrm{e}} A_{\mathrm{e}}^2}{a_{\mathrm{P}}} \end{aligned} \tag{3.26}$$

$$\begin{aligned} b = {} & (\rho_{\mathrm{P},0} - \rho_{\mathrm{P}}) \frac{\Delta V}{\Delta t} - (\rho u_1^* A)_{\mathrm{e}} + (\rho u_1^* A)_{\mathrm{w}} - \\ & (\rho u_2^* A)_{\mathrm{n}} + (\rho u_2^* A)_{\mathrm{s}} - (\rho u_3^* A)_{\mathrm{t}} + (\rho u_3^* A)_{\mathrm{b}} \end{aligned} \tag{3.27}$$

Now, the pressure correction can be solved and consequently the velocity correction.

This iterative procedure is in practice quite slow in converging, thus requiring long computation times. To improve the convergence of the SIMPLE algorithm we have used the SIMPLE R(evised) method, as suggested by Patankar (1980).

In the SIMPLER procedure the pressure is not corrected with the pressure correction. Instead an extra equation is derived, the pressure equation. We define, e.g. for the u_1-velocity,

$$\hat{u}_{1,\mathrm{P}} = \frac{\sum_{\mathrm{nb}} a_{\mathrm{nb}} u_{1,\mathrm{nb}} + b}{a_{\mathrm{P}}} \tag{3.28}$$

Thus we find from eqn. (3.19),

$$u_{1,\mathrm{P}} = \hat{u}_{1,\mathrm{P}} + \frac{(p_{\mathrm{P}} - p_{\mathrm{E}}) A_{\mathrm{e}}}{a_{\mathrm{P}}} \tag{3.29}$$

Substituting this into eqn. (3.25) we now find an equation for the pressure of the form of (3.8), with coefficients,

$$\begin{aligned} a_{\mathrm{P}} &= \sum_{\mathrm{nb}} a_{\mathrm{nb}} \\ a_{\mathrm{E}} &= \frac{\rho_{\mathrm{e}} A_{\mathrm{e}}^2}{a_{\mathrm{P}}} \end{aligned} \tag{3.30}$$

$$\begin{aligned} b = {} & (\rho_{\mathrm{P},0} - \rho_{\mathrm{P}}) \frac{\Delta V}{\Delta t} - (\rho \hat{u}_1 A)_{\mathrm{e}} + (\rho \hat{u}_1 A)_{\mathrm{w}} - \\ & (\rho \hat{u}_2 A)_{\mathrm{n}} + (\rho \hat{u}_2 A)_{\mathrm{s}} - (\rho \hat{u}_3 A)_{\mathrm{t}} + (\rho \hat{u}_3 A)_{\mathrm{b}} \end{aligned} \tag{3.31}$$

Now, the iterative procedure is adapted. First we solve the velocity equations. Then we compute the $\hat{u}_i$ fields, after which we solve the pressure equation. This yields a new pressure field that we use as the initial guess of the pressure field in a new iteration. Thus, the pressure correction p' is not used to correct the pressure but only to calculate the velocity corrections u_i'.

3.3.2 The linear equations solver

For every variable φ of our mathematical model we have derived a transport equation and discretized this equation. The result is a set of linear equations that will have to be solved numerically. Due to the size of the matrix involved direct solvers are prohibitive in computational effort. Therefore we have used several iterative (or indirect) solvers. We have used a number of solvers, all of which can be viewed as TDMA-solvers. However, the standard TDMA is a line-by-line solver of the computational domain. Through remapping of coefficients a_E and others and the source terms, we have used TDMA-variants in which we solved the equations plane-by-plane (plane-TDMA) or in the whole computational domain (space-TDMA). Post (1988) gives an elaborate description of these algorithms, to which the reader is referred. It suffices here to say that the more complex the solver — the space-TDMA is the most complex — the more it resembles a direct solver. The computational effort is then also increased, but since the number of iterations decreases the computational effort may decrease as well.

3.4 Relaxation and convergence

Relaxation During the solution procedure it is often necessary to slow down the rate of change per iteration. Otherwise, the changes could become too large and divergence of the iteration process could occur. To prevent divergence we have used some relaxation techniques, which we will discuss here.

A first relaxation method is to replace an old value φ_P^o by a fraction of this old value and a fraction of the newly computed value with the linear equation solver,

$$\varphi_P = \alpha\varphi_P^n + (1-\alpha)\varphi_P^o, \qquad \alpha > 0 \tag{3.32}$$

For $\alpha < 1$ we have under-relaxation, for $\alpha > 1$ we have over-relaxation. In the present thesis only values of α less than 1 have been used. The relaxation factor α is dependent on the variable, but not on the position.

The second relaxation method is the use of the so-called false time steps. In eqn. (3.9) we find a source term including a Δt in the denominator. For stationary solutions this Δt would be infinite and the resulting source term arising from the time step would be zero. By choosing a small value of the time step Δt one is able to make φ_P deviate only slightly from $\varphi_{P,0}$, which is thus effectively under-relaxation.

For the speed of the computation process it is important to try and find a set of optimum relaxation factors. Too much under-relaxation results in a too large number of iterations needed to get a converged solution, but too small relaxation factors result in divergence or slow convergence with much overshoot per iteration. Finding an optimum set of relaxation factors is a tedious, but rewarding task.

Convergence The iteration process normally starts with guessed initial fields, quite different from the solution when convergence is reached. The solution, however, is

not a priori known and we have therefore the problem of determining when the final solution has been reached. A number of criteria has been used to determine whether the final solution had been reached.

The first criterion is the rate of change per variable. If a variable still changes considerably, convergence can not yet have been reached. Therefore a monitor point in the computation domain was used to monitor the change in all variables per 100 iterations. The rate of change was required to be less than 1 % of the value of the variable in the monitor point.

The second criterion was the value of the pressure correction. The pressure correction is coupled with the continuity equation, meaning that large values of the pressure correction indicate that mass continuity is not yet satisfied in the whole computation domain. The pressure correction is related to the pressure gradient over the furnace, that is of the order of 5 Pa. The maximum value of the absolute value of the pressure correction was required to be less than 0.005 Pa (0.1 % of the total pressure gradient over the furnace) and the sum of the absolute values of the pressure correction over the whole domain was required to be less than 1 Pa.

The third criterion that we used was the so-called residual of a variable φ. The residual is defined as,

$$R_{\varphi,\mathrm{P}} = \frac{a_{\mathrm{P}}\varphi_{\mathrm{P}} - \sum_{\mathrm{nb}} a_{\mathrm{nb}}\varphi_{\mathrm{nb}} - b}{a_{\mathrm{P}}\varphi_{\mathrm{ref}}} \tag{3.33}$$

in which φ_{ref} is a reference value for φ. The residual is a measure of the performance of the linear equation solver in point P. The absolute value of the residual was required to be less than 0.001 per point and the sum of the absolute residuals was required to be less than 0.1.

The fourth criterion of convergence is the overall heat and mass balance. Both balances were required to be correct within 0.1 %.

With the correct use of the convergence criteria it is possible to ascertain the convergence of a solution after a number of iterations. In practice, the third and fourth criterion are the last to be satisfied. These have been used to determine the degree of convergence for most of the solutions that will be presented in this thesis.

Chapter 4

Laboratory model experiments

4.1 Introduction

In this thesis we have studied physical phenomena by simulations. It is essential for the interpretation of the results that the numerical model is verified. In the mathematical description of the flow and the combustion we have introduced several models of which the reliability should be tested. Also the numerical model introduces errors of which the magnitude should be known. It is difficult to test all the assumptions of the model. Therefore we have used models in the FURNACE code that have been used before and that have been tested experimentally. The values of some of the model parameters that were introduced in chapter 2 have been determined experimentally for many flows. However, for the specific application of a high-temperature furnace the question of applicability of the model has to be considered again. To test the applicability many detailed experiments should be done. Because of the high temperatures and the dimensions of the furnace it is difficult to take measurements in the detailed way that would be necessary to test all assumptions. The costs of experimenting in a (semi-) industrial furnace further prohibit extensive measurements. We will compare general results of furnace measurements done by the International Flame Research Foundation (IFRF) in two trials with results of the simulations with FURNACE in a following chapter.

A well known method to test the flow model is to test it experimentally in easily reproducible circumstances. Often a scale model is used at ambient temperature and pressure to perform measurements. The turbulent flow model of FURNACE can easily be used to perform computations at the same conditions and in the geometry of the scale model. The comparison of the results gives a good indication of the applicability of the model, provided proper scaling is used to obtain the scale model. In this chapter we will discuss a scale model of IFRF furnace no. 2 — further introduced in chapter 5 — and the numerical results obtained for this scale model. The results of the comparison of the isothermal flow have been taken into account and have led to model improvements for the computations of flow with combustion.

Table 4.1: Dimensions of the IFRF furnace and the scale model with the applied scale factors.

	IFRF furnace	scale model	scale factor	velocity
furnace length (mm)	3750	2152	0.574	-
furnace width (mm)	955	548	0.574	-
furnace height (mm)	880	505	0.574	-
channel width (mm)	272	157	0.574	10 m/s
pipe diameter (mm)	12	12.9	1.09	125 m/s
air angle (°)	20, 12	12	-	-
gas angle (°)	20, 12	20, 12	-	-

4.2 The scale model

The objective of the laboratory model studies was to perform flow visualization and velocity and concentration measurements in an isothermal scale model of the IFRF furnace no. 2. To achieve a flow situation in the scale model that is representative of the flow in the IFRF furnace, we have followed a three step scaling procedure as was described in Post (1988). The first step is the geometrical scaling of the furnace. The second step consists of the replacement of the separate furnace flows and fluids with different densities by one model fluid with constant density. To obtain a scale model that gives a good representation of the flow in the real furnace, we should account for the different densities of the original flows when they are replaced by the model fluid. For this we have used the equivalent diameter principle that was introduced in chapter 2. The last step consists of the replacement of the model fluid by air at ambient temperature.

For the build-up of a scale model of the IFRF furnace we have used an existing wind tunnel. This tunnel has a fixed width of 505 mm, thus determining the scale factor for the geometrical scale down of the IFRF furnace. Since the width of the IFRF furnace is 880 mm, the geometrical scale factor is 0.574.

In the IFRF furnace we may distinguish between three fluids: natural gas, that enters the furnace with ambient temperature (300 K), combustion air, that is preheated to 1373 K and furnace gases with an average temperature of 1700 K. These fluids have different densities ρ_{ng}, ρ_a and ρ_{av} respectively. In the replacement of these fluids we have replaced them with furnace gases at the average furnace temperature. Using the equivalent diameter principle, this would lead to a somewhat increased area of the combustion air inflow channel. Since the increase is only small (10 %), we have not applied the extra scale factor that would follow from the application of the equivalent diameter principle. For the natural gas inflow pipe, however, the scale factor is considerably larger, viz. $\sqrt{0.75/0.22} = 1.9$. The geometrical scale factor was multiplied by this extra scale factor, which would have resulted in a pipe diameter of 13.1 mm. Since a pipe with diameter 12.9 mm was available as standard we have used this pipe, neglecting the small error.

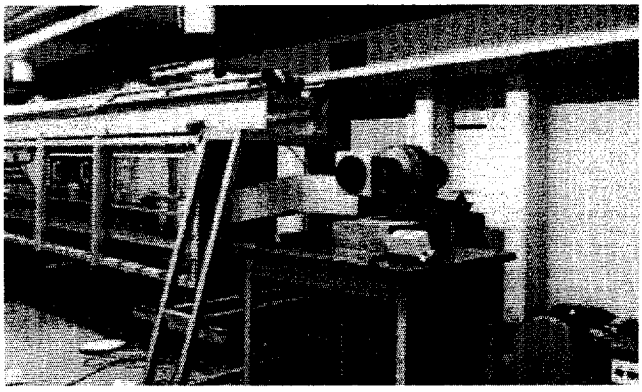

Figure 4.1: Overview of the scale model seen from the side of the inflow.

The third and last step in the scaling procedure is the replacement of the model fluid at 1700 K by air at ambient temperature. In this step, the velocities of the two inflows have been held constant. The final scale factors and dimensions of the isothermal model are listed in table 4.1. In figure 4.1 an overview of the scale model is shown, viewed from the inlet side of the furnace model. The combustion air flow was supplied by a ventilator and was kept smoothly turbulent by applying a fine gauze between the ventilator and the inflow channel. The natural gas flow, replaced by an air flow, was supplied from a high-pressure air supply system since we needed to generate an inflow velocity of 125 m/s.

4.3 Measurement techniques

4.3.1 Flow visualization

A qualitative insight into the flow and the mixing in the furnace can be obtained by making the flow visible. In this way we can determine whether the flow is stationary or whether some oscillatory behaviour is found. This oscillatory behaviour was found by Post (1988), in the case of a natural gas/primary air jet issuing under an angle into a preheated secondary air stream. The jet then behaved more or less like a solid body, causing vortex shedding around the jet. This oscillatory behaviour may explain differences in mixing intensity between the computed and the measured results. Visualization was obtained by injection of a fine haze of small oily particles into one of the air flows. A smoke generator that was able to produce smoke both pulsating and continuous was used. Injection of smoke into the simulated natural gas jet was hindered by the use of the high pressure air system, resulting in only small amounts of smoke in the jet. Observations were photographed for later inspection.

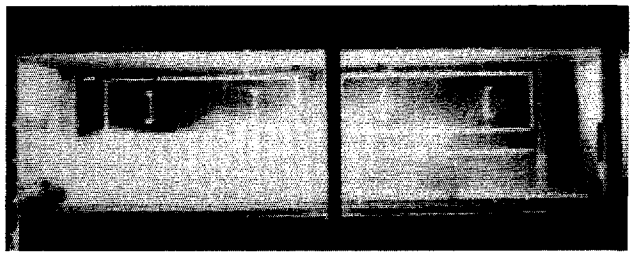

Figure 4.2: Visualization of the flow in the scale model; smoke injection through the air channel.

4.3.2 Helium tracer measurements

Instead of injecting visible components into the air streams for visualization one can inject other components that can be detected quantitatively. An easy way to do this is to inject helium as a tracer gas. The helium concentration can be measured with a katharo-meter. This meter uses the difference in thermal conductivity between air and helium to measure the helium concentration. Using this katharo-meter we were able to measure helium concentrations of up to 2 % (volume). The measurement error of the katharometer was 1 % of full scale.

The helium was injected into the simulated natural gas flow, through the inlet pipe. The helium was supplied from a high pressure cylinder and was fed through a throttle valve to adjust the pressure to the pressure of the air supply system. The concentration of the helium in the natural gas pipe was adjusted to be 1.5 % at the most, so that the detection range of the katharometer was sufficient.

4.3.3 Pitot tube measurements

The Pitot tube measurement method is based on the Bernoulli relation,

$$P_{\text{tot}} = P_{\text{stat}} + \frac{1}{2}\rho v^2 \tag{4.1}$$

Using a Pitot tube the pressure difference $P_{\text{tot}} - P_{\text{stat}}$ was measured and converted to a velocity. The Pitot tube measures only one component of the velocity. For accurate measurements the Pitot tube should be positioned in the direction of the flow. Only small errors arise for angles up to 20° (Post (1988)) so that for our measurements with angles deviating less than 20° from the horizontal we expected no problems.

4.4 Results of scale model experiments and simulations

4.4.1 Visualization of the flow

The main reason for performing visualization experiments was to determine whether the flow is stationary or not. The visualization experiments were performed for the

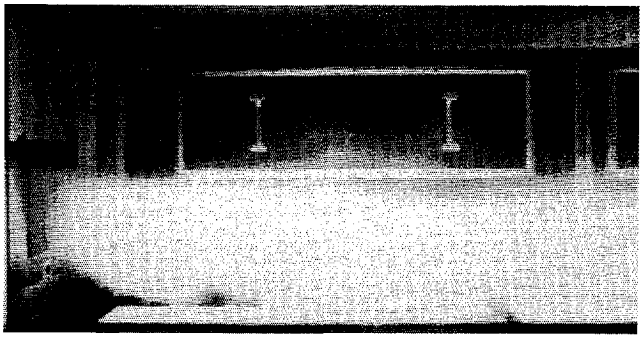

Figure 4.3: Detail of the visualization of the flow in the scale model; first half of the furnace, showing the effect of the gas jet on the smoke in the air stream.

12° (air) - 12° (natural gas) mixing situation. This is a flow configuration in which measurements were also performed by the IFRF, while 12° (air) - 20° (natural gas) was not tested.

It has already been mentioned that injecting smoke into the natural gas pipe was troublesome and was only tried a few times. Unfortunately, the amount of smoke injected into the simulated natural gas flow was very small and resulted in a very low contrast with the background. Conclusions on the question of stationarity of the flow could not be drawn from these visualization experiments.

However, from the experiments with smoke injection into the air channel we can draw some more conclusions. In figure 4.2 a photograph of a visualization experiment is shown. The flow configuration is, as was already mentioned, air injection with a 12° angle downwards and the natural gas injection 12° upwards. The injection velocities were also standard, viz. 10 m/s for the (combustion) air and 125 m/s for the natural gas. On the photograph the burner port is on the left and the outflow is on the right. The photograph was taken approximately 1 second after starting the injection of smoke into the simulated combustion air. The smoke follows the direction of the air, towards the bottom of the furnace, and starts to fill the recirculation in the upper half of the furnace halfway the length of the furnace. Figure 4.3 shows the first half of the furnace, for the same flow configuration. The influence of the gas jet is seen in the extensions of the smoke from the air stream upwards. This shows that the gas jet penetrates into the combustion air stream, but also that the effect is limited since the extensions do not protrude far into the upper half of the tunnel. After approximately 2 seconds the smoke in the recirculation zone fills the tunnel completely, thus making it impossible to determine if an oscillatory behaviour is found in the furnace or if the bulges are only due to increased mixing by the turbulence. Still, the flow pattern that is found in the furnace is made more clear by the visualization experiments.

Thus, no oscillatory behaviour could be found from the visualization experiments. The general information on the flow pattern, specifically on the shape of the

Table 4.2: Positions of the traverses of the velocity measurements.

	12°-12°	12°-20°	x/d_0
A	2.4	2.4	1.86
B	11.3	.	8.76
C	26.2	26.4	20.3
D	41.3	.	32.0
E	56.3	56.2	43.6
F	86.0	.	66.7
G	130.6	.	101.2
H	175.6	.	136.1

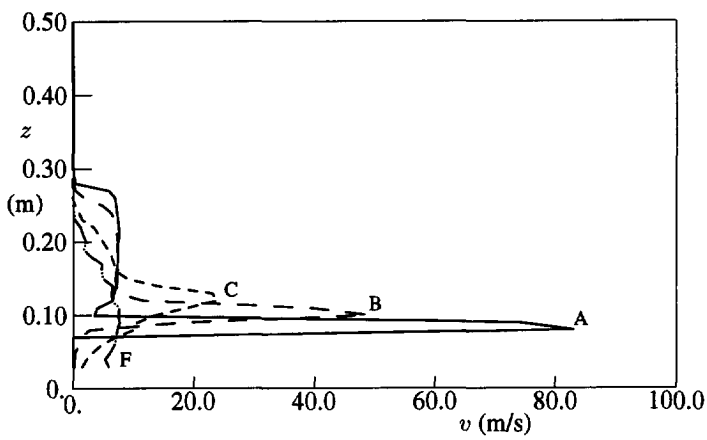

Figure 4.4: Measured velocity profiles at several traverses. A: $y = 0.024$ m, B: $y = 0.113$ m, C: $y = 0.262$ m, F: $y = 0.86$ m.

recirculation zone, has been useful in the interpretation of the numerical results that will be discussed later.

4.4.2 Velocity measurements and simulations

Results of measurements We have measured the axial velocity, i.e. the velocity in the main flow direction, at several traverses in the symmetry plane of the furnace. The measurements have been done for two flow configurations, viz. with the air flow at 12° downwards for both cases and the natural gas flow at 12° and 20° upwards respectively. In table 4.2 the positions of the traverses are listed. Measured velocities in the 12°-12° flow configuration are shown in figure 4.4 for a number of the traverses. In this figure one can clearly observe the decrease of the peak velocity of the jet. The different

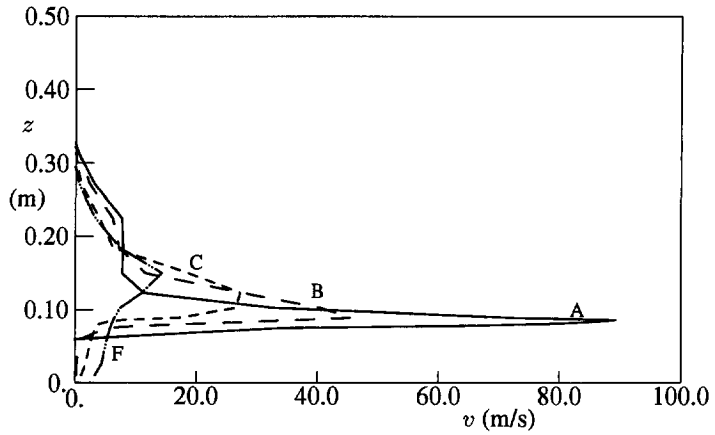

Figure 4.5: Simulated velocity profiles at several traverses. A: $y = 0.024$ m, B: $y = 0.113$ m, C: $y = 0.262$ m, F: $y = 0.86$ m.

vertical positions of the peak velocity for the first three traverses (i.e. traverses A, B and C) are a result of the injection with a 12° upward angle.

The measured data are listed in appendix C. The measured velocities for the 12°-12° flow are listed in table C.3 and those for the 12°-20° flow are listed in table C.1. For the velocity measurements it should be noted that in the upper half of the furnace a recirculation is found, while no attempt was made to measure the reverse velocity by reversing the Pitot tube. The measured data in the upper half of the furnace are thus unimportant.

Results of simulations Using the code FURNACE, that was introduced in the preceding chapters, simulations of the scale model flow were performed. All geometrical and flow circumstances were set to simulate the scale model, with the appropriate temperature and mass flows. In figure 4.5 the axial velocity at the traverses of measurements is shown. These traverses were obtained by interpolation of the axial velocity between the grid nodes that surround the traverses of measurement. In this figure the decrease of the peak velocity is as clearly seen as in the measurements. Also the vertical position of the peak velocity reflects the injection angle of the simulated natural gas. Profiles of the axial velocity in the symmetry plane and two side planes are shown in figure 4.6. The profiles are drawn on the actual computational grid nodes, without interpolation to the traverses of the measurements. The recirculation zone, where the axial velocity is less than zero, is clearly visible in these profiles. About halfway the tunnel the highest velocities towards the roof of the tunnel are found. The size and the place of the recirculation zone are in good agreement to the results of the visualization experiments.

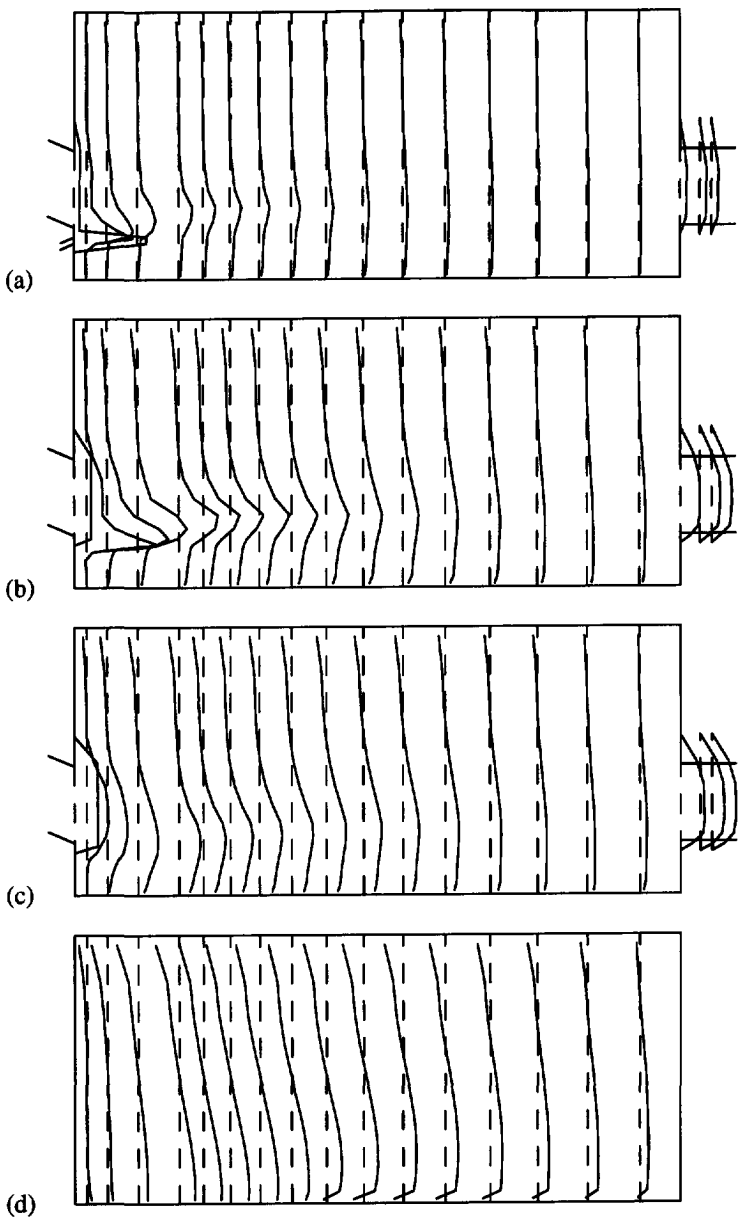

Figure 4.6: Simulated velocity profiles in the symmetry plane and other planes on grid node traverses. a. $x = 0.0$ m, b. $x = 0.008$ m, c. $x = 0.069$ m, d. $x = 0.206$ m

Table 4.3: Positions of the traverses of the concentration measurements.

	12°-12°	12°-20°	x/d_0
A	12.8	12.7	9.92
B	21.9	.	17.0
C	36.7	36.3	28.1
D	51.8	51.8	40.2
E	96.3	.	74.7
F	141.3	.	109.4

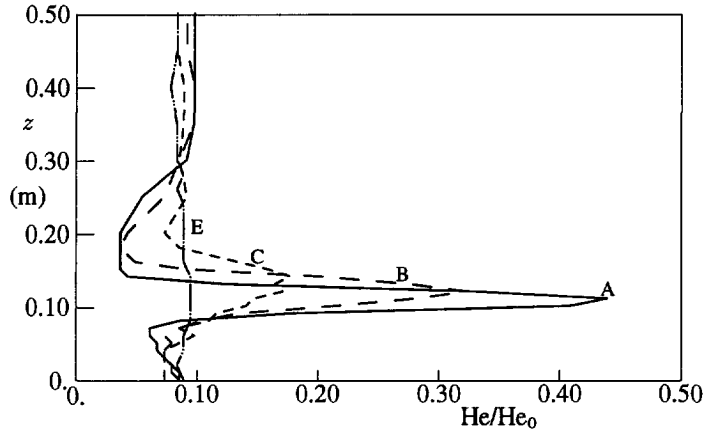

Figure 4.7: Measured concentration profiles at several traverses. A: y = 0.128 m, B: y = 0.219 m, C: y = 0.367 m, E: y = 0.963 m.

4.4.3 Concentration measurements and simulations

Results of measurements As with the velocity measurements we have measured the helium concentration at several traverses in the symmetry plane of the scale model. Due to the positioning possibilities these traverses are not located at the same axial distance as the velocity traverses, but as we will compare the helium concentrations with the simulated concentration distribution this will pose no problem. In table 4.3 the positions of the traverses of the concentration measurements are listed. Measured normalized helium concentrations for the 12°-12° flow configuration are shown in figure 4.7 for a number of the traverses. The normalization was performed based on the value of the helium concentration in the pipe that was used to simulate the natural gas flow. The peak value of the (normalized) helium concentration has already decreased to .45 after 10 d_0. At the height of the air inlet the effect of air inflow without helium is seen in the low (normalized) helium concentration. In the upper half of the furnace the helium concentration is approximately 0.09, which is almost the well-mixed helium

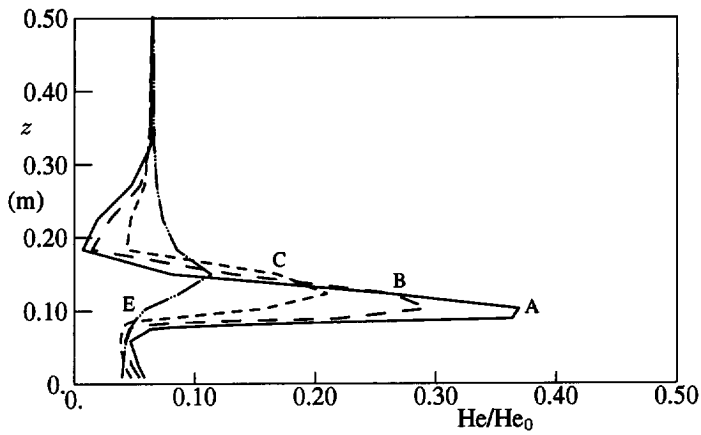

Figure 4.8: Simulated concentration profiles at several traverses. A: $y = 0.128$ m, B: $y = 0.219$ m, C: $y = 0.367$ m, E: $y = 0.963$ m.

concentration. At traverse E the helium jet has completely mixed with the air and no more peak is visible.

Results of simulations The normalized helium concentration was simulated with the help of the mixture fraction f. In the case of no combustion and an isodense flow — air at ambient temperature — the value of the mixture fraction does not influence the flow. It is thus suited to simulate the normalized helium concentration, as we assume that the density of the air in the scale model is not influenced by the small amount of helium that is introduced. In figures 4.8 and 4.9 profiles of f at the traverses of measurement are shown and contours of f in a number of planes, including the symmetry plane. The helium jet is clearly seen in the profiles of f, as is the vertical position of the concentration jet. The values of f were again, as with the velocities, obtained by interpolation between neighbouring grid nodes. At traverse E the simulated jet has not yet completely mixed with the air, in contrast to the result of the measurements. In figure 4.9 the effect of the recirculation, viz. the rising of the f-jet towards the roof of the scale model can be clearly seen about halfway the furnace. This is in good agreement with the visualization experiments, where the rise of the smoke towards the upper half of the furnace is also seen to begin halfway the furnace. The measured helium concentrations are listed in tables C.4 and C.2 for the 12°-12° and 12°-20° flow configurations respectively.

4.4.4 Discussion of the results for the scale model experiments

In figure 4.10 we compare two measured and computed velocity profiles for the 12°-12° flow configuration. These profiles agree with each other very well, for both traverse

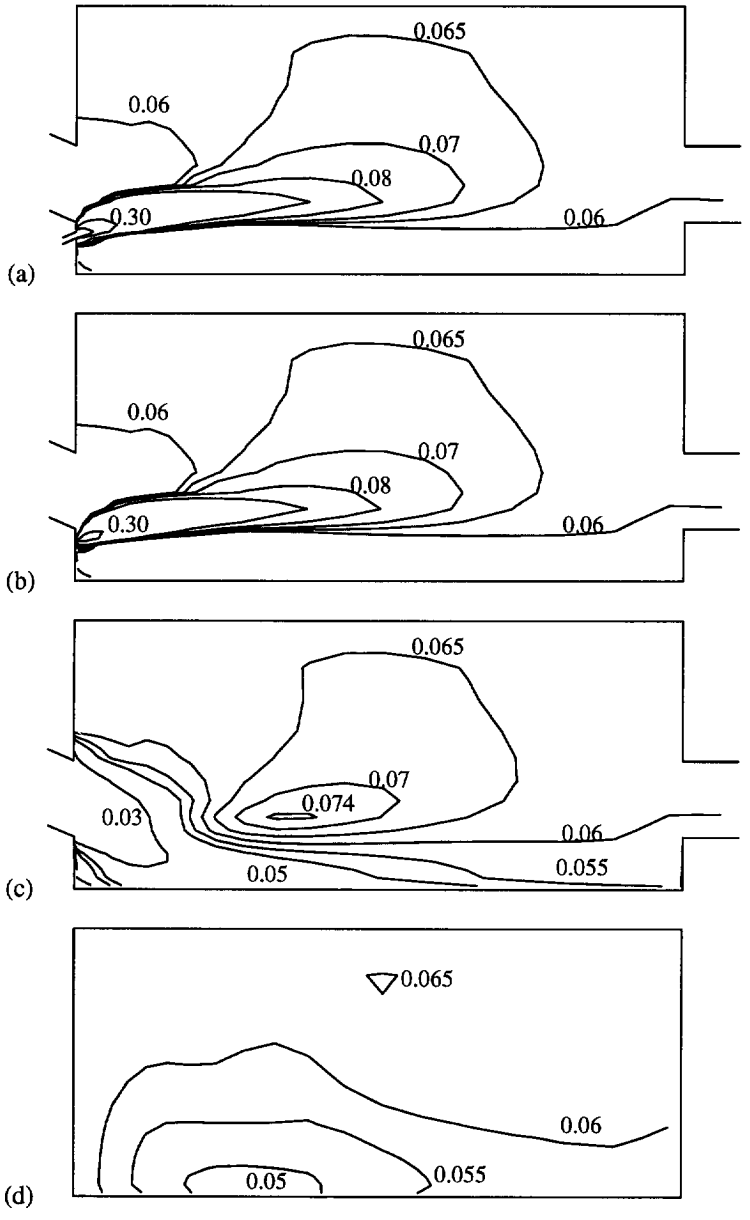

Figure 4.9: Simulated helium concentration contours in several planes of the scale model. a. $x = 0.0$ m, b. $x = 0.008$ m, c. $x = 0.069$ m, d. $x = 0.206$ m

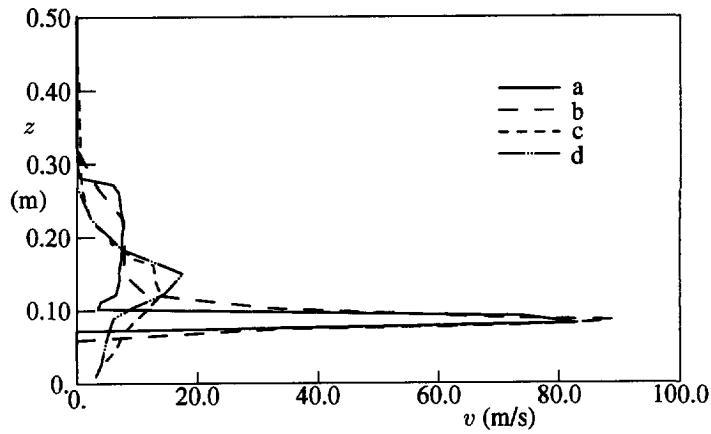

Figure 4.10: Measured and simulated velocities, 12°-12° case. a. Measured profile at y = 0.024 m, b. Predicted profile at y = 0.024 m, c. Measured profile at y = 0.563 m, d. Predicted profile at y = 0.563 m

A — near the burner — and traverse E — at 43 d_0 from the burner. Not only are the peak velocities predicted very well — the differences are less than 20 %, which is satisfactory considering the measurement method — but also the positions of the peak velocities agree very well (see figure 4.12a). For the 12°-12° flow situation this

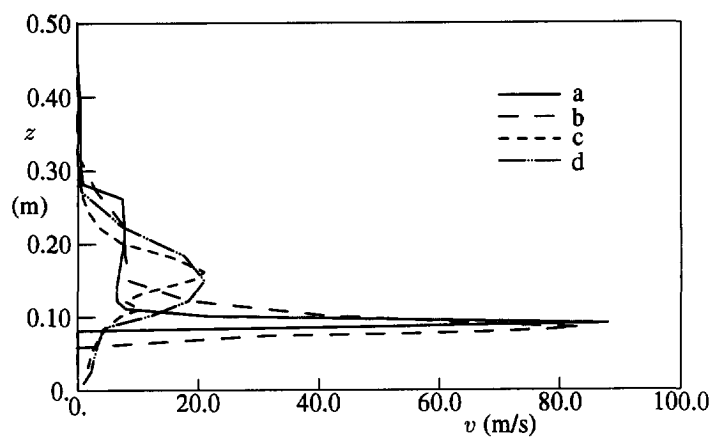

Figure 4.11: Measured and simulated velocities, 12°-20° case. a. Measured profile at y = 0.024 m, b. Predicted profile at y = 0.024 m, c. Measured profile at y = 0.264 m, d. Predicted profile at y = 0.264 m

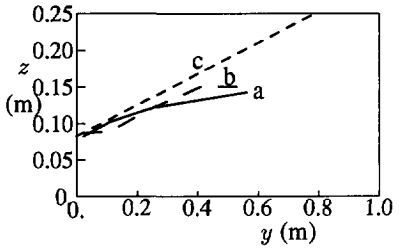

Figure 4.12a: Position of the peak velocity of the jet in the scale model (12°-12° case). a. Measurements, b. Predictions, c. Initial angle.

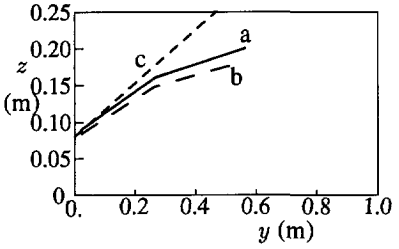

Figure 4.12b: Position of the peak velocity of the jet in the scale model (12°-20° case). a. Measurements, b. Predictions, c. Initial angle.

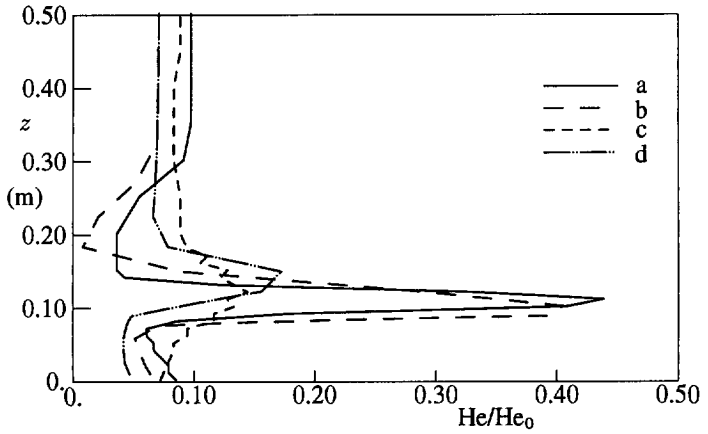

Figure 4.13: Measured and simulated helium concentration, 12°-12° case. a. Measured profile at $y = 0.128$ m, b. Predicted profile at $y = 0.128$ m, c. Measured profile at $y = 0.518$ m, d. Predicted profile at $y = 0.518$ m

means that the deflection of the velocity jet by the air stream is properly predicted by FURNACE.

For the 12°-20° flow case the profiles A and C — at 20 d_0 are shown in figure 4.11. The jet prediction again agrees very well with the measured data, when we consider the peak velocity and the vertical position of the peak velocity. The predicted jet, however, is spread wider, although not very much. When we look at the deflection of the jet from the initial injection angle, shown in figure 4.12b, it is clear that the predictions and the measurements of the velocity jet agree very well.

When we compare measured concentration profiles with computed profiles from FURNACE we find larger discrepancies. In figure 4.13 the profiles at traverses A and

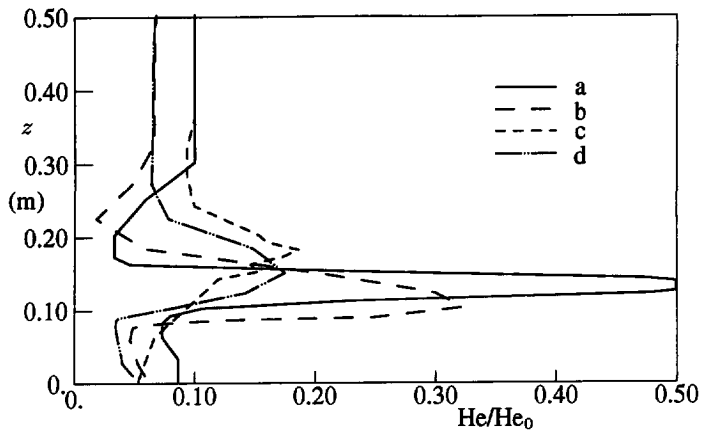

Figure 4.14: Measured and simulated helium concentration, 12°-20° case. a. Measured profile at y = 0.128 m, b. Predicted profile at y = 0.128 m, c. Measured profile at y = 0.518 m, d. Predicted profile at y = 0.518 m

D — at 40 d_0 from the inflow — are shown for the 12°-12° flow configuration. The peak concentrations agree well for traverse A, but further downstream at traverse D the simulations give a somewhat higher peak concentration. The concentration jet seems to spread faster for the computations than for the measurements. This behaviour is also found when we compare the results of the 12°-20° case that are shown in figure 4.14. Here, the peak concentration at traverse A is much lower in the simulations than in the measurements. At traverse D the peak concentrations again agree well. As for the 12°-12° case the predicted jet spreads faster than the measured jet in the wind tunnel. The deflection of the jet from its initial injection angle is shown in figure 4.15. For the 12°-12° case the differences are smaller than for the 12°-20° case, where the deflection in the beginning of the jet is not predicted very well. Further downstream these differences disappear for the most part.

In chapter 2 the theory of a free jet was briefly introduced. We will compare the semi-analytical solution for the centreline velocity and concentration with the measured and predicted results. These are shown in figures 4.16a and 4.16b respectively. From these figures an interesting difference between the jet in the wind tunnel and a free jet becomes clear: in the beginning of the jet, until approximately 30 d_0, the decay of both the centreline velocity and the centreline concentration are faster than would be expected from the free jet development. This may, at least partly, be attributed to the coarseness of the grid. Numerical diffusion gives rise to overestimated development of the simulated natural gas jet, which would result in faster decline of the centreline velocity and concentration than the free jet development. The predictions for the 12°-12° flow (line b in figures 4.16a and 4.16b) agree very well with the measured results (line a). For the 12°-20° situation the differences are much larger. In this

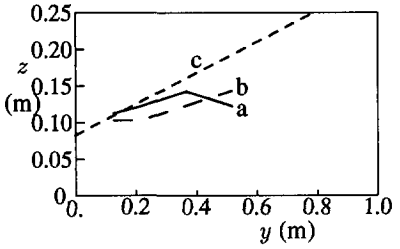

Figure 4.15a: Position of the peak concentration of the jet in the scale model (12°-12° case). a. Measurements, b. Predictions, c. Initial angle.

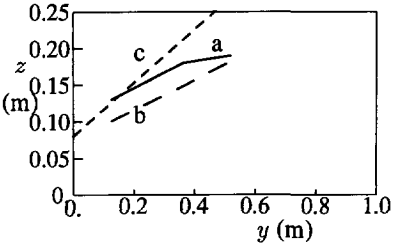

Figure 4.15b: Position of the peak concentration of the jet in the scale model (12°-20° case). a. Measurements, b. Predictions, c. Initial angle.

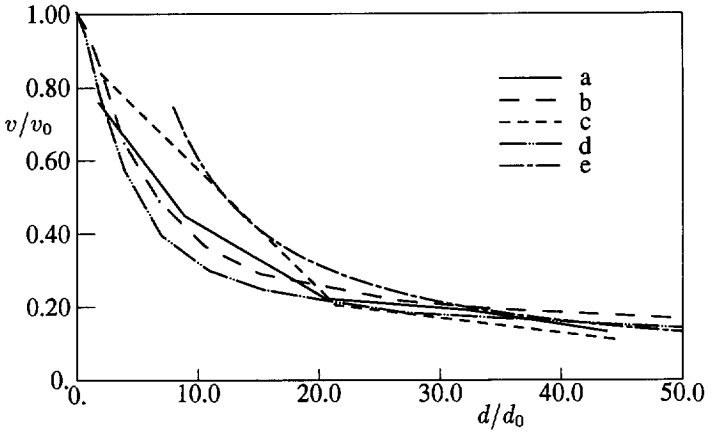

Figure 4.16a: Normalized centreline velocity as a function of the distance to the inflow. a. Measured centreline velocity, 12°-12° case, b. Predicted centreline velocity, 12°-12° case, c. Measured centreline velocity, 12°-20° case, d. Predicted centreline velocity, 12°-20° case, e. Semi-analytical solution for free jet centreline velocity

case the jet in the wind tunnel seems to behave more like the free jet. However, after 25 to 30 d_0 the differences between the measurements, the simulations and the free jet development disappear almost completely. The larger error for the flow with the higher injection angle can partly be attributed to numerical errors. There will be more numerical diffusion at the higher angle, so that a faster decay and greater spread of the jet can be explained. Also, at the higher angles the measurements may give larger errors due to the positioning of the Pitot tube at an angle to the flow direction.

The differences between the measurements, the simulations and the semi-analytical free jet solution disappear after 25 to 30 d_0. This is still in the beginning of the

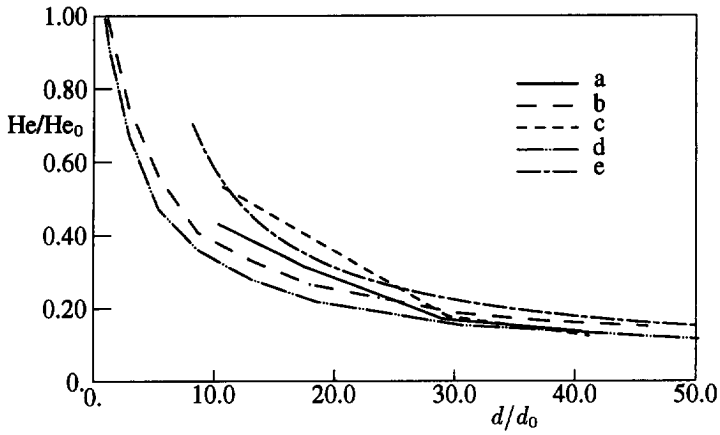

Figure 4.16b: Normalized centreline helium concentration as a function of the distance to the inflow. a. Measured centreline concentration, 12°-12° case, b. Predicted centreline concentration, 12°-12° case, c. Measured centreline concentration, 12°-20° case, d. Predicted centreline concentration, 12°-20° case, e. Semi-analytical solution for free jet centreline concentration

development of the flame in the furnace. In the IFRF furnace 25 d_0 is 0.30 m, compared with the total length of 3.9 m, that was used in the simulations. Since the mixing in the initial region determines the predictions of FURNACE it is very important to simulate the correct behaviour in the beginning of the jet. Considering this, it might be beneficial to impose the analytical solution of the developing free jet as a boundary condition to the computer model. The apparent too fast mixing of the natural gas jet, especially at the higher angles, leads to too fast combustion of gas in the case of calculations with combustion. Numerical diffusion could have its part in this. Generally, this leads to temperatures that are higher than would be measured and consequently to too much NO_x formation. Imposing the analytical solution will prevent numerical diffusion in the highest gradient region and will slow down the mixing and combustion velocity and may result in better predictions with somewhat longer and less NO_x generating flames.

Chapter 5

The NG6 and NG7 trials at the IFRF

5.1 Introduction

This chapter will give a brief outline of the NG6 and NG7 experiments carried out by the IFRF as reported by the IFRF in two reports (Van de Kamp *et al.* (1989); Nakamura *et al.* (1991)). The emphasis will lie on presentation of the results. This will be done in a form suitable for the comparison with the numerical data, that will be presented in chapters 6 and 7. For a complete description of the trials and results we refer to the reports of the IFRF.

5.2 Experimental set-up

5.2.1 Modelling a glass melting furnace

The aim of the IFRF's NG6 and NG7 investigations was to simulate a glass melting furnace and to investigate NO_x reduction techniques. The IFRF furnace no. 2 was to resemble one compartment of a glass melting furnace containing one burner. The furnace refractory was designed to force a heat loss pattern that is normally found in glass melting furnaces. The heat loss through the walls and the roof is in the order of 2 to 5 kW/m^{2}whereas the load heat flux is 50 to 100 kW/m^2. Thus, for IFRF furnace no. 2 the bottom refractory was much thinner (0.06 m) than the roof and wall refractory (0.16 - 0.23 m). The furnace refractory was water cooled through a number of cooling loops surrounding the furnace. These cooling loops were used to measure the heat extraction through the refractory.

The dimensions of the IFRF furnace are compared with the dimensions of two large scale underport fired glass melting furnaces in table 5.1. These figures show that the IFRF furnace has a relatively high combustion chamber when we compare the width/height ratios. The port width/sector width ratio is relatively small for the IFRF furnace, indicating that compared to the port the furnace is wider than the real furnaces. This last feature is necessary since in real glass furnaces several compartments are connected. To ensure a minimum effect of the wall heat losses in the IFRF furnace the combustion compartment was made relatively wide compared to the inlet port. A schematic drawing of the IFRF furnace is shown in figure 5.1.

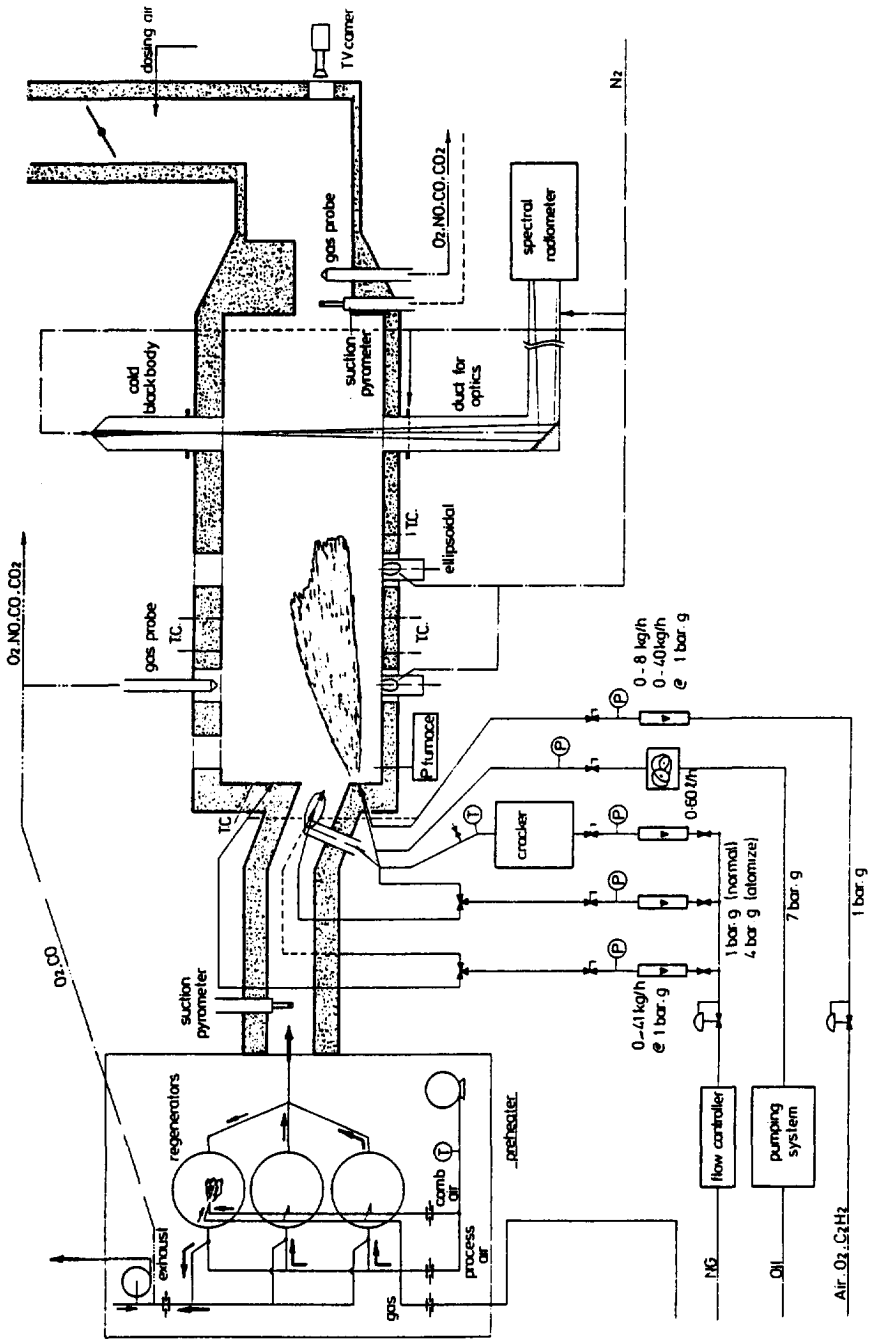

Figure 5.1: Schematic drawing of the furnace set-up. Figure from Nakamura *et al.* (1991).

Table 5.1: Comparison of furnace dimensions between IFRF furnace no. 2 and commercial glass melting furnaces.

	IFRF	A	B
port width/port height	1.0	0.81	1.07
sector height/sector width	1.05	0.67	0.81
sector height/port height	3.50	4.0	3.6
port width/sector width	0.31	0.54	0.48

A - 220 ton/day cross-fired tank with 4 burners/air port
B - 150 ton/day cross-fired tank with 2 burners/air port

An important feature of glass melting furnaces is the high furnace temperature. This not only requires the application of good insulation, but also the use of preheated combustion air. In a real glass furnace the combustion air is preheated by some means of heat retrieval from the flue gas, so as to save on energy consumption. For the NG6 and NG7 trials this would have been too costly to install, so that a separate preheating system was installed. From this system preheated air of up to 1600 K (1300 °C) could be supplied. The system supplies air through a system of three regenerators. During operation one regenerator is heated, while the other two supply air through a mixing chamber. Every minute the heating and heat retrieval is switched between the regenerators, thus giving a periodicity in the combustion air supply. In the furnace this switching is seen through a sudden lack of oxygen and consequently a CO burst in the flue gas. The effect of the switching can be seen on the videos that were made by the IFRF during the trials. In the analysis of the measured data, the switching times of the combustion air supply have been excluded.

5.2.2 Measurement techniques

For most flames the NG6 and NG7 programs provided only input-output measurements. This means that for a set of input parameters a fixed set of output parameters was measured. These output parameters are the flue gas composition and temperature, the heat losses through the walls and the refractory temperature in a number of places in the furnace.

The flue gas composition was measured using a suction probe with subsequent analysers for the several gases in the flue gas:

- NO_x, water cooled probe & chemiluminiscent analyser
- O_2, water cooled probe & paramagnetic analyser
- CO_2, water cooled probe & infra-red analyser
- CO, water cooled probe & infra-red analyser
- H_2, gas chromatography
- H_2O, gas chromatography

The flue gas temperature was measured with a suction pyrometer with a Pt-Pt/Rh (10 %) thermocouple. The suction probe was located in the outflow channel towards

the chimney. The position of the suction probe is approximately in the centre of the channel, which was estimated from photographs supplied by the IFRF.

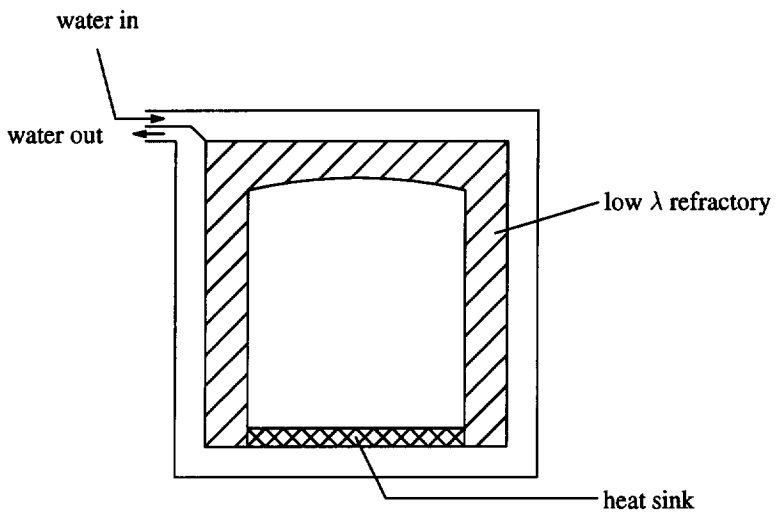

Figure 5.2: Schematic drawing of a cross-section of the IFRF furnace. Figure after Van de Kamp *et al.* (1989).

The heat extraction through the refractory was measured by a number of cooling loops surrounding the furnace. The furnace was divided into thirteen segments, for which the heat extraction was measured by calorimetry. A cross section of the furnace is shown in figure 5.2 with a schematic representation of the cooling loops and the furnace refractory. The temperature difference between input cooling water and the output, combined with the flow rate, gives the heat extraction per segment. Per segment the temperature of the roof, the walls and the bottom were measured with thermocouples.

Beside the input-output measurements also some in-flame measurements were performed. Local gas temperature and composition were measured with a rapid gas quenching probe. Gases are aspirated into this probe and rapidly quenched by mixing with nitrogen. With the known flow of nitrogen to aspirate gas and quench the combustion gases, one is able to compute the gas composition and temperature thermodynamically.

Measurement errors From the IFRF reports it is difficult to form a good impression of the accuracy of the measurements. However, based on the discussion of the measurement errors in the NG7 report (Nakamura *et al.* (1991)) and based on the measurement methods we may be able to say something on this matter.

In the NG6 report it is mentioned that the in-flame measurements were performed with a probe that was not calibrated for the full range of the measurements. The measurements were performed with a probe that was calibrated only up to 1600 °C, while temperatures were measured of up to 1850 °C. For the higher temperatures, at which the furnace performance is mainly determined, this may result in relatively large measurement errors.

For comparison with the simulations, specifically the in-flame measurements, the positioning error of the probe has to be taken into account. In the flame region the gradients are quite large. Over the width of the flame, i.e. the core of the jet towards the burning front, the temperature gradient may be over 1000 K in 0.1 to 0.2 m. Comparison of calculated and measured contours may thus be very difficult due to this error.

The baseline NG6 flame (with a mixing angle of 32°) was reproduced four times during the measurements. From the NG6 reports it becomes clear that the input conditions are not constant for these (baseline) flames. Table 6.1 contains the measured results for these flames. The NO_x emission varies between 1280 and 1950 ppm for these four flames. When we regard flames with the same input conditions, viz. flames 6.044 and 6.109 in table 6.1, the NO_x emission is 1416 ppm for one and 1950 ppm for the other flame. Thus it seems that the measured results are not reproducable. For the NG7 trials several flames were reproduced with excellent agreement.

Based on the discussion in the NG7 report we have assumed the following measurement errors with which we will have to reckon when comparing simulations and measurements.

- temperature, $\pm$ 100 K
- NO_x, $\pm$ 10 %

If we take the reproducability into account the measurement error should be taken larger for NG6 (approximately 20 %, see chapter 6), but for NG7 these estimates are sufficient.

5.3 The NG6 trials

5.3.1 Program of measurements

For the NG6 trials a program of measurements was drafted with the intent of investigating the thermal NO_x formation and of finding applicable NO_x reduction techniques. Several parameters with a known influence on the NO_x formation were varied to test the sensitivity of the NO_x formation. These parameters include the combustion air temperature and the excess air level. Further, the effect of the burner, viz. the mixing of the fuel and combustion air, was investigated. This was done by varying the mixing angle between the natural gas and the combustion air and by varying the natural gas injection velocity.

More parameters were investigated, e.g. the nozzle type, water/steam injection and fuel cracking, but these were not simulated with the computer code FURNACE. We

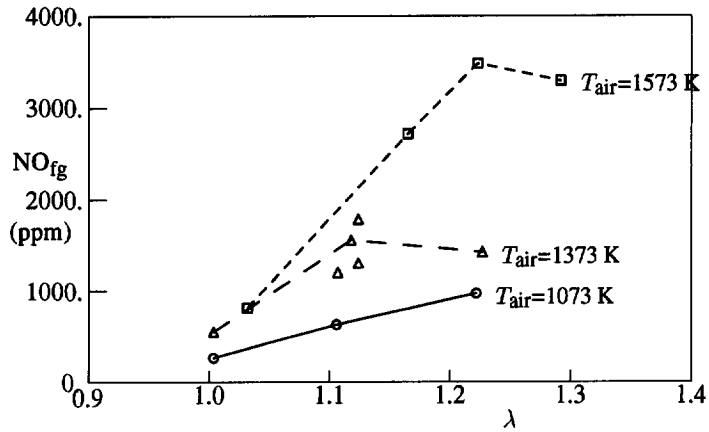

Figure 5.3: Influence of the excess air level on the flue gas NO_x concentration for three air preheat temperatures.

will therefore not introduce the results here, but refer the reader to Van de Kamp *et al.* (1989).

A set of standard conditions was chosen as the baseline flame, with which all other results will be compared. This baseline flame has the following parameters:

- combustion air temperature, 1373 K
- excess air level, +10 %
- gas injection velocity, 125 m/s
- gas injection angle, 12° upwards
- combustion air injection angle, 20° downwards
- thermal input (fuel), 0.5 MW

Variations that were tested are,

- combustion air temperature, 1073 K, 1373 K, 1573 K
- excess air level, +5 %, +10 %, +20 %
- gas injection velocity, 75 m/s, 100 m/s, 125 m/s, 175 m/s, 225 m/s
- burner configurations, -20° air/+20° gas, -20° air/+12° gas, -12° air/+12° gas

In the next section we will present a brief overview of the results of the parameter variations that were obtained by the IFRF.

5.3.2 Results of measurements

Excess air level and combustion air temperature

In figure 5.3 the measured flue gas NO_x concentration (at 0 % O_2) is plotted against the excess air level at the three different combustion air preheat temperatures. In this figure we clearly see the qualitatively expected effect on the NO_x formation of both parameters. The temperature dependence of the NO_x formation, that is seen in the

Table 5.2: Characteristics of measured 20°-12° flames of the NG6 trials: variations of the air preheat temperature and the excess air level.

		T_{air} (K)		
λ		1073	1373	1573
1.0 - 1.05	T_{fg} (K)	1613	1738	1833
	η (%)	38.7	45.2	48.8
	Q_{air} (kW)	150	209	253
	λ	1.00	1.00	1.028
	NO_{fg} (ppm)	215	500	762
	CO_{fg} (ppm)	2500	1500	1500
1.10	T_{fg} (K)	1751	1823	1898
	η (%)	39.3	45.1	47.8
	Q_{air} (kW)	161	236	293
	λ	1.102	1.114	1.161
	NO_{fg} (ppm)	579	1690	2663
	CO_{fg} (ppm)	10	10	20
1.20	T_{fg} (K)	1735	1785	1893
	η (%)	38.3	44.8	47.6
	Q_{air} (kW)	183	251	303
	λ	1.218	1.223	1.219
	NO_{fg} (ppm)	919	1713	3429
	CO_{fg} (ppm)	0	0	10

Arrhenius factors of the NO source term, is reflected in an increasing NO_x emission at higher preheat temperatures. Also, the increasing availability of oxygen with the higher excess air levels is reflected in higher NO_x emissions.

The air preheat temperature also has a strong effect on the thermal performance of the furnace besides the NO_x formation. The excess air level, however, does not influence the thermal performance of the furnace very much.

First, we may look at the efficiency of the furnace. The efficiency will be defined as the total heat transfer to the load divided by the fuel input (.5 MW). Of course, the efficiency could be related to the total heat input, which is the fuel input plus the sensible heat of the combustion air, but in real furnaces the combustion air is normally preheated by the flue gas, so that no separate preheating system is necessary. Therefore we will use the fuel input as the reference for the efficiency. At otherwise standard conditions, the efficiency increases from 39.3 % (at 1073 K) to 45 % (at 1373 K) to 47.5 % (at 1573 K). Related to the total heat input these figures are 29.7 %, 31 % and 30.3 % respectively. At 1573 K the heat loss through the flue gas is relatively high, which reduces the "total" efficiency. The effect of the air preheat temperature can be seen in table 5.2, in which some of the measured results are listed. Included in this table are results of the excess air level variation, that indicate that the efficiency of the furnace

is not much influenced by the excess air level, at least in the range of values that was tested experimentally. The combustion air temperature has a significant influence on the efficiency and the flue gas temperature. Both variables influence the NO_x formation, so that the excess air level seems to be a natural parameter to minimize the NO_x emission at otherwise constant process parameters. The measured flue gas temperature is also included in table 5.2. For the lowest excess level the flue gas temperature is lower than for the other flames. These flames show a considerable amount of CO in the flue gas (CO concentrations up to 1.5 %) so that the low flue gas temperature is probably due to incomplete burnout of the flame. In fact, these flames are unacceptable for industrial applications, where 200 ppm CO is the maximum acceptable number. Thus, the NO_x emission reduction is limited due to the fact that the CO emission requirements have to be met.

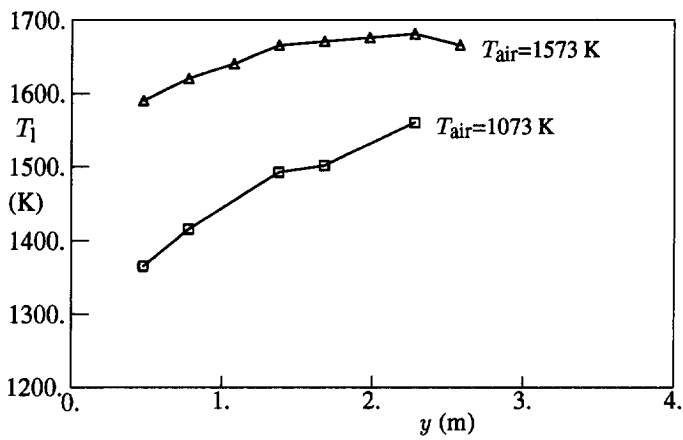

Figure 5.4: Measured temperatures of the load at different combustion air temperatures at otherwise baseline NG6 conditions.

The thermal environment of the furnace changes with the air preheat. The highest roof and load temperature that were measured for the parameter variations that we have discussed so far are listed in table 5.3. It is clear that with an increasing air preheat temperature the furnace on the whole becomes hotter, as do the roof and the load. This was already reflected in the increase of the efficiency of the furnace. The excess air level has no significant influence on the temperature of both the roof and the load. The load temperature distribution in the length of the furnace is shown in figure 5.4. This temperature distribution is one of the boundary conditions for the simulation program FURNACE and is thus an important parameter to be measured accurately. Unfortunately, during the experiments many of the thermocouples in the load were disabled, so that we have had to apply the measured load temperature of only three flames (at the three air preheat temperatures) for all of the simulations.

Table 5.3: Measured highest roof and load temperatures of 20°-12° flames of the NG6 trials: variations of the air preheat and excess air level.

		T_{air} (K)		
λ		1073	1373	1573
1.0 - 1.05	T_r (K)	1575	1689	1755
	T_l (K)	1537	1655	1704
1.10	T_r (K)	1652	1738	1762
	T_l (K)	1553	1682	1711
1.20	T_r (K)	1650	1693	1767
	T_l (K)	1537	1643	1709

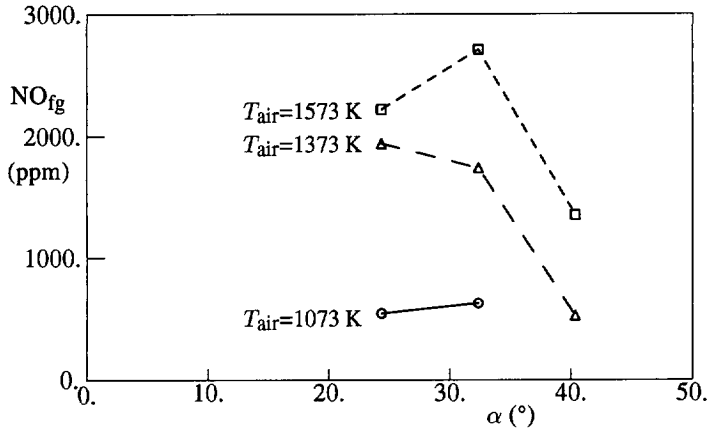

Figure 5.5: Influence of the mixing angle on the flue gas NO_x concentration for three air preheat temperatures.

Mixing angle and gas injection velocity

In the process of firing natural gas the characteristics of a flame can be altered by adjusting the initial mixing between natural gas and combustion air. Since we are studying diffusion flames the mixing determines the rate of combustion and thus other parameters such as the temperature distribution and the species concentration distribution in the furnace. It is not as obvious as for instance with the combustion air temperature, how the combustion and NO_x formation will be influenced by the mixing parameters.

In the NG6 program several mixing parameters were studied. These include the nozzle type — which has not been studied numerically, the mixing angle between natural gas and combustion air and the natural gas injection velocity. The measured effect of the mixing angle can be seen in figure 5.5. The data in this figure represent

Table 5.4: Characteristics of measured flames of the NG6 trials: variations of the mixing angle and the combustion air temperature.

		T_{air} (K)		
α		1073	1373	1573
40°	T_{fg} (K)		1793	1858
	η (%)		45.7	48.5
	λ		1.119	1.103
	NO_{fg} (ppm)		476	1304
	CO_{fg} (ppm)		250	210
	$T_{roof,m}$ (K)		1718	1798
	$T_{load,m}$ (K)		1638	1702
32°	T_{fg} (K)	1751	1823	1898
	η (%)	39.3	45.1	47.8
	λ	1.102	1.114	1.161
	NO_{fg} (ppm)	579	1690	2663
	CO_{fg} (ppm)	10	10	20
	$T_{roof,m}$ (K)	1652	1738	1762
	$T_{load,m}$ (K)	1553	1682	1711
24°	T_{fg} (K)	1757	1835	1873
	η (%)	37.6	44.6	45.6
	λ	1.136	1.131	1.109
	NO_{fg} (ppm)	495	1890	2173
	CO_{fg} (ppm)	10	10	120
	$T_{roof,m}$ (K)	1672	1769	1803
	$T_{load,m}$ (K)	1511	1678	1706

three combinations of injection angles, viz. 20° - 20° (air - gas), 20° - 12°, and 12° - 12°. Data for several combustion air temperatures are represented in this figure. It appears from this figure that the mixing angle has a strong influence on the NO_x formation. The explanation given by the IFRF for this phenomenon was the existence of a penetration effect. This implies that at the higher angles the natural gas jet would penetrate through the combustion air stream into the oxygen lean recirculation zone in the upper half of the furnace. Then, since the recirculation zone is oxygen lean, there would be little oxygen available for the thermal NO_x formation. This would explain the reduction of the NO_x emission at higher mixing angles. In the NG7 trials, as we will see later this chapter, this angle-dependence of the NO_x emission was not found. On the contrary, with increasing natural gas injection angles a slight increase was found in the NO_x emission. In the simulations of these parameter variations this effect was also found, i.e. increasing NO_x emissions at higher mixing angles. Some unexpected difference between the actual and the required furnace conditions may have caused this effect, but the IFRF reports are not conclusive here. In the discussion of the NG6 results, we

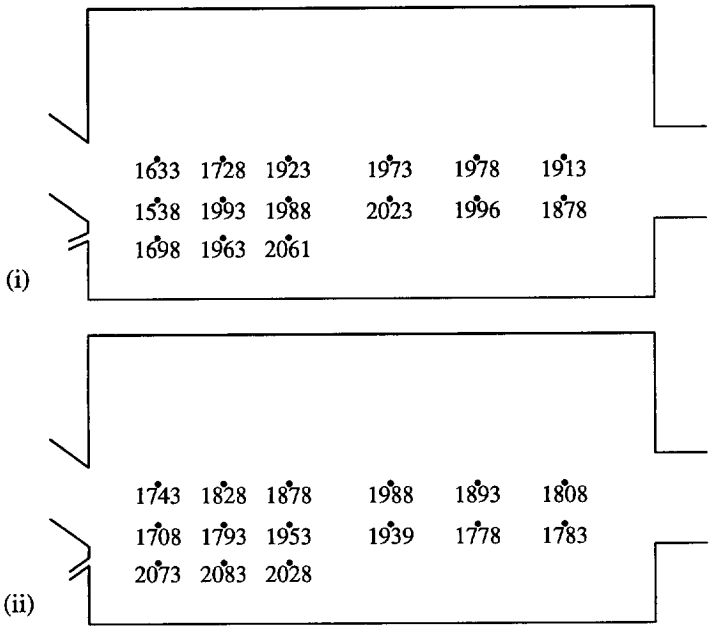

Figure 5.6a: Temperature (in K) at the points of measurement in the symmetry plane of IFRF furnace nr. 2. i. 20°-12° flame, ii. 20°-20° flame.

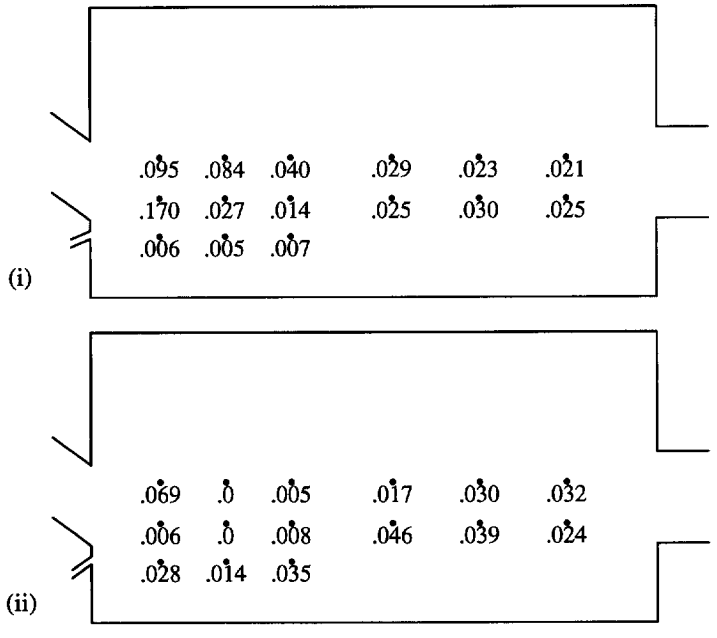

Figure 5.6b: Oxygen concentration (mass fraction) at the points of measurement in the symmetry plane of IFRF furnace nr. 2. i. 20°-12° flame, ii. 20°-20° flame.

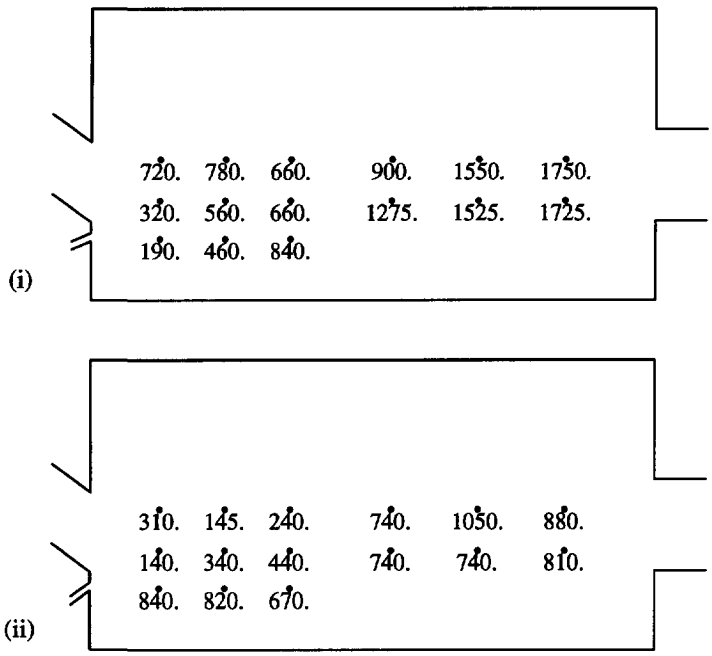

Figure 5.6c: NO concentration (in ppm) at the points of measurement in the symmetry plane of IFRF furnace nr. 2. i. 20°-12° flame, ii. 20°-20° flame.

will regard the NO_x emission results for the mixing angle variation with caution. It is still important to present all other results here, so that we will be able to compare these results later with the results of the simulations.

The thermal performance of the furnace in the mixing angle variations can be seen in the flue gas temperature and the efficiency. Table 5.4 gives these measured results. The mixing angle seems to have no significant influence on the efficiency or the flue gas temperature. This, however, does not mean that the mixing angle does not influence the combustion in the furnace. The results of in-flame measurements at standard (baseline) conditions, with mixing angles of 32° and 40° resp., are shown in figure 5.6. These figures contain the measurements of the temperature, the oxygen concentration and the NO concentration in the symmetry plane of the furnace and were taken from the IFRF report on NG6 (Van de Kamp *et al.* (1989)). It is clear that the combustion fields differ, but the general averaged quantities of the flue gas do not differ. The flue gas NO_x concentration, by contrast, is strongly influenced by the mixing angle as is the NO distribution in the furnace. As previously remarked, a discussion of the mixing angle dependence will follow in chapters 6 and 7, where the results of the simulations will be discussed.

Table 5.5: Characteristics of measured flames of the NG6 trials: variations of the gas injection velocity and the combustion air temperature.

		T_{air} (K)		
v_{gas}		1073	1373	1573
75 m/s	T_{fg} (K)	1738	1828	1902
	η (%)	38.7	44.6	48.4
	λ	1.103	1.131	1.098
	NO_{fg} (ppm)	423	1008	1995
	CO_{fg} (ppm)	110	90	180
	$T_{roof,m}$ (K)	1640	1691	1766
	$T_{load,m}$ (K)	1569	1664	1727
125 m/s	T_{fg} (K)	1751	1823	1898
	η (%)	39.3	45.1	47.8
	λ	1.102	1.114	1.161
	NO_{fg} (ppm)	579	1690	2663
	CO_{fg} (ppm)	10	10	20
	$T_{roof,m}$ (K)	1652	1738	1762
	$T_{load,m}$ (K)	1553	1682	1711
225 m/s	T_{fg} (K)	1723	1792	1865
	η (%)	39.8	45.1	41.0
	λ	1.125	1.116	1.142
	NO_{fg} (ppm)	615	1453	2838
	CO_{fg} (ppm)	10	20	150
	$T_{roof,m}$ (K)	1678	1710	1727
	$T_{load,m}$ (K)	1581	1602	1635

The second parameter that was tested is the natural gas injection velocity. A summary of measured data is given in tables 5.5 and 5.6 in which the velocity variations are combined with respectively the air preheat and the mixing angle variation. The NO_x emission has been plotted against the gas injection velocity in figure 5.7. From this figure the effect of the injection velocity can be seen. At 24° and 32° mixing angles the NO_x emission increases with increasing injection velocity. At the higher velocities the increase becomes relatively small. At 40° the NO_x emission decreases first, reaching a minimum at around 125 m/s and then increasing quite strongly. At the three air preheat temperatures (all with a mixing angle of 32°) the NO_x emission increases (slightly) with increasing gas injection velocity. Thus, concerning the NO_x emission the effect is not univocal. However, for most variations the effect seems to be that the NO_x emission reaches a maximum and then gradually decreases, while only for the 40° mixing angle cases the NO_x emission reaches a minimum after which it increases strongly. The effect of both mixing parameters on the thermal properties of the furnace and on the flue gas properties is small. The 40° flames show a peak heat transfer to the load closer

Table 5.6: Characteristics of measured flames of the NG6 trials: variations of the gas injection velocity and the mixing angle.

		α (°)		
v_{gas}		24	32	40
75 m/s	T_{fg} (K)	1838	1828	1815
	η (%)	45.0	44.6	44.2
	λ	1.113	1.131	1.088
	NO_{fg} (ppm)	1126	1008	581
	CO_{fg} (ppm)	120	90	300
	$T_{roof,m}$ (K)	1731	1691	1737
	$T_{load,m}$ (K)	1656	1664	1651
100 m/s	T_{fg} (K)		1833	1793
	η (%)		43.0	46.7
	λ		1.114	1.137
	NO_{fg} (ppm)		1408	656
	CO_{fg} (ppm)		20	300
	$T_{roof,m}$ (K)		1745	1735
	$T_{load,m}$ (K)		1634	1645
125 m/s	T_{fg} (K)	1835	1823	1793
	η (%)	44.6	45.1	45.7
	λ	1.131	1.114	1.119
	NO_{fg} (ppm)	1890	1690	476
	CO_{fg} (ppm)	10	10	250
	$T_{roof,m}$ (K)	1769	1738	1718
	$T_{load,m}$ (K)	1678	1682	1638
175 m/s	T_{fg} (K)		1823	1798
	η (%)		40.8	42.8
	λ		1.119	1.131
	NO_{fg} (ppm)		1642	825
	CO_{fg} (ppm)		20	20
	$T_{roof,m}$ (K)		1738	1742
	$T_{load,m}$ (K)		1596	1621
225 m/s	T_{fg} (K)	1828	1792	1718
	η (%)	44.5	45.1	43.8
	λ	1.109	1.116	1.109
	NO_{fg} (ppm)	2028	1453	1315
	CO_{fg} (ppm)	10	20	10
	$T_{roof,m}$ (K)	1752	1710	1747
	$T_{load,m}$ (K)	1646	1602	1631

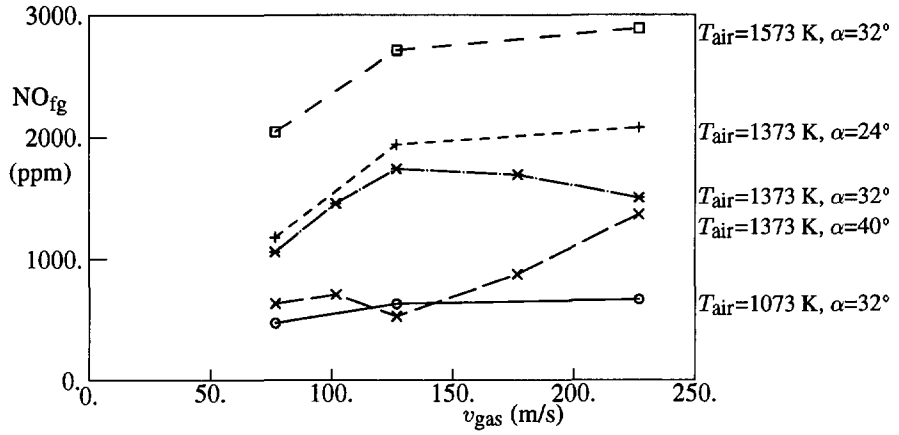

Figure 5.7: Influence of the natural gas injection velocity on the flue gas NO_x concentration for three air preheat temperatures and three mixing angles.

to the burner than the lower mixing angles. The efficiencies, however, do not differ significantly, so that the heat release further downstream seems to compensate for this peak behaviour.

The influence of the mixing angle and injection velocity can be seen in the flue gas CO concentration. At 75 m/s up to 0.15 - 0.30 % CO is measured in the flue gas, while at 225 m/s CO was measured in the flue gas of almost none of the flames. This means that the higher velocities give faster mixing and better burnout. We may thus expect higher flame temperatures in these flames — and also more NO_x formation. The minimum for the 40° mixing angle flames cannot be explained this way, but the penetration explanation is also unsatisfactory since it cannot explain the NO_x emission trend of most flames.

5.3.3 Concluding remarks on the NG6 trials

Both the excess air level and the combustion air preheat have the expected effect on the NO_x emission of IFRF furnace no. 2. As a means of NO_x reduction the excess air level is a parameter that can be optimized at prescribed process conditions. However we should keep in mind that the IFRF tests at the lowest excess air levels lead to unacceptably high CO emissions. For practical applications this indicates that there is a limit to the application of low excess air levels to reduce the NO_x emission. The air preheat influences the whole furnace performance and is less useful for NO_x reduction at prescribed process conditions. Mixing also influences the NO_x emission. Generally, increases in the gas injection velocity resulted in higher NO_x emissions. The precise behaviour, however, is dependent on the mixing angle.

For the analysis of the measured results in chapter 6 and the comparison with the simulations several parameters are of importance. First, the load temperature is a

boundary condition for the numerical program FURNACE. Unfortunately, the measurements of the load temperature were influenced by the refractory that caused breakdown of the thermocouples and possibly a bad thermal contact between the refractory and the cooling loops. Further, the heat loss through and the temperature of the front and back walls are important data to compare with the simulations. These were not measured, so that testing the applicability of the numerical model was made more difficult. Other measured data, however, are useful to test the performance of the numerical program, although the measurement errors will sometimes make comparisons difficult.

5.4 The NG7 trials

5.4.1 Program of measurements

In the NG6 experiments mixing of fuel and combustion air was found to be an important parameter for the NO_x reduction. In NG6 the mixing was influenced by the natural gas injection angle and velocity. Since there was a discrepancy between the results of the measurements and the simulations (see chapter 6 for a discussion of these results) this mixing optimization was again performed during the NG7 trials. At a fixed air injection angle (20° downwards for all flames during NG7) the natural gas injection angle was varied for the underport firing burner. Also, the influence of the gas injection velocity was tested again. Besides, some other parameters like the type of nozzle and the injection of core air with an annular gas injection were tested. These last have not been simulated, so we will not discuss these results here.

Another variable that influences the mixing is the geometry of the burner. During the NG6 trials only underport firing was tested, but since mixing was found to have a distinct influence on the NO_x emission other firing modes were tested during NG7. Both numerically and experimentally a number of natural gas firing modes has been tested, viz. underport, overport, combined underport/overport, sideport and parallel sideport firing. The burner configurations for these firing modes are shown in figure 5.8. In this section we will discuss results obtained by the IFRF during the NG7 trials that have also been simulated.

The set-up of the NG7 experiments was performed so that the results of both trials could be compared. Since there had been problems with the load refractory during NG6 care was taken to prevent their recurrence. Instead of three large sections of load refractory 26 small sections were used. This, however, resulted in an important difference between NG7 and NG6. The thermal contact between load refractory and the cooling loops did not, as in NG6, break down. This resulted in more heat transfer to the cooling loops and consequently lower furnace temperatures. The heat transfer to the load was on average 10 kW/m^2 higher and the temperatures of the roof and the walls were generally 200 K lower during NG7 than during NG6. Generally the flue gas temperature was 100 K lower — 1793 K during NG6 (at 1373 K air preheat) compared with 1693 K during NG7, which indicates that the flame temperature is also lower. This proved to be an important difference, because the NO_x values were much lower in

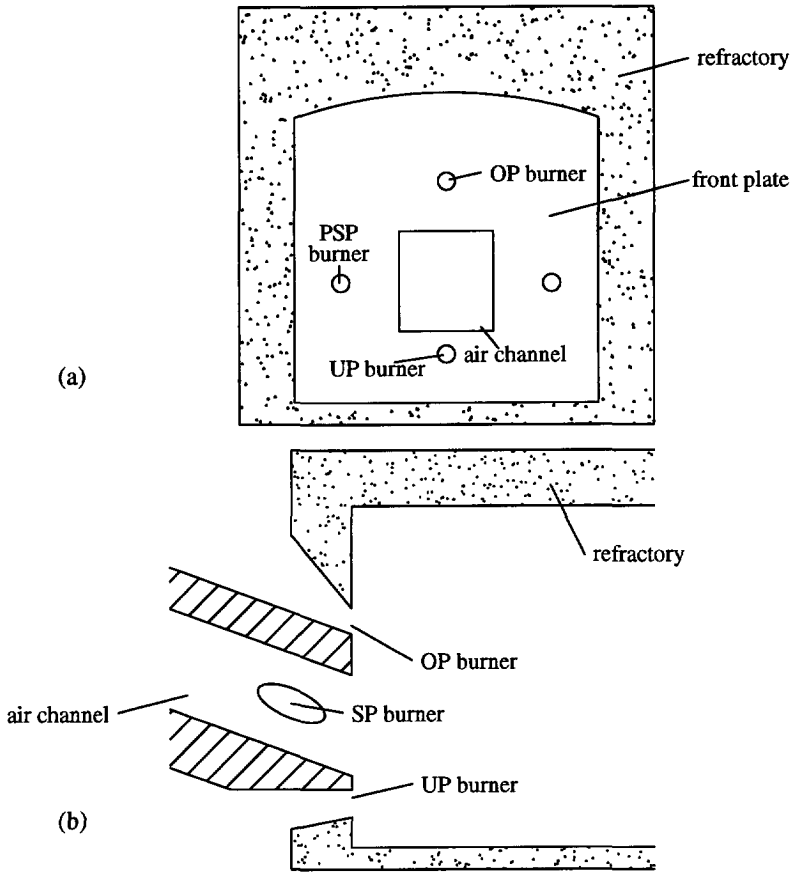

Figure 5.8: Overview of the geometry for the different firing modes.
a. Front view of burner. b. Side view of burner.

NG7. Typically the NO_x emission from NG6 was 1200 ppm, while during NG7 it was 600 ppm (at 0 % O_2). Furthermore the observed NO_x emission trends in NG6 were not fully reproduced in NG7.

5.4.2 Results of measurements

Underport firing

The tests that have been performed for the underport firing mode are a repetition of the tests that were performed during NG6, which tested only underport flames. The results of the mixing optimization are partly consistent with NG6 and partly not. The variation of the gas injection velocity shows an increase in the NO_x emission with increasing velocities, which is the same as in NG6 (see figure 5.9). At the higher mixing angles

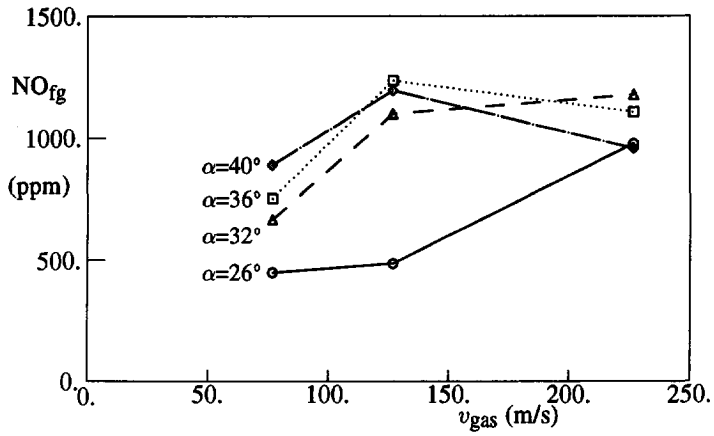

Figure 5.9: NO_x emission vs. natural gas injection velocity (underport, various angles).

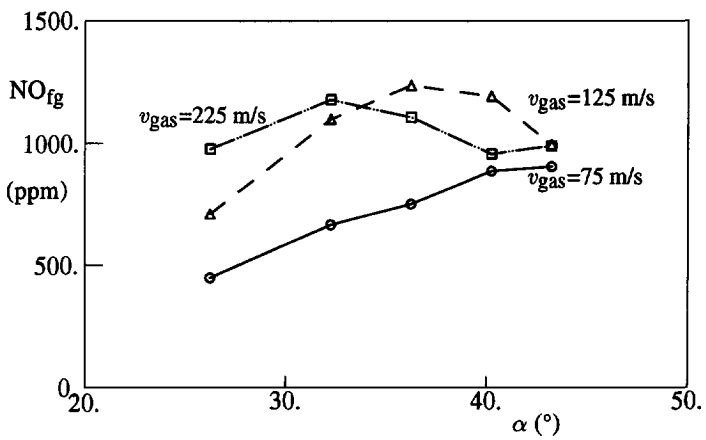

Figure 5.10: NO_x emission vs. natural gas injection angle (underport, various velocities).

there seems to be a minimum NO_x emission at 225 m/s, which was also found in NG6 although then at 125 m/s. This minimum is not clear, however, considering the measurement error, which was estimated by us to be $\pm$ 100 ppm. Taking this error into consideration the existence of a minimum in the NO_x emission can not be proven.

The effect of the mixing angle on the NO_x formation is quite different in NG7 from the effect that was found during NG6.

The NO_x emission increases with increasing gas injection angle (all with air injected 20° downwards), although at the higher angles there seems to be a small

Table 5.7: Characteristics of measured flames of the NG7 trials: variations of the mixing angle and the gas injection velocity (underport firing).

		α (°)			
v_{gas}		26	32	36	40
75 m/s	T_{fg} (K)	1750	1742	1664	1648
	η (%)	51.4	52.4	52.6	53.6
	λ	1.1005	1.095	1.1005	1.106
	NO_{fg} (ppm)	427	643	729	867
	CO_{fg} (ppm)	1127	514	309	117
	$T_{roof,m}$ (K)	1508	1545	1563	1567
	$T_{load,m}$ (K)	1450	1485	1485	1503
125 m/s	T_{fg} (K)	1718	1701	1701	1672
	η (%)	51.6	51.2	53.4	52.6
	λ	1.1005	1.095	1.1005	1.1005
	NO_{fg} (ppm)	687	1077	1214	1173
	CO_{fg} (ppm)	463	99	68	70
	$T_{roof,m}$ (K)	1526	1563	1572	1581
	$T_{load,m}$ (K)	1434	1466	1462	1475
225 m/s	T_{fg} (K)	1794	1701	1734	1726
	η (%)	51.4	51.6	52.8	51.2
	λ	1.117	1.106	1.1005	1.095
	NO_{fg} (ppm)	955	1156	1085	935
	CO_{fg} (ppm)	108	67	80	162
	$T_{roof,m}$ (K)	1540	1581	1594	1590
	$T_{load,m}$ (K)	1457	1457	1448	1434

decrease or stabilization. The data are shown in figure 5.10. For all gas injection velocities the dependence of the NO_x emission on the injection angle is not very large. If we compare the results with those of NG6 (see figure 5.5) the difference becomes clear. The total variation of the NO_x emission (in NG7) at 125 m/s is 690 $\pm$ 70 ppm (at 26° total mixing angle) to 1280 $\pm$ 130 ppm (at 36°). The observed variation in NG6 was 1890 ppm (at 24° mixing angle) to 480 ppm (at 40°). Moreover, the trend in NO_x emission has been reversed. Other measured data for both mixing parameters are listed in table 5.7 for selected parameters that give a good indication of the observed phenomena. The thermal performance is not influenced by the gas injection velocity, although at the lower velocities some CO is found. The efficiency is slightly dependent on the injection angle, which can also be seen in the flue gas temperature that decreases with increasing injection angle.

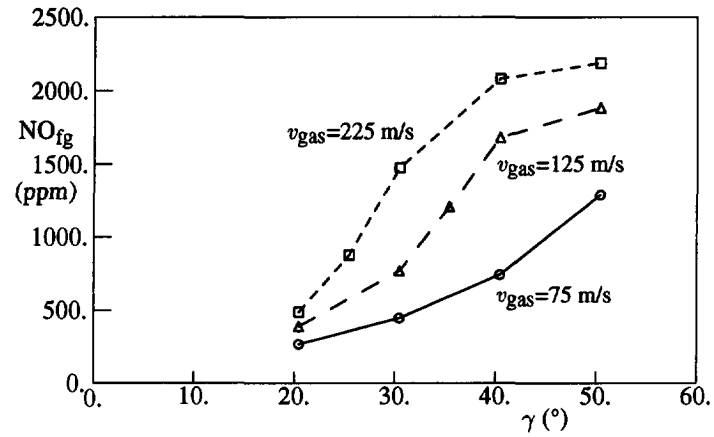

Figure 5.11: NO_x emission vs. natural gas injection angle (overport firing).

Table 5.8: Characteristics of measured flames of the NG7 trials: variation of the mixing angle (overport firing).

	γ (°)				
	20	30	35	40	50
T_{fg} (K)	1721	1692	1688	1677	1630
η (%)	52.0	52.4	52.0	52.8	53.2
λ	1.1005	1.106	1.1005	1.1005	1.095
NO_{fg} (ppm)	342	722	1161	1636	1837
CO_{fg} (ppm)	223	140	132	116	27
$T_{roof,m}$ (K)	1572	1572	1572	1567	1557
$T_{load,m}$ (K)	1516	1517	1507	1525	1516

Overport firing

The first burner geometry variation that we will discuss now is the overport firing mode. In this burner configuration the combustion air is injected 20° downwards as in all other NG7 flames, but the natural gas injection port is placed over the combustion air channel. The natural gas is then also injected downwards, at varying mixing angles to the combustion air. Overport firing was tested because it was expected that combustion in the recirculation zone would be promoted by injecting the natural gas more directly into the recirculation.

In figure 5.11 the influence of the (variable) gas injection angle on the NO_x emission is shown. There is a strong dependency of the NO_x emission on the injector angle, however other properties do not differ very much. E.g. the efficiency is hardly influenced by the angle variation. The CO level in the flue gas decreases with increasing

Table 5.9: Characteristics of measured flames of the NG7 trials: variation of the distribution ratio (underport/overport firing).

	% UP/% OP					
	75/25	60/40	50/50	25/75	13/87	0/100
T_{fg} (K)	1713	1709	1754	1709	1680	1696
η (%)	51.4	-	51.6	51.0	52.6	52.0
λ	1.095	1.095	1.1005	1.095	1.0895	1.106
NO_{fg} (ppm)	1003	871	796	1068	1374	1710
CO_{fg} (ppm)	50	49	140	49	44	47
$T_{roof,m}$ (K)	1613	-	1572	1613	1576	1585
$T_{load,m}$ (K)	1469	-	1490	1474	1498	1507

mixing angle, displaying the effect of enhanced mixing (see table 5.8). It was observed by the IFRF that the 20° - 20° flame, which means parallel natural gas injection to the combustion air for the overport flames, resulted in a poorly mixing flame of indeterminant shape. The low NO_x figure for this flame may be explained by the low flame temperature that will be encountered in situations with very poor mixing. Flames of indeterminant shape, however, are usually not industrially applicable, since the furnace processes depend on the shape of the flame.

Combined underport/overport firing

The two firing modes that we have discussed so far have been combined in the underport/overport firing mode. This combination was expected to give a degree of fuel staging in the furnace. Fuel staging has been investigated many times for its effect on combustion and pollutant formation. Through fuel staging the heat release of the flame is spread over a larger volume, thereby decreasing the flame temperature. In the underport/overport firing the underport fuel mixes with the combustion air first, while the overport fuel is injected into the recirculation gases and mixes with the combustion air later.

In the NG7 trials the effect of the distribution ratio of the fuel between the underport and the overport injector has been studied. Two series of tests were performed, viz. one employing a constant diameter principle — which gives different injection velocities per distribution ratio — and one employing the constant velocity principle, for which the injector diameter is variable for the injector ports. The results that we will present here are those of the constant diameter principle. The other results can be found in Nakamura *et al.* (1991).

For the underport/overport configuration the underport injection angle was fixed at 16° upwards and the overport angle was varied from 20° to 40° downwards. The injector diameter was kept fixed at 8.4 mm for both injectors, resulting in an injection velocity of 250 m/s for a fully underport or overport flame. Since these velocities give large numerical errors in the simulations we have only done computations for the

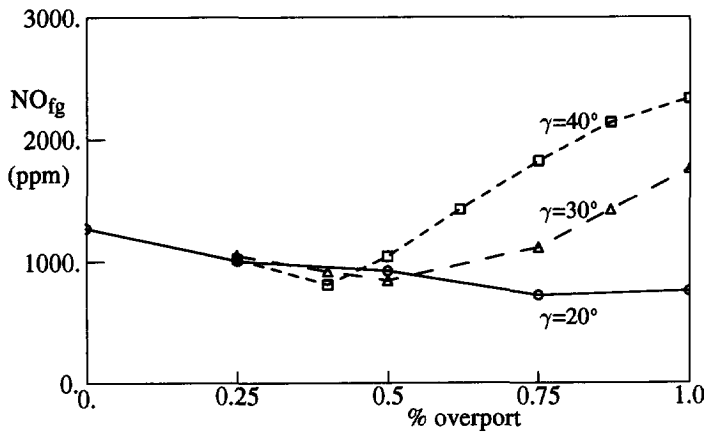

Figure 5.12: NO_x emission vs. distribution ratio at several overport injection angles (underport/overport firing).

75/25, 50/50 and 25/75 distribution ratios. The measured results for the flames with an overport angle of 30° are listed in table 5.9. The dependence of the NO_x emission on the distribution ratio is clear, reaching a minimum at a distribution ratio of 50/50. Still, it is only a weak minimum for this variation. For other overport angles the results are shown in figure 5.12 also, although they have not been simulated. At 40° the NO_x emission increases strongly from the minimum at 60/40 (underport/overport) to the 100 % overport flame. Viewing the results of the overport flames this could already be expected. At the 20° overport angle the effect of slow mixing becomes apparent in the flames with a large overport ratio for both the NO_x emission and the CO level in the flue gas.

Sideport firing

In the sideport and parallel-sideport burner configuration the natural gas is injected into respectively the air channel or the furnace from the side. Sideport firing is an often used method in the industry since the mixing can be well controlled. Thus, the combustion process can be controlled, as well as other processes in the furnace. E.g. in the glass melting process, for which this investigation was initiated, the melting of the glass and subsequent chemical reactions are temperature controlled. Thus, the type of glass and its quality can be influenced by the combustion process and therefore by the mixing. With sideport firing the natural gas is injected directly into the preheated air stream in the air channel. In this way, mixing is enhanced and a small percentage of burnout is already achieved in the burner. This enhances the heat release in the beginning of the furnace and has a positive effect on the efficiency of the furnace. Due to the enhanced mixing in the burner, where the heat loss is relatively small, the temperature of the flame increases. At the standard natural gas injection velocity of 125 m/s this results in

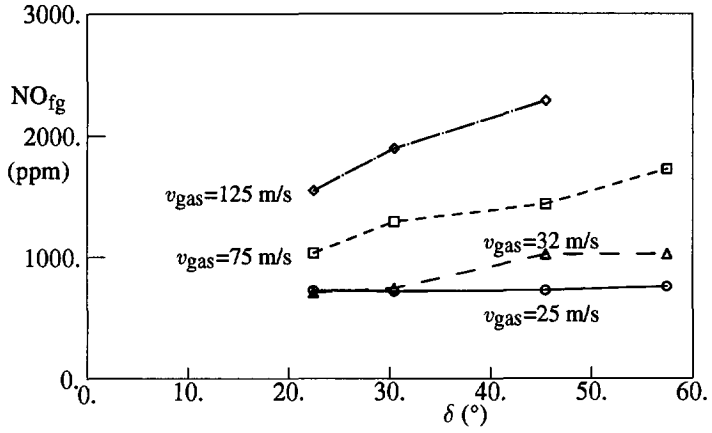

Figure 5.13: NO_x emission vs. horizontal gas injection angle at several gas injection velocities (sideport firing).

Table 5.10: Characteristics of measured flames of the NG7 trials: variation of the mixing angle (sideport firing).

	δ (°)		
	22	30	45
T_{fg} (K)	1711	1703	1682
η (%)	53.2	53.4	53.8
λ	1.095	1.095	1.1005
NO_{fg} (ppm)	1494	1844	2233
CO_{fg} (ppm)	88	55	47
$T_{roof,m}$ (K)	1572	1581	1580
$T_{load,m}$ (K)	1521	1537	1544

a NO_x emission of up to 2000 ppm (depending on the mixing angle). Lower velocities, however, were also tested and resulted in lower NO_x emissions, with a minimum of 650 ppm. Thus, from the viewpoint of NO_x formation, sideport firing does not seem to be an interesting burner configuration. However, since the efficiency is somewhat higher than for other burner configurations, less fuel could be used to generate the same heat transfer to the load. Thus, the detrimental effect on the NO_x emission may be somewhat reduced by the use of less fuel.

We will only discuss some of the results of the injection angle variation here, since numerical computations were performed for this variation only. The results have been listed in table 5.10, for the sideport firing with 125 m/s injection velocity. The natural gas is injected with a vertical angle of 20° downwards, parallel to the combustion air. The horizontal angle, directed towards the middle of the air channel, was varied

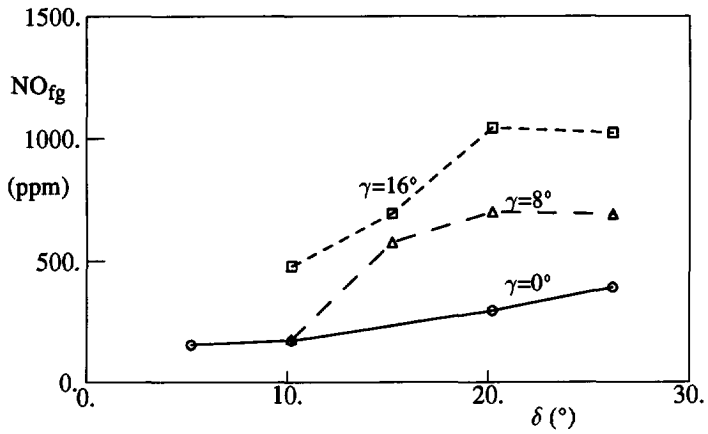

Figure 5.14: NO_x emission vs. horizontal injection angle at several vertical injection angles (parallel-sideport firing).

between 22° and 45°. These are flames with a high NO_x emission, in the 1500 - 2000 ppm range. The NO_x emission is strongly dependent on the gas injection angle, increasing with increasing mixing angle (see figure 5.13). Other results remain almost constant for the three variations that are discussed here. The results seem to indicate that the initial mixing of the air and the natural gas determines the NO_x formation for this type of injector. The overall characteristics do not differ very much, but the NO_x formation is determined by the local species concentrations and the temperature. The highest mixing angle gives the fastest mixing, and it can be concluded from the NO_x emission also the highest flame temperature in a region where there is also oxygen available for thermal NO_x formation.

Parallel sideport firing

Parallel-sideport firing is a variation of sideport firing. The natural gas is not injected into the combustion air channel, but sideways to the air channel, through a burner port in the front plate, directly into the furnace. In this way the mixing of natural gas and air is delayed. This delay can be seen in several of the results. Generally, the efficiency for parallel-sideport firing is lower than for the other firing modes. Also, substantially higher CO levels were measured in the flue gas. These two results indicate poor mixing and slow combustion. As a result, the flame temperature is lower than for fast mixing flames, resulting in lower NO_x emissions. The measured NO_x emissions range from 140 to 1000 ppm, which is generally lower than for the other burner configurations. However, the occurrence of CO in the flue gas limits the applicability for the same reasons that were already mentioned for several other firing configurations and parameters before.

The results of measurements that have also been computed numerically are listed

Table 5.11: Characteristics of measured flames of the NG7 trials: variation of the horizontal injection angle at the 16° vertical injection angle (parallel-sideport firing).

	δ (°)			
	10	15	20	26
T_{fg} (K)	1755	1763	1759	1759
η (%)	53.4	49.6	50.4	50.6
λ	1.106	1.1005	1.095	1.1005
NO_{fg} (ppm)	451	667	1016	995
CO_{fg} (ppm)	119	112	160	200
$T_{roof,m}$ (K)	1572	1567	1563	1567
$T_{load,m}$ (K)	1503	1494	1498	1498

in table 5.11. The natural gas is injected into the furnace with an angle 16° downwards and with varying horizontal angle. With increasing (horizontal) gas injection angle the NO_x emission increases. This may be attributed to the faster mixing and faster combustion. At the IFRF other vertical angles were also tested, viz. 8° and 0°, that give lower NO_x levels than the 16° vertical angle (see figure 5.14). The efficiency is on average lower than for the other firing modes and the CO levels are quite high. Also, the average flue gas temperature of 1750 K is higher than for most other firing modes.

5.4.3 Concluding remarks on the NG7 trials

From the burner geometry variations that were performed during the NG7 trials by the IFRF it becomes clear that optimization of the NO_x emission is possible by influencing the mixing between natural gas and combustion air. Generally, the results indicate that faster, more intense mixing results in higher NO_x emissions. The precise burner configuration is part of the mixing mechanism. Firing modes in which the fuel is injected directly into the combustion air stream give rise to very fast mixing and on average high NO_x emissions. An example of these firing modes is sideport firing. Delaying the mixing, as in parallel-sideport firing, results on average in low NO_x emissions. However, since the mixing is quite slow, these flames have relatively high CO levels in the flue gas, which is not permissible for industrial applications. In-between the extremes of very fast and very slow mixing other burner configurations were tested. Both underport and overport firing produced average NO_x emissions with acceptable CO levels in the IFRF-tests.

Beside the geometrical influences on the NO_x emission other mixing variables were tested by the IFRF. Generally, a high natural gas injection velocity results in a high NO_x emission, due to the enhanced mixing and high entrainment. The mixing angle also influences the combustion and the NO_x emission. Generally, increasing the mixing angle gives rise to an increase of the NO_x emission. These results are valid for most of the burner configurations, so that it is possible to generate relatively fast mixing and a high NO_x emission for an otherwise low NO_x generating burner configuration.

An example of intended fuel staging is the combined underport/overport burner configuration that was tested by the IFRF. In this burner two injection ports were used and the distribution ratio was varied. The results indicate that it is possible to minimize the NO_x emission by adjusting the distribution ratio and the injection velocities.

The objective of the NG7 investigation by the IFRF also was to reproduce some of the results of the NG6 trials. Due to the different thermal environment the results are not directly comparable. However, since the same variations were performed for the underport firing, the observed trends in NO_x emission can be compared. The dependence of the NO_x emission on the mixing angle (underport firing) was different for the NG7 flames than for the NG6 flames. The strong decrease in NO_x emission at higher mixing angles, that was found during NG6, was not reproduced. In the presentation of the results of the simulations this will be discussed further. For the analysis of the simulations it is important that many boundary conditions have been measured. When needed, these results will be presented during the discussion of the numerical simulations.

Chapter 6

Simulations of the NG6 trials

6.1 Introduction

In this chapter we will concern ourselves with the numerical results of the NG6 trials. These results have been obtained with the numerical model that was introduced in chapters 2 and 3. The numerical results will be compared with the results of the measurements by the IFRF. These results were already briefly introduced in chapter 5, but whenever necessary new specific results will be presented and discussed.

We will start the discussion of the numerical results with a sensitivity analysis of the model. We have assessed the sensitivity of the model to some model parameters and to some boundary conditions that were unknown and had to be estimated. These simulations were performed for the baseline 20°-12° underport fired flame and will be compared with the measured baseline flame. Principally, we have used the heat flux distribution to the load to compare measurements with simulations. The flue gas temperature, the oxygen concentration distribution and the temperature distribution and other variables were also used to compare measurements with simulations, as secondary parameters. This sensitivity analysis of the baseline flame simulations has led to a set of parameters and boundary conditions, that we have used as our baseline flame. The set of parameters has been held constant throughout the rest of the simulations.

The effect of grid refinement on the solution of our baseline flame has been tested. We have used three grids with an increasing number of nodes. Based on a comparison of the numerical results we have chosen a suitable grid, that was used for all the simulations of flames of the NG6 trials.

Finally, the results of parameter variations will be presented. In the simulations we have followed the program of the NG6 investigation. We have varied the combustion air temperature and the excess air level, since these two parameters have a distinct (and known) influence on the NO_x production. The mixing of the combustion air and the natural gas jet was influenced by affecting the injection angle of both the natural gas jet and the combustion air and by varying the inflow velocity of the natural gas jet. The results will be presented in this chapter and discussed.

6.2 Baseline flames

6.2.1 The measured baseline flames

In the NG6 trials the IFRF has given attention to reproducing the measurements of some of the important flame configurations. The baseline 20°-12° underport fired flame was reproduced four times. Characteristics of these four flames are listed in table 6.1. It is clear from this table that the input conditions for these four baseline flames are not constant. This makes a comparison with the numerical results difficult. Especially the variation of the airfactor λ complicates this comparison, since the airfactor has a large influence on the NO_x emission. In the simulations we have imposed an airfactor of 1.10. The maximum airfactor for these measurements is 1.12, which means that the excess air level is 20 % higher (viz. 12 % instead of 10 % excess air) than in the simulations.

Table 6.1: Characteristics of measured baseline 20°-12° flames of the NG6 trials.

	6.044	6.054	6.065	6.109
input				
T_{air} (K)	1393	1384	1405	1387
λ	1.120	1.103	1.114	1.120
output				
T_{fg} (K)	1805	1766	1823	1823
$\overline{NO_{fg}}$ (ppm)	1416	1281	1690	1954
$\overline{q''_{l+f}}$ (kW/m^2)	73.1	75.3	72.5	71.6
η_l	.459	.465	.451	.438
η_f	.674	.694	.669	.660

The results of the four reproduced flames differ substantially. The NO_x emission varies strongly from 1280 ppm to 1950 ppm (at 0 % O_2). This variation is not consistently caused by the different input conditions, since e.g. the flame with the highest combustion air temperature (1393 K) and the highest airfactor (1.12) has a NO_x emission of (only) 1410 ppm. Therefore, we will have to take large measurement errors (up to 20 % for the NO_x emission) into account when a comparison is made with the simulated data.

We have used the measured load temperature as the temperature boundary condition for the load in the simulations. Unfortunately, there are no reliable measurements of the load temperature for this baseline flame. Therefore, we have estimated the load temperature using the measured load temperatures of other flames, as shown in figure 6.1. These temperatures were measured in the baseline configuration, with different combustion air temperatures. The used load temperature is also shown in figure 6.1. One should realize that the heat flux to the load is strongly dependent on the local load temperature. There is a large uncertainty in the heat transfer data due to the lack of measured temperature data. When comparing the numerical results to the measured

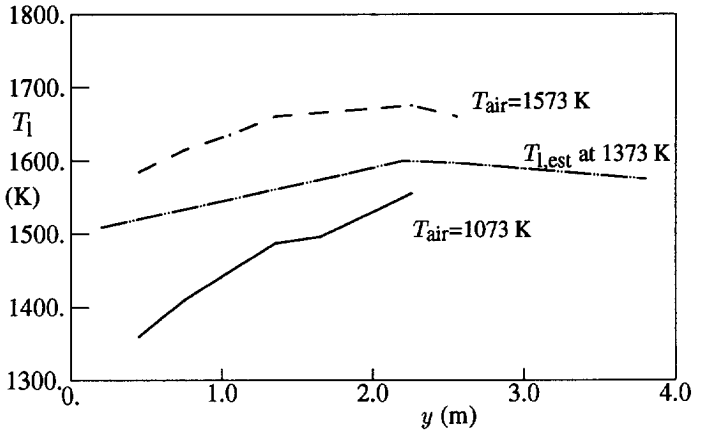

Figure 6.1: Measured temperature distribution of the load for the baseline 20°-12° configuration for different combustion air temperatures and estimated load temperature for the simulations with T_{air} = 1373 K.

results we shall take this uncertainty into account.

The measured heat transfer distribution to the load is shown in figure 6.2. It shows a sharp decrease at the end of the furnace, which was probably caused by a large heat loss to the back wall. This heat loss has not been measured separately during the trials, nor was the back wall temperature measured. This has caused a problem

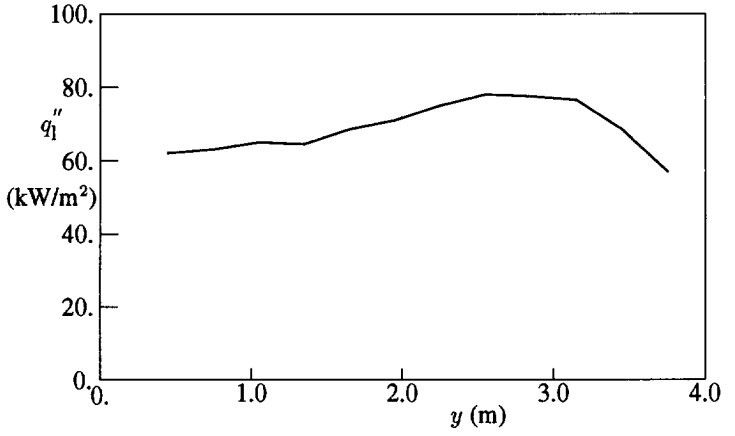

Figure 6.2: Measured distribution of the heat transfer to the load for the baseline 20°-12° configuration.

Table 6.2: Characteristics of simulated baseline 20°-12° flames of the NG6 trials, with different precombustion percentages.

	v150	v074	v153
input			
precombustion (%)	0	3.3	6.6
T_{air} (K)	1373	1373	1373
λ	1.1004	1.0994	1.0994
output			
T_{max} (K)	2390	2395	2459
$\overline{T}$ (K)	1772	1780	1790
T_{fg} (K)	1873	1846	1779
NO_{fg} (ppm)	1461	1409	2530
$\overline{q_l''}$ (kW/m^2)	64.9	65.2	69.1
η_l	.450	.452	.478
η_f	.646	.664	.702
$M_{e,max}$ (%)	110.4	113.7	101.3

for the simulations, because of the already mentioned strong dependency of the heat transfer results on the temperature boundary conditions. In subsections 6.2.3 and 6.2.4 this will be illustrated, when the parameters of the radiative heat transfer model will be discussed.

6.2.2 Development of the natural gas jet

The development of the natural gas jet is an important problem for the simulations. To be able to predict the jet development accurately we would need a very fine mesh locally, which goes beyond our capacity in CPU memory at the moment. Simulations with our fairly coarse grid — it is coarse even in the region where the jet develops — revealed that we had to make certain assumptions about the initial jet development. Otherwise the spread of the jet and the decay of the centreline velocity were not predicted correctly by the numerical code. Therefore we have used an approximation for this initial jet development. As the inflow condition we imposed the approximated solution of a free developing jet at several jet diameters downstream of the inlet. At the distances that we have used the jet is still in its core region (see section 2.7) and it has entrained only a small amount of combustion air. At the inflow we then specify the following conditions:

- The jet velocity is constant and is equal to the jet inlet velocity, that is specified by the NG6 program.
- The jet has entrained a variable amount of combustion air. This means, since we have a "mixed = burned" model, that there is some precombustion. At 5 diameters downstream we assumed that the natural gas jet has entrained half its own mass, which results in a precombustion of about 3 %).

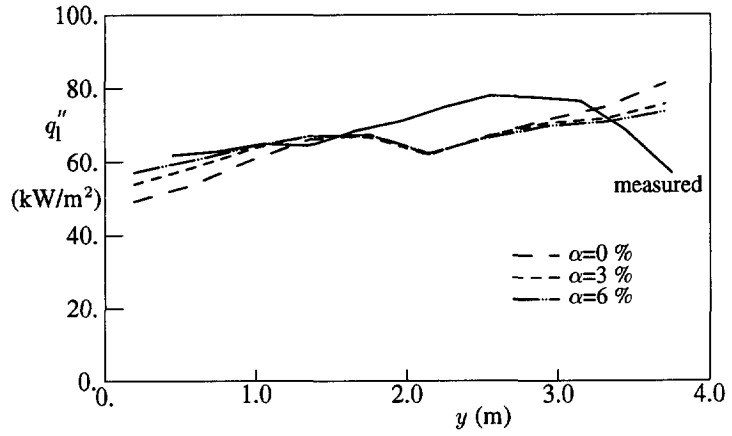

Figure 6.3: Distribution of the heat transfer to the load for several precombustion percentages.

- The diameter of the inflow of the now precombusted jet is computed in such a way that the massflow and velocity conditions will be satisfied. Due to the entrainment of mass and the expansion of the jet, as a consequence of the precombustion, the diameter of the inflow is increased.
- The conditions of the jet at a variable number of diameters downstream are imposed as a boundary condition at the inlet point of the natural gas. We thus have an axial displacement *upstream* of the jet conditions.

The effect of the precombustion is illustrated by simulations with different precombustion percentages. In figure 6.3 the heat transfer distribution to the load is shown for precombustion percentages of 0 %, 3 % and 6 %. A precombustion percentage of 0 % means that the standard boundary conditions are applied, with no assumed development of the jet before entering the furnace. It is clear from this figure that the flame without precombustion develops slower than the flames with precombustion. Compared with the measured flames, it seems to develop too slowly. A small amount of precombustion has therefore been used in the simulations. The highest precombustion, however, seems to give too fast development of the jet. This is supported by the characteristics of the flame that are listed in table 6.2. The maximum temperature that is computed for the 6 % precombustion, is much higher than for the other precombustion percentages. Also, the load efficiency (η_l) is significantly higher with 6 % precombustion than with 3 % precombustion. Comparison with the results in table 6.1 clearly indicates that the 3 % precombusted flame calculation agrees best with the measurements. On account of this we have used a precombustion of 3 % for the rest of the simulations, including the rest of the simulations that were performed for the sensitivity analysis.

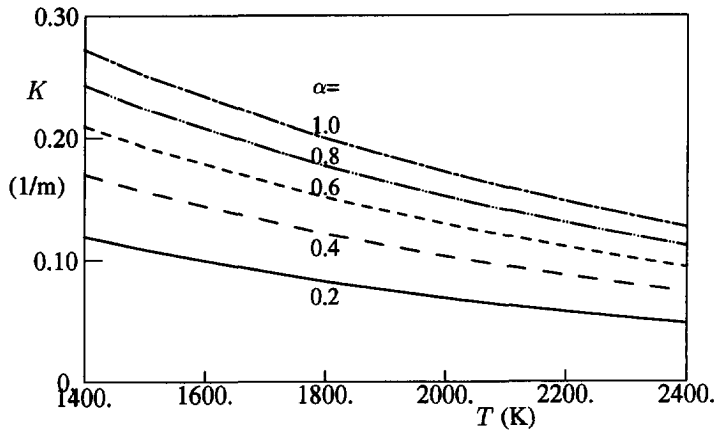

Figure 6.4: Extinction coefficient in the IFRF furnace as a function of the temperature at several burnout percentages.

6.2.3 Extinction coefficient variations

In a natural gas flame the extinction coefficient K of the thermal radiation is not constant. It is composition and temperature dependent. Besides, the extinction coefficient is wavelength dependent, since both CO_2 and H_2O absorb and radiate in bands. In our model, however, we have used a grey gas assumption with constant extinction coefficient. According to Post (1988) the range of values of K in natural gas flames is 0.05 to 0.3 m^{-1}. Post has used a value of 0.08 for K in his computations of a natural gas flame. Since 0.05 – 0.3 m^{-1} is a considerable range we have estimated the value of K that we should use in our furnace. We have used a statistical narrow band model (Goody (1964)) to compute the extinction coefficient. From Ludwig *et al.* (1973) we have used data on the absorption coefficients of the species that are present in our furnace. A model of Wieringa *et al.* (1990) has been used to compute the value of K in our furnace for a range of temperatures and a range of compositions. In figure 6.4 the extinction coefficient is shown as a function of the temperature at a number of burnout percentages. The combinations of burnout and temperature that we encounter in the furnace are low burnout at low temperatures and high burnout at high temperatures. We conclude from the figure that the value of K lies between 0.08 – 0.20 m^{-1} in our furnace.

Our initial estimate of the value of K that we adopted for our simulations was 0.12 m^{-1}. To test the sensitivity of the results to the assumed value of K we have done simulations with the lower and upper boundary of the estimated K from the statistical narrow band model. The result of these simulations is shown in figures 6.5 and 6.6. The heat transfer to the load clearly is very dependent on K. The radiative heat transfer from the flame is higher at the higher emission (= absorption) coefficients. These flames

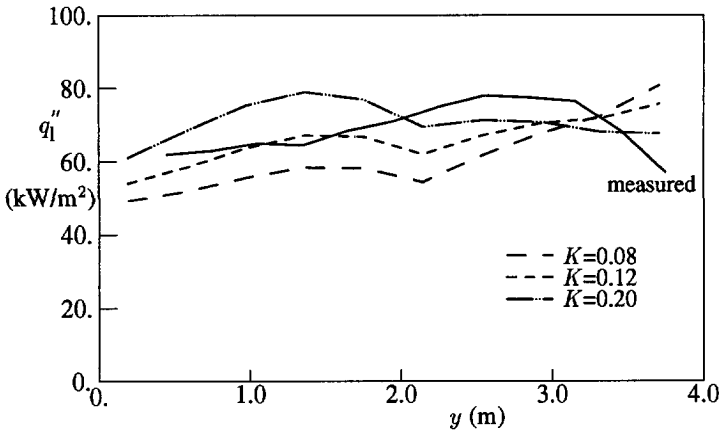

Figure 6.5: Distribution of the heat transfer to the load for several values of the extinction coefficient.

radiate more in the beginning of the furnace. Consequently, they lose much of their heat in the beginning and radiate less at the end of the furnace. Overall, the heat transfer to the load is higher for higher values of K. The flame temperature in the symmetry-plane of the furnace is shown in figure 6.6. The mean temperature decreases with increasing K. Since the oxygen concentration is not much influenced by the variation of K, the NO_x emission decreases considerably with increasing value of K (see table 6.3). In table 6.3 several properties of the mentioned flames are listed.

If we compare the results of the simulations with those of the measurements we see that our initial estimate of $K = 0.12$ fits the data best. Not only is the furnace efficiency predicted well, also the radiative heat transfer to the load in the beginning of the furnace corresponds very well with the measurements (see figure 6.5). At the end of the furnace the measured heat transfer decreases sharply, whereas the simulated heat transfer decreases only slightly ($K = 0.20$) or increases ($K = 0.12$, $K = 0.08$). The measured behaviour is probably due to a high heat loss through the back end of the furnace in the measurements as was already mentioned in subsection 6.2.1. For all three simulated flames we have therefore ignored their behaviour at the end of the furnace. Based on this comparison we have used a K of 0.12 m^{-1} in all simulations of both the NG6 and the NG7 trials, instead of the 0.08 m^{-1} used by Post (1988).

6.2.4 Boundary conditions for the radiation model

Very important for the radiation computations are the boundary conditions as was already mentioned in subsection 6.2.1. The load temperature influences the temperature of the furnace directly. This will be clear when we introduce the NG7 trials in chapter 7. During the NG7 trials, the load temperature was approximately 200 K lower. This resulted in much lower temperatures in the furnace and a higher thermal radiative heat

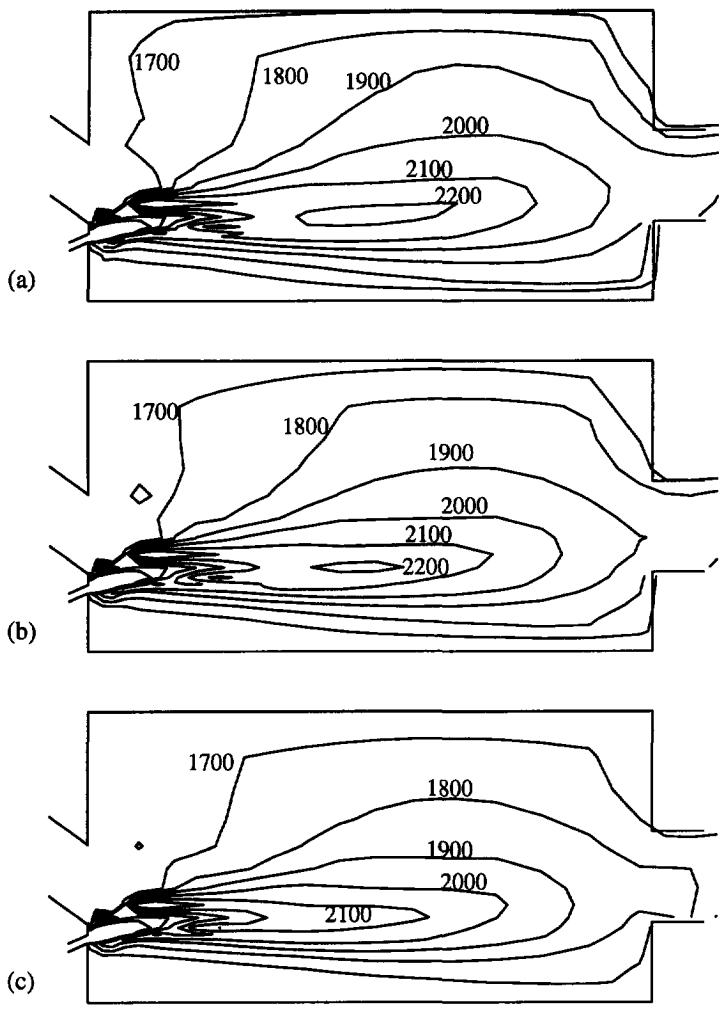

Figure 6.6: Temperature contours (in K) in the symmetry-plane of the furnace for three values of the extinction coefficient. a. $K = 0.08$, b. $K = 0.12$, c. $K = 0.20$.

Table 6.3: Results of simulations of the baseline flame with different values of the extinction coefficient.

	v151	v074	v152
input			
K (m^{-1})	0.08	0.12	0.20
output			
T_{max} (K)	2399	2395	2394
$\overline{T}$ (K)	1827	1780	1733
T_{fg} (K)	1908	1846	1780
NO_{fg} (ppm)	1750	1410	1073
$\overline{q_l''}$ (kW/m^2)	60.5	65.2	70.4
η_l	0.419	0.452	0.487
η_f	0.624	0.664	0.708
$M_{e,max}$ (%)	112.5	113.7	115.3

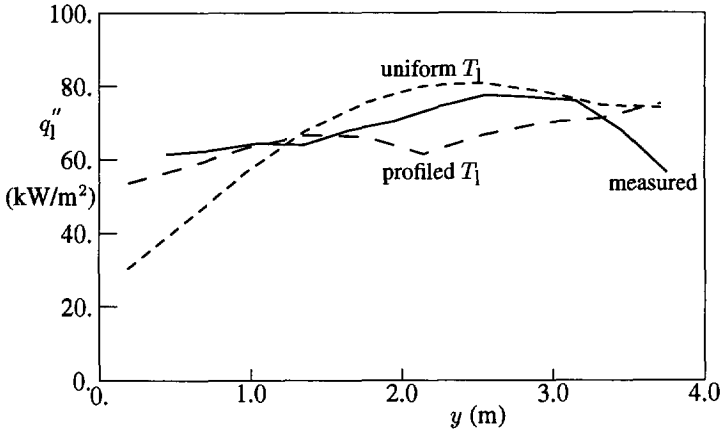

Figure 6.7: Distribution of the heat transfer to the load for two load temperature profiles.

transfer.

At the load we impose a temperature distribution, since we are interested in the heat transfer to the load. For the rest of the walls we impose wall fluxes. In figure 6.7 the importance of the imposed load temperature is illustrated. In this figure the heat transfer distribution to the load is shown for two boundary conditions. The first boundary condition is a constant load temperature of 1550 K, which was an estimate of the load temperature before the trials were performed. The second boundary condition is the estimated load temperature from the NG6 investigation (figure 6.1), which varies between 1500 and 1600 K. Clearly, the load temperature has an enormous influence on the radiative heat transfer computation. The distribution of the heat transfer is strongly

Table 6.4: Results of simulations of the baseline flame with different load temperature distributions.

	v154	v074
input		
T_l	uniform	profile
output		
T_{max} (K)	2396	2395
$\overline{T}$ (K)	1771	1780
T_{fg} (K)	1833	1846
NO_{fg} (ppm)	1408	1410
$\overline{q_l''}$ (kW/m^2)	66.3	65.2
η_l	0.459	0.452
η_f	0.672	0.664
$M_{e,max}$ (%)	114.0	113.7

affected. In the first segments of the furnace, the measured load temperature was only 50 K lower than was assumed in the simulation with the constant load temperature. Still, the heat transfer is 50 % higher in this area. This affects the temperature distribution in the furnace as well as all other variables. The influence on the flue gas properties, however, is weak. In table 6.4 properties of these calculated flames are listed. The average flue gas temperature and the other properties are hardly influenced by the variation of the load temperature boundary condition.

In the rest of the simulations, the estimated load temperature derived from the measurements has been used as the load temperature boundary condition. Since the thermocouples in the load broke down during the NG6 trials, we have mostly used the same temperature distribution as in figure 6.1 for all the simulations with an air preheat temperature of 1373 K.

Another important boundary condition is the heat loss to the walls. The estimate of Van de Kamp *et al.* (1989) is a loss of 2 – 5 kW/m^2 for the refractory of the furnace. This estimate could not be validated by the measurements since only the heat loss through an entire segment could be measured. We have therefore tested the sensitivity of the numerical model to the imposed wall heat fluxes. During the first stages of the simulations we used 5 kW/m^2 heat loss through the walls. As a result the heat transfer to the load was higher than measured and the flue gas temperatures were also higher. Therefore we have raised the estimated heat loss through the walls to 7.5 kW/m^2. This resulted in a heat transfer to the load that corresponded much better with the measurements. Since the estimate of Van de Kamp *et al.* (1989) could not be validated we have used the wall heat flux that gave the best results in comparison with the measurements, viz. 7.5 kW/m^2.

Van de Kamp *et al.* (1989) remark that the heat loss through the front and back wall could have been much higher than 5 kW/m^2, the estimated wall heat flux. We

Table 6.5: Imposed heat losses as the boundary conditions of the radiation model.

	q''_{wall} (kW/m^2)	q''_{front} (kW/m^2)	q''_{back} (kW/m^2)
v074	7.5	15	25
v087	2.5	50	2.5
v091	2.5	35	25
v122	2.5 & 7.5	35	25

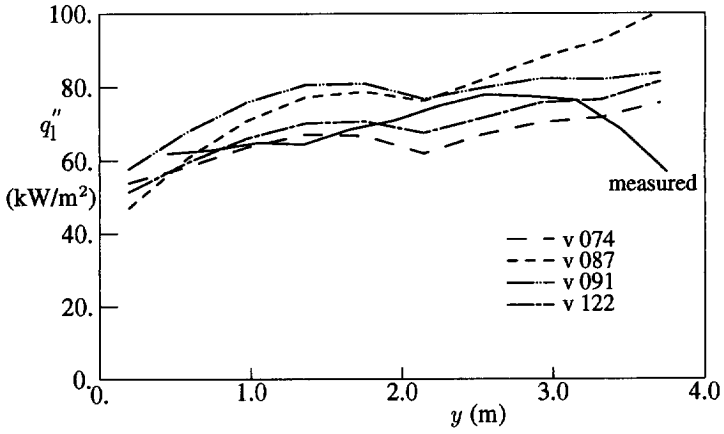

Figure 6.8: Heat transfer to the load. Simulations with different heat losses to the walls.

have therefore made an estimate of the heat loss through these walls for the simulations and tested our estimates by using several other heat losses as well. We have tested the influence of the heat loss distribution in four cases, that are listed in table 6.5. In figure 6.8 the resulting heat flux to the load is shown. From this figure we conclude that the boundary conditions of flame v074 give the best result compared with the measurements. Still, at the end of the furnace the heat flux to the load still increases, unlike the measurements (see subsection 6.2.1), where the heat flux decreases. This may be due, as was already mentioned, to errors in the estimated load temperature at the end of the furnace and to unexpectedly high heat losses through the back wall. As the overall heat flux to the load is predicted well for flame v074 and the flue gas temperatures differ only 30 K (or 2%) on average, we have not tried more simulations with other heat loss distributions or load temperatures to force the heat transfer to the load at the end of the furnace downwards. For the rest of the simulations we decided to use the boundary conditions that both satisfy the measurements reasonably and seem to be probable physically spoken, viz. those of flame v074.

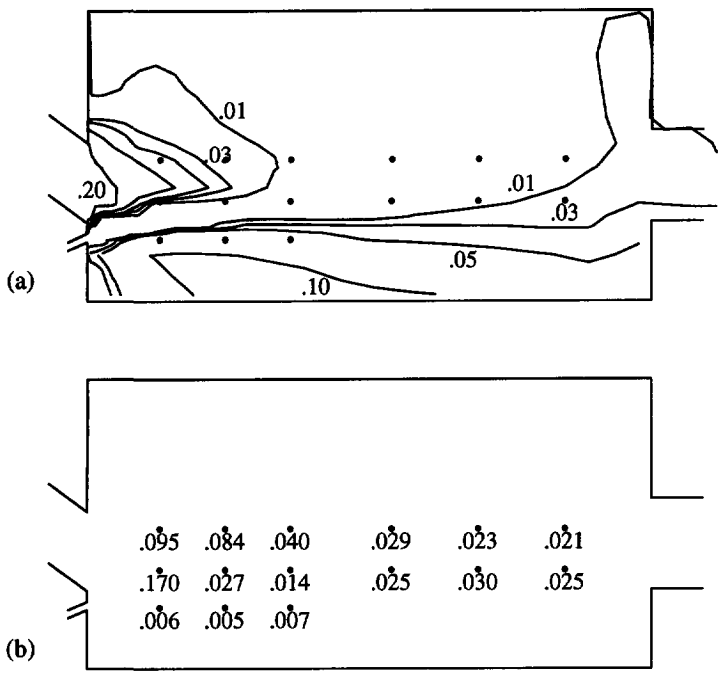

Figure 6.9: Computed and measured oxygen mass fractions.
a. Oxygen mass fraction contours from baseline simulation, with points of measurements of the NG6 trial. (Contour values: 0.20, 0.10, 0.05, 0.03, 0.01)
b. Measured oxygen mass fraction from baseline 20°-12° flame.

6.2.5 Velocity profile in the inflow

An unknown boundary condition for the simulations is the velocity inflow profile of the combustion air. Normally we have used a constant velocity from the air duct, since there were no velocity measurements performed. Since the air duct is not very long and the downward slope starts only approximately 0.5 m before the furnace inlet, common physical sense teaches us that there will be a velocity profile in the combustion air inflow. We have also done some simulations of the inflow duct that indicate that there will be a velocity profile. Moreover, the measurements in the physical model showed a velocity profile with a maximum towards the top of the air-inflow duct (see chapter 4).

The importance of this velocity inflow profile may lie in the effect that it has on the oxygen concentration distribution. The measured oxygen concentration differed from the baseline simulation flame v074 in an important aspect (see figure 6.9). In the measurements we still find some oxygen in the recirculation zone in the top half of

Table 6.6: Results of simulations of the underport fired baseline flame with variation of the combustion air velocity profile.

	v074	v085	v086
input			
Δv (m/s)	-	4	8
output			
λ	1.0994	1.0994	1.0994
T_{max} (K)	2395	2396	2430
$\overline{T}$ (K)	1780	1782	1786
T_{fg} (K)	1846	1826	1805
NO_{fg} (ppm)	1409	1391	1340
$\overline{q_l''}$ (kW/m^2)	65.2	65.6	66.4
η_l	.452	.454	.460
η_f	.664	.675	.687
$M_{e,max}$ (%)	113.7	112.5	114.9

the furnace, whereas the predicted oxygen concentrations are practically equal to zero. Since the NO concentration predictions are influenced by the oxygen concentration predictions, a possible effect of the velocity inflow profile on the oxygen concentration should be investigated.

We have determined whether this velocity inflow profile might be important or not. We have done simulations with two inflow profiles, with a maximum at the top of the inflow channel and linearly decreasing to the bottom. For flame v085 the velocity difference between top and bottom is 4 m/s, for flame v086 it is 8 m/s. The resulting oxygen concentration in the symmetry-plane is shown in figure 6.10. Clearly, the velocity inflow profile does not influence the oxygen concentration in the recirculation.

Other properties of these flames display small differences. The heat flux to the load (see figure 6.11) in the beginning of the flame is increased for the two simulated flames with a non-uniform velocity inflow profile. The load efficiency, listed in table 6.6, and the flue gas properties hardly differ for the three flames. The NO_x emissions are also hardly influenced, which could be expected since the oxygen concentration distribution was hardly affected by the inflow profile, as was shown in figure 6.10. Because of the marginal effects of the inflow profile on the results, we have used a uniform inflow profile for all other simulations.

6.2.6 Turbulent mixing intensity

We have already shown that the velocity profile of the combustion air in the inflow has little influence on the results of the simulations. The inflow profile of the turbulence dissipation rate, however, proved to have a very distinct influence. The inflow profile of ϵ is given by equation 3.13. The length scale of the turbulence, which appears in this equation, was derived for fully developed turbulent pipe flow. However, as was already

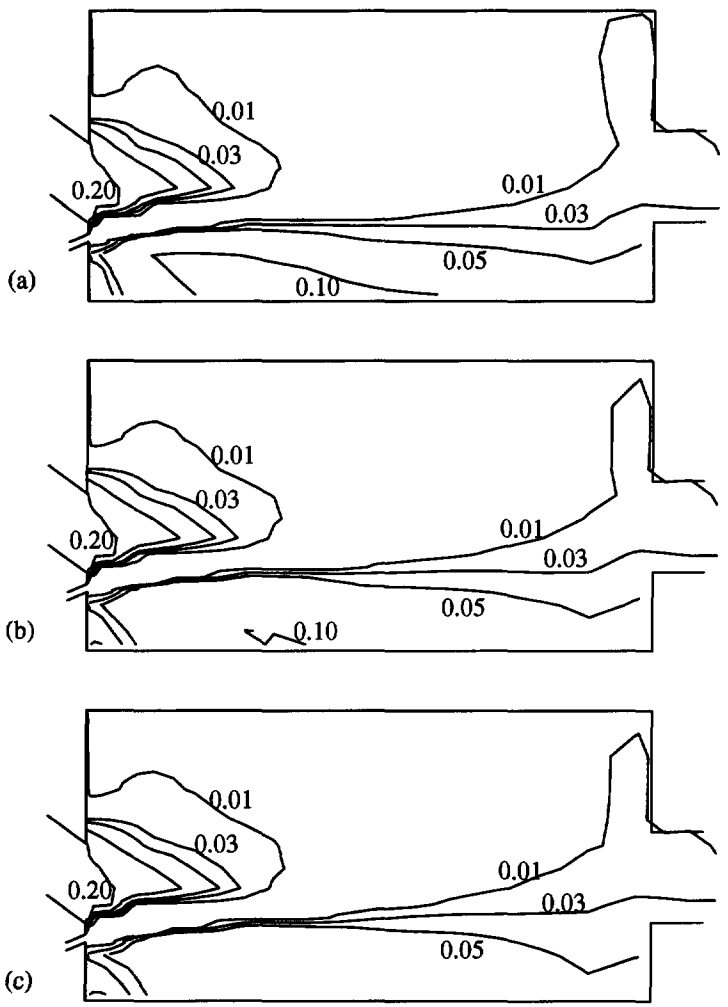

Figure 6.10: Oxygen mass fraction contours from baseline simulation, with different velocity inflow profiles of the combustion air flow. a. Uniform inflow, b. Profile with 4 m/s difference c. Profile with 8 m/s difference.

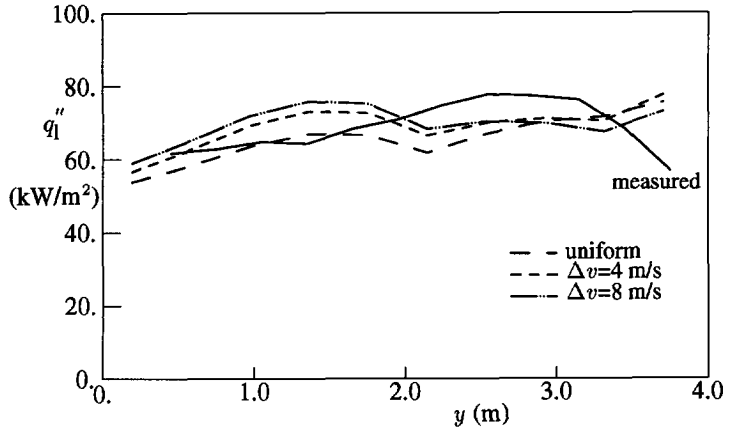

Figure 6.11: Distribution of the heat transfer to the load for the three different inflow profiles.

mentioned before, the combustion air inflow channel is not long enough to create fully developed turbulent flow. For not fully developed turbulent flow the characteristic length scale is larger than for fully developed turbulent flow. Therefore it would seem reasonable to increase the length scale of the turbulence. This decreases the dissipation of turbulent kinetic energy and therefore enhances mixing. Consequently the flame will develop faster with an increasing length scale of turbulence.

The enhanced development of the flame jet for the higher length scales of the

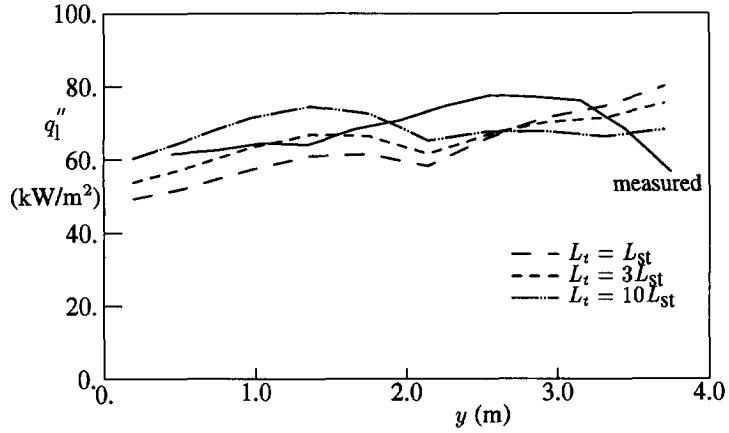

Figure 6.12: Distribution of the heat transfer to the load for several length scales of the turbulence.

Table 6.7: Results of simulations of the underport fired baseline flame with turbulent length scale variation.

	v141	v074	v142
input			
L_t/L_{std}	1	3	10
output			
λ	1.0994	1.0994	1.0994
T_{max} (K)	2453	2395	2383
$\overline{T}$ (K)	1774	1780	1787
T_{fg} (K)	1874	1846	1808
NO_{fg} (ppm)	1378	1409	1390
$\overline{q_{\text{l}}''}$ (kW/m^2)	63.1	65.2	67.8
η_{l}	.437	.452	.470
η_{f}	.644	.664	.689
$M_{\text{e,max}}$ (%)	114.0	113.7	113.0

turbulence is reflected in the heat transfer to the load, that is shown in figure 6.12 for a number of length scales. We have done simulations of the baseline flame with three different length scales, viz. the standard length $L_t = L_{\text{std}}$, $L_t = 3L_{\text{std}}$ and $L_t = 10L_{\text{std}}$. With $L_t = 10L_{\text{std}}$ the heat transfer in the beginning of the flame is higher than was measured, while for $L_t = L_{\text{std}}$ it is lower than measured. At the end of the furnace, where in the measurements a decrease of the heat flux to the load was measured all three simulated flames give an increase in the heat transfer to the load. For the largest turbulent length scale this increase is very small, but for the smallest length scale it is considerable. This behaviour can be explained by the mixing velocity that is increased with increasing length scale of the turbulence. The assumption of fully developed flow for the smallest length scale of the turbulence underestimates the mixing in the beginning of the flame. This flame is therefore longer than would be expected and thus it has a relatively large heat release at the end of the furnace.

If we compare other output data of the simulations (see table 6.7) with the results of the measurements (table 6.1) we see that the flames with increased length scale have an *averaged* flue gas temperature in the range of the measurements. The flame with the standard length scale has a higher flue gas temperature. Therefore it seems that the use of an increased length scale improves the results of the simulations. The computed load and furnace efficiency of the flame with the highest length scale ($10L_{\text{std}}$) is higher than the measured load and furnace efficiencies, while the efficiencies of the flame with $3L_{\text{std}}$ agree very well with the measured efficiencies. Thus, for all our simulations we have used a turbulent length scale in the inflow increased by a factor 3 compared to the standard length scale for fully developed turbulent flow.

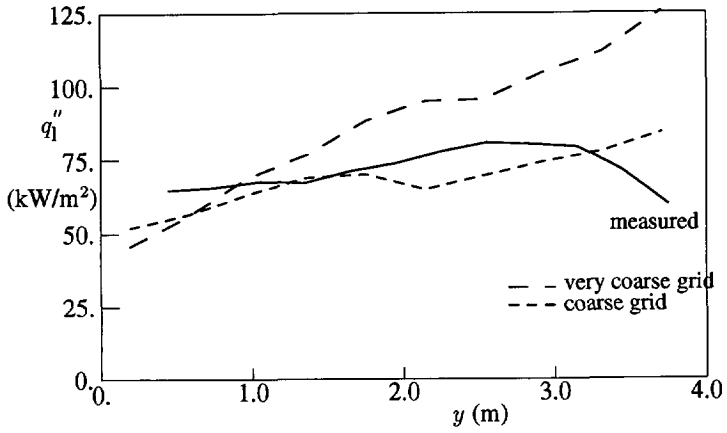

Figure 6.13: Distribution of the heat transfer to the load for a simulation with the coarsest grid (12 × 22 × 16 nodes). The heat transfer from a simulation with the finer mesh, with 0 % precombustion, is shown for comparison.

6.3 Grid refinement

An important issue in the simulation of any flow is the number of grid nodes that is used. Regions with high gradients, near wall regions or regions of specific interest demand a large number of grid points. Also the problem of numerical diffusion arises. Since numerical diffusion is proportional to the grid spacing, a large number of grid points reduces the numerical diffusion. However, CPU time and core memory increase exponentially with increasing grid size. Therefore an optimum has to be found.

In our furnace steep gradients arise in the flame region. For an accurate solution we need many grid points there. This has forced us to use a non-uniform grid, with refinement around and above the natural gas inlet. To determine the total number of grid points we have done simulations on three grids: 12 × 22 × 16 nodes, 18 × 26 × 22 nodes and 26 × 38 × 32 nodes.

In figure 6.13 the heat transfer distribution to the load is shown for the coarsest grid. For this simulation the boundary conditions were estimated and no precombustion (as in subsection 6.2.2) was assumed. Assuming a certain precombustion would have led to large errors, since the grid is so coarse around the inlet pipe of the natural gas that too fast expansion of the flame jet would have been the result. The heat release of the flame with the coarsest grid is compared to that for a flame with a finer grid (18 × 26 × 22 nodes), but without precombustion (see subsection 6.2.2). It is clear from this figure that the coarsest grid is unacceptable. The expansion of the natural gas jet is not predicted well, resulting in an under-prediction of the mixing and consequently a long flame with a very low initial heat release. The flue gas temperature of the flame of 2000 K is much higher than the measured flue gas temperature of approximately

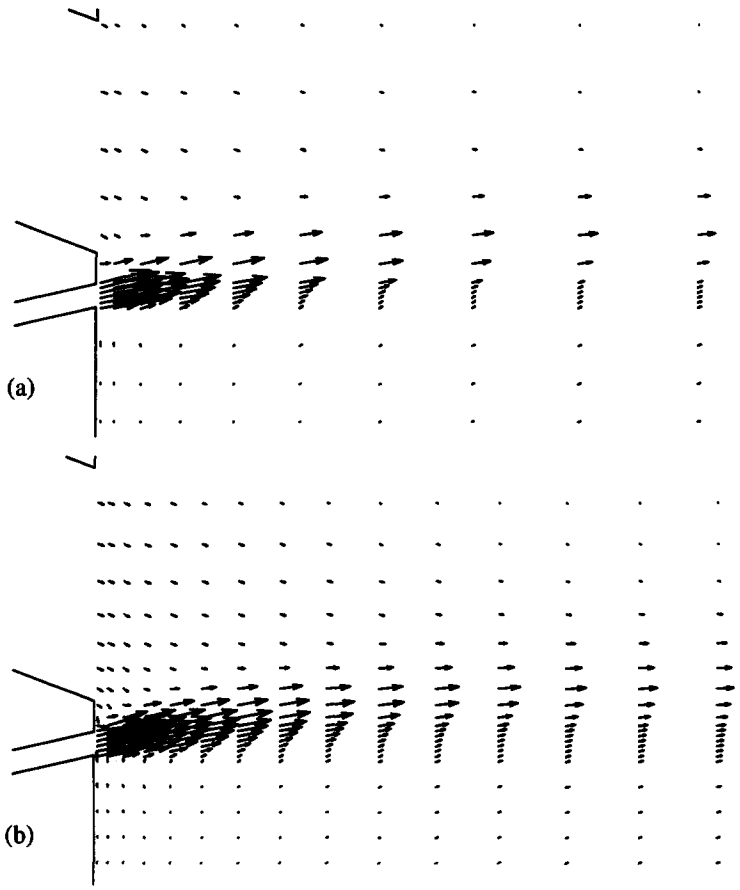

Figure 6.14: Velocity vectors in the jet region of the flame for the two finest grids. a. $18 \times 26 \times 22$ nodes, b. $26 \times 38 \times 32$ nodes.

1800 K, which is also predicted with the finer mesh. The $12 \times 22 \times 16$ grid has not been used for the simulations consequently.

A further refinement of the $18 \times 26 \times 22$ grid has also been tested. For these simulations the measured boundary conditions of the NG6 trials were used, as was the jet expansion with a precombustion of 3 %. For the finest grid refinement has been concentrated around the flame jet. In figure 6.14 velocity vectors in the symmetry plane around the flame jet inlet are shown. Because of the finer grid one would expect to see less numerical diffusion in the computations and consequently a slower development of the flame jet. On comparing the velocity vectors a slower development of the flame in the computation with the finest mesh is indeed found. The decrease of the velocity of the jet is indeed smaller, although the effect is small. Outside the jet region the velocity

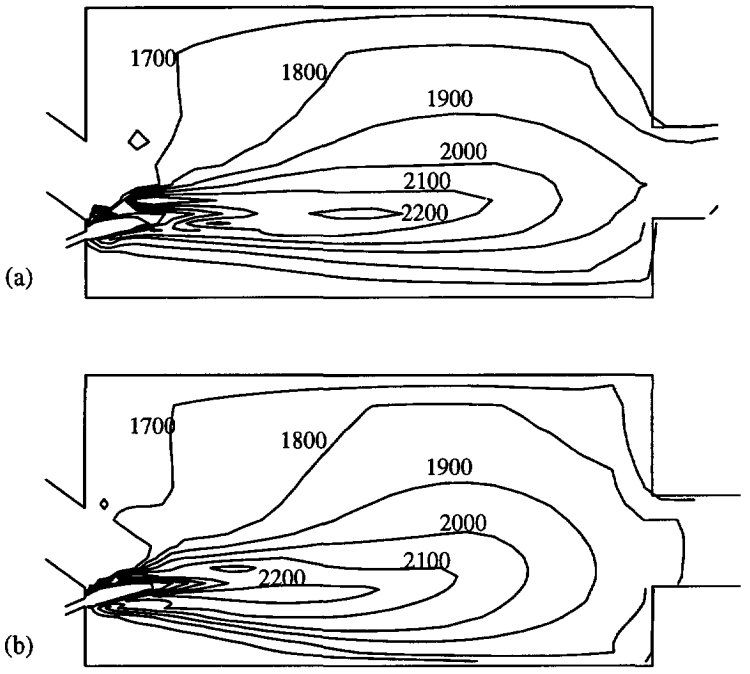

Figure 6.15: Temperature contours in the symmetry-plane of the furnace for the $18 \times 26 \times 22$ (a) and the $26 \times 38 \times 32$ (b) grids.

fields do not differ very much, so that we may conclude that there is only a limited influence by the grid refinement on the velocities.

The effect of the grid refinement on other variables is also limited. This is illustrated in figure 6.15, where temperature contours in the symmetry plane of the furnace are shown. The flame simulation with the finest mesh differs from the coarser mesh especially in the flame region. The finest mesh gives somewhat higher temperatures in the flame and consequently more heat transfer to the load in the beginning of the furnace. This is shown in figure 6.16, where these two flames are compared with the result of the measurements. Because of the higher heat flux to the load in the beginning of the flame, the flame computed with the finest mesh is cooler at the end of the furnace. This can be seen in the temperature contours and it is also reflected in the flue gas temperatures that are listed in table 6.8.

Although there are certainly differences between the results with the coarse mesh and the results with the fine mesh, these differences are not very large. Because the measured and simulated data agree rather well, even for the fairly coarse mesh

Table 6.8: Results of the grid refinement.

	v074	v200
input		
grid	$18 \times 26 \times 22$	$26 \times 38 \times 32$
T_{air} (K)	1373	1373
λ	1.0994	1.0997
output		
T_{max} (K)	2395	
$\overline{T}$ (K)	1780	
T_{fg} (K)	1846	1788
NO_{fg} (ppm)	1409	1255
$\overline{q_l''}$ (kW/m^2)	65.2	69.0
η_l	.452	.478
η_f	.664	.701
$M_{e,max}$ (%)	113.7	

and because the computation time and memory usage were already a problem for the finest mesh, we have not used the finest mesh for the rest of our simulations, but the $18 \times 26 \times 22$ grid. This is a fairly coarse grid, but with the already discussed precombusted and expanded jet as boundary condition for the natural gas jet inflow reasonable results can be obtained. For a really fine mesh a supercomputer would be necessary, considering both core memory and CPU time usage.

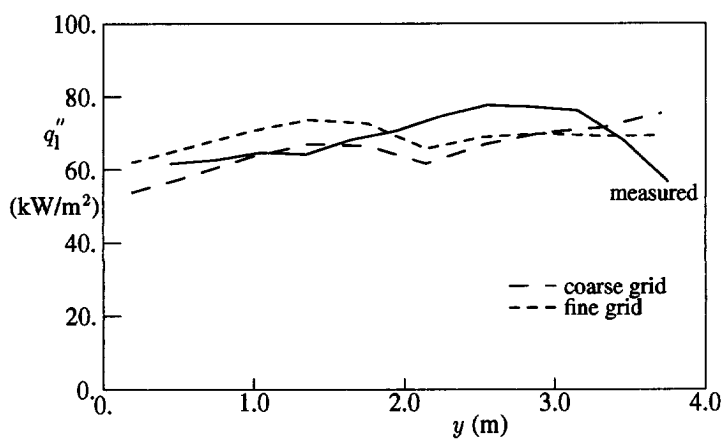

Figure 6.16: Distribution of the heat transfer to the load for the $18 \times 26 \times 22$ and the $26 \times 38 \times 32$ grids.

6.4 Parameter variations of the NG6 trials

6.4.1 Combustion air temperature and excess air level

In the IFRF trials the reduction of NO_x emissions was the primary goal. However, the furnace efficiency and the heat transfer to the load are also very important parameters. Two parameters that influence both the NO_x formation and the efficiency are the combustion air temperature and the excess air level.

Generally, an increasing air preheat temperature results in an increasing furnace temperature. Since radiative heat transfer is the dominant form of heat transfer to the load, this results in an increasing heat transfer and thus a higher efficiency. However, the dependence of the NO_x formation on temperature is very strong, as was discussed in section 2.6. At increasing temperatures the NO_x formation rate increases exponentially. For every 50 K rise in temperature the NO formation rate is doubled.

The excess air level influences both the oxygen availability in the furnace and the furnace temperature. At low excess air levels an increase in the excess air level results in an increase in NO_x emission, due to the increasing oxygen availability. At high levels, however, the cooling effect of large amounts of *relatively* cold combustion air results in lower NO_x emissions. The heat transfer to the load is only slightly influenced by the excess air level. At low excess air levels the combustion of the natural gas is relatively slow, which reduces the heat transfer. At high excess air levels the combustion is fast, but the mean temperature in the furnace is reduced, due to the cooling effect of the combustion air. This results in a slight reduction in heat transfer. Because of the different amounts of heat in the different amounts of combustion air, the furnace

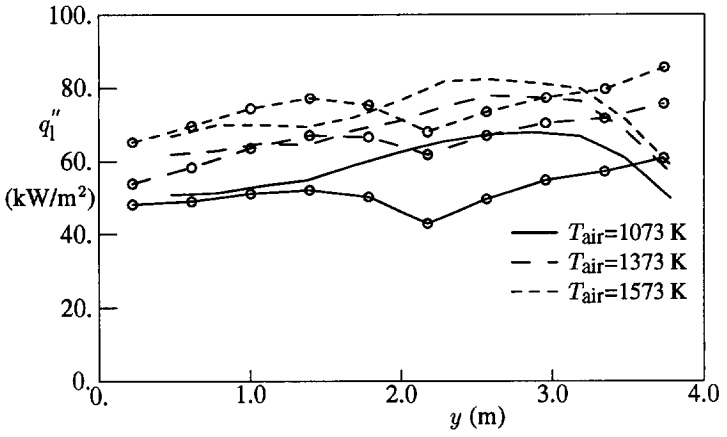

Figure 6.17: Distribution of the heat transfer to the load for three combustion air temperatures. For each combustion air temperature the same type of line has been chosen for both the simulations and the measurements. The results of the simulations are distinguished from the measured results by the markers.

Table 6.9: Characteristics of flames of the combustion air temperature variation.

	simulated			measured		
	v 076	v 074	v 075	6.066	6.044	6.032
input						
T_{air} (K)	1073	1373	1573	1073	1393	1578
λ	1.0994	1.0994	1.0994	1.102	1.120	1.161
output						
T_{max} (K)	2340	2395	2463	-	-	-
$\overline{T}$ (K)	1686	1780	1850	-	-	-
T_{fg} (K)	1741	1846	1916	1751	1805	1898
NO_{fg} (ppm)	407	1409	2573	579	1416	2663
$\overline{q_l''}$ (kW/m^2)	51.3	65.2	74.2	61.2	73.1	76.9
η_l (%)	35.5	45.2	51.4	39.3	45.9	47.8
η_f (%)	58.5	66.4	71.7	56.4	67.4	70.9
$M_{e,max}$ (%)	100.8	113.7	121.3	-	-	-

efficiency is almost constant over the range of values of the excess air level that have been tested.

Heat transfer results To illustrate the effect of the combustion air temperature on the heat transfer to the load, the results at three air preheat temperatures are shown in figure 6.17. These results were obtained in the baseline flame configuration that was defined in section 5.3. The simulations that are shown were obtained with the same set of boundary conditions in all three cases, except for the load temperature. The measured load temperature, shown in figure 6.1 for two air preheat temperatures, was used as the temperature boundary condition for the load. The load temperature boundary conditions for the three flames are thus the only input parameter in which they differ. The properties of these flames are listed in table 6.9, in which results of the measurements are also listed. From this table it is clear that generally the heat transfer is predicted very well. The furnace efficiency is predicted with good accuracy and can be well explained. Due to the temperature rise in the furnace, the heat transfer to the load increases with increasing air preheat temperature. Since radiative heat transfer, proportional to the fourth power of the temperature, is dominant in this furnace and the heat input increases linearly with the air preheat temperature, the furnace efficiency increases with increasing combustion air temperature. It seems however that the flue gas temperature coupled to the furnace efficiency, is predicted less well (see table 6.9). Figure 6.18 illustrates that the use of the mean flue gas temperature, which is used in table 6.9, can be deceptive. The flue gas is not a perfectly stirred gas with uniform properties. As a matter of fact, there are still rather steep temperature gradients in the outflow plane. This makes a comparison of the results difficult, since small positioning errors can result in large temperature differences. However, the difference between

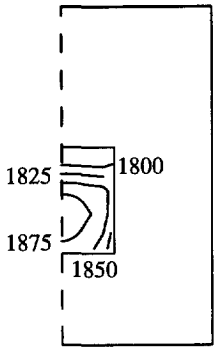

Figure 6.18: Temperature contours in the outflow plane of the furnace. Contour values: 1800, 1825, 1850 and 1875 K.

measurements and simulations is at most some 50 K, which is only 3 % of the measured values and this is quite acceptable.

The distribution of the heat transfer to the load for the excess air level variation is shown in figure 6.19 for several excess air levels. The effect of slow combustion is visible in the simulation with $\lambda = 1.01$ (i.e. 1 % excess air), while the effect of cooling is visible in the $\lambda = 1.30$ simulation in the second half of the furnace. The characteristics of these flames are listed in tables 6.10a and 6.10b for respectively the simulations and

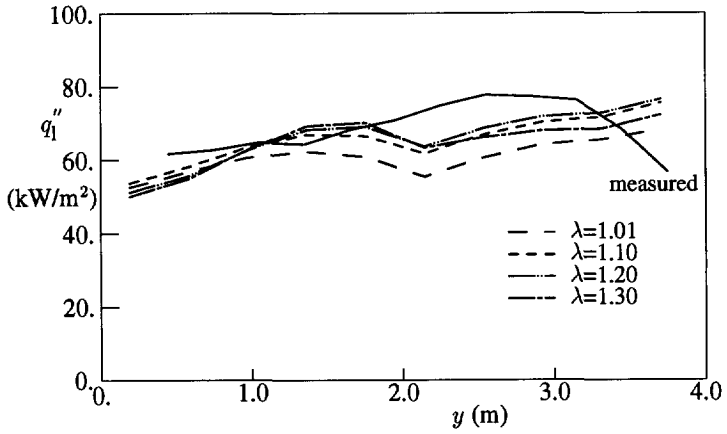

Figure 6.19: Distribution of the heat transfer to the load for several excess air levels.

Table 6.10a: Results of simulated flames with different excess air levels.

	v 080	v 077	v 074	v 081	v 082	v 083	v 109
input							
T_{air} (K)	1373	1373	1373	1373	1373	1373	1373
λ	1.0094	1.0494	1.0994	1.1493	1.1993	1.2493	1.2993
output							
T_{max} (K)	2429	2400	2395	2413	2433	2437	2430
$\overline{T}$ (K)	1770	1776	1780	1779	1776	1773	1770
T_{fg} (K)	1821	1834	1846	1845	1844	1846	1838
NO_{fg} (ppm)	1212	1287	1409	1605	1819	2031	2226
$\overline{q_l''}$ (kW/m^2)	65.2	63.1	65.2	65.9	65.8	65.1	64.3
η_l (%)	45.2	43.7	45.2	45.7	45.5	45.1	44.5
η_f (%)	66.4	66.0	66.4	66.5	66.1	65.4	64.8
$M_{e,max}$ (%)	114.8	115.0	113.7	113.3	112.1	108.7	105.8

Table 6.10b: Results of measured flames with different excess air levels.

	6.045	6.044	6.046	6.043
input				
T_{air} (K)	1373	1373	1373	1373
λ	1.00	1.12	1.143	1.223
output				
T_{max} (K)	-	-	-	-
$\overline{T}$ (K)	-	-	-	-
T_{fg} (K)	1738	1805	1783	1785
NO_{fg} (ppm)	500	1416	2085	1713
$\overline{q_l''}$ (kW/m^2)	81.4	73.1	73.7	71.0
η_l (%)	45.2	45.9	49.0	44.8
η_f (%)	75.0	67.4	67.9	65.4
$M_{e,max}$ (%)	-	-	-	-

the measurements. The flue gas temperatures agree within an acceptable range of error, especially since the average flue gas temperature is used for the simulations, except for the low excess air level flame (flame v080). Here it seems that the numerical model is no longer valid, since the combustion is now no longer determined by the mixing of natural gas and combustion air, but by the chemical reactions that occur in an oxygen lean environment. This can be seen not only from the flue gas temperature, but also from the efficiencies and the NO_x emission, which display large differences between the measurements and the simulations.

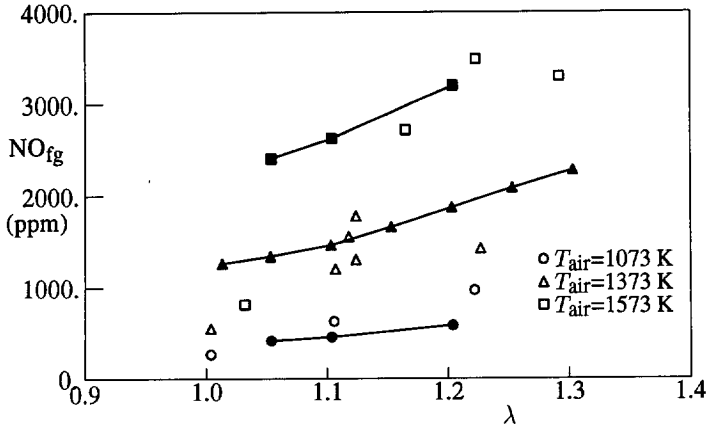

Figure 6.20: Flue gas NO_x (ppm, 0% O_2) dependence on excess air level and combustion air temperature. The simulated results are connected by lines.

NO_x emission results In figure 6.20 the measured and simulated NO_x emissions are plotted as a function of both the excess air level (airfactor) and the combustion air temperature. The trends in NO_x formation that we could expect are found in both the measurements and the simulations. The NO_x emission increases with increasing temperature and with increasing excess air level. The point where the cooling effect of the combustion air starts to gain importance is not yet reached at an airfactor of 1.3. In this figure we see that the simulated flue gas NO_x emissions agree very well with the measured data except at the lowest excess air levels. At these levels the flame is no longer a diffusion flame, which we are modelling, because combustion chemistry starts to play an important role here. We can therefore only apply the model to a suitably high excess air level, which is approximately $\lambda = 1.05$, as the measured and simulated NO_x emissions agree well from this point onwards.

An important feature to determine the NO_x emission level of the furnace is a comparison with the equilibrium NO_x level in the furnace or the flue gas. For a given fuel and airfactor the equilibrium NO_x level can be computed as a function of the temperature. In figure 6.21 the equilibrium NO concentration as a function of the temperature has been plotted at two airfactors ($\lambda = 1.1$ and $\lambda = 1.2$). The NO_x emission results of the simulations and the measurements for the combustion air temperature and excess air level variation have been plotted in this figure against the flue gas temperature. At the lowest combustion air temperature the measured and simulated NO_x emissions are lower than the equilibrium NO concentration at the flue gas temperature. For T_{air} = 1373 K the NO_x emissions are in the range of the equilibrium NO concentration, while for the highest combustion air temperature the measured and simulated NO_x emissions are higher than the equilibrium value at T_{fg}. This shows the importance

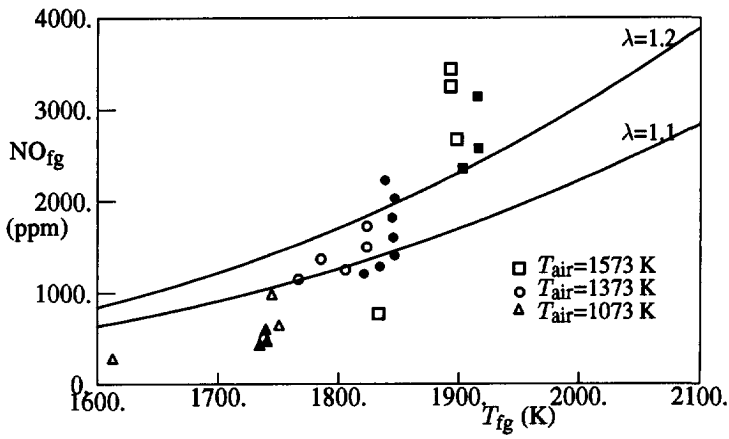

Figure 6.21: Flue gas NO_x (ppm, 0% O_2) against flue gas temperature at several combustion air temperatures, with airfactor between 1.05 and 1.20. Open markers denote the measured results, filled markers denote the simulated results. The solid lines are the equilibrium NO concentration as a function of the temperature for two airfactors, computed thermodynamically.

of the temperature dependence of the NO formation rate. For each increase in the combustion air temperature the highest temperature in the furnace was increased by approximately 60 K in the simulations. This more than doubles the NO formation rate locally, which results in the observed effect. From figure 6.21 it is clear that the simulated results agree very well with the results that were measured by the IFRF for the combustion air temperature and the excess air level variation.

6.4.2 Mixing angle and gas injection velocity

One of the main purposes of our investigation was to investigate methods of reducing the NO_x emissions while keeping other parameters such as the efficiency constant. The two parameters that have been discussed in the previous section had a distinct influence on the efficiency and the heat transfer to the load. Therefore, the effect of some other parameters was investigated, parameters which affect only the mixing and that do not require other adjustments of the combustion process. Both the mixing angle between the natural gas and the combustion air, and the gas injection velocity are parameters that affect the mixing process at constant process conditions. The influence of these parameters was investigated at the baseline conditions, viz. 1373 K combustion air temperature and 10 % excess air ($\lambda = 1.1$).

Heat transfer results The first mixing parameter that we will discuss is the mixing angle between the natural gas and the combustion air. Four flames were simulated, viz.

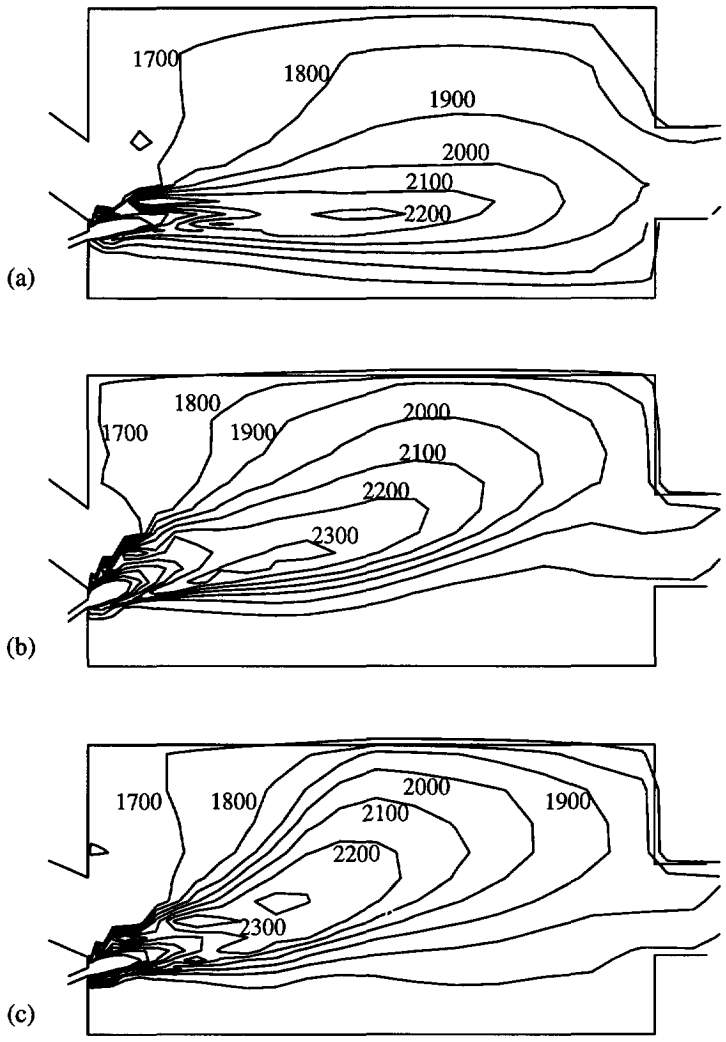

Figure 6.22: Temperature contours in the symmetry plane of the furnace. Contour values 1700, 1800, 1900, 2000, 2100, 2200 and 2300 K.
a. 20°-12° injection (baseline simulation), b. 20°-20° injection, c. 12°-12° injection.

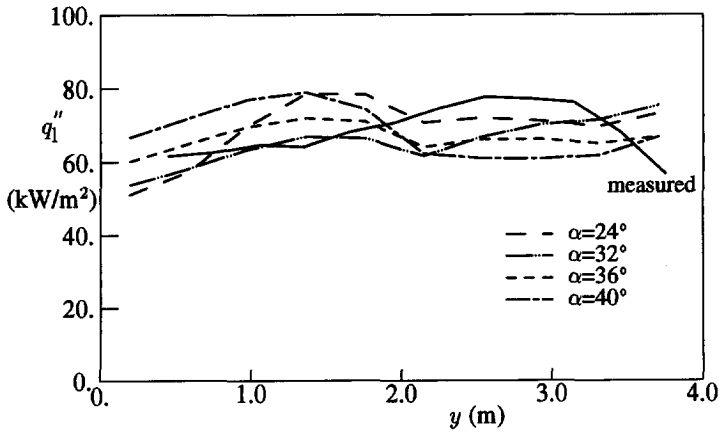

Figure 6.23: Distribution of the heat transfer to the load for the mixing angle variation, compared with the measured heat flux of the baseline flame (20°-12°).

Table 6.11: Results of simulations of the mixing angle variation at otherwise baseline conditions.

	v 089	v 074	v 114	v 088
input				
α (°)	24	32	36	40
output				
T_{max} (K)	2490	2395	2443	2465
$\overline{T}$ (K)	1785	1780	1787	1789
T_{fg} (K)	1797	1846	1800	1787
NO_{fg} (ppm)	2466	1409	1411	1924
$\overline{q_l''}$ (kW/m²)	69.0	65.2	66.4	68.0
η_l (%)	47.8	45.2	46.0	47.1
η_f (%)	69.4	66.4	69.0	69.9
$M_{e,max}$ (%)	75.6	113.7	105.9	110.0

with angles 20°-20° (air-gas), 20°-16°, 20°-12° and 12°-12°. It was shown that for the measured flames the flow in the furnace was very different for the 32° and the 40° mixing angle. The same comparison as in figure 5.6a is shown in figure 6.22, although here for three flames (mixing angles 32°, 40° and 24°). Obviously, the simulated flows are different for these three flames as well. The effect of mixing on the heat transfer to the load is shown in figure 6.23. The fast combustion in the 40° flame is reflected in the high heat flux to the load in the beginning of the flame. The 36° and 32° flames show the same behaviour of the heat flux distribution, only then lower than in the case of the 40° flame. The heat flux distribution of the 24° flame differs in shape from the

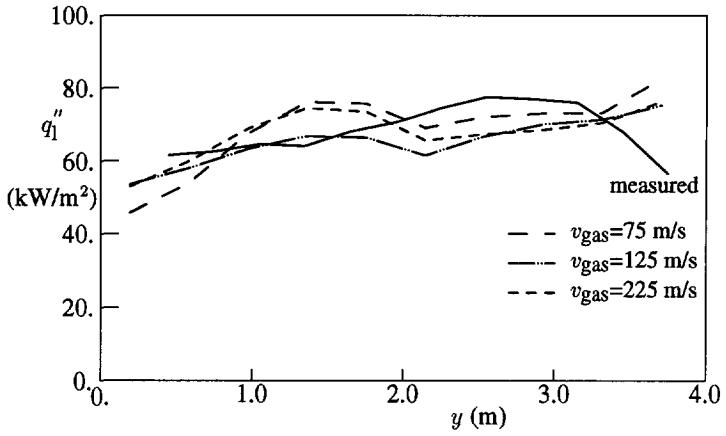

Figure 6.24: Distribution of the heat transfer to the load for three gas-injection velocities, viz. 75, 125 and 225 m/s.

other three flames. It seems that the combustion starts slower here, because the natural gas and the combustion air do not mix very near to the burner, which results in the low heat transfer in the beginning of the flame. Then the two streams mix, resulting in fast combustion and a maximum temperature that is even higher than for the 40° flame, as can be seen in table 6.11. This can be seen in the peak heat flux at about 1.5 m. As a result of the high flame temperature, the efficiency is slightly higher than for the other three flames.

The flue gas temperatures of these flames lie in the same range as the measured flue gas temperatures (see table 5.6 for the measured results). The load efficiencies of the simulated flames agree very well with the measured efficiencies, although for the 24° flame the result of the simulation is somewhat higher.

As the gas-injection velocity influences the mixing between natural gas and air, the combustion velocity is also affected by the gas-injection velocity. This affects the heat transfer to the load, which may affect the furnace temperature. To illustrate the effect of the gas-injection velocity on the heat transfer the results obtained at several velocities are shown in figure 6.24. From this figure it is obvious that the flame with the 75 m/s injection velocity develops slower than the flames with the other two velocities. This flame loses less heat in the first 1.5 m than the other flames and more heat in the second half of the furnace. The total heat loss to the load is somewhat higher for this flame, which can be seen in the load efficiency in table 6.12 and which can also be compared with the results in table 5.6 for the 32° mixing angle. From these tables it becomes clear that the gas injection velocity has only limited influence on the heat transfer results. In both the measurements and the simulations the efficiency is almost constant over the range of velocities. The simulated and measured efficiencies agree well with each other, which is also the case for the flue gas temperatures. These lie for

Table 6.12: Results of simulations of the gas-injection velocity variation at otherwise baseline conditions.

	v 097	v 111	v 074	v 112	v 084	v 113	v 092
input							
v_{gas} (m/s)	75	100	125	150	175	200	225
λ	1.1006	1.1006	1.0994	1.0994	1.0994	1.0993	1.0995
output							
T_{max} (K)	2367	2431	2395	2439	2464	2496	2504
$\overline{T}$ (K)	1774	1779	1780	1779	1780	1784	1780
T_{fg} (K)	1847	1839	1846	1847	1841	1804	1818
NO_{fg} (ppm)	1637	1536	1409	1347	1353	2652	2542
$\overline{q_l''}$ (kW/m^2)	67.7	66.6	65.2	64.5	64.2	68.0	66.7
η_l (%)	46.9	46.1	45.2	44.7	44.5	47.1	46.2
η_f (%)	66.5	66.7	66.4	66.2	66.5	68.6	67.7
$M_{e,max}$ (%)	90.7	105.2	113.7	117.4	121.5	89.3	89.7

both the measurements and the simulations between 1800 and 1840 K.

NO_x emission results The mixing angle has a strong influence on the NO_x emission for the four angles that were simulated. In figure 6.25 the measured and simulated NO_x emissions for the mixing angle variation at otherwise baseline conditions are shown. The trends that can be seen in this figure are completely different for the two series. The measured results display a steady decrease of the NO_x emission, while the simulated results first decrease, from 2466 ppm at 24° to 1409 ppm at 32°, and then increase. Based on the maximum temperature and the temperature distribution in the furnace that is shown in figure 6.22, the predicted NO_x trend can be explained. The 24° flame has a very high maximum temperature of 2490 K, which is 100 K higher than for the 32° flame. Also, the 40° flame has a higher maximum temperature, viz. 2465 K. In the case of the 40° flame, the high temperature can be explained by the fast mixing and fast combustion that occur. There is a relatively large very hot zone in the furnace (see figure 6.22[b]), where NO_x can be formed. In the case of the 24° flame mixing between natural gas and combustion air is delayed as was already seen in the heat transfer to the load. Downstream in the furnace the combustion air and the natural gas mix and the combustion is quick. Here also high temperatures arise, and much NO_x is formed. In the case of the 32° mixing angle the flame is pushed towards the bottom of the furnace by the air stream that envelopes the flame. The hot combustion products do not mix rapidly with the air stream for this flame. For the 24°mixing angle the combustion air does not have enough momentum to force the flame towards the bottom of the furnace, so that the hot flame rises through the air stream towards the roof like a plume. Thus, hot combustion products mix with the combustion air, in which some oxygen is still available, resulting in high NO_x formation.

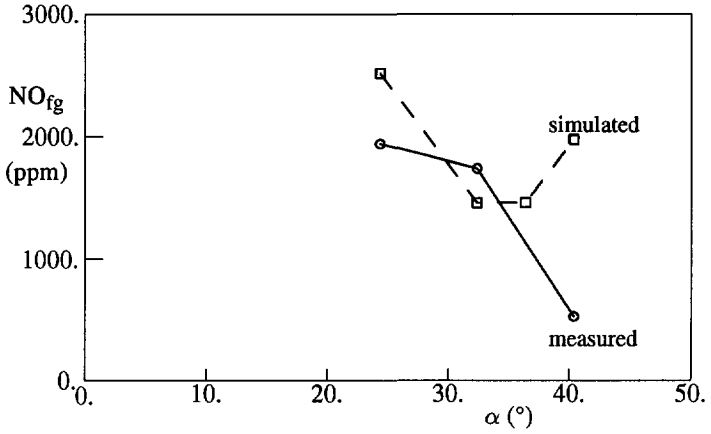

Figure 6.25: Flue gas NO_x (ppm, 0% O_2) dependence on the mixing angle at otherwise baseline conditions.

The comparison with the measured data shows that only for the 40° flame the predictions differ completely from the measurements. Based on the mixing velocity analysis for this flame, the measured result cannot be interpreted. Penetration of the jet into the recirculation zone would require the passing of the natural gas jet through the combustion air, while burning only a small amount of gas. This seems unlikely, even more so since in the NG7 investigation the penetration effect with the mixing angle variation could not be reproduced.

With the variation of the gas-injection velocity a small influence on the NO_x emission is found (see figure 6.26). In general, an increase in the gas-injection velocity resulted in an increased NO_x emission during the measurements. At gas-injection velocities higher than 150 m/s the effect is very small and considering the measurement errors no trend can be distinguished. The simulations also display only a limited effect of the gas-injection velocity on the NO_x emission. At the lower gas-injection velocities an increase of the velocity results in an increased strength of the recirculation and a decrease of the NO_x emission. Only at gas-injection velocities of over 200 m/s a strong increase of the NO_x emission is predicted. At these high injection velocities the results of the simulations are no longer reliable, due to the numerical diffusion that becomes more important at the highest velocities. Not only does the NO_x emission increase suddenly, but also the maximum temperature and the load efficiency increase for these flames. This means that the mixing is enhanced, which is the effect of the numerical diffusion. At the lower velocities the simulated and measured results are similar. Although here an increase is found in the measurements and a decrease in the simulations, these effects are small and the NO_x values agree rather well.

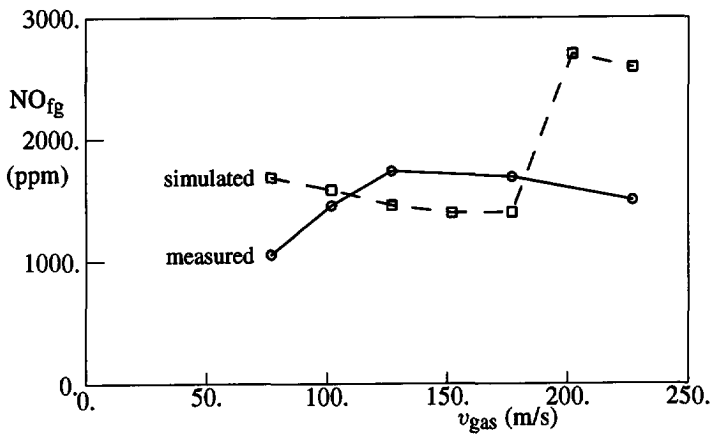

Figure 6.26: Flue gas NO_x (ppm, 0% O_2) dependence on the gas-injection velocity, at otherwise baseline conditions.

6.5 Final remarks on the NG6 simulations

In this chapter a series of simulations was presented for the geometry and the boundary conditions of IFRF furnace no. 2 during the NG6 trials. This was the first series of simulations for this furnace so that care has been taken to validate the used parameters.

First we discussed the development of the natural gas jet in the simulations. Because of the fairly coarse grid it proved necessary to make some assumptions about the initial jet development. In the numerical program FURNACE the jet boundary conditions are obtained by an upstream displacement of the jet conditions at several jet diameters downstream. In this way a small amount of precombustion is achieved, which results in better predictions of the flame jet and the heat transfer to the load.

The Hottel zone model that is used for the radiative heat transfer computations uses the grey gas assumption. The extinction coefficient is an unknown parameter for this model. Using a model developed by Wieringa we have estimated the value of the extinction coefficient. The sensitivity of the model to the value of the extinction coefficient was tested and a standard value for the rest of the simulations was ascertained. The boundary conditions for the Hottel zone model were adapted based on conclusions in the NG6 report (Van de Kamp *et al.* (1989)). We have shown the importance of the load temperature boundary condition to the distribution of the heat transfer to the load. It appeared, however, that the flue gas properties were not sensitive to the load temperature distribution provided that the average load temperature was correct.

Concerning the inflow boundary conditions it was shown that the velocity profile of the combustion air stream has little influence on the predictions of the numerical model. The inflow value of the dissipation rate of the turbulence proved to be an important inflow parameter. The standard boundary condition for this parameter is the

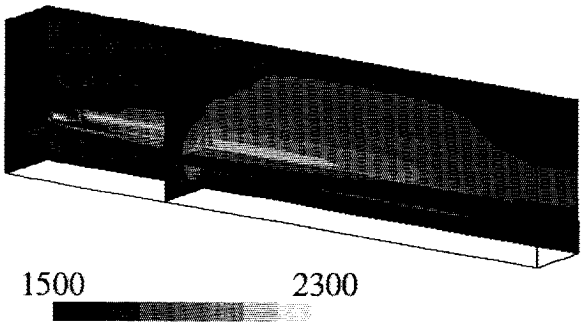

Figure 6.27: Grey scale plot of the temperature in the furnace. Shown are sections of the symmetry plane, two vertical cross-sections of which one through the burner and a horizontal section. Simulation of the 32° flame at baseline conditions.

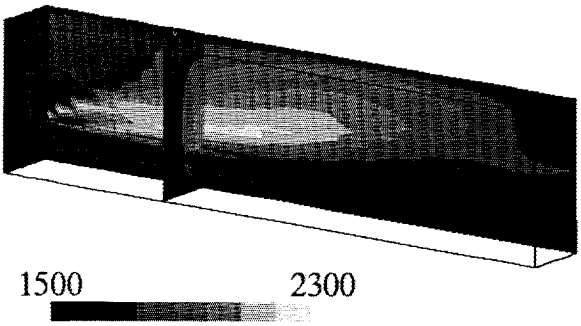

Figure 6.28: Grey scale plot of the temperature in the furnace of the 40° flame. The same sections as in the previous 3-D plot are shown.

value of the turbulence dissipation rate found in fully developed flow. By using a smaller value of the turbulence dissipation rate, the mixing of natural gas and combustion air is enhanced, resulting in better agreement of the simulated heat flux with the measured heat flux.

We have done simulations with FURNACE in the IFRF furnace on three grids, with an increasing number of grid nodes. The results with the coarsest grid were not satisfactory compared with the measurements. The finest grid did not give very different results from the intermediate grid, but it did require much longer computation times and much more CPU memory. Therefore, the intermediate grid with $18 \times 26 \times 22$ nodes was used for most of the simulations.

With the model parameters that were tested in the sensitivity analysis and a sufficiently fine grid some parameter variations of the NG6 experiments were repeated numerically. Two parameters which influence the process conditions were tested, viz. the combustion air temperature and the excess air level. Two parameters which do not

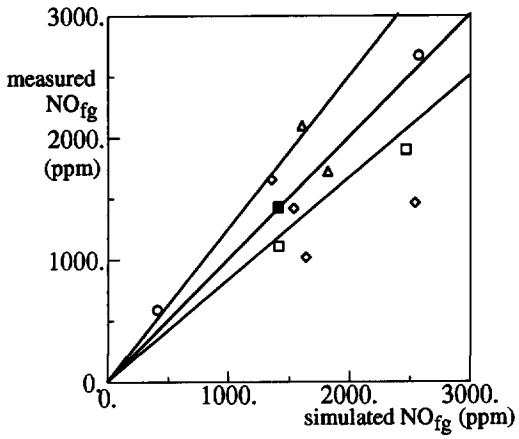

Figure 6.29: Comparison of the simulated and the measured NO_x emissions. The circles correspond with the combustion air temperature variation, the triangle with the excess air level variation, the squares with the mixing angle variation and the diamonds with the gas-injection velocity variation. Also shown are the $\pm$ 20 % deviation lines.

influence the process conditions, viz. the gas-injection velocity and the mixing angle between natural gas and combustion air, were also tested. The mixing angle variation resulted in very different flow fields in the furnace, as can be seen in figure 6.27 and 6.28. These are 3-dimensional grey-scale plots of the temperature in four sections of the furnace. As can be seen in these figures, the 40° flame is shorter and hotter than the 32° flame. The computed NO_x emissions are correspondingly higher.

The heat transfer results for all the simulations give similar values to the measurements. The efficiencies agree well and the differences between the measured and the simulated flue gas temperatures are within the margin of error. The NO_x emissions of all the simulated flames are compared with the measured NO_x emissions in figure 6.29. The largest discrepancy is found for the mixing angle variation. The measured 40° flame gave a very low NO_x emission, while the simulations resulted in a high NO_x emission. This difference in trend could not be explained. However, because this measured trend of the NO_x emission for the mixing angle variation was not reproduced during the NG7 trials of the IFRF, the result is disregarded. Also, at the higher velocities and low excess air levels differences arise. At the higher velocities this can be attributed to numerical diffusion, so that we conclude that using a finer mesh could solve this problem. At low excess air levels the diffusion flame model is no longer applicable, so that a more sophisticated combustion model should be included. The variation of the combustion air temperature showed excellent agreement between the measured and the simulated results.

Chapter 7

Simulations of the NG7 trials

7.1 Introduction

The measurements and simulations of the NG6 trials have indicated possibilities of reducing the NO_x emissions from high temperature furnaces, while maintaining the furnace efficiency at the required level. The most promising results pointed at reducing the NO_x emissions by influencing the mixing of the natural gas and the combustion air. However, the predictions and the measurements did not always give the same trends in NO_x emission when varying the same parameter. Especially the mixing angle between the natural gas and the combustion air gave different trends in NO_x emission for the measurements and the simulations.

In the NG7 trials of the IFRF one of the aims was to investigate the influence of mixing on the NO_x emission further. Not only underport firing was used but also other firing modes such as overport and sideport firing. Underport firing was applied again to test the effect of the mixing angle on the NO_x emission and to provide us with a new comparison with the results of the simulations.

The discrepancy between the measured and the simulated results of the NG6 trials not only called for a new comparison with repeated measurements, but also for model improvements. These improvements were carried out parallel with the simulations of the NG7 experiments. The mathematical model was adjusted in two respects.

Since the predicted temperatures in the furnace seem to be somewhat higher than the measured temperatures, we have incorporated the intermediate formation of CO into our combustion model. This delays the heat release of the flame, resulting in lower maximum temperatures and ultimately in lower NO_x emission predictions.

Not only the combustion model called for improvement, but also the NO_x formation model needed to be improved. The intermittency that is described by the use of the double delta pdf (described in chapter 2) overestimates the influence of the turbulent fluctuations on the NO_x formation. For the combustion the form of the pdf is not very critical (see e.g. Bilger (1980)), since the mean and variance of the mixture fraction (f and g) are computed accurately for all pdf's. The NO_x formation is kinetically determined, not by the mixing process. Therefore, more accurate knowledge of, mainly, the oxygen concentration is needed. A better estimate of the oxygen concentration is

obtained by using a better pdf-model. Therefore, we have included a top-hat pdf model to compute the NO formation.

The simulations of the flames of the NG7 investigation were performed with the measured boundary conditions of the experiments. These boundary conditions were different from those of the NG6 trials. According to Nakamura *et al.* (1991) the load was cooler due to a better thermal contact of the refractory with the cooling loops. Generally spoken, the NO_x levels are 300 – 500 ppm lower in the NG7 investigation than in corresponding cases in the NG6 investigation. We will first compare the results of the different models for the underport-fired case with each other and with the measurements. Then we will discuss the various injection modes that were tested to assess the influence of the mixing on the NO_x formation. Tested and simulated were underport, overport, sideport, parallel sideport and combined underport-overport injection of the natural gas.

7.2 Model improvements

7.2.1 Incorporation of CO

An important intermediate product in the combustion of methane and other hydrocarbons has been neglected so far in our model. The combustion reaction that we have modelled so far is the simple overall reaction 2.46:

$$\text{fuel} + k\,O_2 \rightarrow p\,CO_2 + q\,H_2O$$

The combustion of methane, however, takes place via many chain-reactions, in which many species play an important role. Warnatz (1983a) and Glassman (1987) give extended oxidation schemes of methane. For instance Warnatz presents an oxidation scheme for methane consisting of 26 species and 79 reactions. Computationally it is impossible to use this oxidation scheme in our model. The amount of CPU time needed to solve the conservation equations for these 26 species would multiply the total CPU time by a factor 4. Besides, the solution of a scheme with 79 reactions requires special computational effort. In effect, considering our current computational facilities, this inhibited our use of such a model in our complex 3-D geometry.

However, the oxidation reaction that we have used overestimates the combustion velocity and the heat release in the beginning of the flame. Disregarding the importance of many hydrocarbon reactions, we can improve our model in a relatively simple manner. It is generally known (Warnatz (1983a)) that CO plays an important role in the oxidation of all hydrocarbons. Warnatz presents two reactions, that describe the oxidation of CO to CO_2,

$$\begin{aligned} H + O_2 &\rightarrow OH + O \\ CO + OH &\rightarrow CO_2 + H \end{aligned} \tag{7.1}$$

Warnatz remarks that the predominant influence of these reactions causes the similarity of hydrocarbon flames, irrespective of the hydrocarbon considered. In our model we

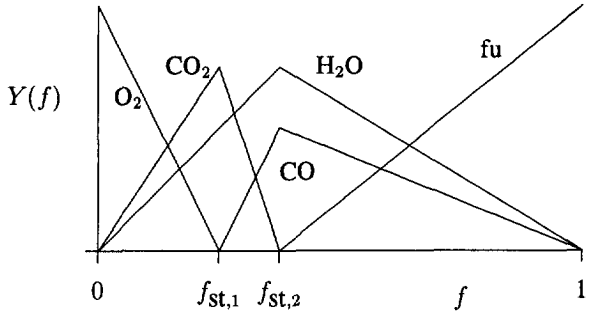

Figure 7.1: Species mass fractions as a function of the mixture fraction for the extended combustion model with full intermediate CO formation.

have no knowledge of the OH, O and H concentrations. We would need a much more sophisticated combustion model, to get accurate estimates of the concentration of these species. Therefore, we have applied an even simpler approach to incorporate the influence of the CO on the flame. First, the fuel is burned to CO, then the CO is burned to CO_2. For example, originally the combustion of methane was modelled as,

$$CH_4 + 2\,O_2 \rightarrow CO_2 + 2\,H_2O \tag{7.2}$$

Now, combustion takes place in two steps,

$$2\,CH_4 + 3\,O_2 \rightarrow 2\,CO + 4\,H_2O \tag{7.3}$$

$$2\,CO + O_2 \rightarrow 2\,CO_2 \tag{7.4}$$

In section 2.4 the stoichiometric mass ratio for the overall combustion reaction was defined. In the same way we can define another stoichiometric mass ratio, viz. for reaction 7.3. The composition dependence on the mixture fraction changes, as well as the sensible heat and the temperature. The original species concentrations as a function of the mixture fraction were already shown in figure 2.1. The adapted composition, accounting for the CO formation, is shown in figure 7.1. Of course, it is possible to take a mixture of reactions 7.2 and 7.3, where we can have a fixed ratio between CO and CO_2 (for $f > f_{st,2}$). This gives us a less extreme formation of intermediate CO and consequently less effects on the temperature and the species concentrations.

$$(n+m)\,CH_4 + (\frac{3}{2}n + 2m)\,O_2 \rightarrow n\,CO + m\,CO_2 + 2(n+m)\,H_2O \tag{7.5}$$

The data shown in figure 7.1 were computed under the assumption that for $f > f_{st,2}$ the fuel is only burned to CO ($n : m = 1 : 0$). We will first show the effect of the extended combustion model using full combustion to CO only (for $f > f_{st,2}$). This

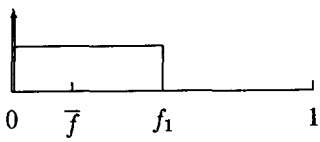

Figure 7.2: Example of top hat pdf, with delta function to account for intermittency.

under predicts the heat release of the beginning flame, as can be expected since some CO_2 will form in the beginning of the flame as well. We have therefore used a fixed CO:CO_2 ratio of 1:1 (for $f > f_{st,2}$) during most of the simulations.

7.2.2 Pdf model for NO_x formation

In the model as we have used it thus far, the NO source term 2.93,

$$\frac{d[\mathrm{NO}]}{dt} = \frac{2[\mathrm{O}]}{k_2[\mathrm{O}_2] + k_3[\mathrm{NO}]} \left\{ k_1 k_2 [\mathrm{O}_2][\mathrm{N}_2] - k_3 k_4 [\mathrm{NO}]^2 \right\}$$

was computed using the double-delta averaged values for the species concentrations and the temperature. The use of these pdf-averaged quantities in the computation of the source term may lead to errors. The Arrhenius factors in equation 2.93 are extremely temperature dependent. A rise in temperature of 50 K can lead to a doubling of the source term.

A better approach for the computation of the NO source term is to take the average of the source term over a pdf, instead of taking averaged quantities to compute the source term. This is the approach we have taken to improve our model. We have used a continuous pdf for the NO source term computation, while at the same time we used the double-delta pdf in the combustion model as before.

In the literature several pdf models have been discussed. Libby (1975) uses a top-hat pdf to compute a turbulent shear layer flow with chemical reaction that is infinitely fast compared to the mixing. Lockwood and Naguib (1975) use a clipped normal pdf to predict free, round-jet, turbulent diffusion flames. On the whole, their predictions agree very well, but they remark that more measurements need to be done to assess the physical modelling. Elgobashi (1977) uses a clipped-Gaussian pdf to account for the turbulent fluctuations. He also remarks that more accurate measurements should be done to assess the value of the chosen pdf, although his predictions seem to agree very good with measurements. Peeters and Van der Meer (1992) have compared predictions of a turbulent diffusion flame obtained with several pdf-models, as the mentioned top-hat and clipped-Gaussian pdf's and a beta-function pdf (see also Rhodes (1975)). They remark that the choice of the pdf is not critical as long as the pdf is continuous. In the case of intermittency, the pdf should be reduced to a continuous part and delta-functions.

For computational reasons we have chosen the simplest pdf-model that satisfies the constraints given by Peeters and Van der Meer (1992). This is the top-hat pdf model,

Table 7.1: Measured NO_x emissions for different gas-injection angles at several gas-injection velocities, comparison of the NG6 to the NG7 results.

v_{gas}	α	NG6	NG7
75	26		430
	32	1010	643
	36		730
	40	750	860
	43		880
125	26		690
	32	1580	1070
	36		1210
	40	520	1170
	43		970
225	26		955
	32	1450	1160
	36		1085
	40	1400	935
	43		970

shown in figure 7.2. Other pdf's require iterative methods to determine the parameters of the pdf locally, which is time consuming (Lockwood and Naguib (1975)). As Peeters and Van der Meer (1992) show, the differences between the predictions with the top-hat pdf and those with the clipped-Gaussian or beta-function pdf are acceptably small. Implementation of the top-hat pdf model is straightforward. The equation of the pdf is given in appendix A, together with the computation of the parameters of the pdf.

7.3 Application of the model improvements

Underport-fired flames were again tested during the NG7 trials with two varying parameters that are of interest to us: the gas-injection angle and the gas-injection velocity. Several other parameters were varied, such as the type of gas-nozzle, but since these variations were not simulated we will not discuss them here (see Nakamura *et al.* (1991)).

The measured effect of the gas-injection angle on the NO_x emissions at a number of gas-injection velocities was shown in figure 5.10. Especially important are the measurements with v_{gas} = 125 m/s, since the simulations have been done with this injection velocity. The NO_x emissions of corresponding gas-injection angle variations of the NG6 and NG7 trials are listed in table 7.1. It is clear that on the whole the results are quite different. In the NG6 investigation, at 125 m/s gas-injection velocity, a sharp decrease of the NO_x emission was measured when the gas-injection angle was increased from 12° to 20°. Now, at the same variation, the NO_x emission increases slightly. The

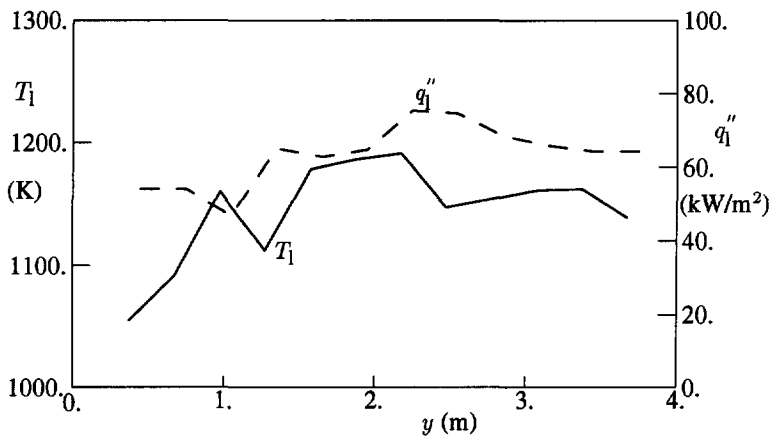

Figure 7.3: Measured load temperature and heat transfer to the load for the 32° mixing angle underport fired flame.

different thermal environments between the two trials, caused by a better thermal contact between the refractory and the cooling loops, may explain these different results partly.

The different thermal environment is something that we should account for in our simulations. The load temperature, approximately 200 K lower in the NG7 investigation than in the NG6 investigation, has a large influence on the furnace temperature and thus on the NO_x formation. In the NG7 trials the load temperature was measured for all flames. We have used these measured load temperatures in our simulations. The measured load temperature for the 12° gas-injection angle (at v_{gas} = 125 m/s) is shown in figure 7.3, together with the measured heat transfer to the load. For the different gas-injection angles of the underport fired flames of NG7 the differences in load temperature are less than 20 K. The results of measured underport flames with 125 m/s gas-injection velocity are listed in table 5.7.

7.3.1 Simulations of underport flames

Standard model simulations We will first discuss the simulations of the NG7 underport fired flames done with the standard model as it was used for the NG6 trials. We have done these simulations for three cases, viz. three gas-injection angles: 12°, 16° and 20°. These simulations were also performed for the NG6 trials, but due to the different thermal boundary conditions we find different NO_x levels in the NG7 simulations. The trend of the NO_x emissions from the NG6 simulations, however, is reproduced as can be seen in figure 7.4. For comparison, the measured NO_x levels are also shown in this figure. It is clear from figure 7.4 that the differences between the measurements and the simulations are larger than the assumed ± 10 % measurement accuracy for some of the flames. The difference between the two trials is made clear

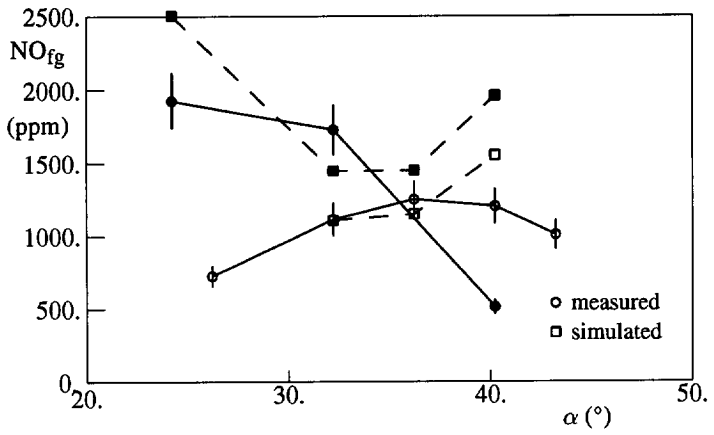

Figure 7.4: NO_x emission levels for the underport fired flames as a function of the gas-injection angle. The simulated data were obtained with the standard model. Filled markers denote the NG6 results, open markers the NG7 results. For the measured results the ± 10 % accuracy interval has been indicated.

by plotting the NO_x emissions against the flue gas temperature as in figure 7.5. The influence of the increased heat transfer to the load is seen in the decrease of the flue gas temperature by approximately 100 K. The predicted NO_x emissions are consistently lower for all flames (approximately 400 ppm), but the measured NO_x emissions did not show completely the same trend, as was already mentioned.

The measured and simulated heat fluxes to the load for the 32° mixing angle are shown in figure 7.6. The prediction of the heat flux in the beginning of the the furnace is higher than measured in NG7. This is due to the load temperature that was imposed as the boundary condition. In the first two segments the measured load temperature was more than 50 K lower than the temperature in the third segment. We will show later in this section that the heat transfer to the load is very sensitive to the imposed load temperature. However, overall the predictions of the heat transfer agree quite good with the measurements. The furnace efficiency is predicted with good accuracy and the flue gas temperature also agrees reasonably. We should take into account that the measurement error of the measured flue gas temperature is at least 50 K. This is not only due to measurement errors of the equipment, but also due to the positioning of the suction probe. In our simulations we find a temperature difference of over 50 K over the outflow (see figure 7.7). Thus the differences between the measurements and the simulations can be accounted for by the accuracy of the measurements. The relevant data for these flames are listed in table 7.3a, in which the flames simulated with the standard model are numbered 600 – 602.

We will now discuss simulations of the underport flames with the varying mixing angle with the first model improvement incorporated. This is the extended combustion

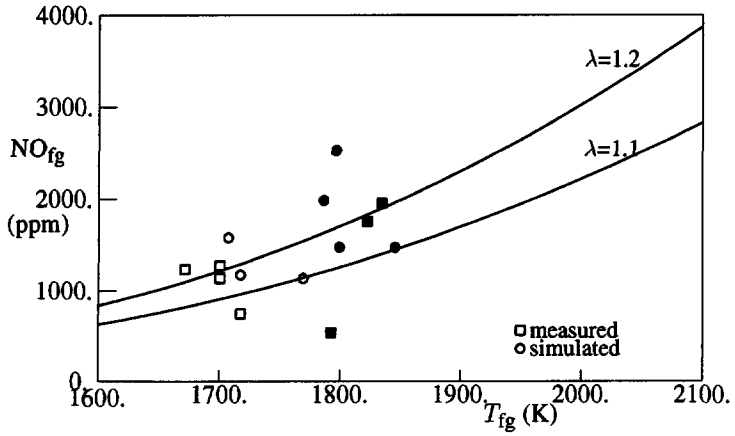

Figure 7.5: Flue gas NO_x (ppm, 0% O_2) against the flue gas temperature for the mixing angle variation of NG7, standard model simulations. Open markers denote the NG7 results, filled markers denote the NG6 results. The solid lines are the equilibrium NO concentration as a function of the temperature for two airfactors, computed thermodynamically.

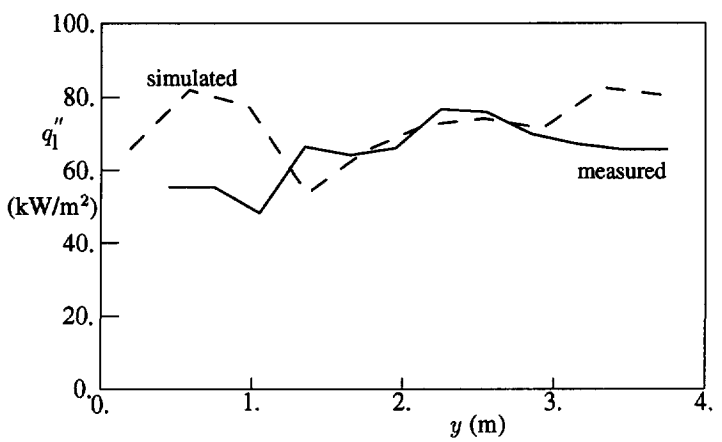

Figure 7.6: Measured and simulated heat flux to the load for the 20°-12° underport fired flame with measured boundary conditions (NG7).

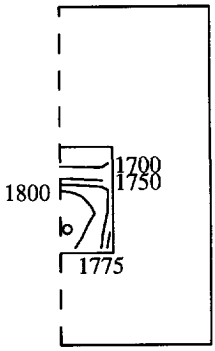

Figure 7.7: Computed temperature contours in the outflow of the furnace. NG7 underport fired flame simulation with complete model, with v_{gas} = 125 m/s and gas-injection angle 12°. The position of the temperature probe as reported by the IFRF is denoted by the marker.

model, with a simple model for the CO formation. Here, the influence of one model parameter should be tested, viz. the CO:CO_2 ratio.

Extended combustion model simulations (1) The simulations of the NG7 underport fired flames, that were just discussed, have been repeated with the extended combustion model (section 7.2.1). First the ratio CO:CO_2 has been chosen to be 1:0 (for $f > f_{st,2}$) for these simulations to show the full effect of CO incorporation.

The effect of the CO model incorporation on the simulations becomes clear when the temperature in the furnace is regarded. The maximum temperature in the furnace decreases from 2402 K for the standard model at the 32° mixing angle to 2332 K for the full CO combustion model at the same parameters (see tables 7.3a and 7.3b). The overall efficiency and the heat flux to the load are not influenced very much by the CO incorporation. This could be expected, since the total volumetric heat release in the furnace does not change with the incorporation of the CO combustion. The heat transfer to the load is determined mainly by the radiative heat transfer from the walls and the roof and not by the radiation from the gas. As can be seen in figure 7.8, the heat flux to the load is hardly influenced by the incorporation of the CO combustion model.

If we compare the NO_x emission predictions of the extended combustion model with the measurements of the NG7 trials, we see that the emissions decrease to values much lower than the measured NO_x emissions (cf. table 5.7 and 7.3b). We therefore conclude that the CO:CO_2 ratio of 1:0 overestimates the formation of CO in the flame

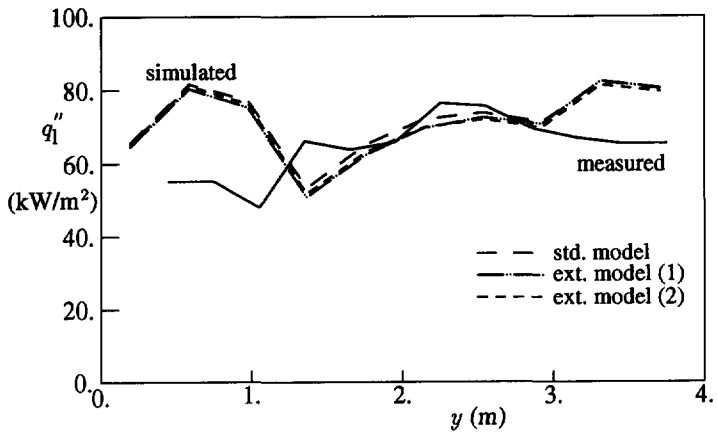

Figure 7.8: Predicted heat flux to the load for the 20°-12° underport fired flame with measured boundary conditions (NG7).
Shown are the measured heat flux and the simulated heat flux with three models, viz. standard, extended(1) and extended(2).

and thus underestimates the flame temperature. Therefore we have done the rest of our simulations of the NG7 trials with a ratio CO:CO_2 of 1:1 (for $f > f_{st,2}$).

Extended combustion model simulations (2) The simulations of the extended combustion model with CO:CO_2 = 1:0 at $f > f_{st,2}$ have been repeated with a CO:CO_2 ratio of 1:1. This has not been done because the NO_x emission predictions were too low when a ratio of 1:0 was used, but mainly because a CO:CO_2 ratio of 1:0 seems an unrealistic assumption. More realistic is both CO_2 and intermediate CO formation. Computations with FURNACE with a restrained equilibrium model for the combustion chemistry confirm the occurance of both CO and CO_2 in the flame. The CO:CO_2 ratio that could be computed from the restrained equilibrium model is approximately 1:1 in the regions of the flame where the CO is important. The heat flux to the load for the simulation of the 20°-12° underport fired flame is shown in figure 7.8 together with the previous results of the standard model and the extended combustion model with a CO:CO_2 ratio of 1:0. The heat flux hardly changes with respect to the two already discussed results. The results of the combustion simulation are listed in table 7.3c, where the results of the complete model are listed. The only difference between the complete model and the extended (2) model is the NO formation model, so that the results of the combustion program are the same. The NO_x results of the extended (2) model are only listed in table 7.2.

The maximum temperature is higher than for the simulations with a CO:CO_2 ratio of 1:0, viz. 2363 K vs. 2332 K. For the standard model, the highest computed

Table 7.2: Comparison of the NO_x emission predictions from the different models, compared with the measurements.

α	32°		36°		40°	
	NO_f	% red.	NO_f	% red.	NO_f	% red.
measured	1077	-	1214	-	1173	-
standard model	1072		1112		1517	
extended model (2)	875	18.4	906	18.5	1244	18.0
extended model (1)	705	34.2	724	34.9	1012	33.2
complete model	937	12.6	907	18.4	1093	27.9

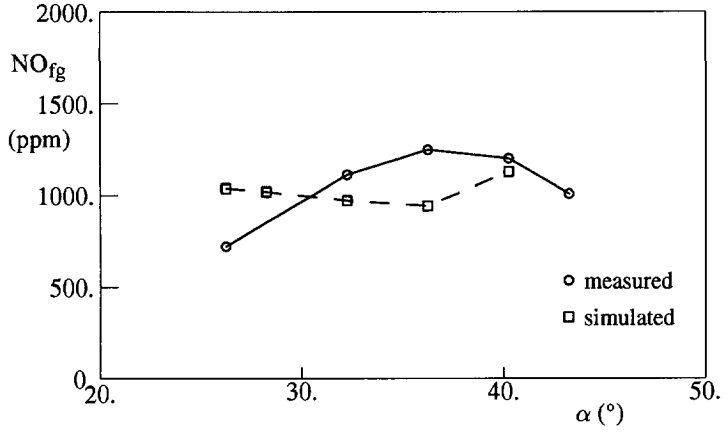

Figure 7.9: NO_x emission levels for the underport fired flames as a function of the gas-injection angle (complete model calculations) compared with the measured NO_x emission (NG7).

temperature in the furnace is 2402 K. Thus the mixed $CO:CO_2$ combustion gives results in-between the two extremes, as one would expect.

The influence of the CO incorporation is seen clearly in the reduction of the NO_x emission. This reduction is mainly a temperature related effect, since they are reduced with an almost constant percentage for any of the three mixing angles (see table 7.2).

Complete model simulations With the complete model (i.e. extended combustion model with $CO:CO_2$ ratio of 1:1 and NO_x source term calculation with the top-hat pdf model) we have again done the simulations of the underport fired flame with several gas-injection angles. The combustion results have already been presented in the previous paragraph, as we only changed the NO_x formation model now. The NO_x emission results are shown in figure 7.9. We see that overall the numerical results now

Table 7.3a: Results of simulations of underport fired flames with the standard model in the baseline NG7 configuration for several mixing angles.

	v 600	v 602	v 601
input			
α (°)	32	36	40
λ	1.0994	1.0994	1.0994
output			
T_{max} (K)	2402	2442	2464
$\overline{T}$ (K)	1702	1713	1714
T_{fg} (K)	1770	1718	1708
NO_{fg} (ppm)	1072	1112	1517
$\overline{q_l''}$ (kW/m^2)	72.0	73.9	75.0
η_l (%)	49.9	51.2	52.0
η_f (%)	71.6	74.6	75.2
$M_{e,max}$ (%)	117.0	108.7	113.7

agree very well with the measurements for all angles. Taking the measurement errors into account, we find hardly any trend in the NO_x emission between the 32° and 43° mixing angles.

Discussion of the results of the three models We have presented results for the different models that we have used. The characteristics of these flames are listed in

Table 7.3b: Results of simulations of underport fired flames with the extended (1) model in the baseline NG7 configuration for several mixing angles.

	v 700	v 702	v 701
input			
α (°)	32	36	40
λ	1.0994	1.0994	1.0994
output			
T_{max} (K)	2332	2370	2387
$\overline{T}$ (K)	1701	1710	1715
T_{fg} (K)	1767	1718	1704
NO_{fg} (ppm)	705	724	1012
$\overline{q_l''}$ (kW/m^2)	70.7	72.3	74.2
η_l (%)	49.0	50.0	51.4
η_f (%)	70.9	73.8	74.8
$M_{e,max}$ (%)	117.0	108.2	109.7

Table 7.3c: Results of simulations of underport fired flames with the complete model in the baseline NG7 configuration for several mixing angles.

	v 805	v 804	v 800	v 802	v 801
input					
α (°)	26	28	32	36	40
λ	1.0994	1.0994	1.0994	1.0994	1.0994
output					
T_{max} (K)	2370	2374	2363	2411	2434
$\overline{T}$ (K)	1682	1690	1701	1711	1715
T_{fg} (K)	1837	1814	1766	1715	1702
NO_{fg} (ppm)	1002	984	937	907	1093
$\overline{q_l''}$ (kW/m^2)	69.5	70.2	70.8	72.6	74.4
η_l (%)	48.1	48.6	49.0	50.3	51.6
η_f (%)	67.1	68.2	71.0	74.0	74.9
$M_{e,max}$ (%)	118.9	121.9	116.9	108.2	111.9

table 7.3. In figure 7.10 the NO_x emission results for the different models are shown. On the whole, the incorporation of the intermediate CO formation and the NO_x pdf model seem to have a positive effect on the results. The trend in NO_x formation is predicted better when both new models are incorporated. The CO incorporation alone gave lower NO_x levels, but did not change the trend in NO_x emission. The trend of the NO_x emission only changed when the NO_x pdf model was incorporated, although the

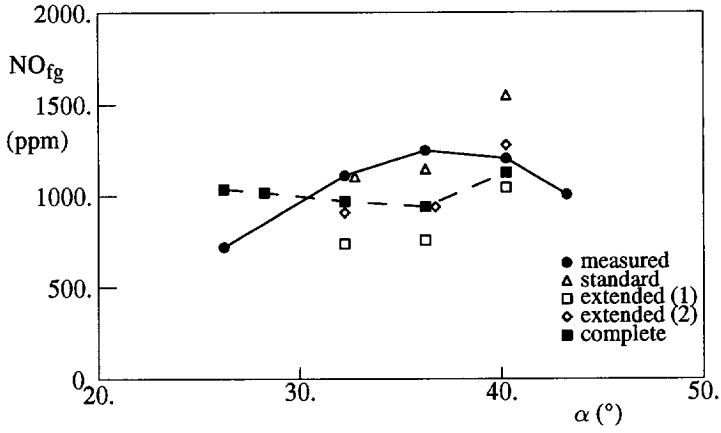

Figure 7.10: NO_x emission levels for the underport fired flames as a function of the gas-injection angle. Comparison of the predictions of the different models with the measurements.

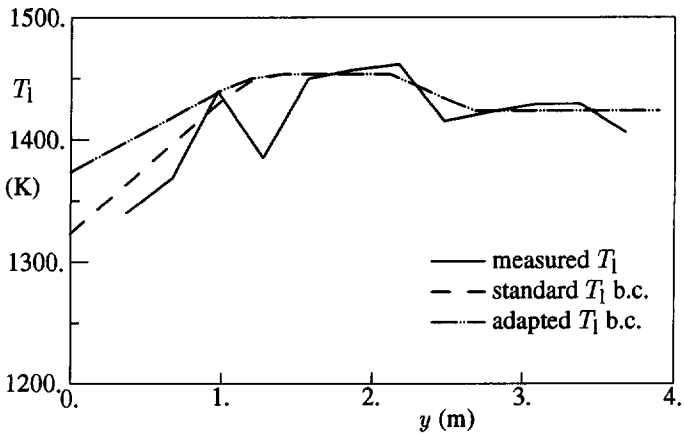

Figure 7.11: Measured load temperature and used standard and adapted boundary conditions for the complete model simulations of the underport 32° flame (v 800 & v 803).

maximum in NO_x emission measured at 16° was not reproduced in the simulations. Other characteristics of the flames, such as the heat transfer to the load, the flue gas temperature and composition, did not show large differences. The furnace efficiency, flue gas temperature and composition are all very much alike and agree very well with the measurements. On the basis of these results, we have used the complete model for the simulations of the NG7 investigation.

7.3.2 Load temperature variation

In the discussion of the simulated NG6 flames the importance of the load temperature boundary condition was already shown. The main influence of the load temperature is on the heat flux to the load. Thereby it influences the temperature in the furnace and thus the NO_x formation. In subsection 7.3.1 it was already mentioned that the measured load temperature in the first two segments of the furnace is more than 50 K lower than in the third segment (and further). When we used the measured load temperature as the boundary condition we found that the predicted heat flux to the load in the first segments is much higher than measured. To assess the influence of the temperature boundary condition of the first two segments we have done a simulation in the same configuration, but with the temperature in the first two segments raised by 50 K. The measured load temperature and the used boundary conditions are shown in figure 7.11. The resulting heat flux to the load is shown in figure 7.12 compared with the original simulation with the complete model and the measured heat flux. The predicted heat flux now agrees very well with the measured heat flux, except near the end of the furnace where the influence of the back wall and the chimney can be seen in the heat flux measurements. The rest of the data are also influenced, although not as much as

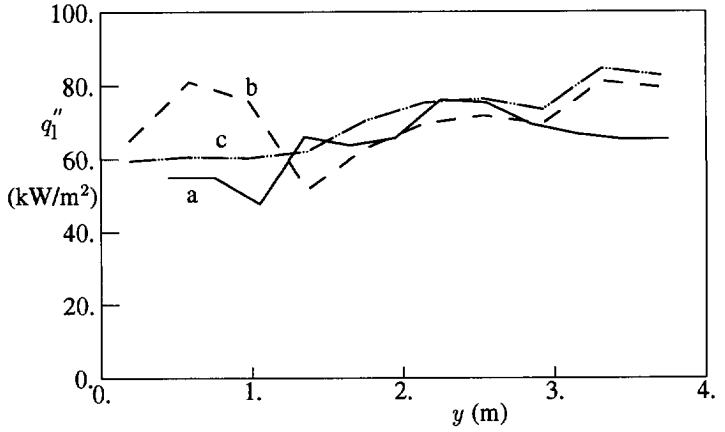

Figure 7.12: Heat flux to the load for the 20°-12° underport fired flame. a. measured, b. simulated with measured temperature boundary conditions (NG7, v 800), c. simulated with adapted measured b.c. (v 803).

Table 7.4: Results of measured and simulated underport fired flames with 12° gas injection. Comparison of simulations with the measured load temperature boundary condition to the adapted boundary condition. For reference measured data are also listed.

	v 800	v 803	7.020
	simulated		measured
input			
T_{air} (K)	1373	1373	1378
λ	1.0994	1.0994	1.1115
output			
T_{max} (K)	2363	2362	
$\overline{T}$ (K)	1701	1710	
T_{fg} (K)	1766	1772	1738
NO_{fg} (ppm)	937	972	1078
$O_{2,flue}$ (%)	1.90	1.90	2.2
$\overline{q_l''}$ (kW/m²)	70.8	70.5	
η_l (%)	49.0	48.8	53.0
η_f (%)	71.0	70.7	
$M_{e,max}$ (%)	116.9	116.3	

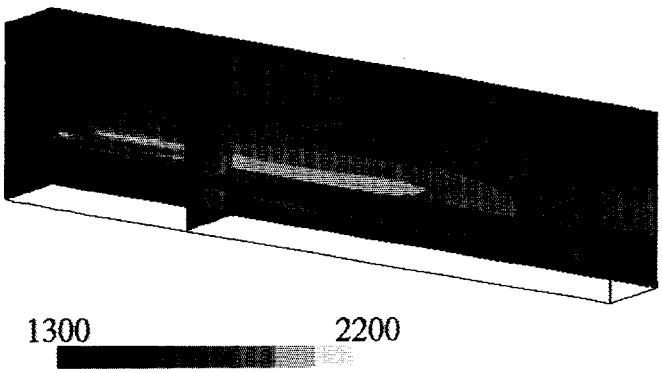

Figure 7.13: Grey-scale plot of the temperature (in K) in the furnace in the underport configuration. Baseline NG7 conditions (v 800), mixing angle 32°. Shown are a section of the symmetry plane, two vertical cross-sections and a horizontal section.

the heat flux. The total heat transfer to the load for instance is almost constant, as are the maximum and average furnace temperature (table 7.4). Now, from these data we conclude that the high heat flux to the load near the inlet of the furnace in the original simulation is due to the temperature boundary condition. The measured temperature in the first two segments seems to be too low, which could be expected since it is so much lower than the temperature in the third segment. However, the influence of the temperature boundary condition is very weak with respect to the other results such as the total heat transfer and even the NO_x emission. Therefore we have used the measured temperature boundary conditions for all the NG7 simulations, even though the measured temperature in the first two segments seems to be too low in many cases.

7.4 Firing mode variations

In the NG7 investigations several firing modes of the natural gas were investigated. The different firing modes induce different degrees and ways of mixing of the natural gas and the combustion air and are therefore suitable for mixing optimization investigations. In this section we will discuss the influence of the position of the natural gas injection point on the combustion and the NO_x formation. In figures 7.13 and 7.14 the influence of the position of the injection port is illustrated for the 32° (mixing angle) underport fired flame and the 30° overport fired flame respectively. These flames are very different, due to the position of the natural gas injection port. Underport firing was already discussed in the previous section. We will thus now start with the first different burner geometry, as illustrated in figure 7.14, viz. overport firing.

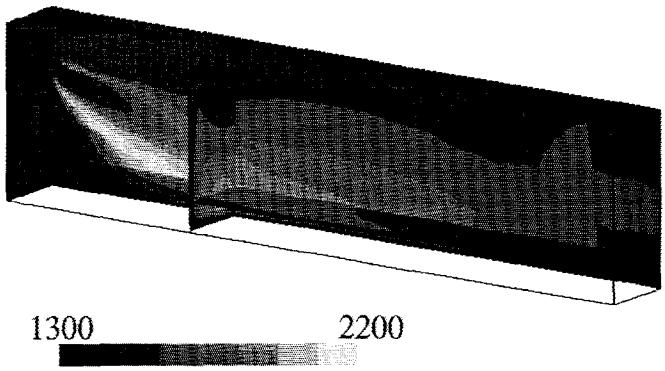

Figure 7.14: Grey-scale plot of the temperature (in K) in the furnace in the overport configuration with an overport injection angle of 30° (v 821). Shown are a sections of the symmetry plane, two vertical cross-sections and a horizontal section.

7.4.1 Overport firing

The mixing of natural gas and combustion air is strongly affected by the change from underport to overport firing. In the case of overport firing both the natural gas flow and the combustion air flow are directed towards the bottom of the furnace. The flame is thus also directed towards the bottom of the furnace (see figure 7.14), whereas the underport fired flames are more horizontal and slightly upwards to the roof of the furnace. For both firing modes the combustion air is injected at an angle of 20° downwards towards the furnace load. Thus, we find an oxygen rich zone near the load and an oxygen lean recirculation in the upper half of the furnace for both configurations.

At high mixing angles in the underport fired flames the natural gas jet lifts

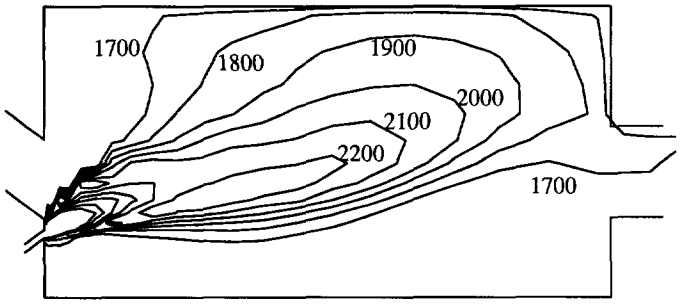

Figure 7.15: Temperature contours from simulation in the symmetry plane of the 40° underport fired flame. (Contour values: 1700, 1800, 1900, 2000, 2100 and 2200 K.)

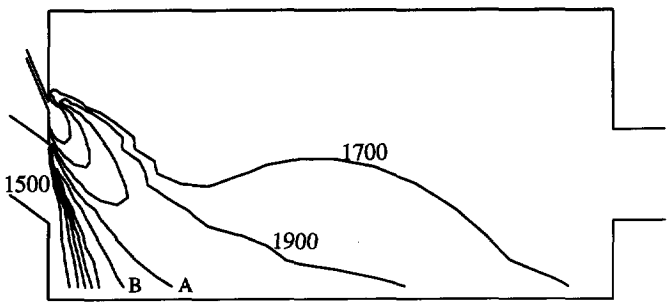

Figure 7.16: Temperature contours from simulation in the symmetry plane of the 50° overport fired flame. (Contour values: 1500, 1700, 1900, 2100 (contour A) and 2300 K (contour B).

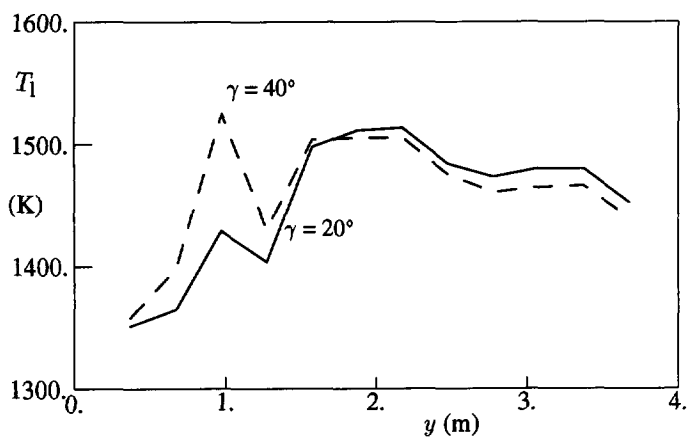

Figure 7.17: Measured load temperature of overport fired flames with $v_{gas} = 125$ m/s at 20° and 40° gas injection angle.

through the air stream into the oxygen lean recirculation zone in the upper half of the furnace. For the 40° mixing angle underport fired flame at otherwise baseline NG7 conditions temperature contours are shown in figure 7.15 to illustrate this. The overport flames with high mixing angles, however, penetrate through the combustion air stream into the oxygen rich zone near the load. This is illustrated in figure 7.16. This figure shows temperature contours for the 50° overport flame, from which impingement of the flame onto the load is clearly visible. Thus, at high mixing angles we encounter increased mixing of natural gas and oxygen and consequently faster combustion, higher

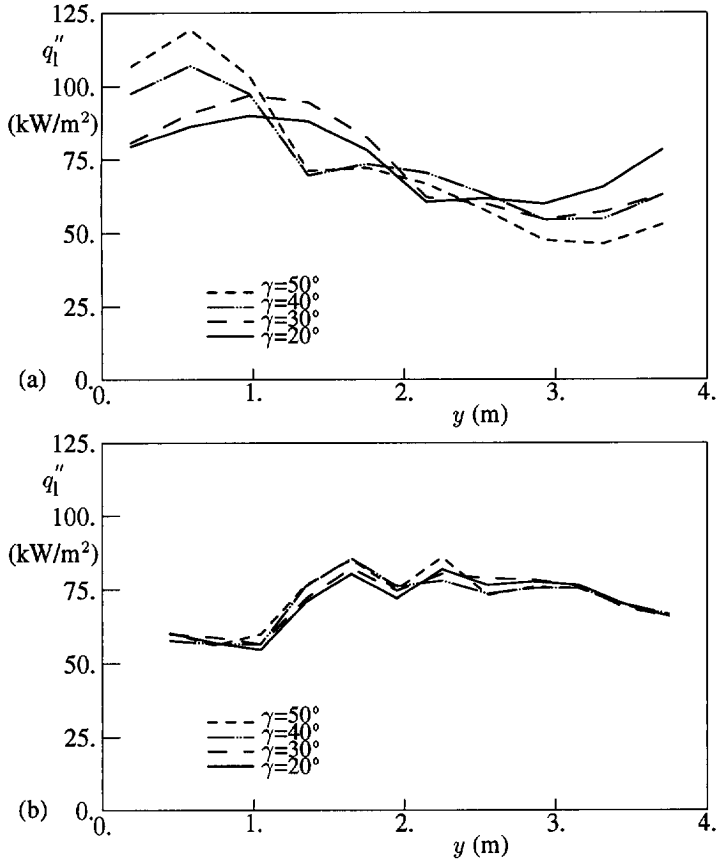

Figure 7.18: Simulated and measured heat transfer to the load of overport fired flames with v_{gas} = 125 m/s.
a. Results of simulations, b. Results of measurements.

Table 7.5a: Results of simulations of overport fired flames with the complete model: variation of the overport angle.

	v 820	v 821	v 822	v 823
input				
γ (°)	20	30	40	50
T_{air} (K)	1373	1373	1373	1373
λ	1.0994	1.0994	1.0994	1.0994
output				
T_{max} (K)	2304	2404	2419	2448
$\overline{T}$ (K)	1719	1714	1722	1723
T_{flue} (K)	1764	1725	1665	1660
NO_{flue} (ppm)	741	1015	1313	1477
$\overline{q_{\text{l}}''}$ (kW/m^2)	73.0	74.4	74.0	73.9
η_{l} (%)	50.5	51.5	51.3	51.2
η_{f} (%)	71.3	73.6	75.1	77.5
$M_{\text{e,max}}$ (%)	99.5	91.5	88.4	84.8

temperatures in the furnace and this leads to higher NO_x emissions. This effect of the mixing angle can be clearly seen in both the measurements and the simulations. During the investigations by the IFRF, impingement of the flames on the load was observed. On the heat transfer results this did not seem to have any effect, as we will show later.

In the overport burner geometry we have done simulations with several overport injection angles at a gas injection velocity of 125 m/s. These simulations were performed with the complete model that was defined and discussed in sections 7.2 and 7.3. We have used the measured load temperatures as the boundary condition in these simulations. As an example the load temperature that was used for the simulations of the 20° and 40° (gas injection) flame is shown in figure 7.17. As for the underport flames the measured load temperature seems to be too low in the first two segments. Since the influence of this boundary condition has been tested for the underport flame already, we have not again modified this temperature boundary condition. The influence on general quantities such as the flue gas temperature and flue gas composition or the overall and the load efficiency was small for the underport fired flames and will thus be neglected further.

Heat transfer results The heat transfer to the load for the overport angle variation is shown in figure 7.18. The measured results were obtained by the IFRF from the cooling loops surrounding the furnace refractory. The simulations and the measurements give different results in the first half of the furnace. The impingement of the flame on the bottom of the furnace is reflected in an increased heat transfer for the predictions, while in the measurements no effect at all can be seen. This difference may have been caused by the load temperature. In the simulations this was taken as low as the measured

Table 7.5b: Results of measured flames of the NG7 trials: variation of the mixing angle (overport firing).

	γ (°)				
	20	30	35	40	50
T_{fg} (K)	1721	1692	1688	1677	1630
η (%)	52.0	52.4	52.0	52.8	53.2
λ	1.1005	1.106	1.1005	1.1005	1.095
NO_{fg} (ppm)	342	722	1161	1636	1837
CO_{fg} (ppm)	223	140	132	116	27
$T_{roof,m}$ (K)	1572	1572	1572	1567	1557
$T_{load,m}$ (K)	1516	1517	1507	1525	1516

load temperature, although there are some reasons to doubt the measurements, because they seem to be too low in our opinion. This is supported by the variation of the load temperature that we have already discussed in section 7.3.2, where we assumed a higher T_l in the first two Hottel zones which resulted in better agreement between the measured and simulated heat fluxes. The peak heat fluxes for the 40° and 50° flames are found in the first two segments of the Hottel zone model, where the low temperatures are applied as the boundary condition. This causes an already high heat flux in these two segments, but in the case of the impinging flames the heat flux is further increased by the high temperature zones that exist near the refractory.

The flue gas temperatures of the simulated flames agree very well with the measured flue gas temperatures (see table 7.5b for the results of the measurements and table 7.5a for the simulations). In the first half of the furnace the predicted flames radiate more heat to the load, in the second half the measured heat flux is higher. This compensates, thus giving the similar results. The efficiencies seem to differ a little, but this may be due to the fact that the IFRF claims very low heat losses to the walls and consequently a higher heat transfer to the load. The difference is approximately 2 % for the four compared overport flames, with no difference in trends between the measurements and the simulations.

NO_x emission results The measured and simulated NO_x emission results are similar. With increasing gas injection angle, thus with increased mixing and consequently higher maximum temperatures, the NO_x emission increases. In the measurements the increase is very strong, from 340 ppm (at 0 % O_2) at 20° gas injection angle to 1840 ppm at 50° (see table 7.5b). In the simulations the increase is less strong than in the measurements, viz. from 741 ppm at 20° to 1477 ppm at 50°. At the lowest angle the predicted and the measured NO_x emission give the largest difference. This is a slowly developing flame, with too high a CO emission to be applicable in industry. For this case the numerical model over-predicts the combustion rate and consequently also the flame temperature and the NO_x formation. At the higher angles the differences are smaller, e.g. for the 40°

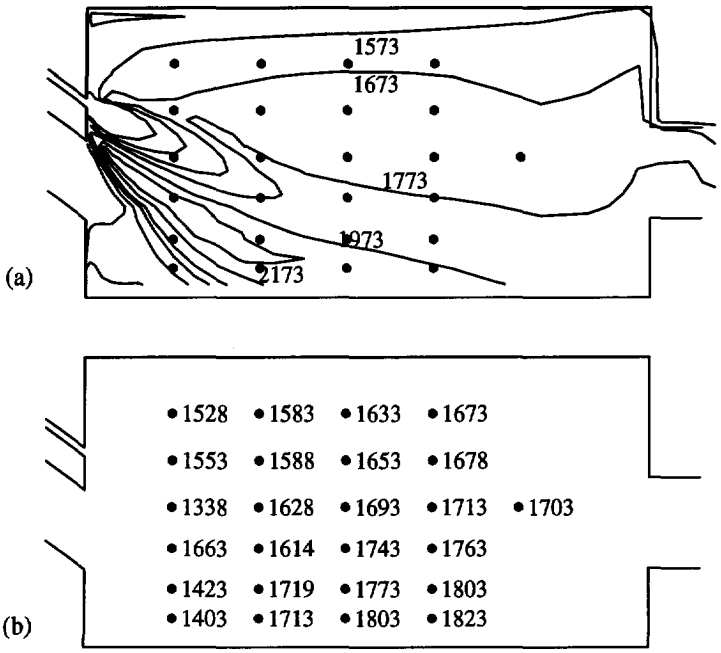

Figure 7.19: Computed and measured temperature in the symmetry plane of the furnace for the 20° overport fired flame.
a. Temperature contours from simulation, with points of measurement of NG7. (Contour values: 1473, 1573, 1673, 1773, 1973 and 2173 K.)
b. Measured temperatures in IFRF furnace. Temperatures in K.

overport angle the difference between the predicted and the measured NO_x emission is 20 %. In table 7.5a the highest temperature in the furnace, encountered in one or more of the flow volumes, is listed for the simulated flames. The difference is 140 K between the 20° and the 50° flames. This may serve as a sufficient explanation for the strong increase of the NO_x emission.

Discussion of the results of the overport flames At the low mixing angles there is a relatively large difference between the NO_x emission predictions and the measurements. These differences may be explained if we compare the temperature and the oxygen concentration distribution in the furnace that were measured with the predictions. For the 20°-125 m/s gas injection flame in-flame measurements were performed. In figures 7.19 - 7.21 the results of these in-flame measurements and the predictions are shown for the symmetry plane of the furnace. In figure 7.19 we see that the predicted temperatures in the upper half of the furnace agree very well with the measured tem-

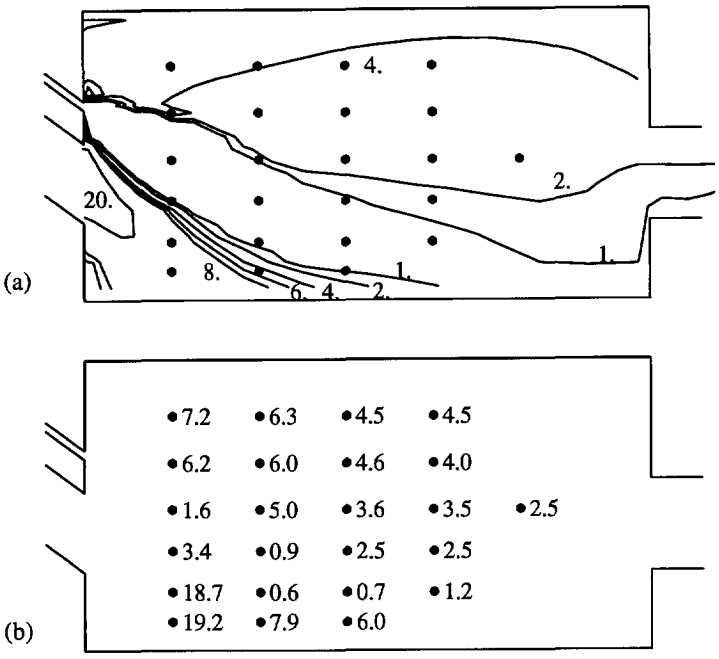

Figure 7.20: Computed and measured O_2 concentration in the symmetry plane of the furnace for the 20° overport fired flame.
a. O_2 concentration contours from simulation, with points of measurement of NG7. (Contour values: 1, 2, 4, 6, 8 and 20 % (mass fraction).)
b. Measured O_2 concentration (% mass fraction) in IFRF furnace.

peratures. The recirculation zone has a temperature of 1600 - 1750 K, which indicates that the NO_x formation should be very slow considering the temperature dependence of the Arrhenius coefficients. In the lower half of the furnace, which contains the flame, the temperature predictions differ considerably from the measurements. The highest measured temperature is 1830 K at 2.4 m from the inlet. In the predictions, however, the highest temperature is 2250 K, at approximately 1 m from the inlet. The predictions show fast combustion at the interface between the air stream and the natural gas jet flowing into the furnace from approximately 5 cm above the air inflow duct. The measurements show the temperature effect of the combustion only near the load between 2 - 3 m from the inlet. Thus, it seems that the model compared with the measurements predicts too fast mixing and combustion, which may partly be caused by numerical diffusion. Besides, this flame is relatively strongly sooting (considering that it is a natural gas flame) due to the slow combustion (see Nakamura *et al.* (1991)). Then, the emissivity of the flame is increased, thereby decreasing the flame temperature.

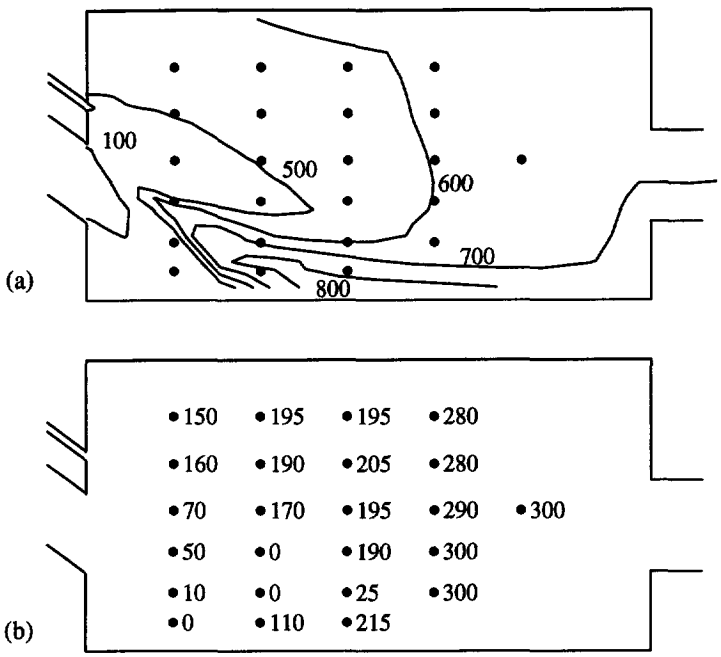

Figure 7.21: Computed and measured NO concentration in the symmetry plane of the furnace for the 20° overport fired flame.
a. NO contours from simulation, with points of measurement of NG7. (Contour values: 100, 500, 600, 700 and 800 ppm.)
b. Measured NO concentrations (in ppm) in IFRF furnace.

Thus, for a good estimate of the flame temperature it seems necessary to use a position dependent emissivity, in which the soot concentration would play an important role. This, however, is beyond the scope of this thesis.

The oxygen concentration distribution, shown in figure 7.20, is predicted with good accuracy. The oxygen concentration in the recirculation zone is 2 - 5 % (mass fraction), which means that the recirculation consists of recirculated combustion air and intermediate combustion products. The predicted NO_x concentration distribution (figure 7.21) follows the temperature distribution in the furnace. The highest NO_x concentrations are found in the region with the highest temperatures, where still some oxygen is present for the Zel'dovich reactions. A plot of the NO_x formation velocity in the symmetry plane of the furnace is shown in figure 7.22. Clearly, the zone with temperatures above 2100 K determines the NO_x formation for this flame.

The other simulated overport flames agree better with their measured counterparts. Since the flames with higher mixing angles have faster and better combustion

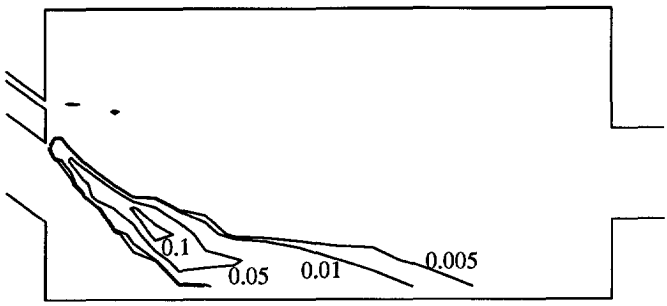

Figure 7.22: Computed NO source term in the symmetry plane of the furnace for the 20° overport fired flame. Contour values: 0.1, 0.05, 0.01 and 0.005 mole/s.

than the flame with parallel natural gas - combustion air injection, we would expect this. Faster burning flames have more flow mixing and less soot formation and our grey gas radiative heat transfer model gives better results for these flames. Therefore our temperature predictions and consequently also our NO_x emission predictions are more accurate, as is seen from the results in table 7.5[a,b].

7.4.2 Combined underport-overport firing

In the underport-overport fired flames the natural gas injection is partitioned between the two burner ports under and above the combustion air port. The effect of combined underport-overport firing was expected to lie in the injection of natural gas in the self-induced flue gas recirculation zone in the upper half of the furnace. This was expected to have a fuel staging effect, thereby decreasing the furnace temperature and thus the NO_x formation. As an example the temperature distribution is shown in a number of sections of the furnace in figure 7.23 for the underport-overport flame with equal partitioning between the underport and the overport injection. One can clearly see the two flames emerging from the underport and the overport injectors, later combining to form one flame. The temperature distribution is a mixture between the underport flame of figure 7.13 and the overport flame of figure 7.14.

The distribution ratio of the natural gas over the two burner ports has been varied in both the measurements and the simulations. The variation of the distribution ratio can be done in two ways with different effect on the gas velocity, viz.

- constant injector diameter, thus varying gas injection velocities.
- varying injector diameter, with constant gas injection velocities.

In the simulations we have applied the constant diameter principle, since then one grid can be used for all simulations. The choice of this velocity criterion has direct influence on the flow situation in the furnace. In the fully underport or overport situation the gas injection velocity was 250 m/s (gas injection diameter 8.4 mm). The gas

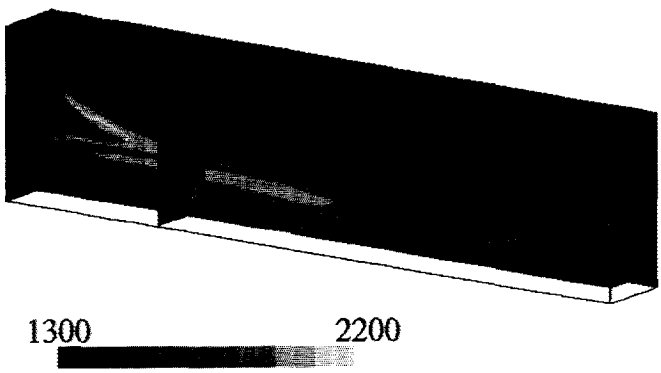

Figure 7.23: Grey-scale plot of the temperature (in K) in the furnace in the underport-overport configuration with an equal distribution of the gas-injection over the two ports (v 860). Shown are a section of the symmetry plane, two vertical cross-sections and a horizontal section.

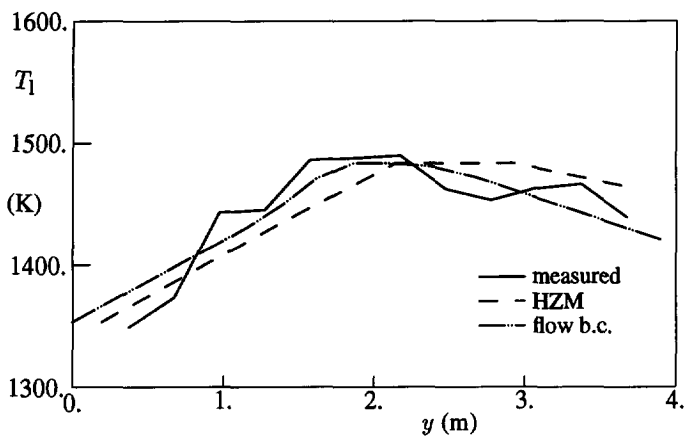

Figure 7.24: Measured load temperature of the 50/50 underport/overport fired flame, together with the used boundary conditions.

injection velocity varies linearly with the distribution ratio. Because of the high injection velocities we have not done the simulations of the fully underport or the fully overport fired flames. We have simulated underport-overport ratios of 75% - 25%, 50% - 50% and 25% - 75%. As the standard configuration for the simulations of the underport-overport fired flames, we have used 30° overport injection and 16° underport injection.

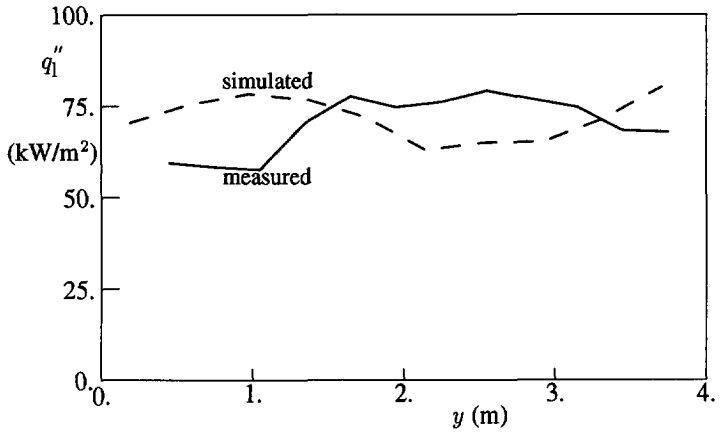

Figure 7.25: Measured and simulated heat transfer to the load for the 50/50 underport/overport fired flame with 30° overport and 16° underport injection.

Heat transfer results As with the overport fired flames the measured load temperatures were used for the simulations. For the flame with an underport/overport ratio of 50/50 the measured load temperature and the used boundary conditions for both the Hottel zone model and the flow model are shown in figure 7.24. The resulting heat transfer to the load is shown in figure 7.25. In the beginning of the flame the computed heat transfer is higher than was measured, as could be expected given the low temperature of the load that was applied as the boundary condition. From 1.5 m onwards the the predictions and the measurements are similar. Other results for the underport/overport flames can be found in table 7.6b for the measurements and table 7.6a for the simulations. The flue gas temperatures are in good agreement, again with the remark that for the simulations the average flue gas temperature is given. The load efficiencies for the underport/overport flames are in the same range as those of the already presented underport and overport flames. There is little variation for the varying underport/overport distribution ratios. There is a small difference between the measured and predicted load efficiencies, probably due to the claim of very low wall heat losses by the IFRF.

NO_x emission results The results of the simulated underport-overport fired flames are listed in table 7.6a. The predicted NO_x emissions differ from the measured NO_x emissions (see figure 7.26) only a little bit. In the measured results a weak minimum around the equal distribution between overport and underport fired natural gas is found. Towards the flames with high overport ratios, a strong increase of the NO_x emission is found. This can be explained by regarding the mixing of natural gas and combustion air for these flames. At the higher overport gas injection velocities the mixing between natural gas and combustion air is increased, thereby increasing the local temperature.

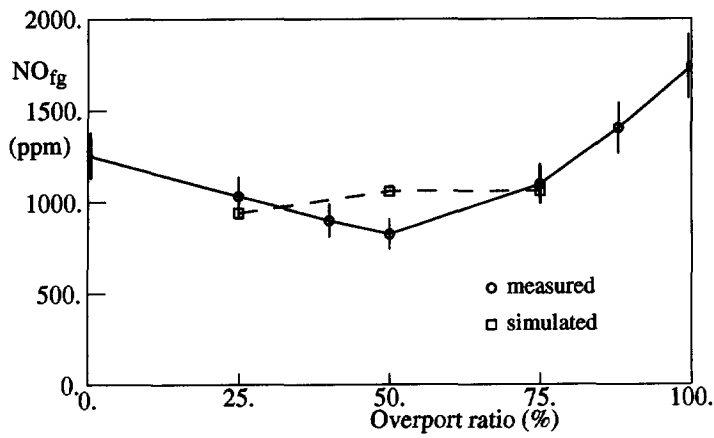

Figure 7.26: Measured and simulated NO_x emissions as a function of the distribution ratio for the underport-overport fired flames with an overport angle of 30° and underport angle 16°. For the measured results the ± 10 % accuracy interval has been indicated.

The flame develops near the inlet, because of the angles of the overport natural gas injection and the combustion air injection, so that there is oxygen available for the NO formation.

Flames with a high overport ratio were not simulated because of the high natural gas injection velocities (at 75 % overport firing the gas injection velocity already becomes 188 m/s). The cases that were simulated agree reasonably well with the measurements, but in the range that was simulated the NO_x emissions are almost constant for the different underport/overport ratios. Because of the limited effect on the NO_x emission, at the lower overport ratios, and because of the measurement errors, the expected effect of fuel staging is not very clear.

7.4.3 Sideport firing

Until now we have discussed flames emerging from a point in the symmetry plane of the furnace. This position of the natural gas injection influences the flame development considerably, as will be shown for the sideport and the parallel-sideport fired flames. These two kinds of flames are generated by injecting the natural gas into the furnace sideways from the combustion air. With sideport firing the natural gas is injected into the combustion air channel, so that two flames start to develop from the side of this channel. Depending on the gas injection velocity and the injection angle these two flames later combine in the furnace forming one flame. Because of the injection of the natural gas directly into the combustion air a well controllable flame exists. In industry this type of flame is commonplace, because of the good control of the combustion process. A disadvantage of this injection method is the high flame temperature that arises by the fast mixing. The NO_x emissions are quite high and this requires further investigations

Table 7.6a: Results of simulations of underport-overport fired flames with the complete model: variation of the underport/overport ratio.

	v 861	v 860	v 862
input			
UP/OP ratio	75/25	50/50	25/75
T_{air} (K)	1373	1373	1373
λ	1.0994	1.0994	1.0994
output			
T_{max} (K)	2389	2406	2332
$\overline{T}$ (K)	1709	1712	1708
T_{fg} (K)	1778	1740	1693
NO_{fg} (ppm)	911	1031	1031
$\overline{q_l''}$ (kW/m^2)	68.3	71.4	74.6
η_l (%)	47.3	49.5	51.6
η_f (%)	68.6	70.6	73.5
$M_{e,max}$ (%)	131.8	95.5	105.1

Table 7.6b: Results of measured flames of the NG7 trials: variation of the distribution ratio (underport/overport firing).

	% UP/% OP					
	75/25	60/40	50/50	25/75	13/87	0/100
T_{fg} (K)	1713	1709	1754	1709	1680	1696
η (%)	51.4	-	51.6	51.0	52.6	52.0
λ	1.095	1.095	1.1005	1.095	1.0895	1.106
NO_{fg} (ppm)	1003	871	796	1068	1374	1710
CO_{fg} (ppm)	50	49	140	49	44	47
$T_{roof,m}$ (K)	1613	-	1572	1613	1576	1585
$T_{load,m}$ (K)	1469	-	1490	1474	1498	1507

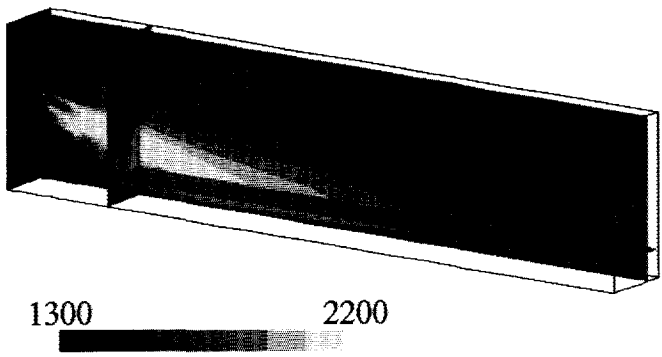

Figure 7.27: Grey-scale plot of the temperature (in K) in the furnace in the sideport configuration with a horizontal mixing angle of 30° (v 881). Shown are a section of the symmetry plane, two vertical cross-sections and a horizontal section.

of the sideport and parallel-sideport firing modes. The temperature distribution in a number of sections of the furnace is shown in figure 7.27 for the sideport flame with a 30° horizontal mixing angle. In this figure the result of fast mixing can be observed in the short and compact flame in the first part of the furnace, which has a relatively high temperature.

In the sideport flames the natural gas was injected with a 20° angle downwards, which is parallel with the combustion air. The horizontal mixing angle was varied between 22° and 57° in the measurements, but in the simulations only three flames were tested viz. with 22°, 30° and 45° injection. The natural gas injection velocity was kept at 125 m/s, so that these flames can be compared with the flames in the other injection modes.

Heat transfer results The influence of the injection into the air channel can be seen in table 7.7a in the highest temperature in the furnace, that is a result of the simulations. For the three simulated sideport flames these temperatures are 2480 - 2490 K in the flame region. This is at least 50 K higher than for the other flames, even in the case of overport firing with the natural gas injected 50° downwards, directly into the air stream. In other respects the sideport flames are similar with the other simulated flames. E.g. the flue gas temperatures are approximately 1660 K, which we have encountered in other underport and overport flames as well.

The heat transfer to the load is also not very different from other flames. The measured heat fluxes are shown in figure 7.28 and the simulated in figure 7.29. Only in the first part of the furnace there are again some differences between the measured and the simulated results, further downstream they are very similar. The efficiencies that are computed from the simulated results are somewhat lower (about 4 %) than the measured efficiencies. As was remarked before, this is probably due to the estimate of

Table 7.7a: Results of simulations of sideport fired flames with the complete model with an injection velocity of 125 m/s: variation of the horizontal injection angle.

	v 882	v 881	v 880
input			
δ (°)	22	30	45
T_{air} (K)	1373	1373	1373
λ	1.1006	1.1006	1.1006
output			
T_{max} (K)	2492	2484	2490
$\overline{T}$ (K)	1732	1743	1753
T_{fg} (K)	1650	1665	1667
NO_{fg} (ppm)	2094	2253	2250
$\overline{q_l''}$ (kW/m^2)	65.4	66.6	65.8
η_l (%)	48.7	49.7	49.0
η_f (%)	78.6	76.7	76.9
$M_{e,max}$ (%)	93.4	97.4	93.4

Table 7.7b: Results of measured flames of the NG7 trials: variation of the mixing angle (sideport firing).

	δ (°)		
	22	30	45
T_{fg} (K)	1711	1703	1682
η (%)	53.2	53.4	53.8
λ	1.095	1.095	1.1005
NO_{fg} (ppm)	1494	1844	2233
CO_{fg} (ppm)	88	55	47
$T_{roof,m}$ (K)	1572	1581	1580
$T_{load,m}$ (K)	1521	1537	1544

the heat loss to the wall by the IFRF. Results of simulations and measurements of the sideport fired flames are listed in table 7.7a and 7.7b respectively.

NO_x emission results The NO_x emissions (listed in table 7.7a) of the simulations show only a slight injection angle dependence. For the measurements at 125 m/s some dependence was found of the NO_x emission on the gas injection angle (see table 7.7b), but at lower injection velocities hardly any dependence was found (see figure 5.13).

At the lower angles, the numerical model over-predicts the combustion rate which results in the difference in NO_x emission of 1500 ppm for the measurements and 2100 ppm for the simulations. At the higher angles the mixing due to the flow is faster and the differences between the measurements and the simulations are smaller.

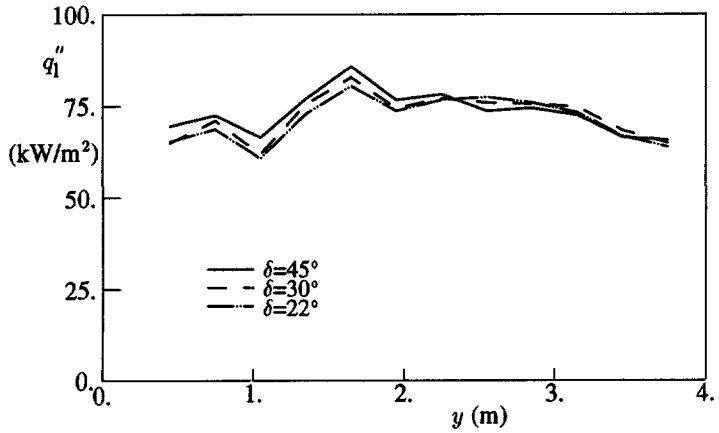

Figure 7.28: Measured heat transfer to the load of sideport fired flames with v_{gas} = 125 m/s.

The high NO_x emissions can be attributed to the forced mixing in the combustion air channel that leads to the already noted high maximum temperatures. The small differences between the simulated flames can be explained by viewing the temperature distribution in the furnace. As an example the temperature distribution in the plane next to the wall of the combustion air channel is shown in figure 7.30 for the three sideport flames. It appears from this figure that the mixing is so fast for all three mixing angles that the temperature distributions are hardly influenced. Consequently

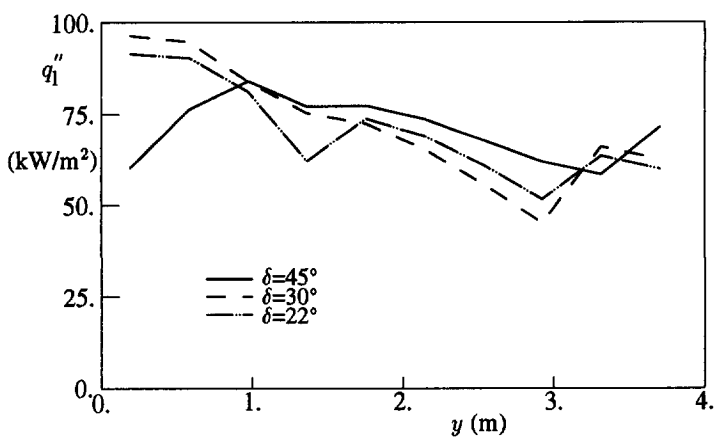

Figure 7.29: Simulated heat transfer to the load of sideport fired flames with v_{gas} = 125 m/s.

the NO_x emissions are nearly the same for these flames. For the 22° flame, with a somewhat lower NO_x emission, the temperature distribution is very much like the two other flames. The difference in the NO_x formation here lie in the oxygen concentration distribution, that also has an important influence on the NO_x formation.

7.4.4 Parallel sideport firing

With sideport firing the natural gas is injected directly into the combustion air. This forces fast mixing and the result is a high flame temperature and consequently a high NO_x emission. A variation of sideport firing is the so-called parallel sideport firing. Here the natural gas is not injected into the combustion air channel, but into the furnace from beside the combustion air channel (see figure 5.8 for the placement of the parallel sideport burners). The injection into the furnace and not into the air channel ensures delayed mixing of combustion air and natural gas. This is illustrated in figure 7.31 in which the temperature distribution is shown for the parallel sideport fired flame with a horizontal injection angle of 20° at otherwise standard NG7 conditions. The slow mixing is observed through the absence of the high temperature region that was found for the sideport fired flame in figure 7.27.

When firing from the parallel sideport burner it is possible to vary both the horizontal and the vertical angle. In the case of a very small vertical angle the mixing is extremely slow, like the overport flame with injection of the natural gas parallel to the combustion air. In the case of larger angles a certain degree of mixing is forced, because the natural gas is then directed towards the combustion air stream. The simulations were performed for a vertical angle of 16° downwards, to ensure good mixing at the larger horizontal angles.

Three horizontal angles were tested, viz. 10°, 20° and 30°. The gas injection velocity was kept at 125 m/s as for most of the other flames.

Heat transfer results It was already remarked in the discussion of the measured parallel sideport flames that these flames are in general less efficient than flames in the other firing modes. Also, due to the slow mixing low NO_x levels but relatively high CO levels were measured in the flue gas. The flames that we have simulated, with a vertical angle of -16° and a gas injection velocity of 125 m/s do not differ very much from the flames in other firing modes. This is due to the mixing that is ensured by our choice of gas injection angle and velocity.

The heat transfer to the load, shown for both the simulations and the measurements in figure 7.33 is in the same range as e.g. the underport flames. In the computed heat flux the influence of the temperature boundary condition is clearly visible. The measured load temperature in the first two Hottel zones is at least 50 K lower than in the rest of the furnace. This causes the peak heat transfer in the beginning of the flame.

The efficiency of the flames is almost constant for the different horizontal injection angles (see tables 7.8b and 7.8a for respectively the measurements and the simulations). Between the simulated and the measured results there is a difference of

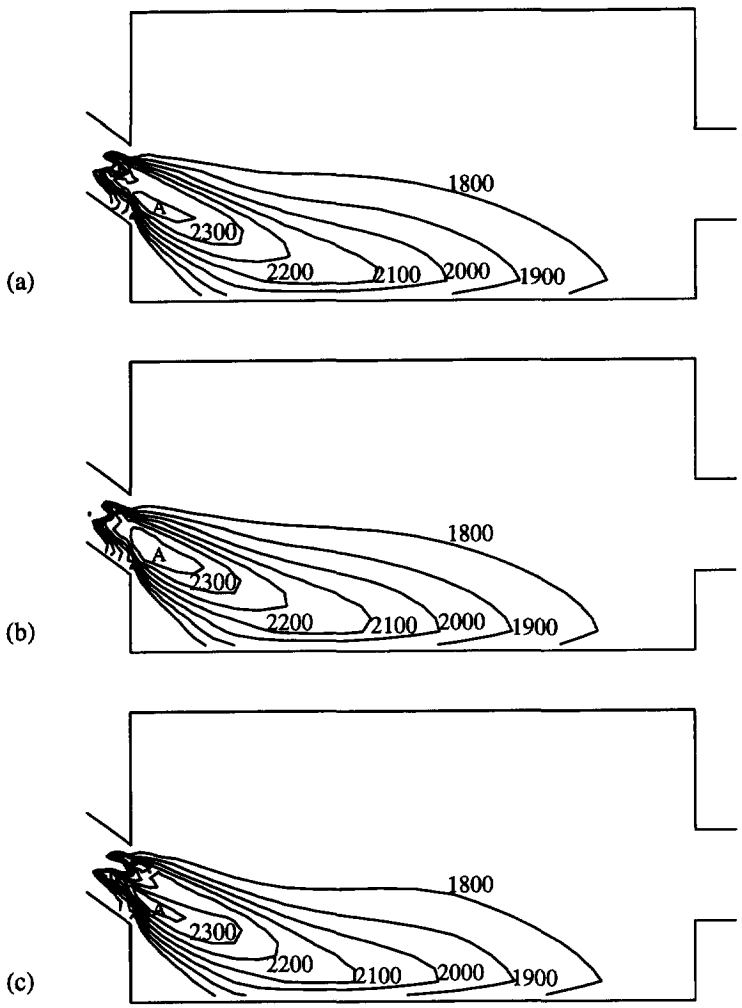

Figure 7.30: Contours of the temperature in the plane next to the wall of the combustion air channel for the sideport fired flames with $\lambda = 1.1$ and $T_{air} = 1373$ K. Contour values: 1800, 1900, 2000, 2100, 2200, 2300 and 2400 K. The 2400 K contour is indicated in the figures with an A.
a. 45° horizontal mixing angle (v880), b. 30° horizontal mixing angle (v881), c. 22° horizontal mixing angle (v882).

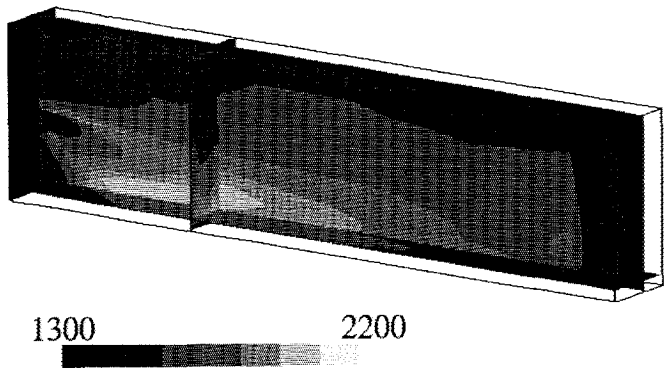

Figure 7.31: Grey-scale plot of the temperature (in K) in the furnace in the parallel-sideport configuration with a horizontal mixing angle of 20° (v 840). Shown are a section of the symmetry plane, two vertical cross-sections and a horizontal section.

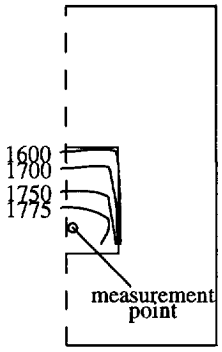

Figure 7.32: Temperature contours in the outflow plane of the furnace for the parallel-sideport fired flame with 30° horizontal mixing angle. The point of measurement is indicated. Contour values 1600, 1700, 1750 and 1775 K.

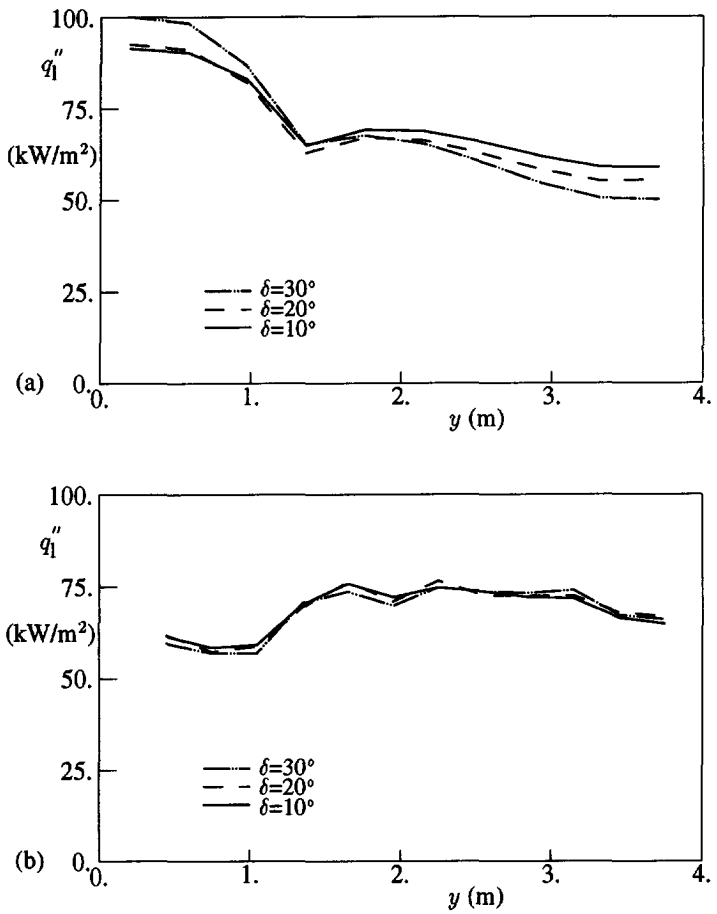

Figure 7.33: Simulated and measured heat transfer to the load of parallel sideport fired flames with v_{gas} = 125 m/s for several horizontal injection angles.
a. Results of simulations, b. Results of measurements.

Table 7.8a: Results of simulations of parallel-sideport fired flames with the complete model with an injection velocity of 125 m/s.

	v 841	v 840	v 842
input			
δ (°)	10	20	30
T_{air} (K)	1373	1373	1373
λ	1.0995	1.0995	1.0995
output			
T_{max} (K)	2343	2326	2309
$\overline{T}$ (K)	1716	1710	1713
T_{fg} (K)	1687	1676	1649
NO_{fg} (ppm)	1398	1253	1127
$\overline{q_l''}$ (kW/m^2)	71.1	69.1	69.6
η_l (%)	49.3	47.9	48.2
η_f (%)	73.9	74.5	76.0
$M_{e,max}$ (%)	85.8	85.9	81.8

about 2 %. The computed flue gas temperature seems to deviate from the measured result quite a lot. There is however a rather steep temperature gradient in the outflow plane, which accounts for this error. In figure 7.32 temperature contours, ranging from 1600 K to 1775 K, are shown in the outflow plane. It is clear that the point of measurement influences the result that is reported by the IFRF. The point of measurement, approximately in the symmetry plane at a height of 0.34 m above the load, has been indicated in figure 7.32. In the simulations this is just in the high temperature region in the outflow, where the computed temperature is in the range of the reported flue gas temperature.

NO_x emission results In the measurements of the parallel sideport flames the NO_x emission increased with an increasing horizontal injection angle. Between 10° and 26° the emission ranged from 450 - 1000 ppm. In the simulations a small decrease of the NO_x emission was predicted for increasing injection angles. The simulated values of the NO_x emission are 1400 - 1100 ppm. Especially at the lowest injection angle there is a large difference between the measurements and the simulations. At 20° and 30° the measurements and the simulations agree very well (see tables 7.8b and 7.8a). At 10°, however, 450 ppm was measured and 1400 ppm predicted. This large difference is probably due to the mixing velocity. At 10° the mixing between natural gas and combustion air is relatively slow. As we have seen before, e.g. the overport flame with parallel natural gas and combustion air injection, the numerical model then overestimates the combustion velocity at the interface between natural gas and combustion air, probably due to numerical diffusion. At this interface locally high temperatures arise, while there is still oxygen available in the combustion air stream.

Table 7.8b: Results of measured flames of the NG7 trials: variation of the horizontal injection angle at the 16° vertical injection angle (parallel-sideport firing).

	δ (°)			
	10	15	20	26
T_{fg} (K)	1755	1763	1759	1759
η (%)	53.4	49.6	50.4	50.6
λ	1.106	1.1005	1.095	1.1005
NO_{fg} (ppm)	451	667	1016	995
CO_{fg} (ppm)	119	112	160	200
$T_{roof,m}$ (K)	1572	1567	1563	1567
$T_{load,m}$ (K)	1503	1494	1498	1498

Thus, here much NO_x is formed, which results in the high simulated NO_x emission. At the higher mixing angles the combustion products are mixed with the relatively cold air stream, which results in lower local temperatures. This is supported by the simulated maximum flame temperature that is listed in table 7.8a. For the lowest injection angle the highest maximum flame temperature is predicted.

7.5 Final remarks on the NG7 simulations

For the simulations of the NG7 configurations some model improvements were incorporated. These include a simple CO formation model and an extended pdf model for the NO source term computation.

First the influence of the improvements was tested for the underport fired flames with varying mixing angle. The incorporation of the CO formation model resulted in lower flame temperatures and consequently in lower NO_x emissions. The reduction of the NO_x emission due to the lower furnace temperature was the same for the three tested mixing angles. The pdf model for the NO source term had a different effect on the different flames. The predicted trend of increasing NO_x emissions at increasing mixing angles was weakened for the underport flames. On average the agreement with the measured results was better.

The improved model was called the complete model. With this complete model simulations of the NG7 experiments with different firing modes have been performed. For these simulations the measured boundary conditions of the NG7 experiments were used. The measured load temperature in the first two segments of the furnace caused us some doubt, because they were (more than) 50 K lower than the load temperature in the rest of the furnace. With this measured load temperature as the boundary condition for our simulations the predicted heat flux to the load was higher than measured in the beginning of the furnace. With an adapted temperature boundary condition the predicted heat flux to the load was in much better agreement with the measured results. Since the other properties, including the NO_x emission, were hardly influenced by this

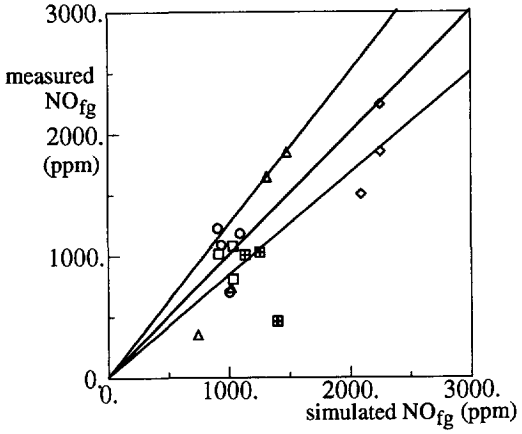

Figure 7.34: Comparison of the simulated and the measured NO_x emissions of the NG7 trials. The circles correspond with the underport flames, triangles with the overport flames, squares with the underport/overport flames, diamonds with the sideport flames and squares with cross with parallel sideport flames. Also shown are the $\pm$ 20 % deviation lines.

variation, the parameter variations of the NG7 experiments were simulated with the measured load temperature as the boundary condition.

The main part of the NG7 simulations was concerned with the burner geometry variations and the variation of the mixing angle. For the combined underport/overport flames the underport/overport ratio was varied at fixed injection angles. The burner geometry variations resulted in different flow situations in the furnace, with a different influence of the mixing parameters on the NO_x emission.

As an example of the different flow for each of the burner configurations grey-scale plots of the temperature have been shown in figures 7.13, 7.14, 7.23, 7.27 and 7.31 for respectively underport, overport, combined underport-overport, sideport and parallel-sideport firing. In each of these plots the vertical section in the length of the furnace has been chosen in the plane of the natural gas injection port, so that the (cold) natural gas injection and the shape of the flame is visible. It is obvious from these plots that each burner position gives a different flow situation. Due to the differing mixing intensities caused by the position of the burner different temperature and species concentration distributions arise. This leads to NO_x emissions, that are not only different at standard conditions (125 m/s gas-injection velocity, standard mixing angles for each burner), but also to a different dependence on the mixing parameters.

In general, the properties that are mainly determined by the radiative heat exchange model, such as the heat flux to the load, the efficiency and the flue gas temper-

ature are predicted in good agreement with the measured results. The NO_x emissions are predicted more accurately for the NG7 trials than for the NG6 trials. This can be seen in figure 7.34, in which the simulated and the measured NO_x emissions for corresponding flames have been plotted against each other. The largest discrepancies arise in the flow configurations where the mixing between natural gas and combustion air will be slow. This was already remarked for the NG6 simulations, but also in the case of e.g. the overport flames the parallel injection of natural gas and combustion air leads to over-predictions of the combustion velocity and the flame temperature. For the slowly mixing flames the predicted NO_x emissions are generally too high. The code probably leads to numerical diffusion and to large mixing in the first part of the flame. Implementing the semi-analytical solution of a free jet with combustion is expected to lead to improvements of the numerical code for the first part of the flame. Also, for the slowly mixing flames soot formation was observed by the IFRF. With the implementation of soot formation also improvements of the simulations can be expected. However, if we disregard these results, the combustion is predicted correctly and the resulting NO_x emissions are generally spoken in good agreement with the measured results, with maximum deviations of 20 %.

Chapter 8

General conclusions

The aim of this study has been to assess the influence of several parameters on combustion and NO_x formation in a high temperature furnace as applied in the glass industry. To achieve this aim simulations were performed of the flow, combustion, radiative heat transfer and the NO_x formation in the geometry of IFRF furnace no. 2 for the NG6 and NG7 trials. First some conclusions will be drawn on the validation of the numerical model. Then we will discuss the results concerning the NO_x emissions and the effect of mixing on the NO_x formation.

8.1 Validation of the numerical model

It is imperative for the discussion of the results of the numerical model, that the predictions of the model are verified with reliable measured data. In this thesis verification was achieved for an isothermal scale model of the IFRF furnace and for many measured flames in the IFRF furnace itself.

An isothermal scale model of the IFRF furnace was used for flow visualization and measurements of the axial velocity and of the distribution of the concentration of a tracer species in the symmetry plane of the scale model. The measured data were compared with the results of isothermal simulations of the scale model and were also compared with the semi-analytical solution of a free jet. In a burner configuration with a small mixing angle good agreement between the simulations and the measurements was achieved for the flow and the mixing. At a larger mixing angle the results differ more but they are still satisfactory. From the comparison with the semi-analytical solution it was concluded that applying the solution of the initial part of a developing free jet as a boundary condition in the furnace may be beneficial for the simulations.

In a sensitivity analysis of the model for several of the parameters of the model and for unknown boundary conditions it was decided that a small amount of precombustion should be used to achieve good predictions of the flame jet development. The influence of other parameters was tested and the results were verified against the baseline flames of the NG6 investigation. The estimates of e.g. the extinction coefficient were validated using the measured heat flux to the load and other measured data. These parameters were kept fixed during the rest of the simulations described in this thesis.

During the initial stages of the numerical work grid (in)dependence of the solution of the numerical model for the baseline flame was determined. It was concluded that full grid independence had not yet been achieved, but that the differences to results with a finer mesh were sufficiently small for the $18 \times 26 \times 22$ grid to be used for the simulations. This is still a fairly coarse grid, but it was argued that a fine mesh capable of giving accurate solutions of the jet development would require too much computer time to be practical for our engineering purposes. Therefore it was decided to use a partially precombusted jet as boundary condition, as this gave solutions that were similar to the measured results, and not to use a finer mesh which would require much more computer time.

Verification of the simulation model in the case of combustion in the high temperature IFRF furnace was achieved for many measured flames. Two trials, viz. NG6 and NG7, have been described and the important characteristics of the flames have been given. A comparison of the measured and the simulated flames was performed for the heat transfer results and the furnace performance for both series. For the general performance the following parameters were compared: T_{fg}, η_f, η_l and q_l''. Also, in-flame measurements of the temperature and the oxygen and NO concentration in the symmetry plane of the IFRF furnace were compared with the simulated distributions in the symmetry plane.

- For both trials the measured temperature at the suction point was compared with the average flue gas temperature that was a result of the simulations. The highest differences between these two results were approximately 100 K, but in general the differences were less than 50 K. It was argued that the use of the average flue gas temperature from the simulations is deceptive. In the outflow plane a temperature distribution was found in the simulations. On comparison of the simulated flue gas temperature in the suction point with the measured flue gas temperature the observed difference is much smaller. In this case the differences are at most 50 K for all flames. Since the measurement error was assumed by us to be 100 K, we conclude that there is excellent agreement between the flue gas temperature predictions and measurements.
- The IFRF furnace temperature was 200 K lower during the NG7 investigations than during NG6. This resulted in a higher heat transfer to the load and a higher *load* efficiency.
  - The flames from NG6 had an efficiency between 43 – 47 % at baseline conditions, i.e. at 1373 K combustion air temperature and 10 % excess air. The variations of the NG6 trials did not give a clear trend for the mixing parameters or the excess air level. Only the combustion air temperature had a clear influence on the load efficiency, viz. 35 % at 1073 K, 45 % at 1373 K and 50 % at 1573 K. The simulated and measured load efficiencies are very similar, the differences are at most 3 %.
  - The NG7 flames had an efficiency between 49 – 54 %, when all measured data are taken into account. The results of the simulations are very similar, viz. 48 – 52 %. There are only small differences for the different burner

geometries, where in the measurements e.g. the sideport fired flames seemed more efficient than the parallel sideport fired flames. For the different mixing angles that were discussed in this thesis no particular trend was found, neither in the measurements nor in the simulations.

The differences between the measurements and the simulations that arise when the load efficiencies are compared may be attributed at least partly to the estimate of the wall and roof heat losses by the IFRF. The IFRF only measured the heat loss through a cooling loop, completely surrounding the furnace, and applied an estimated heat loss of 3 kW/m^2 for the roof and the walls. This estimated heat loss was subtracted from the measured heat loss through one loop, resulting in the heat loss through the load. In our opinion a higher heat loss is more probable, in the range of 5 to 7.5 kW/m^2. This was verified for the NG6 baseline flame. Using a higher wall loss would result in lower heat fluxes to the load and consequently lower load efficiencies.

- The overall *furnace* efficiency is dependent on the flue gas temperature. During NG6 the furnace efficiency was 65 to 70 %, at the baseline temperature. Only for the combustion air temperature variation were clear trends measured, as was also the case for the load efficiency. During NG7 the furnace efficiency was 70 to 75 %. The differences between the measured and simulated overall efficiency are smaller than for the load efficiency. This supports our analysis that the IFRF has underestimated the heat loss to the walls and the roof.
- The heat flux distribution shows some differences between the measurements and the simulations for all flames for both trials. For the NG6 trials the load temperature has not been measured for most flames, because the thermocouples had broken down. We have used an estimated load temperature profile for the simulations. In the first part of the flame the agreement between measurements and simulations is good. Only for flames where slow mixing and a slow flame development could be expected, the model over-predicts the combustion rate in some cases and consequently also the heat transfer to the load. At the end of the furnace, however, the measured heat flux decreases, while the predictions display an increase. This is most probably caused by the temperature boundary condition in the outflow plane. The influence of the chimney could not reasonably be accounted for in the simulations, which has probably caused our use of a too high back wall temperature and consequently too low heat losses to the back wall. This difference has not resulted in serious discrepancies for other properties, so that this point was assumed of minor importance for the accuracy of the simulations. During the NG7 trials the load temperature was measured for each flame. It was concluded, however, that in the first two sections of the furnace the measured load temperature was systematically too low. In the simulations this gives rise to an increased heat flux in the first part of the flame. Further downstream the simulated heat flux was generally lower than was measured by the IFRF. At the end of the furnace the same discrepancy as for the NG6 trials was found, viz. predictions of the heat flux that are too high compared with the

measured results.

- The in-flame measurements showed differences between the measurements and the simulations. For the NG6 (underport fired) 20°-12° flame it was shown that the oxygen concentration prediction in the recirculation was too low. However, since the temperature of the recirculation is not very high this does not influence the predicted NO_x emission. For the NG7 overport fired flame with parallel injection of natural gas and combustion air in-flame measurements have also been performed. The predicted oxygen concentration distribution agreed very well with the measured oxygen concentration distribution, but the temperatures displayed large differences. The model over-predicts the combustion rate for this flame, which results in much higher flame temperatures. Also, the NO_x concentration displayed large differences due to the temperature predictions.

The NO_x emissions were computed with reasonable accuracy. For the flames of the NG6 investigation the discrepancies between the measurements and the simulations are larger than for NG7. This is a result of the model improvements that were carried out in-between the two trials. Overall, the NO_x emissions ranged from 500 to 2800 ppm for the NG6 investigation, where the limits were set by the combustion air temperature variation. In NG7 the NO_x emissions ranged from 400 to 2200 ppm for the measurements and the simulations. Here, sideport firing gave the upper limit and overport firing with parallel injection of natural gas and combustion air the lower.

The largest differences in NO_x emission between the measurements and the simulations arose when the mixing between fuel and air and the combustion of the fuel were expected to be slow. For this kind of flame it was found that the simulation model over-predicts the combustion rate and that the flame temperature and the NO_x emission are too high. Partly this may be attributed to the numerical diffusion that is found with the fairly coarse grid that we have used. For the other flames, however, the differences for the NG7 flames were shown to be at most some 20 % of the measured NO_x emission. For the NG6 flames the differences are larger in a few cases, especially for the mixing angle variation and the flames with a low excess air level. The mixing angle result was disregarded, because of the repeated variation during NG7 where good agreement was found. For low excess air levels it was concluded that the model is no longer applicable.

The limits of the applicability of the model that we find from the comparison between the measured and the simulated results may be summarized as follows.

- There should be some excess air, not less than 5 %.
- At mixing angles or injection positions where one would expect very slow mixing, the numerical model over-predicts the combustion rate. However, a drawback of these slowly mixing flames is the high CO level which was measured by the IFRF, which makes these flames less applicable in practice.
- Very high gas-injection velocities demand a finer mesh than was used for this thesis.

The IFRF furnace was operated under such conditions that the predominant NO_x

formation route was the thermal NO_x formation that was modelled for this thesis. Less hot furnaces may demand the inclusion of a prompt NO_x model.

Further improvement of the results of the simulations may be achieved in a number of ways. A finer mesh reduces the numerical diffusion, so that the predictions of slowly mixing flames become more accurate. Also, for the slowly mixing flames soot formation may be important. Incorporation of soot formation requires the use of a radiative heat transfer model with a position dependent extinction coefficient. The discrete transfer model is suitable for this kind of calculations. In this thesis we have used a partially precombusted natural gas jet as the inflow condition for the furnace. It may be beneficial to use the semi-analytical solution of a free jet as the boundary condition, as was found from the isothermal measurements in the scale model.

With the model that we have used in this thesis, however, it is already possible to make reasonable predictions of the NO_x emission of furnaces. The differences between the measured and simulated NO_x emissions are at most 20 %. The model is suitable for trend studies in a furnace and can be used to predict the effect of burner geometry variations.

8.2 The effect of mixing on the NO_x emission

In the introduction two aims of this thesis were stated concerning the mixing in the furnace and its influence on the NO_x formation. It was already argued in the theoretical analysis of the flow and the combustion in the furnace, that the mixing was expected to have a distinct influence on the combustion. Because the combustion is determined by the rate of mixing of fuel and air in this type of flame, fast mixing gives rise to fast combustion and consequently a high flame temperature. The thermal NO_x formation is strongly temperature dependent and generally spoken follows the temperature predictions.

To assess the influence of mixing, we will now regard the results for the different burner configurations as they were obtained for NG7.

The sideport flames are generally the fastest mixing flames. The natural gas is injected directly into the air stream, and fast combustion is observed. E.g. the heat transfer to the load in the beginning of the furnace is higher than for the other flames. The maximum temperature that resulted from the simulations is also much higher than for the other flames, except for the very fast mixing overport flame with high mixing angle. The resulting NO_x emissions are generally higher than for the other flames (up to 2200 ppm).

The overport flames very clearly display the influence of both the mixing angle and the general flow direction. At the parallel injection of natural gas and combustion air a slowly mixing flame is found. The mixing is so slow that complete burnout is not achieved and the CO level in the flue gas is unacceptably high. For the flames with the higher mixing angles a steep increase of the NO_x emission is found. Here, the direction of both the natural gas flow and the combustion air flow play an important role, since

they are oriented in the same direction, viz. towards the load. Here the mixing is not only forced by the mixing angle, but also by the fact that the natural gas is forced to mix with combustion air only. The result for this flame is a high NO_x emission (1500 ppm).

The underport flames are injected into the furnace with mixing angles between the natural gas and the combustion air injection that were used for the overport flames as well. However, for these flames the natural gas not only mixes with combustion air but with recirculated combustion gases as well. This results in much lower temperatures than for the overport flames with the same mixing angle and consequently in lower NO_x emissions (approximately 1000 ppm). However, the tested underport flames did not delay the mixing as long as the parallel injected overport flame. The very low NO_x emission for this overport flame could thus not be reproduced for the underport flames with a low mixing angle.

The combined underport/overport injection showed little effect of the underport/overport ratio on the NO_x emission in the range that was simulated. In the simulations a small increase of the highest flame temperature was observed, because of the two flames that melt into one in the furnace. The mixing of the natural gas follows the same pattern as for the underport fired flames, only at a slightly higher temperature. The predicted NO_x emission is also somewhat higher.

Due to the position of the natural gas injection port and the angles at which the natural gas is injected into the furnace, the parallel sideport flames are, generally spoken, the flames with the lowest NO_x emission. For the high injection velocity that was used in the simulations, the mixing is not quite as slow as for the lower velocities. The corresponding flame temperatures are therefore also quite high, which results in the average NO_x emissions for the simulated flames (approximately 1200 ppm).

The influence of the gas-injection velocity is dependent on the burner position. For the underport flames a higher velocity results in increased mixing with the combustion air and the recirculated gases. There is little effect on the NO_x emission (cf. NG6 flames) because the increased mixing spreads the temperature peak over a larger volume. Thus, only a small effect of the velocity on the NO_x emission is found. For the sideport flames or the overport flames at a high mixing angle an increased gas injection velocity forces mixing of the natural gas with the combustion air. For these flames an increase of the NO_x emission is found.

The questions that we asked ourselves in the introduction can now be answered. The influence of the mixing can be stated in these two points:

- Increased mixing between natural gas and combustion air results in higher flame temperatures and higher NO_x emissions.
- Increased mixing with recirculated gases lowers the flame temperature and the NO_x emission.

The position of the natural gas injection point relative to the combustion air determines whether the natural gas will mix predominantly with combustion air or with recirculated furnace gases. A well placed burner uses recirculated gases to lower the flame temperature, while it is still possible to achieve the required efficiency at the prescribed process conditions.

Appendix A

Pdf shapes

A.1 Double delta pdf

The double-delta pdf is described by:

$$P(f) = \alpha_0\,\delta(f - f_0) + \alpha_1\,\delta(f - f_1) \tag{A.1}$$

The pdf parameters to be determined are α_0, α_1, f_0 and f_1. These parameters can be determined by integration of $P(f)$, $fP(f)$ and $f^2P(f)$ over the interval [0,1].

$$1 = \int_0^1 P(f)df \tag{A.2}$$

$$\overline{f} = \int_0^1 fP(f)df \tag{A.3}$$

$$\overline{f'^2} = \int_0^1 f^2P(f)df - \overline{f}^2 \tag{A.4}$$

Five different cases can be distinguished:

a) $\overline{f'^2} = 0$: No turbulent fluctuations.

The pdf reduces to the single-delta function pdf, which is formally described by,

$$\alpha_0 = \alpha_1 = \frac{1}{2}$$

and

$$f_0 = f_1 = \overline{f}$$

b) $\overline{f'^2} \leq \overline{f}^2$ and $\overline{f'^2} \leq (1 - \overline{f})^2$.

This is the standard case, with no clipping of the pdf at $f = 0$ or $f = 1$. The parameters are

$$\alpha_0 = \alpha_1 = \frac{1}{2}$$

and

$$f_0 = \overline{f} - \sqrt{\overline{f'^2}}\,;\, f_1 = \overline{f} + \sqrt{\overline{f'^2}}$$

c) $\overline{f'^2} > \overline{f}^2$ and $\overline{f'^2} \leq \overline{f}(1-\overline{f})$.
This will only occur if $\overline{f} < \frac{1}{2}$ and the fluctuations are so large that f_0 would become negative. Therefore the pdf is clipped at $f = 0$. The parameters are

$$\alpha_0 = \frac{\overline{f'^2}}{\overline{f'^2} + \overline{f}^2} \; ; \alpha_1 = 1 - \alpha_0 = \frac{\overline{f}^2}{\overline{f'^2} + \overline{f}^2}$$

and

$$f_0 = 0 \; ; f_1 = \overline{f} + \frac{\overline{f'^2}}{\overline{f}}$$

d) $\overline{f'^2} > (1-\overline{f})^2$ and $\overline{f'^2} \leq \overline{f}(1-\overline{f})$.
This will only occur if $\overline{f} > \frac{1}{2}$ and the fluctuations are so large that f_1 would become larger than 1. Therefore the pdf is clipped at $f = 1$. The parameters are

$$\alpha_0 = \frac{(1-\overline{f})^2}{\overline{f'^2} + (1-\overline{f})^2} \; ; \alpha_1 = 1 - \alpha_0 = \frac{\overline{f'^2}}{\overline{f'^2} + (1-\overline{f})^2}$$

and

$$f_0 = \overline{f} - \frac{\overline{f'^2}}{1-\overline{f}} \; ; f_1 = 1$$

e) $\overline{f'^2} > \overline{f}(1-\overline{f})$.
Now the fluctuations are so large that clipping at both ends is needed. The parameters are

$$\alpha_0 = 1 - \overline{f} \; ; \alpha_1 = 1 - \alpha_0 = \overline{f}$$

and

$$f_0 = 0 \; ; f_1 = 1$$

A.2 Top-hat pdf

The top-hat pdf is described by:

$$\begin{aligned} P(f) \;\; = \;\; & \alpha_0 \, \delta(f - f_0) + \alpha_1 \, \delta(f - f_1) \\ & + P_{\text{unif}} \{ H(f - f_0) - H(f - f_1) \} \end{aligned} \tag{A.5}$$

where H is the Heaviside step function, defined as:

$$H(x) = \begin{cases} 0 & \text{for } x < 0 \\ 1 & \text{for } x \geq 0. \end{cases} \tag{A.6}$$

The pdf parameters to be determined are α_0, α_1, f_0, f_1 and P_{unif}. These parameters can be determined by integration of $P(f)$, $fP(f)$ and $f^2P(f)$ over the interval [0,1]. Six different cases can be distinguished:

a) $\overline{f'^2} = 0$: No turbulent fluctuations.
The pdf reduces to the single-delta function pdf, which is formally described by, $P_{\text{unif}} = 0$; $\alpha_0 = \alpha_1 = \frac{1}{2}$; $f_0 = f_1 = \overline{f}$.

b) $\overline{f'^2} \leq \frac{1}{3}\overline{f}^2$: No intermittency effects.
This is the general case where fluctuations are relatively small, giving $\alpha_0 = \alpha_1 = 0$. Applying the normalisation condition yields,

$$P_{\text{unif}}(f_1 - f_0) = 1$$

Furthermore, we have:

$$\overline{f} = \int_{f_0}^{f_1} f P(f) df = \frac{1}{2} P_{\text{unif}}(f_1 - f_0)(f_1 + f_0)$$

Combining these two relationships gives $\overline{f} = \frac{1}{2}(f_0 + f_1)$, as expected. The second moment is written as:

$$\overline{f'^2} = -\overline{f}^2 + P_{\text{unif}} \int_{f_0}^{f_1} f^2 df = -\overline{f}^2 + \frac{1}{3} P_{\text{unif}}(f_1^3 - f_0^3) = \frac{1}{12}(f_0 - f_1)^2$$

This gives:

$$f_0 = \overline{f} - \sqrt{3\overline{f'^2}} \;\; ; \;\; f_1 = \overline{f} + \sqrt{3\overline{f'^2}}$$
$$P_{\text{unif}} = (12\overline{f'^2})^{\frac{1}{2}}$$

c) $\frac{1}{3}\overline{f}^2 \leq \overline{f'^2} < \frac{2}{3}\overline{f} - \overline{f}^2$.
In this case we have intermittency at $f = 0$, but not at $f = 1$. This will only occur if fluctuations are moderately large and $\overline{f} < \frac{1}{2}$. Now we have $f_0 = 0$ and $\alpha_1 = 0$. Applying the three integrations conditions (A.2), (A.3), (A.4), we find:

$$\alpha_0 = \frac{\overline{f'^2} - \frac{1}{3}\overline{f}^2}{\overline{f'^2} + \overline{f}^2}$$

$$f_1 = \frac{2\overline{f}}{1 - \alpha_0}$$

$$P_{\text{unif}} = \frac{1 - \alpha_0}{f_1} = \frac{(1 - \alpha_0)^2}{2\overline{f}}$$

d) $\frac{2}{3}\overline{f} - \overline{f}^2 < \overline{f'^2} < \overline{f} - \overline{f}^2$: Intermittency at both sides.
This will only occur if fluctuations are very large. As a result we have $f_0 = 0$, $f_1 = 1$, with which we obtain:

$$P_{\text{unif}} = 6(\overline{f} - \overline{f}^2 - \overline{f'^2})$$

$$\alpha_0 = 1 - \overline{f} - \frac{1}{2} P_{\text{unif}} \;\; ; \;\; \alpha_1 = \overline{f} - \frac{1}{2} P_{\text{unif}}$$

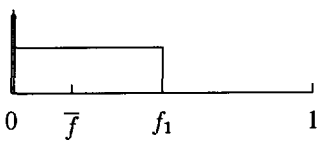

Figure A.1: Top-hat pdf (case **c**)

e) $\overline{f} - \overline{f}^2 \leq \overline{f'^2}$: Fully intermittent flow.
Fluctuations are so large that only delta-spikes near the interval edges remain. This gives $P_{\text{unif}} = 0$, $f_0 = 0$, $f_1 = 1$, $\alpha_0 = 1 - \overline{f}$ and $\alpha_1 = \overline{f}$.

f) $\frac{1}{3}(1-\overline{f})^2 < \overline{f'^2} \leq \frac{4}{3}\overline{f} - \overline{f}^2 - \frac{1}{3}$.
This case is analogous to case c, but now we have $\overline{f} > \frac{1}{2}$ and $\overline{f}$ replaced with $1 - \overline{f}$. Hence, $\alpha_0 = 0$, $f_1 = 1$. Moreover,

$$f_0 = \frac{\frac{3}{2}(\overline{f} - \overline{f}^2 - \overline{f'^2})}{1-\overline{f}} - \frac{1}{2}$$

$$\alpha_1 = 1 - P_{\text{unif}}(1 - f_0) = 1 - 2\frac{1-\overline{f}}{1-f_0}$$

$$P_{\text{unif}} = \frac{2(1-\overline{f})}{(1-f_0)^2}$$

The top-hat distribution is easy to compute numerically. The width of the pdf is known accurately: $f \in [f_0, f_1]$. In most cases the width of this interval will be much smaller than 1. This enables an accurate quadrature without an excessive number of integration intervals. A suitable quadrature scheme is the trapezoidal rule with 50 or 100 integration intervals, which is sufficient for most pdf quadratures.

Appendix B

Properties of the natural gas

B.1 Composition of the fuel and other properties

The natural gas composition in the present study is (volume fraction at 298 K, 1 atm):

CH_4	0.8532
C_2H_6	0.0556
C_3H_8	0.0119
C_4H_{10}	0.0065
N_2	0.0715
CO_2	0.0013

The density of the natural gas at stp is 0.812 kg/m^3.

The lower calorific value of the natural gas is 44.7 MJ/kg. For the fuel we then find a lower calorific value of 49.7 MJ/kg. The stoichiometric mixture fraction $f_{st,1}$ is 0.06204.

The molecular masses of the species that we find in the flow are (in kg/kmole),

CH_4	16.0426
C_2H_6	30.0694
C_3H_8	44.0962
C_4H_{10}	58.1230
N_2	28.0134
CO_2	44.0098
H_2O	18.0152
O_2	31.9988
fuel	17.5624
air	28.8447

B.2 Specific heat at constant pressure

In the present study we have used a temperature dependent specific heat at constant pressure, denoted as $C_{p,i}$, for all constituting species. The mean specific heat in a certain

temperature interval $[T_0, T_1]$ is computed as,

$$\begin{aligned} C_{pm,i} &= \frac{1}{T_1-T_0}\int_{T_0}^{T_1} C_{p,i}(s)ds = \\ &= \frac{1}{T_1-T_0}\left[IC_{p,i}(T_1) - IC_{p,i}(T_0)\right] \end{aligned} \tag{B.1}$$

in which $IC_{p,i}$ is the primitive function of $C_{p,i}$.

The expressions for $IC_{p,i}$ for all species i will be given next. These relations are based on correlations given by Van Wylen and Sonntag (1976) and Tribus (1961).

Air

$$\begin{aligned} IC_{p,\text{air}} &= a_0T + a_1T^2 + a_2T^3 \\ a_0 &= 0.94699648 \cdot 10^3 \\ a_1 &= 0.10665806 \\ a_2 &= -0.10340849 \cdot 10^{-4} \end{aligned} \tag{B.2}$$

Fuel

$$\begin{aligned} IC_{p,\text{fuel}} &= a_0T + a_1T^{1.25} + a_2T^{1.75} + a_3T^{0.5} \\ a_0 &= -4.2054375 \cdot 10^4 \\ a_1 &= 6.9528999 \cdot 10^3 \\ a_2 &= -2.8093449 \cdot 10^1 \\ a_3 &= -4.0485000 \cdot 10^5 \end{aligned} \tag{B.3}$$

Nitrogen

$$\begin{aligned} IC_{p,\text{N}_2} &= a_0T + a_1T^2 + a_2T^3 \\ a_0 &= 0.97561914 \cdot 10^3 \\ a_1 &= 0.11117486 \\ a_2 &= -0.11311742 \cdot 10^{-4} \end{aligned} \tag{B.4}$$

Oxygen

$$\begin{aligned} IC_{p,\text{O}_2} &= a_0T + a_1T^2 + a_2T^3 \\ a_0 &= 0.88020900 \cdot 10^3 \\ a_1 &= 0.98389375 \cdot 10^{-1} \\ a_2 &= -0.78057755 \cdot 10^{-5} \end{aligned} \tag{B.5}$$

Carbon dioxide

$$\begin{aligned} IC_{p,\text{CO}_2} &= a_0T + a_1T^2 + a_2\sqrt{T} \\ a_0 &= 1.71505960 \cdot 10^3 \\ a_1 &= -0.21271836 \cdot 10^{-2} \\ a_2 &= -0.30063942 \cdot 10^5 \end{aligned} \tag{B.6}$$

Product

$$
\begin{aligned}
IC_{p,\text{prod}} &= a_0 T + a_1 T^2 + a_2 T^3 a_3 \sqrt{T} \\
a_0 &= 0.16734839 \cdot 10^4 \\
a_1 &= 0.17514061 \\
a_2 &= -0.16401698 \cdot 10^{-4} \\
a_3 &= -0.16895935 \cdot 10^5
\end{aligned}
\qquad (B.7)
$$

Appendix C

Measured data from the scale model

Table C.1: Measured velocities in the scale model for the 12°-20° flow case.

z	v (m/s)		
	A	C	E
0.03	0.1	1.8	2.9
0.05	0.1	2.4	3.7
0.06	0.2	.	.
0.07	0.1	3.6	3.5
0.08	0.1	4.4	3.8
0.09	88.0	5.6	5.7
0.10	21.5	7.2	6.2
0.11	8.1	10.5	7.1
0.12	6.7	8.0	8.0
0.13	.	10.5	8.4
0.14	6.5	15.0	8.9
0.15	.	19.5	9.5
0.16	6.9	21.0	9.6
0.17	.	.	10.5
0.18	7.3	15.6	11.0
0.19	.	.	11.1
0.20	7.7	7.2	10.7
0.22	7.8	3.8	9.8
0.24	7.6	2.0	7.7
0.26	7.5	1.0	2.9
0.28	1.0	0.5	2.2
0.30	0.6	0.3	1.0
0.35	0.5	.	0.2
0.40	0.4	.	.
0.45	0.0	.	.
0.50	0.0	.	.

Table C.2: Measured normalized helium concentration in the scale model for the 12°-20° flow case.

z	He/He_0		
	A	C	D
0.00	0.0867	0.0533	0.0733
0.03	0.0867	0.0600	0.0667
0.06	0.0733	0.0667	0.0800
0.08	0.0733	0.0800	0.0933
0.09	0.0800	.	.
0.10	0.1067	0.0933	0.0933
0.11	0.2333	.	.
0.12	0.4800	0.1067	0.1000
0.13	0.5400	.	0.1067
0.14	0.4733	0.1200	0.1067
0.15	0.2333	0.1533	0.1133
0.16	0.0467	0.1467	0.1133
0.17	0.0333	0.1733	0.1200
0.18	.	0.1867	0.1333
0.19	.	0.1600	0.1267
0.20	0.0333	0.1533	0.1267
0.24	.	0.1000	0.1267
0.25	0.0600	.	.
0.28	.	0.0933	0.1133
0.30	0.1000	.	.
0.32	.	0.0933	0.1067
0.35	0.1000	.	.
0.36	.	0.1000	0.1067
0.40	0.1000	0.1000	0.1000
0.45	0.1000	0.1000	0.1000
0.50	0.1000	0.1000	0.1000

Table C.3: Measured velocities in the scale model for the 12°-12° flow case.

z	v (m/s)							
	A	B	C	D	E	F	G	H
0.03	0.0	0.2	1.5	3.0	4.9	5.9	5.4	2.0
0.04	0.0	0.2	2.2	3.5	6.0	5.3	4.4	3.6
0.05	0.0	0.4	3.3	5.0	6.8	6.2	4.2	2.7
0.06	0.0	0.9	4.8	6.8	7.3	6.9	4.3	3.1
0.07	0.0	1.2	7.0	8.0	8.1	7.1	3.8	2.8
0.08	83.0	2.7	10.0	10.8	9.2	7.3	4.4	2.7
0.09	74.0	18.0	10.5	12.0	10.5	7.7	4.7	3.0
0.10	3.5	49.0	13.5	14.0	11.8	7.5	4.4	2.1
0.11	4.0	39.1	19.0	16.2	12.8	7.6	4.3	2.4
0.12	6.5	11.8	24.0	19.5	14.0	6.5	4.7	3.2
0.13	6.8	7.4	23.0	20.5	13.4	6.3	4.3	3.0
0.14	7.1	7.2	14.0	19.5	13.0	6.6	4.2	2.9
0.15	7.0	7.3	9.0	17.0	12.9	5.0	2.6	3.4
0.16	7.2	7.4	7.2	13.5	12.7	4.7	2.4	2.9
0.17	7.4	7.7	6.8	11.2	9.0	4.8	2.6	3.0
0.18	7.5	7.4	6.4	7.2	8.1	3.0	2.0	3.1
0.19	7.5	7.3	5.8	5.4	5.7	1.8	1.5	2.8
0.20	7.5	7.4	5.0	4.2	5.6	2.2	1.6	2.8
0.21	7.7	7.3	4.3	3.4	3.9	1.7	2.3	2.2
0.22	7.6	7.2	3.5	3.0	2.7	1.3	1.2	2.4
0.23	7.5	7.0	1.6	2.6	2.1	0.4	1.2	1.8
0.24	7.3	6.3	1.0	2.1	1.8	0.2	0.8	2.3
0.25	7.2	4.9	0.4	1.3	1.4	0.1	0.9	2.0
0.26	7.0	1.9	0.0	0.9	1.1	.	.	.
0.27	6.0	0.5	0.0	0.8	0.8	.	.	.
0.28	0.5	0.1	0.0	0.4	0.7	.	.	.
0.29	0.2	0.0	0.0	0.3	0.7	.	.	.
0.30	0.1	0.0	0.0	0.3	0.6	.	0.4	1.2
0.31	0.1	.	.	.	.	.	.	.
0.32	0.0	.	.	.	.	.	.	.
0.33	0.0	.	.	.	.	.	.	.
0.34	0.0	.	.	.	.	.	.	.
0.35	0.0	0.0	0.0	0.1	0.5	.	0.2	1.0
0.40	0.0	0.0	0.0	0.0	0.4	.	0.0	0.7
0.45	0.0	0.0	0.0	0.0	0.0	.	0.0	0.4
0.50	0.0	0.0	0.0	0.0	0.0	.	0.0	.

Table C.4: Measured normalized helium concentration in the scale model for the 12°-12° flow case.

z	He/He_0					
	A	B	C	D	E	F
0.00	0.0854	0.0854	0.0732	0.0722	0.0889	0.0879
0.01	0.0793	0.0854	.	.	.	.
0.02	0.0793	0.0793	0.0732	0.0778	0.0833	.
0.03	0.0732	0.0793	.	.	.	0.0879
0.04	0.0671	0.0732	0.0732	0.0833	0.0889	.
0.05	0.0671	0.0793	0.0854	0.0833	.	.
0.06	0.0610	0.0732	0.0976	0.0944	0.0889	0.0879
0.07	0.0610	0.0854	0.0854	0.0944	.	.
0.08	0.0854	0.1037	0.1098	0.1167	0.0944	.
0.09	0.1768	0.1342	0.1159	0.1167	.	0.0879
0.10	0.4085	0.2134	0.1402	0.1333	0.0944	.
0.11	0.4390	0.2805	0.1463	0.1278	.	.
0.12	0.3293	0.3232	0.1707	0.1444	0.0944	0.0879
0.13	0.1220	0.2744	0.1646	0.1333	.	.
0.14	0.0427	0.2012	0.1768	0.1222	0.0944	.
0.15	0.0366	0.0915	0.1585	0.1278	.	0.0879
0.16	0.0366	0.0488	0.1342	0.1056	0.0889	.
0.17	.	.	.	0.1111	.	.
0.18	0.0366	0.0366	0.0854	0.0944	0.0889	0.0824
0.20	0.0366	0.0427	0.0732	0.0889	0.0889	.
0.21	.	.	.	.	.	0.0824
0.22	.	.	.	.	0.0889	.
0.24	.	.	.	.	0.0889	0.0879
0.25	0.0549	0.0732	0.0915	0.0889	.	.
0.26	.	.	.	.	0.0833	.
0.27	.	.	.	.	.	0.0824
0.28	.	.	.	.	0.0889	.
0.30	0.0915	0.0854	0.0854	0.0833	0.0833	0.0824
0.35	0.0976	0.0976	0.0889	0.0833	0.0833	0.0824
0.40	0.0976	0.0976	0.0889	0.0833	0.0778	0.0824
0.45	0.0976	0.0915	0.0833	0.0889	0.0833	0.0769
0.50	0.0976	0.0915	0.0833	0.0889	0.0833	0.0824

Principal symbols

a	coefficient in discretisation	
A	Van Driest constant	(-)
A	Arrhenius constant	
b	source term in discretisation	
C_p	specific heat at constant pressure	(J kg^{-1} K^{-1})
C_μ	empirical constant	(-)
d_0	inflow diameter	(m)
E	integration constant	
E	activation energy	(J kmole^{-1})
e	emissive power	(W m^{-2})
f	mixture fraction	(-)
G	production term of turbulent kinetic energy	(m^2 s^{-3})
g	mixture fraction fluctuation	(-)
g_i	gravity, i-th direction	(m s^{-2})
$\overline{g_i g_k}$	direct exchange area (gas-gas)	(m^2)
H	enthalpy	(J kg^{-1})
i'	intensity	(W m^{-2} sr^{-1})
K	absorption coefficient	(m^{-1})
k	kinetic energy of turbulence	(m^2 s^{-2})
k	reaction rate	
L	flame length	(m)
M_i	molecular mass of a species i	(kg kmole^{-1})
M_e	entrained mass	(-)
$\underline{n}$	unit normal vector	(-)
P	probability density function	(-)
p	pressure	(Pa)
Q	(radiative) heat flow	(W)
q''	heat flux	(W m^{-2})
R	universal gas constant	(J kmole^{-1} K^{-1})
r	radius	(m)
$\underline{r}$	positional vector	(m)
S	general source term	
s	stoichiometric mass ratio	(-)
$\overline{s_i s_j}$	direct exchange area (surface-surface)	(m^2)

$\overline{s_i g_k}$	direct exchange area (surface-gas)	(m^2)
T	temperature	(K)
t	time	(s)
U	internal energy	($J\,kg^{-1}$)
U	velocity parallel to wall	($m\,s^{-1}$)
U^*	friction velocity	($m\,s^{-1}$)
u_i	velocity component, i-th direction	($m\,s^{-1}$)
V	jet inflow velocity	($m\,s^{-1}$)
w	chemical reaction rate	($kmole\,s^{-1}$)
x	distance from symmetry plane in furnace	(m)
$\underline{x}$	position	(m)
x_i	coordinate, i-th direction	(m)
Y_i	massfraction of a species i	(-)
y	direction perpendicular to a wall	(m)
y	axial distance in furnace	(m)

Greek symbols:

α	mixing angle	(°)
α	precombustion or burnout	(-)
Γ_i	exchange coefficient of species i	(Pa s)
γ	vertical angle of overport burner	(°)
δ	horizontal angle of sideport burner	(°)
δ	Dirac delta function	(-)
δ_{ij}	Kronecker delta function	(-)
ϵ	dissipation rate of turbulent kinetic energy	($m^2\,s^{-3}$)
η	efficiency	(-)
θ	(polar) angle	(rad)
κ	Von Karman constant	(-)
λ	airfactor	(-)
λ	thermal conductivity	($W\,m^{-1}\,K^{-1}$)
λ	wavelength	(m)
μ	dynamic viscosity	(Pa s)
ξ	Schvab-Zel'dovich coupling function	(-)
ρ	density	($kg\,m^{-3}$)
σ	Prandtl or Schmidt number	(-)
τ	transmissivity	(-)
τ_{ij}	shear stress tensor	(Pa)
ϕ	general variable name	
ϕ	(polar) angle	(rad)
φ	general variable name	
Ω	solid angle	(sr)

subscripts:

air	(combustion) air
C	convection
D	diffusion
F	fuel
f	furnace
fg	flue gas
fuel	fuel
gas	of the natural gas
inert	inert chemical species
l	load
mix	of the mixture
O	oxygen
P	products
prod	products
r	roof
rad	radiative
ref	reference value
sens	sensible
st	stoichiometric
stat	static
std	standard
tot	total
t	turbulent
w	at or to the wall

superscripts:

$\overline{(.)}$	averaged
$(.)^-$	leaving from a surface
$(.)^+$	incident on a surface
$(.)'$	fluctuation term

Bibliography

Abbasi, H.A., Khinkis, M.J. and Fleming, D.K. (1984) Development of NO_x control methods for glass melting furnaces. Technical report, Gas Research Institute.

Abramovich, G.N. (1963) *The theory of turbulent jets.* The MIT Press, Massachusetts.

Barklage-Hilgefort, H. (1991) Reduktion der NO_x-Emission von Glasschmelzöfen durch Primärmaßnahmen. *VDI-Berichte*, 922:295–304.

Baulch, D.L., Drysdale, D.D., Duxbury, J. and Grant, S.J. (1973) *Evaluated Kinetic Data for high Temperature Reactions, Vol. 2: Homogeneous Gas Phase Reactions of the H_2–N_2–O_2 System.* Butterworths, London.

Beckervordersandforth, C.P., Flamme, M. and Kremer, H. (1987) Untersuchung NO_x-mindernder Maßnahmen an Industrie-Gasbrennern für Hochtemperaturprozesse. *VDI-Berichte*, 645:279–297.

Beér, J.M. and Chigier, N.A. (1972) *Combustion aerodynamics.* Applied Science Publishers.

Beerkens, R.C.G. (1986) *Deposits and condensation from the flue gases in glass furnaces.* PhD thesis, Eindhoven University of Technology, Eindhoven, The Netherlands.

Bilger, R.W. (1980) Turbulent flows with nonpremixed reactants. In Libby, P.A. and Williams, F.A., editors, *Turbulent Reacting Flows*, chapter 3. Springer Verlag.

Bird, R.B., Stewart, W.E. and Lightfoot, E.N. (1960) *Transport Phenomena.* John Wiley & sons, New York.

Bockhorn, H. (1989) Modellierung turbulenter Flammen: Berücksichtigung chemischer Reaktionen und Empfindlichkeitsanalyse des turbulenten Verbrennungsmodells. *VDI Berichte*, 765:45–55.

Bowman, C.T. (1975) Kinetics of pollutant formation and destruction in combustion. *Prog. Energy Combust. Sci.*, 1:33–45.

Caretto, L.S. (1976) Mathematical modeling of pollutant formation. *Prog. Energy Combust. Sci.*, 1:47–71.

Carvalho, M.G. (1983) *Computer simulation of a glass furnace.* PhD thesis, Imperial College, London.

Carvalho, M.G., Durão, D.F.G., Heitor, M.V., Pereira, J.C.F., Lockwood, F.C., Durst, F., Sommerfeld, M. and Silva, B. (1988) Improved design for glass smelting kilns. In Pilavachi, P.A., editor, *Industrial Processes, proceedings of a contractors' meeting.* Commission of the European Communities.

Doormaal, J.P. van and Raithby, G.D. (1984) Enhancements of the SIMPLE method for predicting incompressible fluid flows. *Num. Heat Transfer*, 7:147–163.

Drake, M.C. and Blint, R.J. (1991) Relative importance of nitric oxide formation mechanisms in laminar opposed-flow diffusion flames. *Combustion and Flame*, 83:185–203.

Elgobashi, S. (1977) Studies in the prediction of turbulent diffusion flames. In Launder, B.E., editor, *Studies in Convection*, pages 141–189. Academic Press.

Fenimore, C.P. (1971) Formation of nitric oxide in premixed hydrocarbon flames. *Proc. 13th Symposium (Int) on Combustion*, pages 373–380.

Flamme, M., Kremer, H. and Beckervordersandforth, C.P. (1989) NO_x-Emission und -Minderungspotential von Industriegasbrennern mit Verbrennungslufttemperaturen bis zu 1000 °C. *VDI Berichte*, 765:311–323.

Flamme, M. and Kremer, H. (1991) NO_x output from industrial burners using combustion air preheated to 1000 °C and NO_x control techniques. In *Proceedings of the 2nd European Conference on Industrial Furnaces and Boilers*, Vilamoura, Portugal.

Glassman, I. (1987) *Combustion*. Academic Press, 2nd edition.

Goody, R.M. (1964) *Atmospheric Radiation I, theoretical basis*. Oxford Clarendon Press.

Guenther, R. (1966) *Gaswärme*, 15:376.

Hanson, R.K. and Salimian, S. (1984) Survey of rate constants in the N/H/O system. In Gardiner, W.C., editor, *Combustion Chemistry*, chapter 6. Springer Verlag.

Hinze, J.O. and Hegge Zijnen, B.G. van der (1949) Transfer of heat and matter in the turbulent mixing zone of an axially symmetrical jet. *J. Appl. Sci. Res.*, A1:435–461.

Hottel, H.C. and Sarofim, A.F. (1967) *Radiative Transfer*. McGraw-Hill, New York.

Hyde, D.J. and Truelove, J.S. (1977) The discrete ordinate approximation for multi-dimensional radiant heat transfer in furnaces. Technical report, AERE, Harwell U.K., Thermodynamics Division.

Kamp, W.L. van de, Smart, J.P., Nakamura, T. and Morgan, M.E. (1989) NO_x reduction and heat transfer characteristics in gas fired glass furnaces. Technical Report IFRF Doc.No. f 90/a/4, IFRF, IJmuiden, The Netherlands.

Khalil, E.E. (1982) *Modelling of Furnaces and Combustors*. Energy and engineering science series. Abacus Press, Kent.

Kircher, U. (1986) NO_x-Emissionen und minderungsmaßnahmen in der Glasindustrie. *Gas Wärme International*, 35(4):207–212.

Launder, B.E. and Spalding, D.B. (1972) *Mathematical models of turbulence*. Academic Press, London.

Lefebvre, A.W. (1983) *Gas turbine combustion*. McGraw - Hill.

Libby, P.A. (1975) Studies related to turbulent flows involving fast chemical reactions. In Murthy, S.N.B., editor, *Turbulent mixing in nonreactive and reactive flows*, pages 333–365. Plenum Press.

Lockwood, F.C. and Naguib, A.S. (1975) The prediction of the fluctuations in the properties of free, round-jet, turbulent, diffusion flames. *Combustion and Flame*, 24:109–124.

Ludwig, C.B., Malkmus, W., Reardon, J.E. and Thomson, J.A.L. (1973) *Handbook of Infrared Radiation from Combustion Gases.* NASA.

Lundgren, T.S. (1967) Distribution functions in the statistical theory of turbulence. *The Physics of Fluids*, 10(5):969–975.

Miller, J.A. and Bowman, C.T. (1989) Mechanism and modeling of nitrogen chemistry in combustion. *Prog. Energy Combust. Sci.*, 15:287–338.

Nakamura, T., Kamp, W.L. van de and Smart, J.P. (1991) Further studies on high temperature natural gas combustion in glass furnaces. Technical Report IFRF Doc.No. f 90/y/7, IFRF, IJmuiden, The Netherlands.

O'Brien, E.E. (1980) The probability density function (pdf) approach to reacting turbulent flows. In Libby, P.A. and Williams, F.A., editors, *Turbulent Reacting Flows*, chapter 5. Springer Verlag.

Patankar, S.V. and Spalding, D.B. (1972) A calculation procedure for heat, mass and momentum transfer in three-dimensional parabolic flows. *Int. J. Heat Mass Transfer*, 15:1787–1806.

Patankar, S.V. (1980) *Numerical Heat Transfer and Fluid Flow.* Hemisphere, New York.

Peeters, T.W.J. and Meer, Th.H. van der (1992) Assumed shape pdf modelling in combustion simulations. submitted for Comb Flame.

Peters, N. (1984) Laminar diffusion flamelet models in non-premixed turbulent combustion. *Prog. Energy Combust. Sci.*, 10:319–339.

Pope, S.B. (1976) The probability approach to the modelling of turbulent reacting flows. *Combustion and Flame*, 27:299–312.

Post, L. (1988) *Modelling of flow and combustion in a glass melting furnace.* PhD thesis, Delft University of Technology.

Rhine, J.M. and Tucker, R.J. (1991) *Modelling of gas-fired furnaces and boilers and other industrial furnaces.* British Gas technical monographs, McGraw-Hill.

Rhodes, R.P. (1975) A probability distribution function for turbulent flows. In Murthy, S.N.B., editor, *Turbulent mixing in non-reactive and reactive flows*, pages 235–241. Plenum Press, New York.

Rodi, W. (1984) *Turbulence models and their application in hydraulics.* IAHR, Delft.

Siddal, R.G. (1986) Accurate evaluation of radiative direct-exchange areas for rectangular geometries. In *Proc. 8th Int. Heat Transfer Conf.*, pages 751–755, San Francisco.

Spalding, D.B. (1971) Mixing and chemical reaction in steady confined turbulent flames. *Proc. 13th Symposium (Int) on Combustion*, pages 649–657.

Tennekes, H. and Lumley, J.L. (1972) *A first course in turbulence.* MIT Press, Cambridge.

Thring, M.W. and Newby, M.P. (1953) Combustion length of enclosed turbulent jet flames. *4th Symp. on Combustion*, pages 789–796.

Tribus, M. (1961) *Thermostatics and Thermodynamics.* Van Nostrand.

Trier, W. (1984) *Glasschmelzöfen, Konstruktion und Betriebsverhalten.* Springer, Berlin.

Van Wylen, G.J. and Sonntag, R.E. (1976) *Fundamentals of classical thermodynamics.* Wiley.

Warnatz, J. (1983) Hydrocarbon oxidation at high temperatures. *Ber. Bunsenges. Phys. Chem.*, 87:1008–1022.

Warnatz, J. (1983) Survey of rate coefficients in the C/H/O system. Technical Report, Sandia Report SAND83-8606, Sandia National Laboratories.

Warnatz, J. (1984) Survey of rate constants in the C/H/O system. In Gardiner, W.C., editor, *Combustion Chemistry*, chapter 5. Springer Verlag.

Westley, F. (1980) Table of recommended rate constants for chemical reactions occuring in combustion. Technical Report NSRDS-NBS 67, National Bureau of Standards.

Wieringa, J.A., Elich, J.J.Ph. and Hoogendoorn, C.J. (1990) Spectral effects of radiative heat-transfer in high-temperature furnaces burning natural gas. *Journal of the Institute of Energy*, LXIII(456):101–108.

Wieringa, J.A. (1992) *Spectral radiative heat transfer modelling.* PhD thesis, Delft University of Technology, Delft, The Netherlands.

Zel'dovich, J. (1946) The oxidation of nitrogen in combustion and explosions. *Acta Physicochimica URSS*, XXI(4):577–628.

Summary

In this thesis flow, combustion and NO_x formation in natural gas fired high temperature furnaces is discussed. In particular the geometry of a test furnace of the International Flame Research Foundation has been studied. For this study the numerical model FURNACE, with which flow, turbulence, combustion of natural gas and radiative heat transfer can be simulated, has been used. This study has two aims, (*i*) verification of the used model and (*ii*) investigation of the influence of mixing on the formation of nitric oxide.

The numerical model FURNACE has been developed before by Post (1988) for a compartment of a cross-fired regenerative glass melting furnace. The model describes turbulent combustion by a one-step combustion reaction. Intermittency — the alternating presence in time of natural gas and fuel at a particular point in the furnace — influences the combustion and is described by a pdf (probability density function) consisting of two delta functions. In this thesis the existing combustion model has been extended with a simple model for the intermediate formation of CO in the flame.

To the simulation model FURNACE a post-processor has been added that describes the formation of thermal NO_x. This sub-model describes the formation of NO via the Zel'dovich mechanism. First, the averaged quantities that are computed by the combustion model were used to compute the source term of NO. Later, averaging of the source term over a (clipped) top hat pdf has been used for the NO source term computation to account for the turbulent fluctuation of the temperature and the species concentrations.

We have performed measurements in an isothermal scale model of the test furnace of the IFRF to validate the turbulent flow model. This scale model is a 1:2 model of the IFRF furnace. Visualization of the flow was used to get a general impression of the flow in the furnace. Measurements of the velocity and of the mixing of a passive scalar (helium) supplied data that could be compared with the results of simulations of the scale model. The results of the simulations of the scale model agree well with the measured data. The flow field is predicted with good accuracy, which could be seen in the comparison of the measured and simulated velocities. The turbulent mixing is also predicted reasonably accurate. The comparison of the simulated and the measured data with the semi-analytical solution of a free jet has led to the recommendation to use the solution for a free jet as a boundary condition for the simulations to improve the predictions in the first part of the jet.

We have verified the numerical model against measurements of the IFRF in the case of combustion at high furnace temperatures. First we have used the baseline flame of the NG6 investigations as a reference for a sensitivity analysis of the model. Several model parameters were tested and our initial guesses were validated. E.g. the extinction coefficient K for the thermal radiation model is an unknown model constant. We have verified our initial guess of $K = 0.12$ by performing simulations with FURNACE for the upper and lower boundary of K, that were computed with a statistical narrow band model. We have used the heat flux distribution to the load, the flue gas temperature and the efficiency for the comparison of the simulated results with the measured results. Beside this model constant also some boundary conditions for the model were tested. It has been shown that the load temperature boundary condition has a large influence on the results of the simulations. Therefore, whenever possible, we have used the measured load temperature as the boundary condition for the simulations. For the simulations a fairly coarse grid has been used. We have tested the grid dependence of the results by using several grids and comparing the results of the simulations. It was concluded that grid independence had not yet fully been reached, but that the grid was sufficienctly fine. Ultimately, the sensitivity analysis resulted in a set of parameters and boundary conditions and a grid size that has been used throughout most of the simulations.

Next, some parameter variations of the NG6 and NG7 experiments by the IFRF were simulated with the computer model. Comparison of the simulated data with the measured data gives the following results:

- The largest differences between the simulated and measured flue gas temperatures are approximately 50 K. Since this is less than the estimated error of measurement, the flue gas temperatures agree very well.
- The measured and computed furnace efficiencies also agree very well. Differences between the measured and computed load efficiencies may be attributed to the value of the heat loss to the walls that is used by the IFRF for the computation of the load heat flux. Taking a larger value for this heat loss than the IFRF leads to smaller differences between the computations and the measurements.
- The heat flux to the load has been computed with reasonable accuracy. The load temperature boundary condition has a large influence on the results of the simulation model. For the simulations of the NG6 flames a load temperature profile was used, which resulted in a good agreement of the heat flux in the first part of the flame. At the end of the furnace the agreement was less good, which was attributed to the temperature boundary condition of the back wall. For the NG7 flames the measured load temperature has been used as the boundary condition. In the first two segments the measured load temperature was more than 50 K lower than in the next segments. In the simulations this measured load temperature profile was used, which resulted in too high heat fluxes in the first two Hottel zones. It was shown that increasing the load temperature in the first two Hottel zones for the simulations resulted in a much better agreement with the measurements.
- In-flame measurements of the temperature and species concentrations were com-

pared with simulated results. For the baseline NG6 underport fired flame (32° mixing angle) the temperature predictions appeared to be accurate, but the oxygen concentration showed discrepancies, especially in the recirculation zone. For the NG7 overport fired flame with parallel injection of natural gas and combustion air, however, the temperature predictions were too high. The simulation resulted in a rather short hot flame, while the measurements showed a slowly developing, relatively cool flame. For this overport flame, however, the oxygen concentration was predicted quite accurately, also in the recirculation zone.

- Except for a few cases where the simulation model or a sub-model is no longer valid, the computed NO_x emissions differ at most 20 % from the measured NO_x emissions. This is true for both the NG6 trials and the NG7 trials. Results of the NG6 trials that are incompatible with results of the NG7 investigation have been disregarded. Considering the accuracy of the measurements, which we estimated to be not better than 10 % for the NO_x emissions, this discrepancy between measurements and simulations is satisfactory.

To assess the influence of mixing of natural gas, combustion air and combustion products on the formation of NO several injection modes were tested.

Underport firing is a commonly used injection method in industrial furnaces. The influence of both the mixing angle and the gas-injection velocity was tested in the simulations. The mixing angle displayed only a limited influence on the NO_x emission. The range of NO_x emissions is 900 to 1100 ppm during NG7, with a slight minimum at the 32° to 36° mixing angles. Increasing gas-injection velocities resulted in slightly decreasing NO_x emissions (cf. NG6). This could be explained by the increased strength of the recirculation that is found for increasing gas-injection velocities.

Overport firing was expected to give lower NO_x emissions because the natural gas is injected more directly into the recirculation zone. The observed effect of the mixing angle, however, showed that the overport natural gas mixes with combustion air predominantly, especially at the higher mixing angles. At the low mixing angles the combustion is so slow that full burnout is not achieved, so that these flames, although low in NO_x emission, are not applicable. The predicted NO_x emissions range from 750 ppm at the lowest mixing angle to 1500 ppm at the highest mixing angle.

The combination of underport and overport firing showed some effect on the NO_x emission in the measurements. The NO_x emission ranged from 1200 ppm for the fully underport flame (with v_{gas} = 250 m/s) to 800 ppm at equal distribution between the underport and the overport injection ports (with v_{gas} = 125 m/s) to 1700 ppm at the fully overport flame (with v_{gas} = 250 m/s. Around the equal distribution ratio there is only a small effect of the distribution ratio on the NO_x emission. For distribution ratios around the equal distribution ratio, simulations have been performed, with results that agree well with the measurements.

Sideport firing generally gives the fastest mixing flames. The natural gas is injected directly into the combustion air, which results in fast combustion, high temperatures and a high NO_x emission. For the simulated flames the range of the NO_x

emission for the various mixing angles was 2000 to 2200 ppm.

Parallel sideport firing generally gives the lowest NO_x emissions. For the high gas-injection velocity that was used in the simulations, the mixing is not quite as slow as for the lower velocities. This resulted in average NO_x emissions for the simulated flames, viz. approximately 1200 ppm.

From the injection mode variations the influence of the mixing of natural gas, combustion air and combustion products has become clear. In the case of natural gas injection into regions where one would expect mixing of the natural gas with mainly combustion products, increased mixing, results in a lower NO_x emission. The increased mixing lowers the temperature of the flame, which gives the desired effect. On the other hand, if the natural gas is injected in such a way that the natural gas mixes predominantly with combustion air, increasing the mixing will lead to increased NO_x emissions. This is caused by the faster combustion that occurs for these flames, which results in a higher flame temperature and consequently higher NO_x formation.

The comparison between the measurements and the simulations shows that the model that we have used is capable of predicting NO_x emission trends. The range of the NO_x values is predicted with an difference of at most 20 % with the measurements. Through the simulations of several injection modes ("burners") it has been shown that the model is capable of evaluating different burner concepts.

Samenvatting

In dit proefschrift wordt stroming, verbranding van aardgas en vorming van stikstofoxiden in hoge temperatuur ovens beschreven. Het onderzoek heeft zich toegespitst op de geometrie van een semi-industriële proefoven van de International Flame Research Foundation te IJmuiden. In dit onderzoek is het numerieke model FURNACE gebruikt, waarmee stroming, turbulentie, verbranding van aardgas en straling in hoge temperatuur ovens berekend kunnen worden. Het onderzoek heeft zich gericht op twee doelen, (*i*) het valideren van het numerieke model en (*ii*) het onderzoeken van de invloed van menging op de vorming van stikstofoxiden.

Het numerieke model FURNACE was reeds eerder door Post (1988) ontwikkeld voor een compartiment van een dwarsgestookte regeneratieve glasoven. Het model beschrijft de turbulente verbranding met behulp van een eenstaps-verbrandingsreactie, waarop intermittentie — het afwisselend voorkomen in de tijd van brandstof en zuurstof op één plaats — beschreven door een kansdichtheidsfunctie (pdf, probability density function) bestaande uit twee delta-functies invloed heeft. Het bestaande verbrandingsmodel is uitgebreid met een eenvoudig model voor de vorming van koolmonoxide in de vlam.

Als post-processor is een submodel voor de vorming van thermische NO_x aan FURNACE toegevoegd. Hierin wordt de vorming van NO volgens het Zel'dovich mechanisme beschreven. In eerste instantie is bij de berekeningen van de NO_x-vorming uitgegaan van de gemiddelde grootheden, zoals bijvoorbeeld temperatuur en stofconcentraties, die door het stromingsmodel waren berekend. Later is weging met een "top hat" pdf gebruikt voor de berekening van de bronterm, waardoor de invloed van turbulente fluctuaties van de temperatuur en de concentraties van verschillende stoffen op de vorming van stikstofoxide beschreven wordt.

Er zijn metingen gedaan in een koud schaalmodel van de testoven van het IFRF om het turbulente stromingsmodel te valideren. Dit schaalmodel is een isotherm 1:2 model van de IFRF-oven. Hierin is door middel van visualisatie een algemene indruk van het stromingspatroon in de oven verkregen. Snelheidsmetingen en metingen van de opmenging van een passieve component (helium) leveren quantitatieve gegevens over de stroming die goede overeenstemming vertonen met de resultaten van berekeningen met FURNACE in het koude model. De gemeten en berekende gegevens zijn vergeleken met de semi-analytische oplossing van een vrije straal. Dit heeft tot de aanbeveling geleid om deze semi-analytische oplossing als randvoorwaarde aan het programma op te leggen om de berekeningen van het eerste gedeelte van de vlam te verbeteren.

Resultaten van berekeningen zijn vergeleken met metingen door het IFRF in de oven met verbranding bij hoge temperatuur. Allereerst is de standaardconfiguratie van een serie metingen (NG6) gebruikt als referentie voor een gevoeligheidsanalyse van het model. Hierin zijn van enkele modelparameters de oorspronkelijke aannames geverifieerd. De extinctiecoëfficient K in het stralingsmodel bijvoorbeeld, is een van te voren onbekende parameter. Onze oorspronkelijke aanname, nl. $K = 0.12$, is geverifieerd door ook enkele simulaties uit te voeren met een hogere en een lagere waarde voor K. De verdeling van de warmteoverdracht naar de bodem en enkele globale grootheden zoals de rookgastemperatuur en het ovenrendement zijn gebruikt om de simulaties en de metingen met elkaar te vergelijken. Ook is de invloed van de gebruikte randvoorwaarden getest. Zo is aangetoond dat de temperatuur van de bodem een grote invloed heeft op het resultaat van de simulaties. Waar mogelijk is de gemeten bodemtemperatuur als randvoorwaarde opgelegd voor de simulaties. Er is een vrij grof rooster gebruikt voor de simulaties. De roosterafhankelijkheid is getest door op verschillende roosters berekeningen te doen en de resultaten te vergelijken. Hoewel de resultaten nog niet volledig onafhankelijk waren van het gebruikte rooster, is geconcludeerd dat het gebruikte rooster voldoende fijn was. Uiteindelijk is een standaardmodel voor de simulaties vastgesteld, met parameters en randvoorwaarden die in de overige simulaties constant zijn gehouden.

Vervolgens zijn enkele van de parametervariaties van de metingen van het IFRF (NG6 en NG7 meetseries) met behulp van het computermodel gesimuleerd. Een vergelijking van de gemeten en berekende gegevens geeft het volgende resultaat:

- De grootste verschillen tussen de gemeten en berekende rookgastemperaturen zijn ongeveer 50 K. Dit is minder dan de geschatte meetfout, dus er is een goede overeenstemming tussen de gemeten en de berekende rookgastemperaturen.
- De gemeten en berekende ovenrendementen komen goed met elkaar overeen. Verschillen tussen de gemeten en berekende bad-rendementen kunnen verklaard worden uit de schatting van de wandverliezen door het IFRF. Worden grotere dan de geschatte wandverliezen aangenomen dan zijn de verschillen kleiner.
- De badbelasting word redelijk goed voorspeld. De temperatuur randvoorwaarde van de bodem heeft een grote invloed op het resultaat. Voor de NG6 simulaties is een goede schatting gebruikt als randvoorwaarde, waardoor de metingen en de simulaties in de eerste helft van de oven met elkaar in overeenstemming zijn. Aan het einde van de oven treden verschillen op in de badbelasting, wat waarschijnlijk wordt veroorzaakt door de temperatuur randvoorwaarde van de achterwand. Voor de simulaties van NG7 zijn de gemeten bodemtemperaturen gebruikt. Doordat de bodemtemperatuur in de eerste twee segmenten van de oven 50 K lager was dan in de volgende segementen, voorspelt het model hier te hoge badbelastingen. Er is aangetoond dat het verhogen van de bodemtemperatuur bij de simulaties verbetering van de resultaten te zien geeft.
- Door het IFRF zijn lokale metingen van de temperatuur en stofconcentraties in de vlam uitgevoerd. De metingen van de temperatuur in de underport vlam met een menghoek van 32° tijdens NG6 stemden goed overeen met de berekende

resultaten. De zuurstofconcentratie gaf echter vrij grote verschillen te zien, met name in de recirculatiezone. De overport vlam met parallelle injectie van aardgas en lucht tijdens NG7, laat echter grote verschillen zien tussen de berekende en de gemeten temperatuur. De berekeningen laten een korte vlam zien met een hoogste temperatuur van 2200 K op 1 m van de instroom, terwijl de metingen een lange relatief koude vlam laten zien. Hierbij is de hoogste temperatuur 1823 K op 2.5 m van de instroom. De berekende en de gemeten zuurstofconcentraties van deze vlam stemmen daarentegen goed overeen.

- Behoudens een enkele situatie waarin het model niet meer geldig is, of het gekozen rooster te grof, geven de NO_x-emissies verschillen van maximaal 20 % te zien. Dit geldt voor zowel de NG6 als de NG7 variaties, waarbij metingen van NG6 die strijdig zijn met die van NG7 zijn weggelaten. Gezien de geschatte meetfout van 10 % voor de NO_x-emissie, is dit een bevredigend resultaat.

Om de invloed van de menging van aardgas, verbrandingslucht en verbrandingsproducten op de NO_x-emissie te bepalen zijn verschillende aardgas injectiepunten getest.

Underport injectie van aardgas is een veelgebruikte methode in industriële ovens. De invloed van de menghoek en de gasinjectiesnelheid op de NO_x-emissie is bepaald. Tijdens NG7 had de menghoek een beperkte invloed op de NO_x-emissie. Bij de 32° en 36° menghoek vertoonde de NO_x-emissie een minimum, over het gehele geteste gebied varieerde de NO_x-emissie tussen de 900 en 1100 ppm. Tijdens NG6 is de gasinjectiesnelheid gevarieerd. Bij toenemende snelheid werd in de simulaties een sterkere recirculatie gevonden en lagere NO_x-emissies.

Bij overport injectie werd een lagere NO_x-emissie verwacht omdat het aardgas in de gerecirculeerde gassen geïnjecteerd wordt. Uit de resultaten blijkt echter dat er voornamelijk menging met verbrandingslucht optreedt, met name bij de grotere menghoeken. Bij parallelle injectie van aardgas en verbrandingslucht is de verbranding zeer traag en brandt de vlam niet helemaal uit in de oven. Daarom is deze vlam niet bruikbaar, hoewel de gemeten NO_x-emissie laag was (350 ppm). De simulaties gaven NO_x-emissies van 750 ppm, bij de laagste menghoek, tot 1500 ppm.

Gecombineerd underport/overport injecteren gaf bij de metingen een zekere invloed op de NO_x-emissie te zien. Volledig underport injecteren van aardgas gaf 1200 ppm NO_x in de rookgassen, een gelijke verdeling tussen underport en overport injectie gaf 800 ppm en volledig overport injecteren gaf 1700 ppm. Rondom het minimum is de invloed van de verdeling gering. De simulaties stemden goed overeen met de metingen rondom het minimum.

Sideport injectie geeft in het algemeen de snelste menging. Door de directe injectie van het aardgas in de verbrandingslucht treedt snelle verbranding op, is de vlamtemperatuur hoog en vinden we hoge NO_x-emissies, in de orde 2000 tot 2200 ppm voor de gesimuleerde vlammen.

Parallel sideport injectie geeft in het algemeen de laagste NO_x-emissies. Omdat er alleen vlammen zijn gesimuleerd met een vrij hoge gasinjectiesnelheid zijn de

berekende NO_x-emissies (1100 tot 1400 ppm) van gemiddelde waarde.

Uit deze variaties van het injectiepunt van het aardgas blijkt dat de positie van het injectiepunt invloed op de NO_x-emissie heeft. Het punt waarop het aardgas in de oven geïnjecteerd wordt, bepaalt waarmee het aardgas zich in de oven zal mengen. Bij zodanige injectie dat er voornamelijk met verbrandingsproducten gemengd wordt, heeft een vergroting van de menging door bijvoorbeeld een vergrote menghoek een NO_x-emissie verminderende invloed. Door de menging met voornamelijk verbrandingsproducten wordt de vlamtemperatuur enigszins verlaagd, wat het beoogde effect veroorzaakt. Bij zodanige injectie, dat er voornamelijk met verbrandingslucht gemengd wordt, heeft een vergroting van de menging versnelling van de verbranding tot gevolg. Dit resulteert in hogere vlamtemperaturen en als gevolg van de sterke temperatuurafhankelijkheid van de NO_x-vorming ook in een verhoging van de NO_x-emissie.

De vergelijking van de gemeten en de berekende resultaten blijkt dat het model in staat is trends van de NO_x-emissie te voorspellen. De waarde van de NO_x-emissie wordt tot op 20 % nauwkeurig voorspeld. Uit de simulaties met verschillende injectiepunten van het aardgas blijkt dat het model gebruikt kan worden om verschillende branders en ovens te evalueren.

Acknowledgements

Op deze plaats wil ik een ieder bedanken die betrokken is geweest bij de realisatie van dit proefschrift. In de eerste plaats ben ik prof. Hoogendoorn erkentelijk voor de kundige begeleiding tijdens mijn promotiewerk. Zijn fysisch inzicht is van groot belang geweest voor het onderzoek.

De discussies met Theo van der Meer over de resultaten van het numerieke werk hebben veel bijgedragen tot de uiteindelijke voltooiing van dit proefschrift. Tim Peeters wil ik graag bedanken voor het feit dat ik van hem de uitgebreide pdf modellering en het gebruik van tabellen om de berekeningen te versnellen heb kunnen overnemen.

Met Jan Wieringa, mijn kamergenoot gedurende vier jaar, heb ik vele discussies gevoerd over ons beider werk. Deze discussies, en het prettige samen werken op een kamer, heb ik zeer gewaardeerd. Ook wil ik Jan graag bedanken voor het feit dat ik enkele resultaten van zijn spectrale modellen heb mogen gebruiken voor dit proefschrift.

Bij Jaap Beekman heb ik altijd kunnen aankloppen als ik een probleem met een computer had, ook al had hij eigenlijk geen tijd. Hiervoor, en voor het vertrouwen dat ik kreeg met betrekking tot het beheer van het computerpark, wil ik hem graag bedanken. Rob Kuyper wil ik bedanken voor zijn hulp met AVS en allerlei andere nuttige (LaTeX!) en minder nuttige computerprogramma's. Ook toen hij met zijn eigen proefschrift was begonnen was hij nog bereid met computerwerk te helpen.

Rimmert Hoekstra wil ik bedanken voor zijn onmisbare hulp tijdens de korte tijd dat ik experimenteel werk heb gedaan. Alleen door zijn inzet heb ik de metingen in zo korte tijd kunnen afronden.

Verder wil ik iedereen van de sectie Warmtetransport bedanken voor de prettige tijd, tijdens afstuderen en promoveren, die ik in de groep gehad heb.

Met Kees Dijkstra van Gasunie heb ik in de moeilijke begintijd nuttige discussies over mijn numerieke werk en het experimentele werk van het IFRF gevoerd. Ook nadat hij niet meer de begeleider vanuit Gasunie was bleef hij zijn betrokkenheid bij het onderzoek tonen. Leo Korstanje, die Kees' positie overnam heeft in korte tijd het onderzoek leren kennen en vele nuttige vragen gesteld.

I would like to thank both Willem van de Kamp and Tsuneaki Nakamura of the IFRF for their friendly cooperation. They have provided me with many insights into the experimental research of combustion. Also, I would like to thank them for providing me with the experimental data, that constitute such an important part of the validation of the numerical model. The permission of the NGNOx consortium, consisting of the

following companies: NV Nederlandse Gasunie, British Gas, Gaz de France, Osaka Gas, Tokyo Gas and Snam, to use the data of the NG6 and NG7 trials is gratefully acknowledged.

Tot slot wil ik graag mijn familie en vrienden bedanken voor de belangstelling die altijd werd getoond voor het onderzoek en de mentale ondersteuning bij het schrijven van het proefschrift.

About the author

July 17th, 1964 : born in Rotterdam, The Netherlands

1976 - 1982 : Gymnasium β at the Revius Lyceum, Doorn, The Netherlands

1982 - 1987 : Applied Physics study at Delft University of Technology, The Netherlands

Ingenieur thesis (MSc thesis), performed in the Section Heat Transfer, Faculty of Applied Physics:
Numerical modelling of flow in a single wafer Chemical Vapour Deposition reactor.

1988 - 1992 : PhD study at Delft University of Technology, Faculty of Applied Physics, Section Heat Transfer, under the supervision of Prof. ir. C.J. Hoogendoorn

1993 : Research Physicist in the Process Physics Department of the Institute of Applied Physics (TPD - TNO/TU Delft), Delft, The Netherlands